The University Of Sheffield.

High density heat storage for homes

James Kenneth William Moore

Supervisors:

Dr Solomon Brown

Professor Peter Styring

A Thesis Submitted for the Degree of

Doctor of Philosophy

Department of Chemical and Biological Engineering

Saturday, 19 December 2020

Abstract

The United Kingdom has an objective of reducing fossil fuel emissions to 80% lower than 1990s' levels by 2050 mandated by the UK Climate Change Act [1]. With 47% of total final energy demand in the UK as of 2012 attributable to heating demand [2], methods to decarbonise the UK's heating supply are essential to hitting emissions targets.

Phase change material (PCM) based heat storage, a subset of energy storage, presents a unique opportunity to temporally displace the consumption of energy from its production, providing a solution to reduce the economic costs of transitioning to a low carbon energy supply.

This thesis details experimental and computational fluid dynamic modelling investigations, (with Ansys Fluent), using temperature dependant properties of the melting process of beeswax and paraffin wax in several isothermal configurations intended to emulate underfloor heat storage using phase change. The effect of changing a key parameter of these models, the mushy constant is also investigated and analysis is performed with dimensionless and non-dimensionless variables.

Experimentation quantified the melt process of these materials with temperature sensors, thermal and visual camera imagery for validation of the generated models.

Moderate agreement is found with the latter paraffin wax model and experimental data however beeswax models were found to be invalid with larger domain models having issues with model convergence and mesh resolution / time step insensitivity.

Experimentation had success with visual and thermal imaging despite thermal attenuation by the vessel walls; thermal imaging was found to be unable to visualise small length scale phenomena.

The temperature sensor matrix had some success despite over-prediction of melt fraction due to lack of sensors at the vessel edges. In addition, these sensors contributed negatively to isotropy due to heat losses through the wires from the melting material.

1 Acknowledgements

I would like to first thank my supervisors Dr Solomon Brown and Professor Peter Styring for their support and encouragement throughout the years of my PhD studies, particularly Solomon, who helped shape and direct my work directly into this thesis.

I would also like to thank the Sheffield University Chemical and Biological engineering workshop team who've helped me put together the various pieces of test equipment required for experimentation and additionally CiCS / the CiCS High Performance Computing team without which I would never have been able to run so many simulations.

Thanks also go to Sharon Brown of the EPSRC CDT in Energy Storage and its Applications for her help in the day to day administration of the CDT and my involvement within it.

I express a great deal of gratitude to my parents and family members who have had to endure on more than one occasion my ramblings about my PhD, related CFD, melting based phenomena and general chemical engineering (aka everything is a type of pipe engineering.)

This research has been funded via the EPSRC CDT in Energy Storage and its Applications (EP/L016818/1) grant.

Contents

List of Figures

List of Tables

Nomenclature

Variables

β	the coefficient of thermal expansion (K^{-1})
C	mushy zone constant (kg/s)
C_P	specific heat at constant pressure (J/kg K)
F	external body forces (N)
g	gravitational acceleration (m/s^2)
Gr	Grashof number
h	sensible enthalpy (J/kg)
h_{ref}	reference enthalpy at reference temperature (K)
h_c	convective heat transfer coefficient ($Wm^{-2}K^{-1}$)
H	total enthalpy of material (J/kg)
ΔH	latent heat (J/kg)
k	thermal conductivity of material (W/m K)
L	material latent heat enthalpy (J/kg)
L_h	Characteristic length 0.025 (m) flat plate, 0.01 (m) pipe –2D hot surface length [3]
Δm	mass difference (kg)
Nu	Nusselt Number
P	Pressure (Pa)
Pe	Peclet number
Pr	Prandtl number
ρ	density (kg/m^3)
ρ_f	fluid density (kg/m^3)
Ra	Rayleigh number
Re	Reynolds number
S	source term

t	time (s)
T	temperature (K)
T_L	liquidus temperature (K)
T_S	solidus temperature (K)
T_{ref}	reference temperature (K)
τ_S	surface temperature – 353.15° (K)
τ_∞	bulk temperature (K) – computed as a 2D volume average
τ	time (s)
$\overline{\tau}$	stress tensor
$\bar{v}$	fluid velocity (m/s[1])
ν	kinematic viscosity (Pa ·s)
V	probe volume (m^3)
γ	liquid fraction
$\in$	= 0.001 , a small constant used to avoid division by zero

Abbreviations

TES – Thermal Energy Storage.

DSC – Differential Scanning Calorimetry.

DECC – Department of Energy and Climate Change, now DBEIS.

DBEIS – Department of Business, Energy and Industrial Strategy.

PCM – Phase Change Materials.

GHG – GreenHouse Gases.

HTF – Heat Transfer fluid.

COP - Coefficient Of Performance.

CAD – Computer Assisted Design.

PMMA - Poly(methyl-methacrylate), acrylic, acrylic glass, Perspex or Plexiglas.

Preface

Rerum Cognoscere Causas

-University of Sheffield motto

Quanta calor ille inter tabulatum?

-Further ostentatious Latin

1 General Introduction

1.1 Introduction

The world is facing an unprecedented crisis due to global warming caused by emission of greenhouse gases (GHGs) which are majorly driven by the human requirement for heating, cooling and transportation.

With increases in energy demand related to a growing world population, industrial and technical developments and a worldwide increase in quality of life, it is becoming absolutely critical to efficiently and sustainably generate and distribute energy.

Over the previous several decades great strides have been made in various sectors such as renewable energy to address this; however these technologies are not without their own shortcomings.

Depending on the specific type of renewable energy, they can have extremely energy low conversion factors, large seasonal production variation, geo-physical restrictions etc… These issues considered, the primary issue with the majority of renewable energy production methods is the inability to schedule their supply to match human demand.

One technology to avoid this problem and assist with electrical grid stability in general is energy storage. An energy storage vector would allow for the buffering / storage of energy during periods of excess supply then to be resupplied during periods of excess demand.

The motivation for heat storage is similar or the same as the drivers for energy storage in general, either a need to store energy on a mobile basis, or as a means of optimising a larger system / arbitrage, or the ability to deal with unsteady generation sources and abatement of capital intensive grid reinforcement.

In order to reduce or avoid the damage associated with climate change the efforts to decarbonise the UK (and numerous other countries) will without a doubt require some forms of energy storage.

In particular, in addition to the UK Climate Change Act (and wider EU directives) establishing binding targets to reduce carbon dioxide emissions, the UK has also set a national target for an 80% reduction in greenhouse gas emissions by 2050 [2]. This has direct ramifications in terms of lowering carbon intensity. Consequently, heat storage is starting to receive increasing

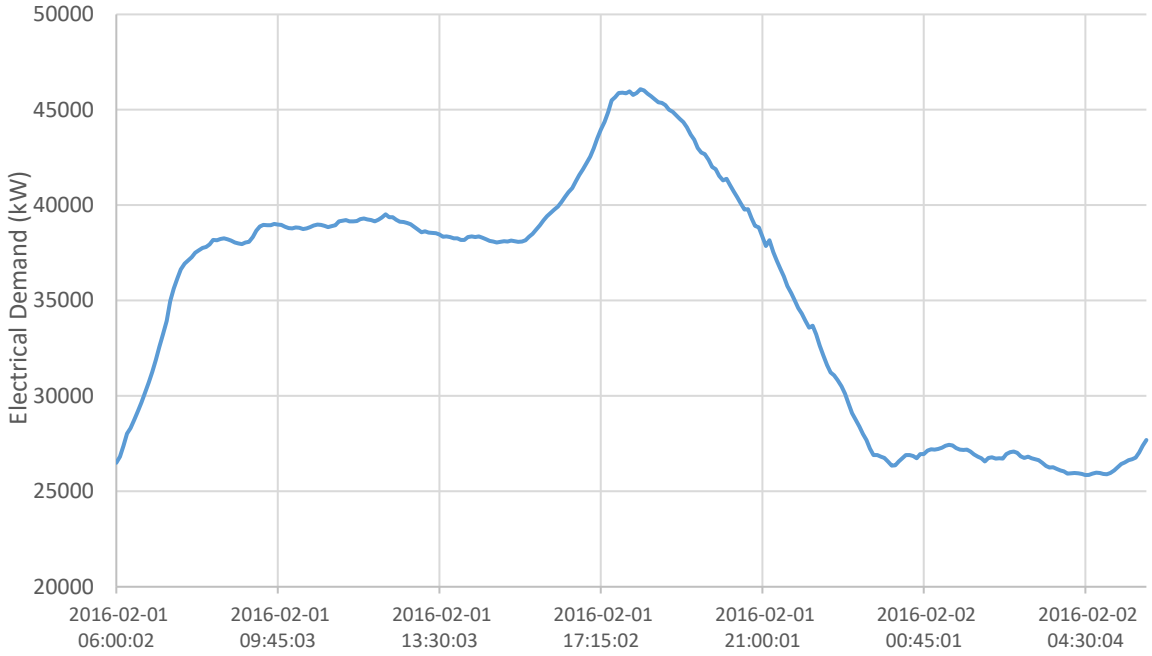

Figure 1 - United Kingdom electrical energy demand from February 1st 2016 [5].

attention and will likely require forms of storage somewhere in the energy supply chain to maintain low carbon intensity due to supply and demand patterns.

In the UK there are a very predictable seasonal and daily patterns in energy consumption. A typical day to night cycle can be found above in Figure 1 and features an initial rise in the morning which briefly flattens before peaking around 6pm and tailing off to a fixed lower demand overnight.

Over the course of a year, the winter months drive up gas demand to a peak almost three times the amount during summer as can be seen in Figure 2. There is also a similar albeit far

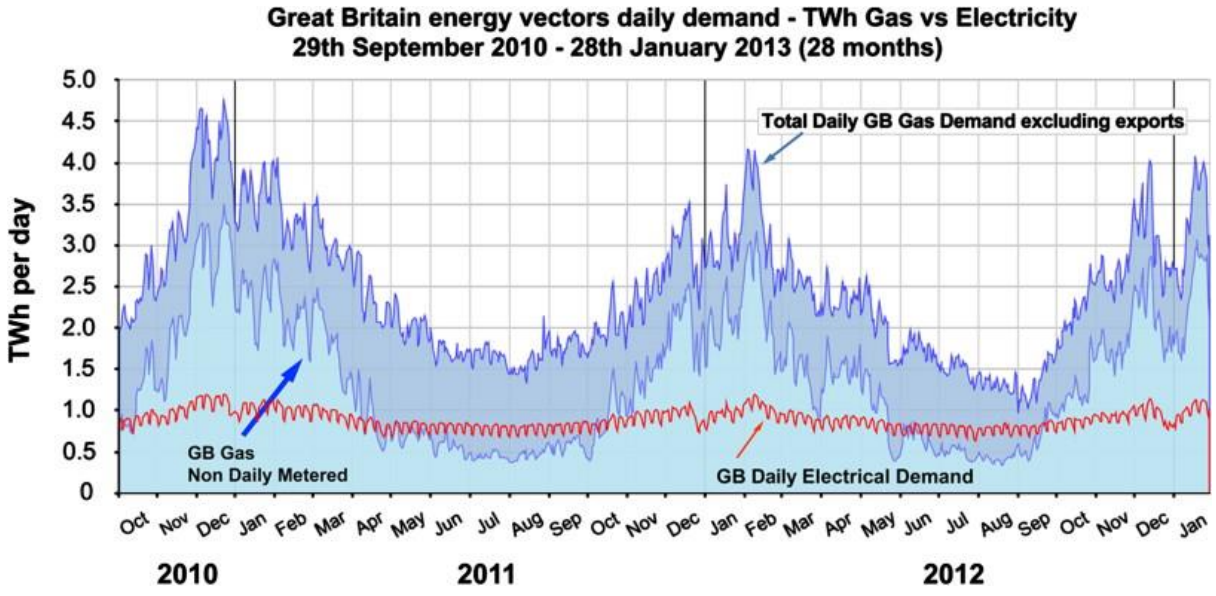

Figure 2 - Great Britain daily energy demand trend of gas and electricity from September 2010 to January 2013 [6]

less pronounced effect on the electrical grid, with a maximum demand in 2014/15 of 53858 MW on January 19th 2015 [4] and a minimum in the same year on July 12th of 18041 MW [5]. The minimum for electricity however is mainly due to the day-night cycle as the maximum demand for the same day of July 12th was 30030 MW [5], while the yearly peak was almost 1.8 times this value.

If the UK seeks to decarbonise the production of heat, the majority of this variable gas load is likely to be electrified causing not only an enormous seasonal swing in electrical demand, but also one across the time period of hours and days. This will be due to the weather and the daily cycle of space heating in the morning and evening.

Even a partial transfer of this gas load (30%) onto the electrical grid (with differing coefficients of performance for various heating methods), could result in doubled daily demand for resistive heating (COP:1), or 25% increased with heat pumps (COP:3)[6], see Figure 3.

The ability to shift the load of heat pumps is also problematic due to lower temperatures requiring large water stores (700 L with a well-insulated house) or other methods required to shift their usage to off peak periods [7].

The true scale of this issue of de-carbonising heat production is reflected in [6], "*UK energy consumption in 2011 for space heating and hot water for all sectors (domestic, service and industry) was provisionally 497 TWh (ECONUKa, 2012). Energy used for domestic space heating and hot water accounts for the majority of this total (354 TWh). By comparison, the overall final energy consumed for ALL sectors for electricity in 2011 was 318 TWh.*"

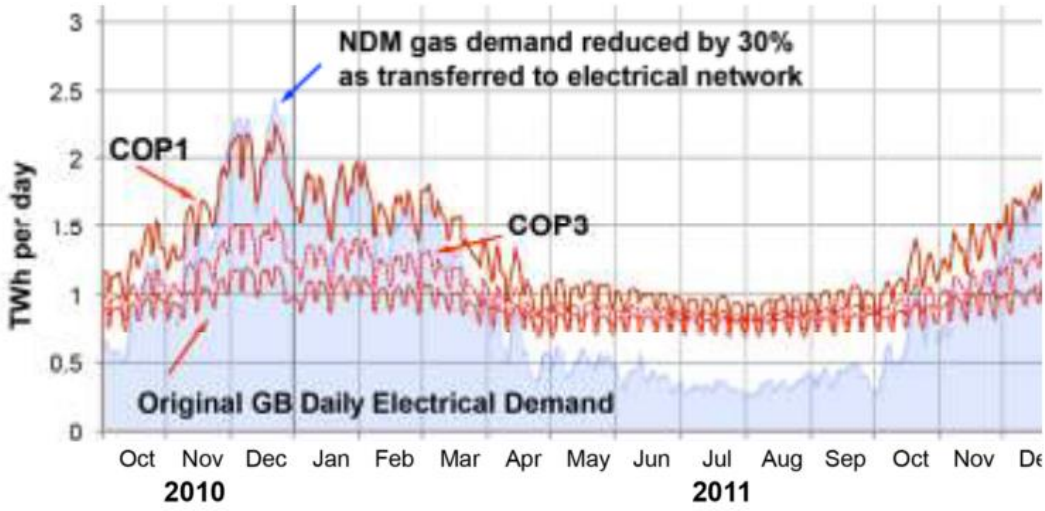

Figure 3 - Transfer of 30% of heat and hot water demand from Gas to Electrical network utilizing historical data [6]

Another report confirmed that between 45-47% of the total final energy consumption of the UK is used to produce heat with 80% derived from fossil fuel [2].

Decarbonising this energy would have large effects on the National Grid: to maintain grid stability, extensive grid reinforcement and vastly increased amounts of generation infrastructure with a reduced utilization factor, (due to the peaking nature of current consumption), will be required. These issues are likely to be reflected worldwide depending on geography, with similar heating or cooling issues for domestic heating, cooling or supply of hot water depending on climate.

The ability to store heat both in the home and at scale has the potential to alleviate the aforementioned capital-intensive grid reinforcement and generation infrastructure construction while increasing the utilization factor of existing assets. There is also flexibility in the choice of heat storage schemes:

While larger heat storage schemes, (particularly those involving combined heat and power are attractive through economies of scale), reduce risk and potential heat integration from industrial processes, the capital investment and disruption to install such systems is enormous. They are also location specific and tend to require a lot of support from consumers, business and local authorities to get installed; in the UK there are very few large scale heat supply or storage schemes compared to in the rest of Europe. Existing or new district heating schemes would however have a compelling case to utilize heat storage during certain periods assuming the cases are economic. For example, the Veolia Sheffield combined heat and power district heating system has certain short periods of the year, (typically several half hour periods), where it would be more economical to produce larger amounts of electrical power at the expense of heat supply .This is currently not possible without a form of storage due to the sizing of the system.

Systems for high density heat storage in the home are attractive due to avoidance of large infrastructure development. The capital investment can be made by consumers rather than government or large corporations but retain the ability to be used more like a larger piece of equipment via aggregation. These systems would also be more flexible during local grid instability assuming they could be tied into a “smart grid” where larger installations could, in contrast, contribute to this instability.

Additionally, consumers are motivated by existing Economy 7 and Economy 10 (electricity only tariffs) in the UK and similar schemes in other countries e.g. France and the Heures Creuses tariff. These tariffs use a price differential, more expensive during peak and cheaper during off peak hours; accordingly, users are encouraged to use more energy during cheaper periods. The off-peak periods typically last 7 hours. The rewards for adopting this tariff can be enormous but the tariff could actually cost the user more than a standard tariff if the consumptive pattern is sub-optimal.

A brief investigation into these tariffs in the UK in December of 2015 based on the UK Northern Powergrid, with the average energy consumption figure (18639 kWh per annum), found that a consumer able to schedule most of their energy consumption into off peak periods could save considerable amounts of money compared to standard tariffs. It was found that there was a best savings case of **£1,225.28 per annum,** (from the worst standard tariff to the best Economy 7 tariff with 70% of consumption off peak), and a best standard tariff to Economy 7 savings case **£622.10 per annum** (best case standard tariff to best case economy 7 tariff with 70% of consumption off peak.) It is important to note that even with only 20% of energy consumption during off peak, the best case Economy 7 tariff still saves **£50.00 per annum** but the worst case, (best standard tariff compared to the worst Economy 7 tariff with only 20% of energy consumed off-peak), actually costs the user an additional **£975.77 per annum**. The potential savings present a large motivator for consumers or local authorities to peak shift their energy usage assuming they can find a suitable tariff.

1.2 Background

This section presents the general background concerning domestic heat production and storage. Initially there is a brief summary of the existing and future domestic heating technologies followed by a summary of available heat storage technologies.

The final part of this chapter contains a brief outline of what a domestic heat storage would technically require.

1.2.1 Existing and Future Domestic Heating Technologies

In order to develop a sensible course of research in storing heat in a home, one must consider the existing and future generation sources of heat in homes.

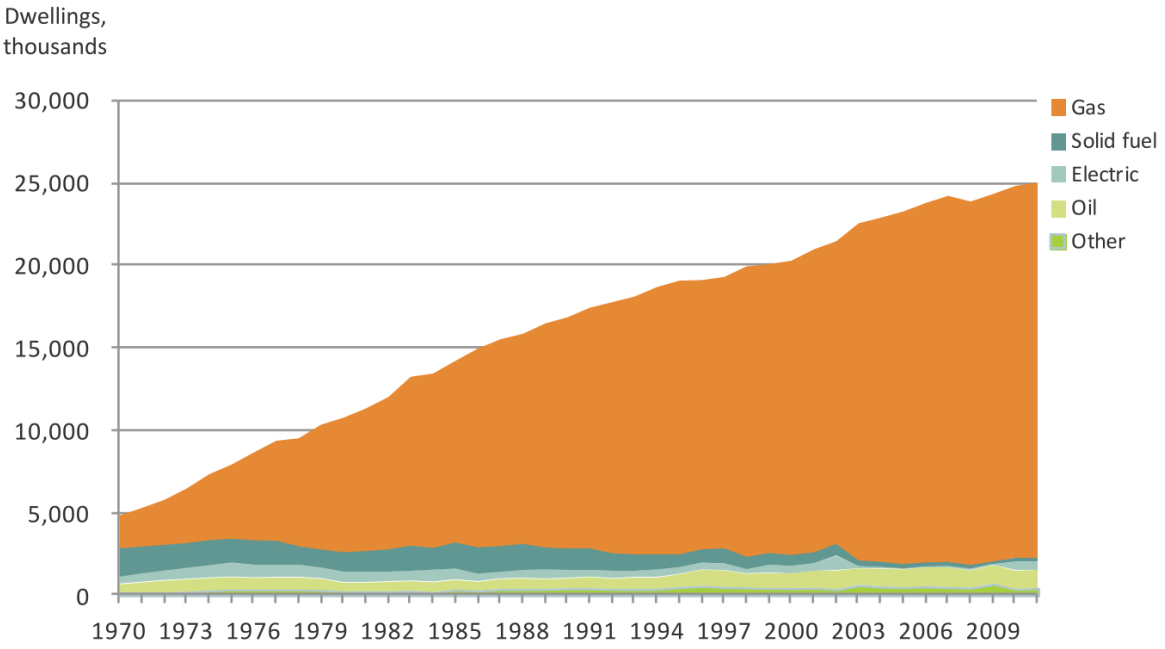

Figure 4 - Main form of heating for UK centrally heated homes (thousands) [8]

The distribution of the various technologies can be seen in Figure 4 and Figure 5 and demonstrate that the vast majority of UK houses have central heating provided by gas combustion.

In 2011, the distribution of houses with central heating stood at 9 out of 10 and of these, 91 % use gas [8]. Unsurprisingly the distribution is very different for non-centrally heated domiciles,

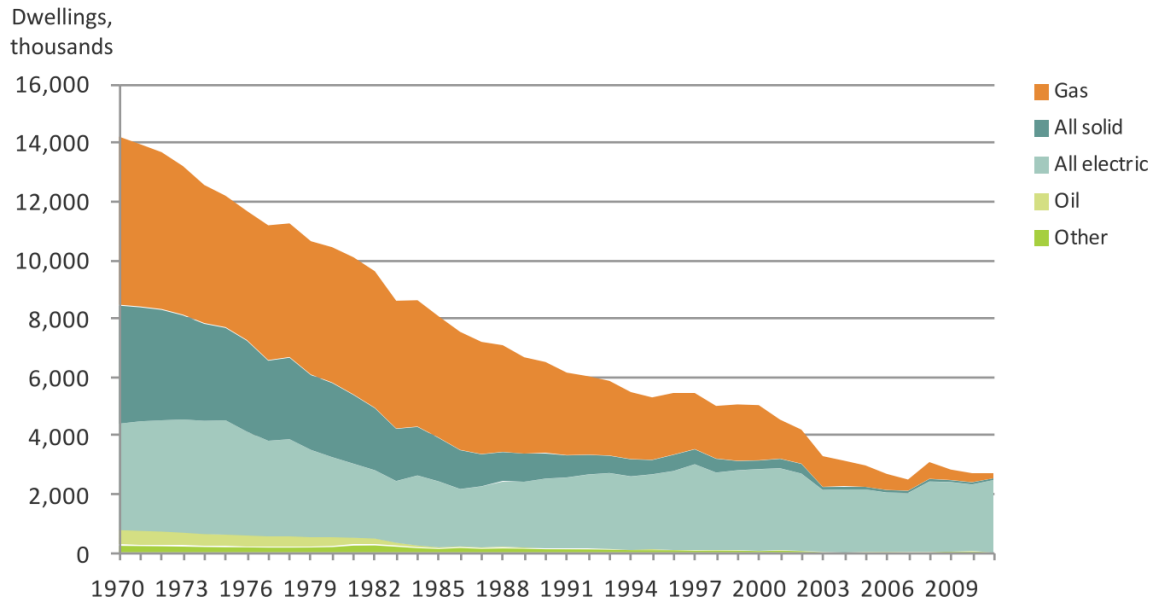

Figure 5 - Main form of heating for UK non-centrally heated homes (thousands) [8]

not only has the number of domiciles with non-central heating decreased, but electrical heating dominates with 82% as of 2011. This domination is likely due to increasing housing stock of flats and usage of electricity due to safety and lower installation cost.

A more in-depth explanation of the various heating technologies is listed in the categories below.

1.2.1.1 Existing Domestic Heating Technologies

1.2.1.1.1 Natural Gas Fired

The vast majority of domestic buildings in the UK use gas fired boiler technology in various forms in order to provide both hot water and space heating.

The majority of modern installed gas fired boilers in the UK are of a gas condensing type, ~50% [8]. These boilers are of a higher efficiency due to the recovery of heat from condensing water in the exhaust gas.

Many of these systems (60 %) provide instantaneous domestic hot water and space heating (combination boilers) of which 66% are condensing type [8].

The remainder of the systems tend to be older non-condensing boilers of either the combination type or utilizing a hot water storage tank if not capable of instantaneous heating. The condensing type of boiler has efficiencies up to 90%, around 10-12% better than predecessor boilers.

A poll over 120 houses in the UK found the temperatures of regular boilers to be 52.9 °C and combi boilers at 49.5°C, far below the expected 60°C [9]. The achievable temperature ranges for these systems is typically above this setting up to boiling point at 100° although most boilers will be limited below this to avoid potential pressure issues.

1.2.1.1.2 Oil Fired

Oil fired systems are typically of the same method as gas fired boilers, with and without condensing variants. They are also typically utilized in combination and non-combination setups with similar efficiency figures as the gas fired systems.

1.2.1.1.3 Resistive Electrical

Resistive electrical heating systems use wiring resistive to electrical current causing the wire to heat up, giving out heat via radiation and convection. These systems usually take the form of under floor heaters, baseboard, wall mounted or storage heaters. Some of these will be fan assisted; storage heaters are typically forced with fan assistance to aid in removing heat from the storage medium (usually clay or bricks.)

The heating elements typically get red hot (500–1000°C), and distribute energy via convection, conduction and radiation directly into the air. These systems typically discharge air in a temperature range slightly above the room temperature to increase room temperature. Under floor heaters typically utilize more comfortable cooler heating elements with temperatures around 30°C.

Other variants of electrical heaters include immersion heaters (where an electricity resistant thick coil of metal is directly submerged in water within a tank) and radiative heaters (where a heating element is heated to be red hot in a vacuum tube directly radiating heat to users). Immersion heaters are typically set at 60°C and can heat water up to 100°C. However, safety rules limit the temperatures below this.

Electrical heating is usually extremely energy efficient and normally reported as 100% despite some energy wastage in the form of light.

1.2.1.1.4 Solid Fuel

Solid fuel heating typically utilizes coal or wood firing within boilers, furnaces or open fires to provide heat via conduction, convection and radiation directly into the air and to the user or into water for central heating. Temperatures for these systems vary based upon the type of fuel (coal ~ 2000°C, wood 600 - 800°C) which provides similar heating temperatures of water to gas fired and electrical systems.

1.2.1.1.5 Solar Thermal

Solar thermal technologies make use of sunlight in order to raise the temperature of a heat exchange fluid to a sufficiently high temperature to heat a storage tank of water or directly heat the air within the domicile.

Domestic buildings typically make use of lower temperature non-sunlight concentrating technology variants with temperatures typically varying from external temperature, up to 60°C surface temperature and room temperature air for ventilated systems. For flat plate or evacuated tube to internal water storage tank thermal exchangers, heat exchange fluid temperatures can reach 120°C with water storage temperature as high as safety allows.

Efficiencies for these systems are typically not considered important as the “fuel” is free. In addition, the vast majority of these systems in the UK are used to assist other heating systems in reducing carbon footprint and cost because a solar thermal collector alone cannot provide enough heat.

1.2.1.2 Future Domestic Heating Technologies

1.2.1.2.1 Heat Pumps

Heat pump systems include ground and air source heat pumps and make use of an electrically driven compression and expansion cycle to add or remove energy from the source [10][11]. This is the same principle used for the cooling in refrigerators. These pumps can be used for both domestic hot water and space heating; however operational temperatures are nominally lower than fossil fuel or other electrical heating methods outputting up to 60° C utilizing ground sources that are around 10°C. This production method of heat is desirable as coefficients of performance (COP) can reach above 1, meaning that for every unit of energy provided electrically more than one unit of heat is produced. The limit on the upper output temperature is a function of the source temperature and energy input. The attainable COPs increase with a rising source temperature with COPs of 2.0-2.8 realised in 18°C ambient air and 2.0 / 2.72 (water heating and space heating) in ambient air 4.5°C [12]. Further values of COP can be found in Table 1 of [10].

These characteristics make ground and air source heat pumps attractive for a future UK electrified heat strategy as not only are they over 100% efficient and would mitigate electrical demand peaks but they can provide cooling and heating while being familiar, safe and acceptable to consumers. The downsides to their use in the UK are the amount of space required for the heat exchanger in the source typically a large pipe array in the ground and the diminished COP likely due to the UK climate and seasons.

1.2.1.2.2 District Heating

District heating is a system for centralised heat production for distribution and use in other distant buildings. These systems can be simple boiler systems but are commonly found as part of a combined heat and power scheme at smaller electrical production facilities. This usage of combined heat and power and district heating is common on the European continent with incineration of domestic waste typically used for this purpose. Both technologies are significantly less frequent but still present in several locations within the UK, i.e. the Sheffield Veolia incinerator heat network, the Leeds district heat network, and various systems in Manchester and London [13].

Efficiencies of these systems will be similar to existing boiler systems in conventional heating cases; however combined heat and power plants can see their overall energy efficiency rise above 80% compared to the typical 40% of a conventional power station. Specific values of savings are difficult to estimate due to the nature of the specific characteristics of a system (fuel source, outputs, operational modes etc…) but further information can be found for specific cases in the literature.

These systems typically reduce carbon emissions, reduce end-user energy bills and reduce energy transmission and distribution costs due to their close proximity to utilization.

Prior to the closure of the UK Department of Energy and Climate Change (DECC) in 2016, they published a strategy document called “The Future of Heating: A strategic framework for low carbon heat in the UK” which called for the development of heat networks in suitable municipal areas considering the integration of waste heating or cooling from industrial processes as core to long term strategy. It is expected that this technology will be widely adopted in the coming decades due to its many advantages. This same strategy was also highlighted in a research report from the UK ERC, recommending the use of district heating with attention to waste heat sources [2].

1.2.1.2.3 Geothermal heating

Geothermal heating makes use of geothermal gradients within the earth’s crust. This is typically realised using boreholes in deep thermal wells with direct to rock contact with a heat exchange fluid or via the utilization of heat pump technology. Shallow depth technologies are synonymous with the heat pumps section above.

Deep well technology usually makes use of radioactively decaying geology to provide heat with output temperatures in engineered wells easily reaching 100 - 200°C. As advantageous as a carbon free and cost free source of heat is, geothermal heating is limited by opposition to fracking/boreholes, the complexity of the systems and the need for consumers to be nearby which is hindered by the location of the geology.

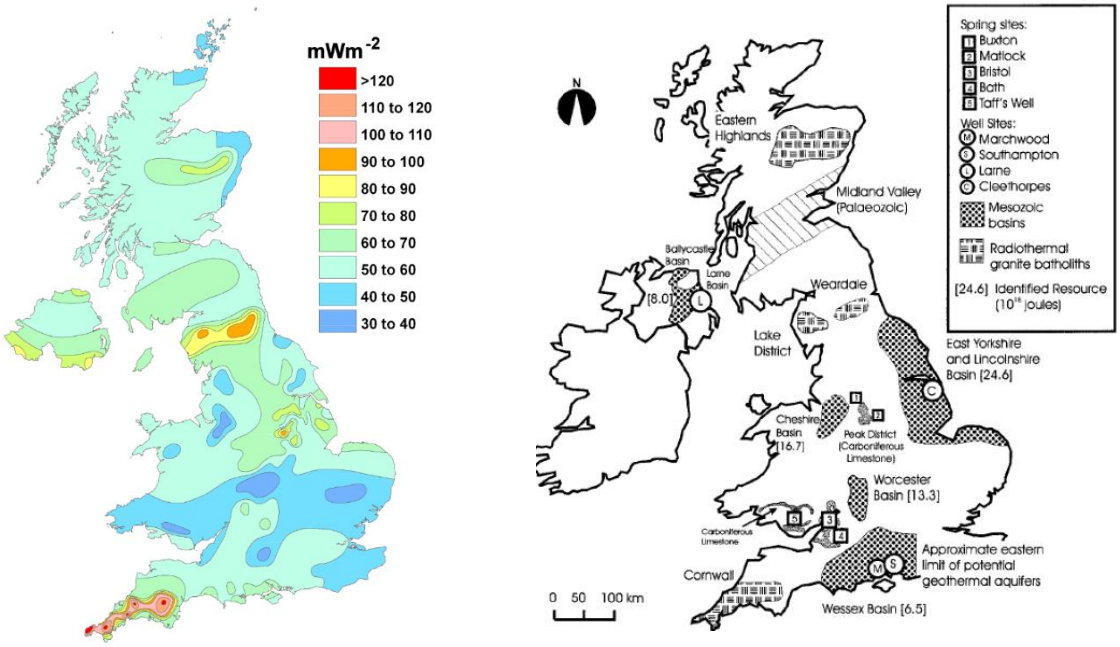

Figure 6 - Heat flow map, location of sedimentary basins and major radiothermal granites [14].

The UK is stable, lacking both active fault lines and volcanoes which usually result in high geothermal gradients which goes some way to explaining why the uptake of geothermal heat production is so low (a small fraction of the total renewable supply). The UK does still have significant geothermal resources that can be exploited in deep sedimentary basins in the north and radio-thermal deposits in the south east as can be seen in Figure 6.

The DECC has been encouraging the uptake of geothermal resources via numerous methods, existing (Renewables Obligation, Renewable Heat Incentive) and newer (Contracts for difference, CfD and CfD feed in tariffs,) alongside grants [14].

1.2.2 Heat Storage General Principles

1.2.2.1 Types of Heat Storage

Heat storage can be classified into several discrete classifications: these are sensible / conventional heat storage, latent heat storage and thermo-chemical / sorption heat storage [15].

Example storage temperature versus storage amount profiles can be seen below in Figure 7 for these technologies with E – stored energy and T – time.

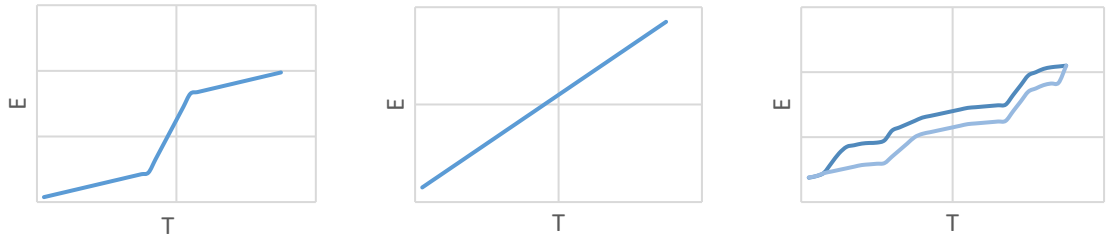

(a) (b) (c)

Figure 7- Graphs of temperature versus stored energy profiles of latent heat storage (a), sensible/conventional heat storage (b) and sorption/thermochemical heat storage (c).

Further detail into each classification and specific sub-types of each class of TES (thermal energy storage) can be found below.

1.2.2.2 Conventional / Sensible Heat Storage

The conventional / sensible method of heat storage involves the use of the specific heat of materials over a temperature range in order to store heat. This class of technology is the oldest, best understood and most widely used. The equation that governs this, the relationship between energy, the specific heat capacity and the change in temperature is seen below.

$$E = MC_p\Delta T \quad (1)$$

Temperatures typically used in this class of technology are between 0 -100 °C due to the use of water with additional costs for pressurised or steam systems. Water is typically used due to its ubiquity, high specific heat and familiarity of use [16].

For larger temperatures, 400 °C and above other materials such as molten salts, ceramic materials, gravel beds, natural and synthetic oils are used. Larger seasonal type stores utilize

larger tanks, pit stores of gravel or water, boreholes using the ground or aquifers using the ground water.

Energy stored by this method is typically linearly related to the increase in temperature. In applications requiring more storage, where possible the material is normally changed to one with a larger specific heat or a larger temperature range is selected. The utilization of higher temperatures is not ideal due to the relationship of increasing heat loss with increased temperatures as is seen in Figure 8.

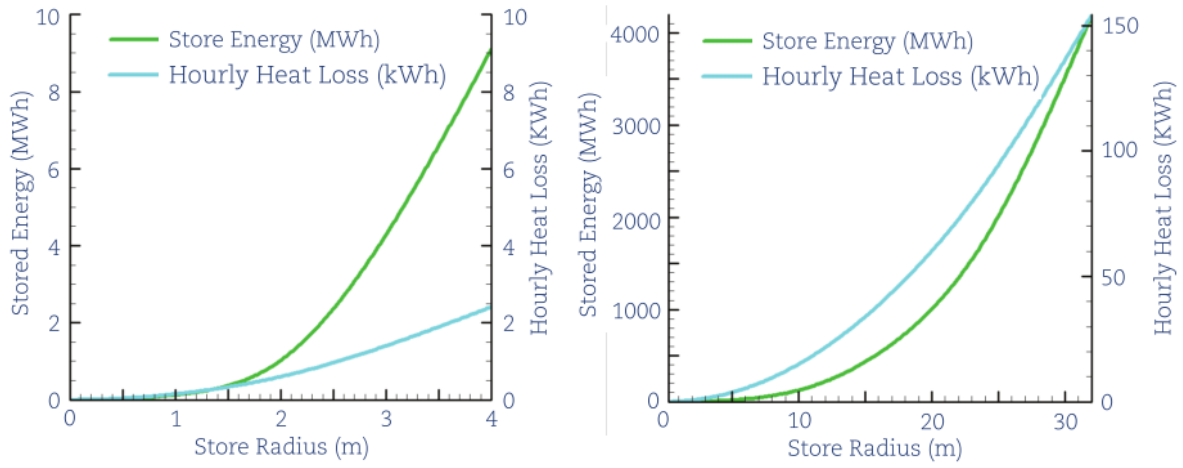

Figure 8 – Relationship between energy storage capacity and heat loss determined by radius in a spherical store [2]

Sensible heat can be utilized with active processes, (requiring transport, agitation or some form of mechanical work to be utilized) such as residential central heating, or passive processes, (stationary, not requiring any mechanical work) with applications such as trombe walls and conventional walls.

In order to charge the materials, heat can simply be added, and to discharge, it is removed. Both of these processes would normally be achieved by the use of heat exchangers and a heat exchange fluid.

Sensible heat storage is typically used diurnally though it can be used seasonally, but the efficiency of storage decreases the longer a store is not discharged. Inter-seasonal stores are typically implemented using solar thermal or waste heat in conjunction with heat pump technology to maintain a high COP.

1.2.2.2.1 Solar Ponds

Solar ponds are an implementation of typically large scale heat storage and there are various types including salt gradient ponds, partitioned ponds, viscosity stabilised ponds, shallow ponds etc... In practice, these ponds usually utilize chemical or physical barriers to prevent convection across discrete layers to achieve lower heat losses.

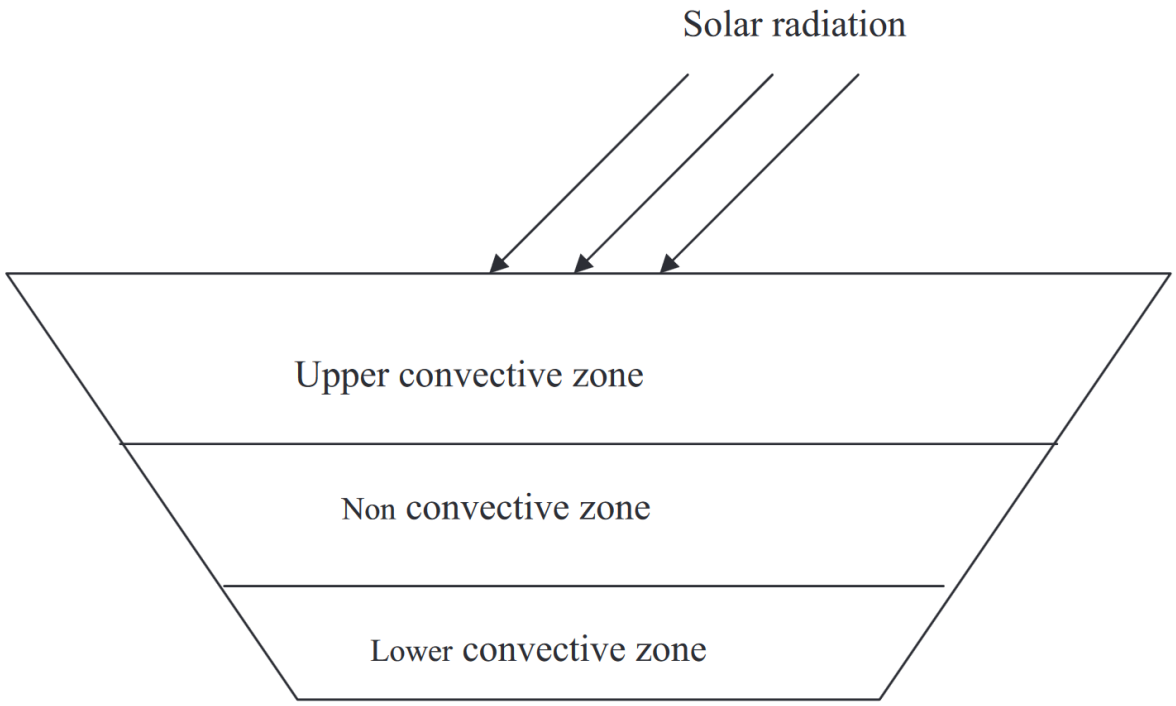

Figure 9 - Diagram of a salt gradient pond. [17].

In salt gradient ponds, the salt water naturally forms a vertical salinity gradient called a halocline. Lower salinity water floats above higher salinity water and the gradient increases in concentration until a certain depth is reached, upon which a uniform high salinity water layer progresses to the pond floor.

Due to the salinity gradient, higher salinity water at depth does not readily mix with lower salinity water inhibiting convection in between these layers leading to an insulating effect. The separation of convective zones achieved can be seen in Figure 9

Solar ponds make use of this effect by supplying the heat to the higher salinity lower level and can allow for temperatures of up to 95 ° C [18]. The usage of salt does however have higher maintenance costs associated with the increased corrosivity.

Viscosity stabilized ponds make use of a polymer gel in order to form the barrier to convection, while physical partitions are used in other systems. Shallow ponds are usually well insulated with a glass cover and are more typically used to supply heat rather than store it as they collect solar thermal energy.

These systems are cheap but very large with very low efficiencies and are usually designed as part of an operation to generate energy rather than simply store it.

One example of a solar pond is the Bhuj solar pond in India, a large-scale pond at 6000 m^2 which supplies around 15 million litres of hot water to a dairy at around 75°C.

1.2.2.2.2 Aquifer Storage

Subterranean ground water aquifers can be used to store heat via the utilization of boreholes. This is typically implemented between two boreholes into separate groundwater wells. When storing energy, water is removed from the cold well, heated and then pumped into the hot well and vice versa for retrieval. The heat is usually supplied from suitable sources such as solar thermal or extracted when necessary (building cooling). The round trip efficiency of these systems is around 70% [19].

These systems are large, rely on geology; they can be shallow (<400 m) or deep (>400 m) and are typically operated seasonally. The storage temperature range varies by regional law e.g. between 5 – 25 ° in the Netherlands where other countries set a maximum change in ground water temperature e.g. Switzerland at 3° C [20]. The United Kingdom has recommended a temperature difference of 10° C and a maximum temperature of 25° C for open type systems though closed systems have no such limits.

Practical problems and temperature limitations are associated with these systems and there are differences between the open and closed loop system types (where closed loops use a heat exchange fluid that does not leave the pipework), such as pipe fouling, corrosion and groundwater contamination. There are also concerns about interference from close proximity systems [19].

One example of an aquifer storage system would be the system installed for the German Parliament building (Reichstag) in Berlin. The system utilizes two aquifers at different depths to store cold and heat. The heat in this case was supplied by combined heat and power engines inside the building and can be seen in Figure 10.

The system was simulated and found to have a relatively good agreement with real world data. The conditions and results of this simulation were:

The heat storage side injects at 70° C and retrieves at 65 – 35 ° C where the cold side injects at 5 ° C and retrieves at 6 – 10 ° C storing 2650 MWh and 4250 MWh annually with efficiencies of 77% and 93%.

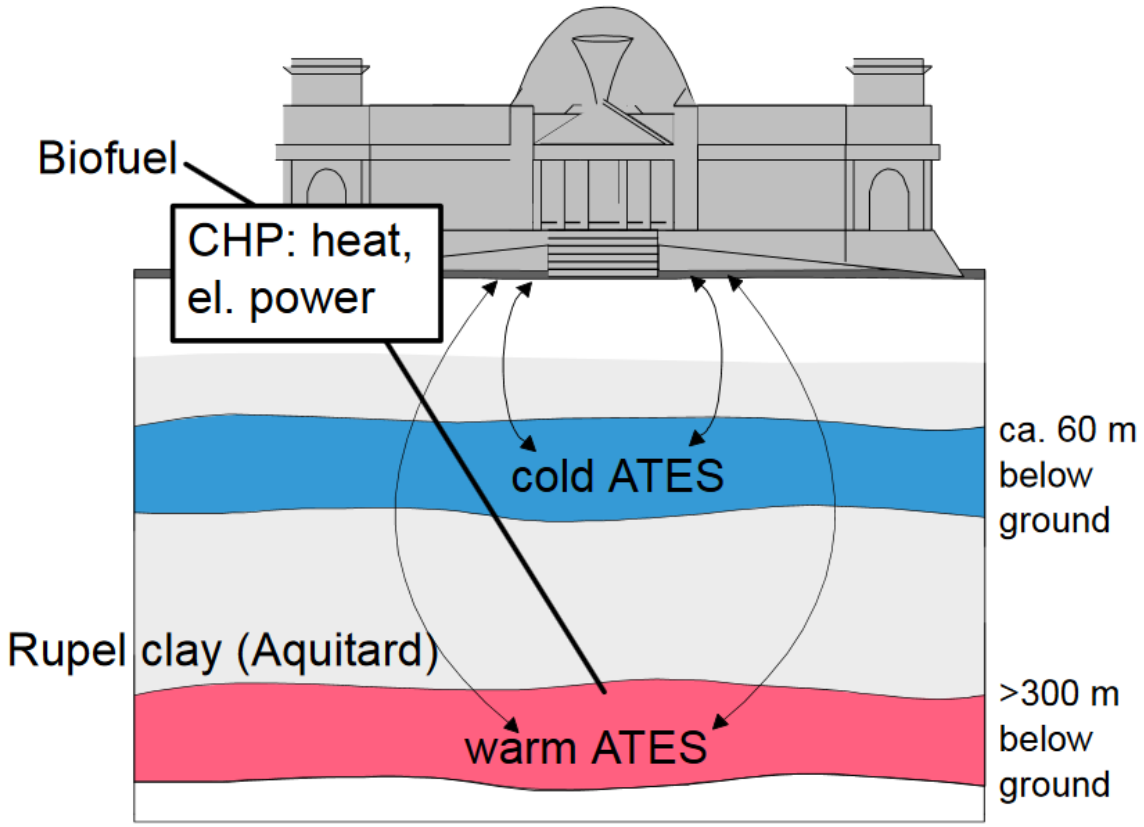

Figure 10 - Schematic of the two ATES layers beneath the Reichstag building [21].

1.2.2.2.3 Rock Bed / Gravel Systems

Rock bed / gravel systems use the principle of storing heat via temperature changes in large containers or tanks but importantly, due to the storage being in solids, it does not suffer from convection heat losses and can benefit from temperature stratification. Unfortunately, the rock or gravel does have a lower specific heat which results in poorer volumetric heat storage density.

Heat or cold is transferred into the beds via a heat transfer fluid, typically air or water with some of these systems retaining water inside the beds to assist in heat transfer due to higher conductivity. Temperature ranges for these systems are typically dictated by the heat or cold production method and application e.g. solar thermal can provide 50 – 100 °C which might be utilized for space heating in a building. Most of these systems are large (supplying numerous buildings) and store heat seasonally.

Rock-air systems can store the heat energy at temperatures exceeding 1000°C depending on the material choice, but rock-water systems are usually limited to 100°C to avoid the necessity of pressurising the system to increase the boiling point of water.

One example of a system is the ITW system at the University of Stuttgart can be seen in Figure 11, a system integrated with a heat pump, a combined heat and power plant with solar thermal collectors [22].

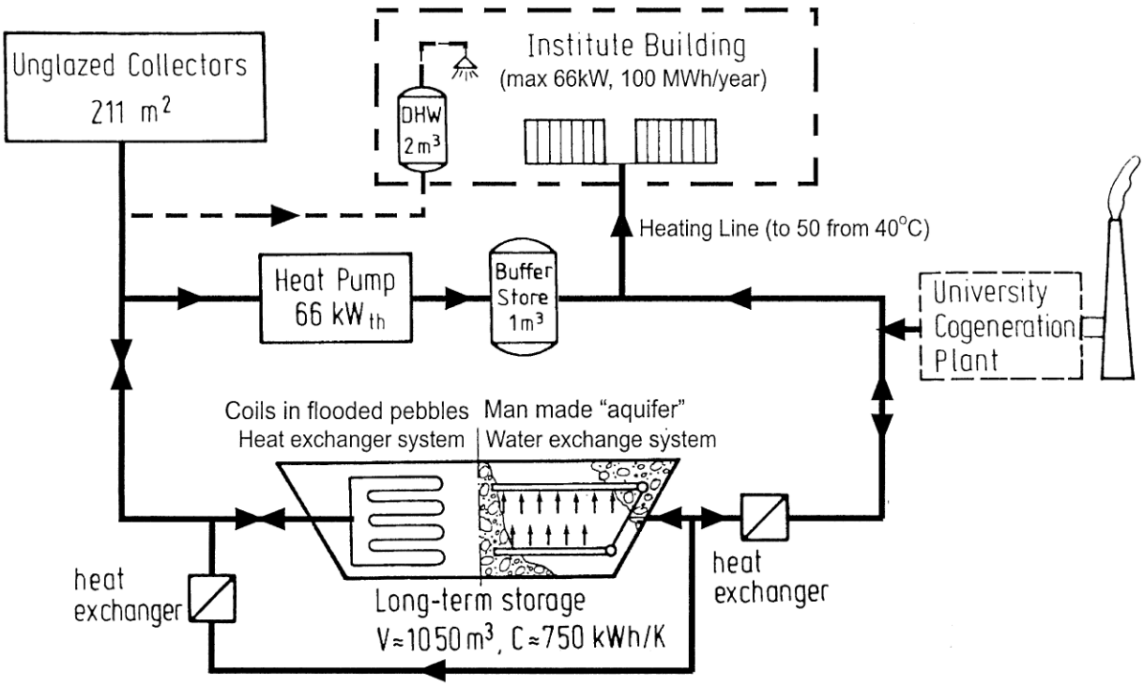

Figure 11 - Scheme of the ITW solar heating system [22].

The gravel bed was a flooded type with 1050 m^3 of pebbles 16 to 32 mm at the top and bottom and 8 – 16 mm in the central space. This configuration was intended to vary the flow resistance, with it being reduced at the top and bottom of the store. Importantly, the sides and bottom of this store were not insulated leading to additional heat storage being tapped directly from the available ground. It was subsequently found that around 50% of the heat commuted to the ground was recovered. The round-trip efficiency of this store was found to be ~ 80% with approximately 70 MWh stored annually.

1.2.2.2.4 Borehole /Duct Systems

Borehole or duct systems follow the same principles as aquifer storage (drilling boreholes underground to store heat or cold in the ground) but avoid groundwater to prevent the loss of energy associated with moving it and are dug up to hundreds of meters in depth.

Due to these systems using the ground with a lower heat capacity than water, the volume required to store the same energy is between 3 – 5 times in comparison. These systems typically utilize ground source heat pumps, as the stored heat is at a lower temperature than required, and the higher temperatures increase the coefficient of performance of the heat pump.

The construction of borehole storage relies on permissive geology and consists of one to hundreds of drilled boreholes with heat supplied and removed by high-density polyethylene (HDPE) pipes which are usually connected radially from the inside out to assist with stratification.

Like aquifer stores, these systems are usually utilized for seasonal heat storage with heat provided from waste sources or sources with excess heat such as solar thermal during summer. Their operational temperatures range from 10 – 80 ° C.

An example of these systems is the borehole seasonal heat store at the Drake Landing Solar Community seen below in Figure 12. The system consists of 144 boreholes distributed radially and dug to a depth of 35m. The heat is supplied by 2293 m^2 of flat-plate solar collectors installed on the rooftops of the community's homes.

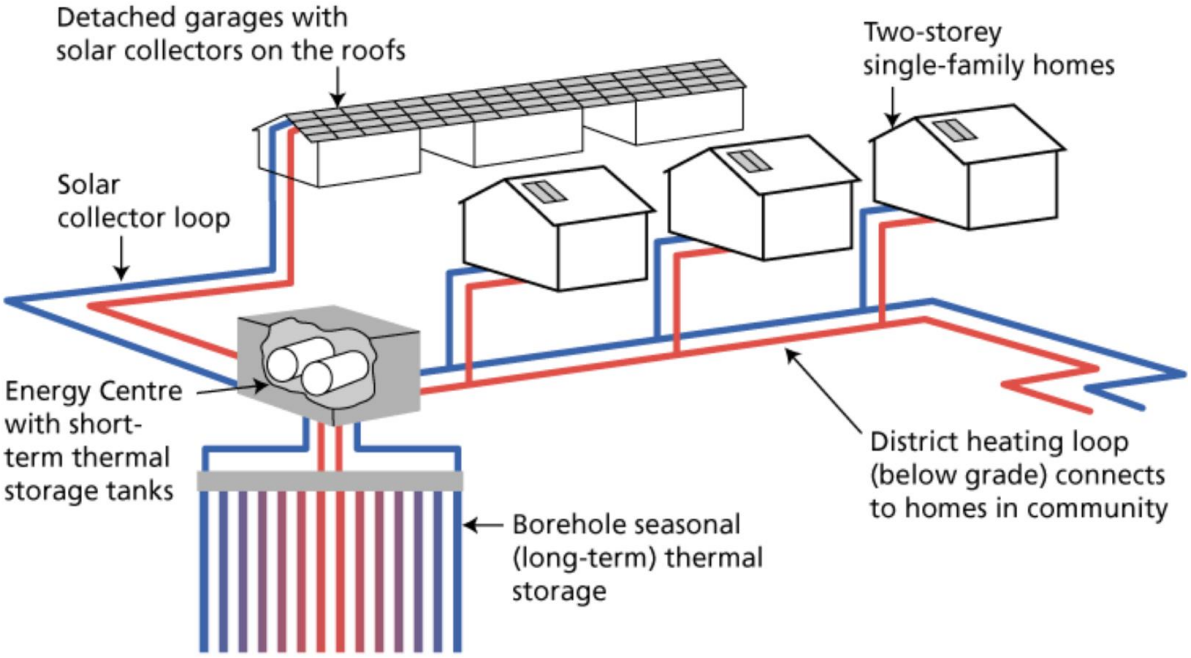

Figure 12 - Schematic diagram of the solar seasonal storage heating system at Drake Landing Solar Community [23]

The system took several years to fully come up to temperature (ground temperature ~ 80°C) upon which the efficiency of the borehole system varied between 30 - 56% with ~ 2300-2600 GJ of energy supplied [23].

1.2.2.2.5 High temperature liquid systems

Some systems make use of oils or molten salts in order to store heat at higher temperatures, e.g. >100° C. Such systems can have heat provided by purpose-built systems such as in concentrated solar thermal power or can be used to recover waste heat from other processes.

Oils can be used at temperatures up to 400 ° C [24] (for stability and safety), where molten salts can be used up to 800° C or higher depending on material selection.

Examples of molten salts include NaCl, lithium liquid salts, nitrite and nitrate salts. All of these salts are capable of operating between 200 – 500 ° C [25]. Eutectic mixes can also be used.

Examples of oils include Dowtherm® A, Syltherm XLT [24]. Thermal oils usually have low viscosity and superior flow and compatibility characteristics. Molten salts have a high volumetric energy density, high boiling points, thermal stability and virtually no vapour pressure. Unfortunately, these oils tend to be expensive and molten salts tend to have significant issues with corrosion.

These materials can be used in place of air or water inside of tanks or pebble beds, will readily stratify and are utilized in industry as thermal storage or heat exchange fluid for solar and concentrating solar thermal plants.

Torresol Gemasolar in Spain is an example of a concentrating solar power station with 15 hours of molten salt backed (8500 tonnes) thermal storage with a possible storage cycle efficiency of 99% [26].

1.2.2.2.6 Hot water storage based

Hot water storage dominates within thermal storage technologies due to the simplicity of the design and implementation, the ubiquity of water and the well-established needs of hot water for central (space) heating and sanitary hot water. These tanks are typically used on a diurnal schedule for low volumes of storage and seasonally with large volumes of storage. Efficiencies of these tanks widely vary depending on design, installation, use case and type.

Hot water storage in conventional tanks and stratified tanks is well established in both commercial and residential applications. These tanks scale well (from tens of litres to thousands of cubic meters), store large amounts of energy due to the high heat capacity of water, are relatively cheap and are widely available.

Normal/stratified tanks store the heat in the water by elevating temperatures up to 95 °C (in non-pressurised systems) and tanks are enlarged to store more energy. These tanks are usually well insulated with larger systems being insulated and buried.

Stratified tanks make use of a thermocline (water will form layers from hottest to coldest from the top to the bottom due to the change in density associated with temperature), which can improve heat transfer and exergetic efficiency.

Unfortunately, there is a trade-off between the volume of water stored and the increasing tank surface area. This results in increased heat losses, in addition to the dilution of temperature by incoming water reducing exergy in non-stratified tanks.

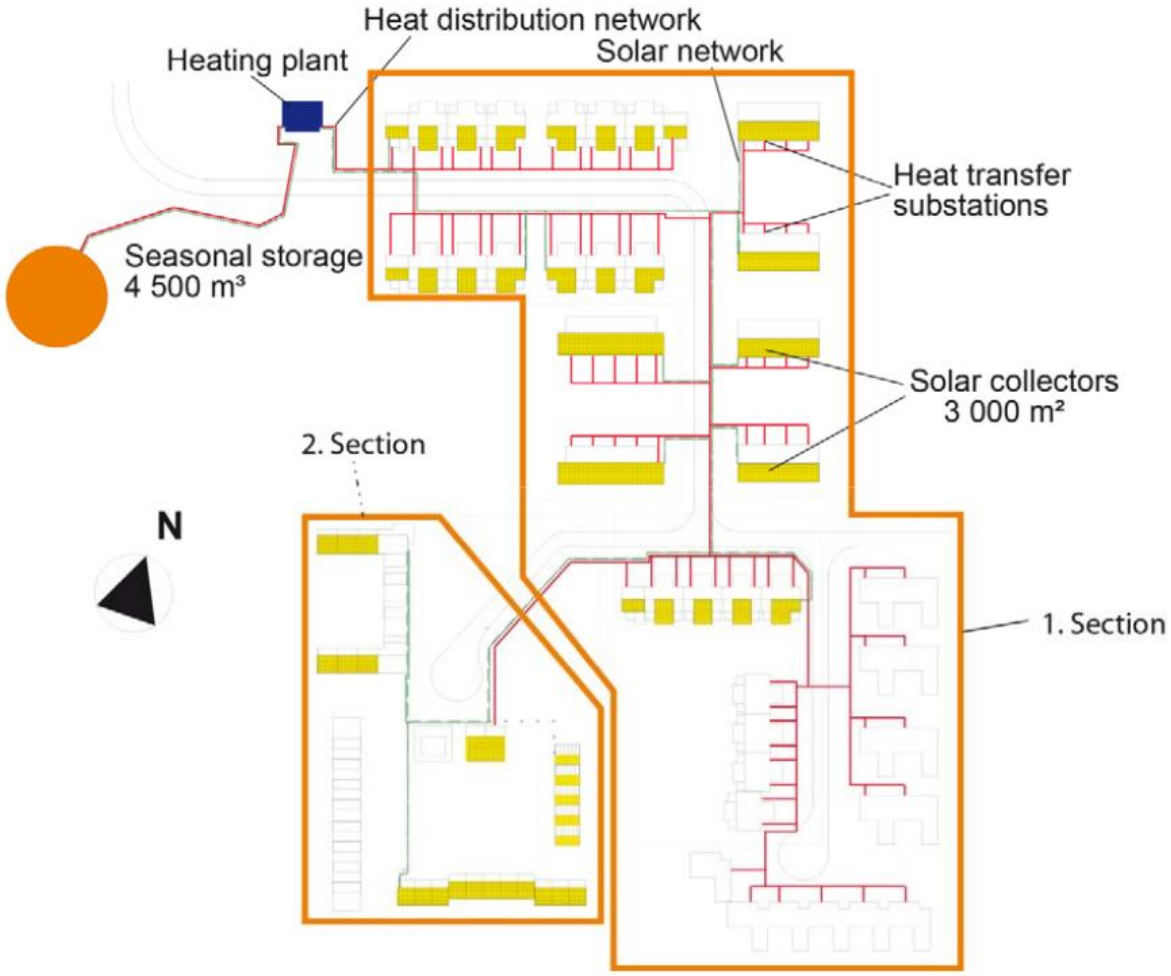

Figure 13 - Site plan of the solar thermal generation and thermal storage plant in Hamburg-Bramfeld

Figure 13 shows an example of a large seasonal store, the Hamburg-Bramfeld project in Germany which was a 2040 kW central solar heating plant with 4500m^3 seasonal storage in a ground buried concrete tank. It was operated in this configuration until 2009 when it was converted to “multifunctional storage” [27].

Solar thermal collectors heated the water in the tank which was subsequently used for domestic hot water and space heating in residential properties. The efficiency was 46% compared to its 89% design value due to poor and humidified insulation.

1.2.2.3 Sorption Heat Storage

Sorption heat storage utilizes the ability of certain materials to absorb or adsorb vapour to its structure.

Typically utilizing water, when vapour is adsorbed/absorbed the bonding energy of this process is released as heat and vice versa. This is sometimes classed as a thermochemical form of storage due to the uptake of water technically being a hydration reaction and vice versa. A diagram of this reversible process can be found in Figure 14.

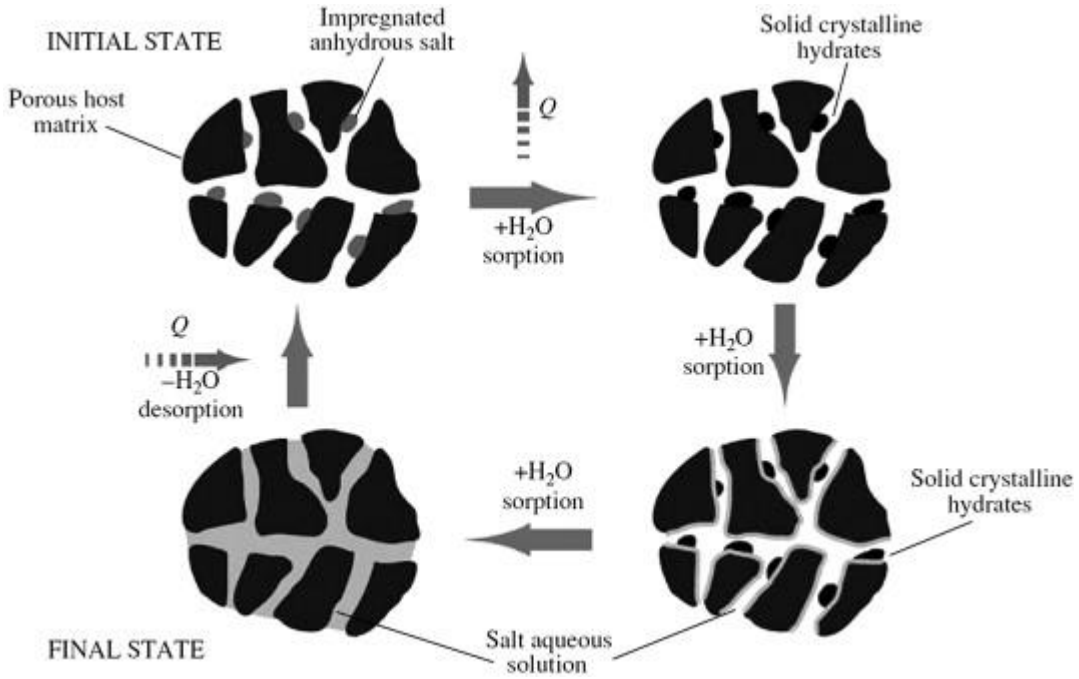

Figure 14 - Sorption process for a water sorbent [28][15]

The sorption material is an adsorber if it attaches the vapour to the surface of the material without changing the structure. It is an absorber if the vapour attaches to the bulk of the material, changing the structure. Absorbates and adsorbates can be liquids or gases, where absorbants can be liquids or solids; adsorbers are always solids.

Another division in sorption heat storage is whether the process is physical (Van der Waals or hydrogen bonding based) or chemical in nature (covalent bonding).

Common adsorbers are silica gel, zeolites and activated carbon. Common absorbers are lithium bromide, ammonia and copper / magnesium sulphate. Various classes and materials in use for absorption and adsorption can be found in Figure 15.

In order to charge the material, liquid is removed from the structure by heating. It can be discharged by adding adsorbate vapour. These processes can take place in open or closed systems, the former typically using ambient air as a source and the latter having a condensed working fluid. These systems usually require a source of low grade heat to aid in the evaporation phase, usually from buildings, to provide cooling and vice versa in the discharge phase by applying moist air.

Open systems have been determined to be 69% efficient and closed ones 50% [28].

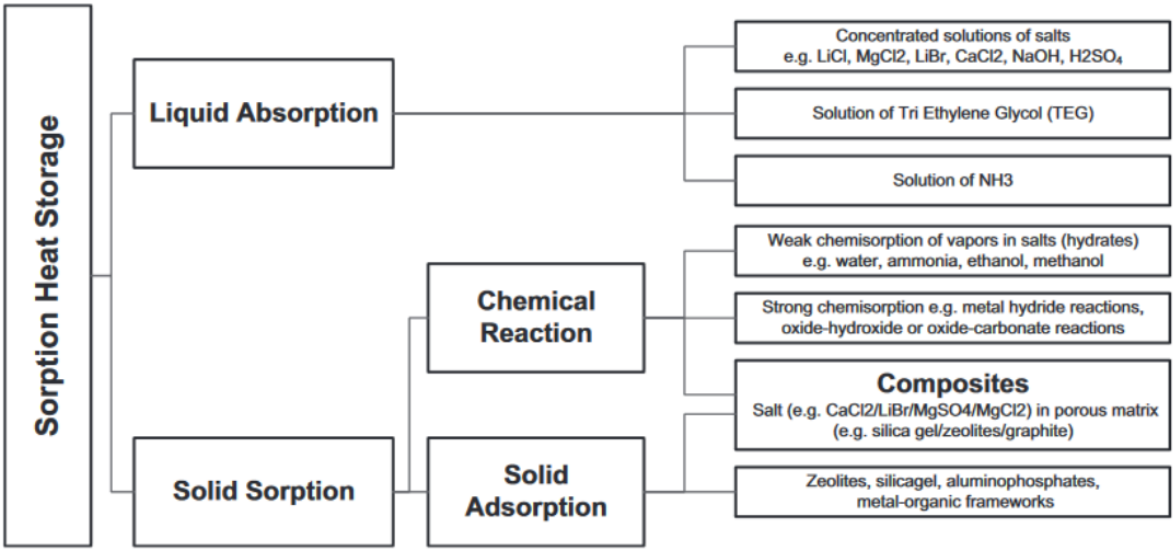

Figure 15 - Classes of sorption heat storage [29].

Sorption heat storage is still within the research phase and is normally associated with both short term (hours and days with respect to day-night cycle) and long term seasonal storage coupled with solar thermal energy generation (with respect to seasonal solar radiation fluctuation).

Figure 16 shows a range of sorption materials classified by operation temperature and energy storage density. The majority are paired with water, unless noted differently.

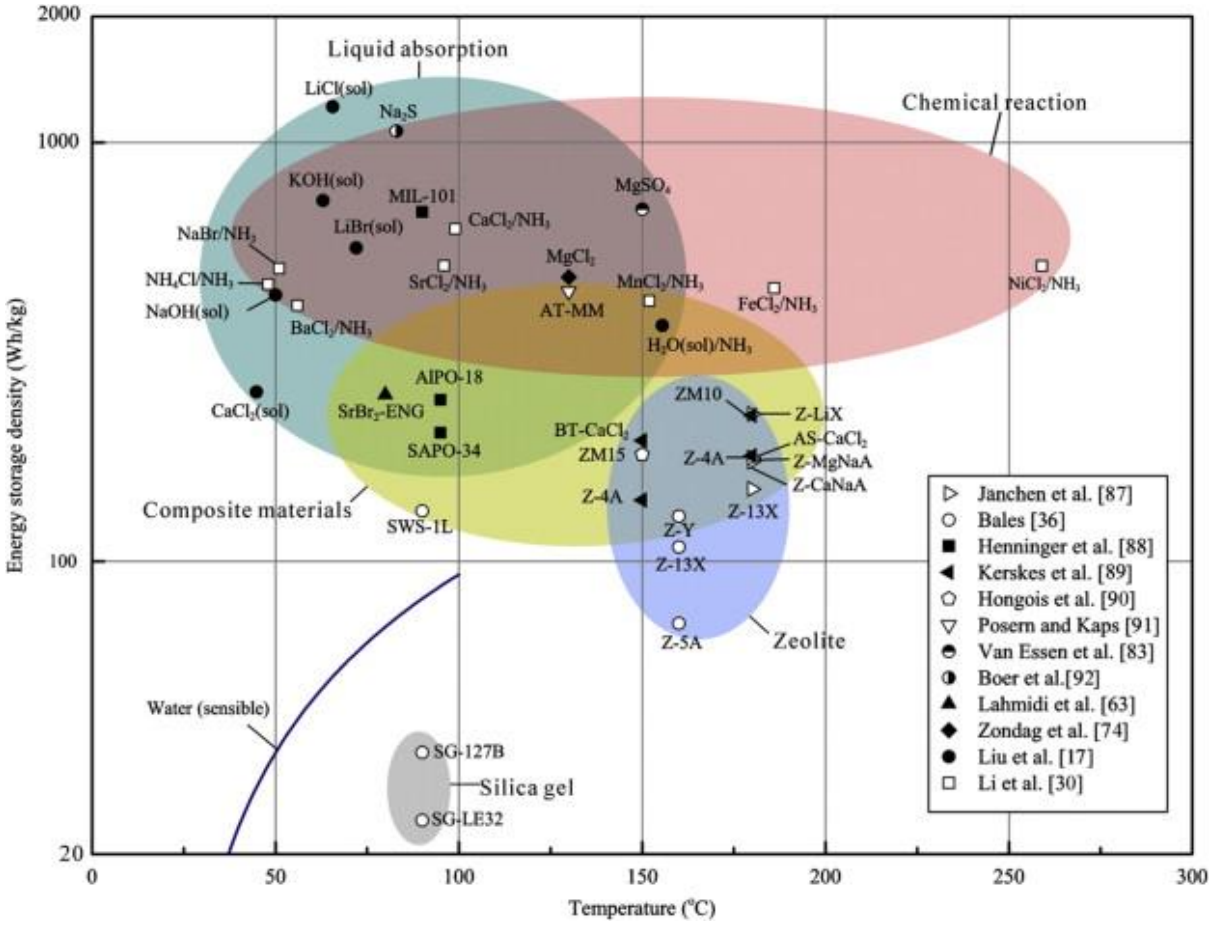

Figure 16- Range of sorption materials classified by operational temperature and energy density, includes sensible water heat storage reference [28].

Some of these materials and systems suffer from relatively low energy density, thermal and structural stability and compatibility (i.e. too corrosive). It has been concluded that further research is needed to find suitable sorption materials' pairs in addition to economic and key performance indicators being utilized to more readily compare to other technologies [29].

1.2.2.3.1 Zeolite Based Systems

Zeolite based systems adsorb water vapour via an exothermic reaction. This process is reversible and thus can be used for thermo-chemical or adsorption-based heat storage.

While still in the research phase, experimentation with capacities between several to hundreds of kilowatt hours have been undertaken. One such pilot system was installed into a school building in Munich, Germany in 1996 and was connected to the local district heating network, the modes of operation for this system can be found in Figure 17 [30].

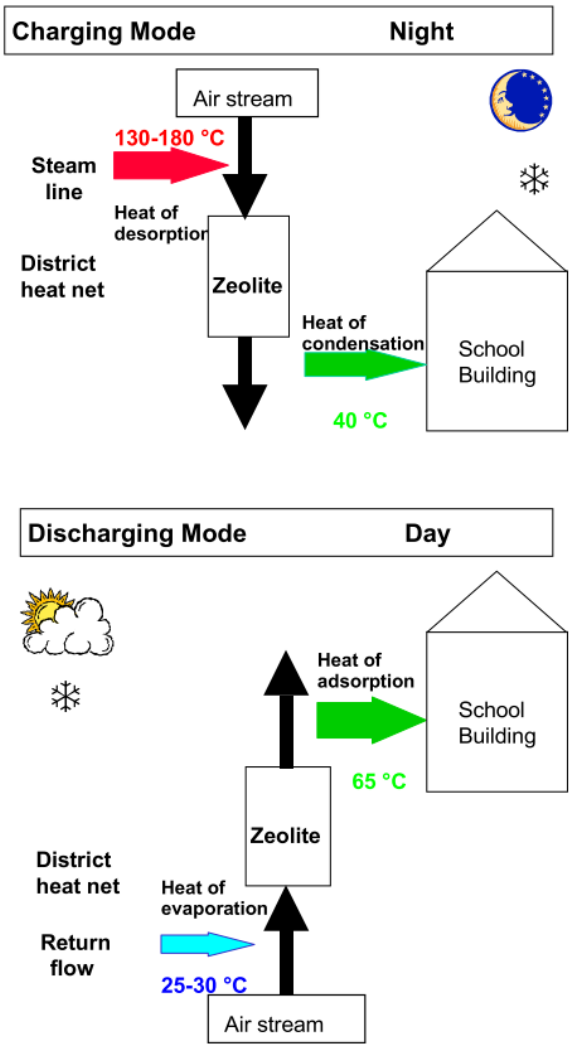

Figure 17 - Charging and discharging mode of Zeolite based thermal storage system from [30].

This system was open cycle rated at 95kW and was composed of 7000 kg of zeolite 13X. The system was designed to cover a heat load for 14 hours and was charged with off peak district heating network generated heat with temperatures between 130 – 180 ° C. An energy density of 124 kWh/m^3 was achieved by 1997 with a coefficient of performance of 0.92 compared to the 81 / 86% of theoretically calculated. A picture of the plant equipment used for this system can be found in Figure 18.

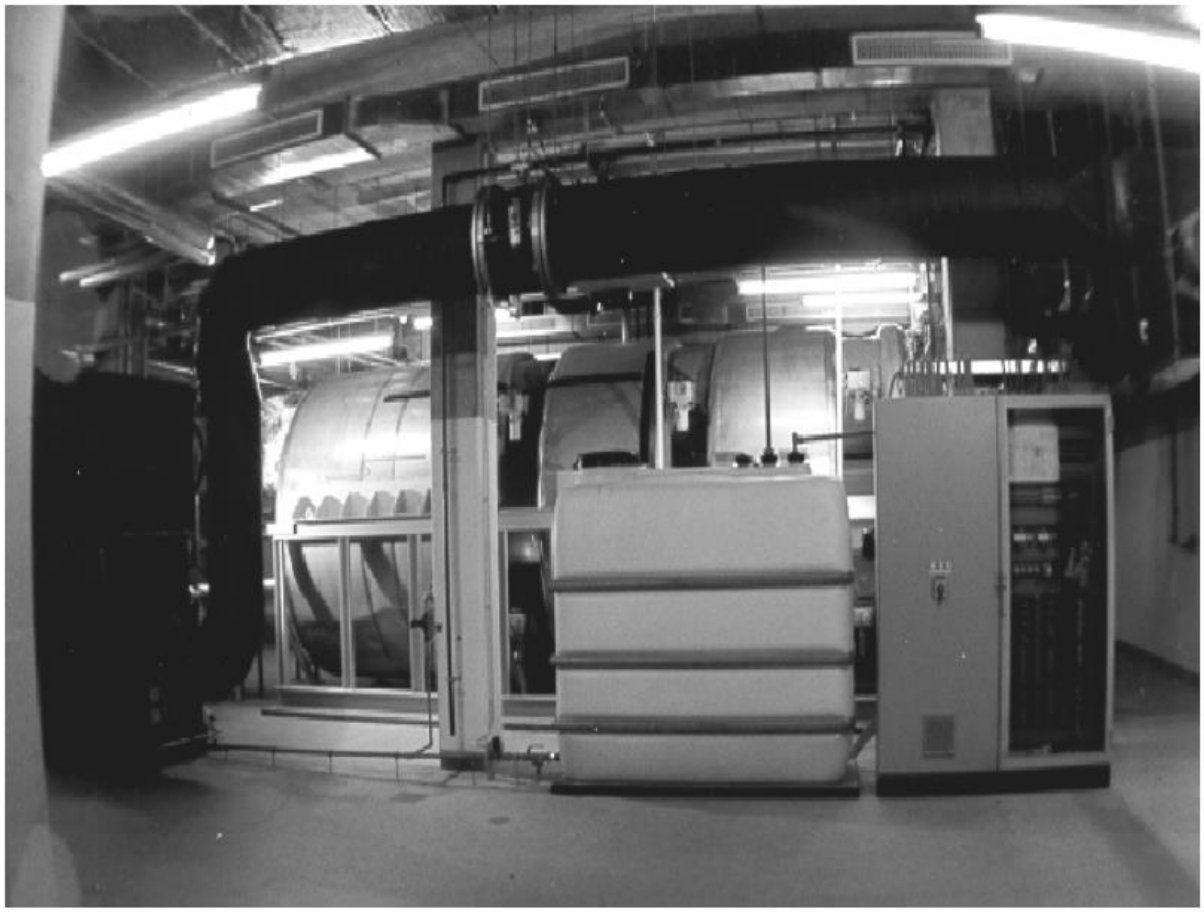

Figure 18 – Plant equipment from Zeolite based thermal storage system from [30], humidifier, water tank and control system (left to right) with 3 zeolite storage modules to the rear.

1.2.2.3.2 Water – Salt Based systems.

Water-salt based systems utilize water as the adsorbate or absorbate and (typically) a metal salt to be hydrated. These salt hydrate systems are known to have a higher theoretical energy density than other materials while desorption temperatures are still within the temperature range from waste heat sources, solar thermal production and domestic hot water.

There are some downsides to these materials, such as only partial cycles can take place as fully drying the material would require much higher desorption temperatures and fully dissolving the material would cause mass transfer which can cause system blockages. With salt based systems, increased corrosivity also becomes a concern.

One such water-salt based system was developed at the Energy Research Centre of the Netherlands. The SWEAT (Salt Water Energy Accumulation and Transformation) project developed a prototype cooling system intended for domestic and residential application [31].

The system utilized sodium sulphide and water (Na_2S-H_2O) in a shell and tube heat exchanger design. Each module contained a copper finned tubular heat exchanger filled with the sorbent.

This was intended to demonstrate a system with corrosion protection using industry standard manufacturing processes.

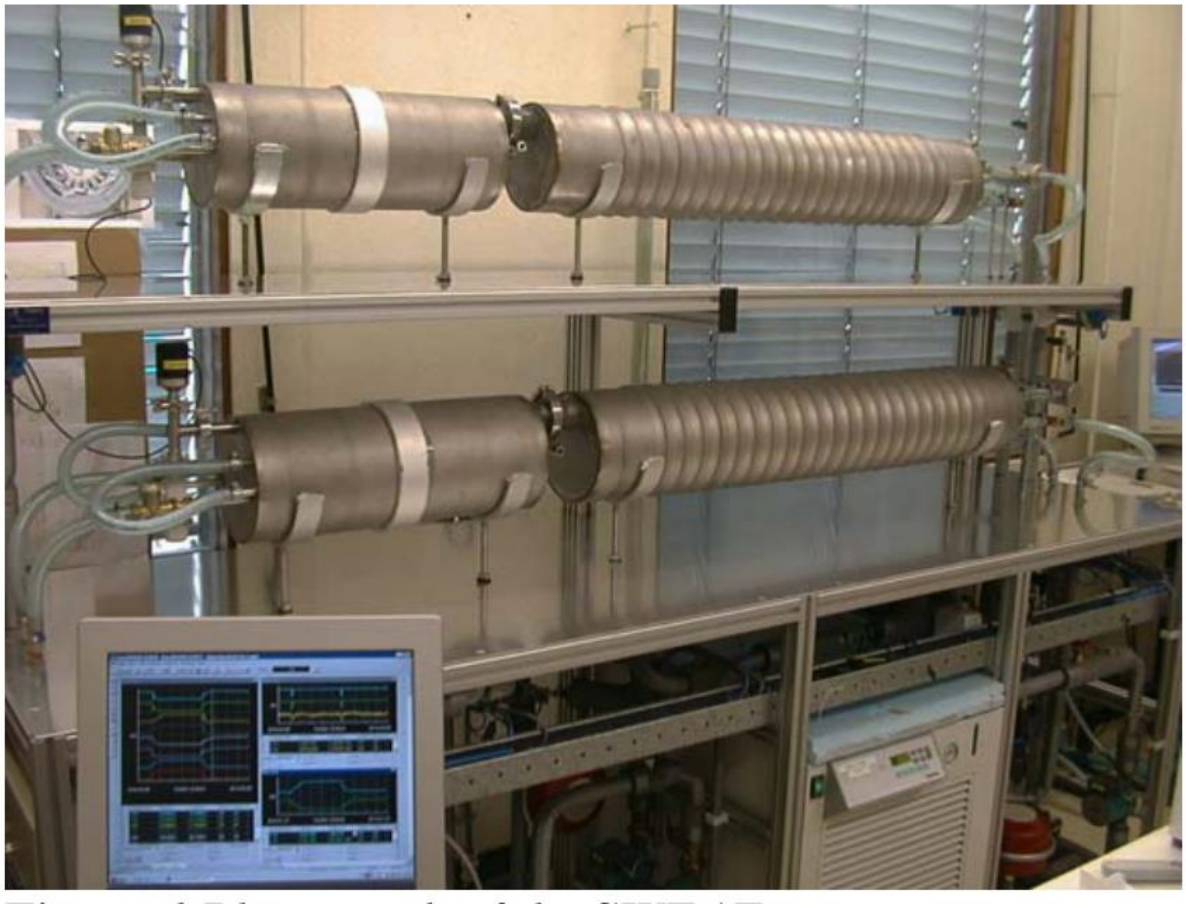

Figure 19 - Image of the SWEAT prototype water-salt system [31].

The prototype system (Figure 19) consisted of two units which could be used in continuous or batch mode, with each containing 3kg of Na_2S. Each unit was connected to 3 water loops; one hot water circuit to regenerate the sorbent; a cold water supply for cooling the condenser and sorbent, and a chilled water loop connected to the evaporator. Each loop was temperature adjustable to measure performance at different working conditions.

The salt-water system operated at temperatures between 35 and 83 °C (absorption and desorption swing but avoiding a eutectic melting point at 83 °C,) and a temperature differential of 57K was required or 63K to achieve 100% charge. The system achieved a maximum cooling power of 1500 watts; however, this was only achievable with the evaporator operating at 20 °C or higher (not practical for most applications). When it was operated in the range of 10 -15 °C lower, cooling powers of 500 – 700 watts were recorded.

The theoretical coefficient of performance was 0.66 while the measured maximum of 0.57 was attained with an efficiency of 84% with 3.7 kWh heat in and 3.2kWh heat out – storing 2.1kWh of cooling. The researchers concluded the system favoured night time charging due to more

favourable external temperatures for condensing, where a cheap overnight source of heat was available (e.g. Economy 7) and cooling demand was required during the daytime.

1.2.2.3.3 Non-water sorbents and exotic sorbates

It is important to note that not all sorbent-based systems utilize water as the adsorbate/absorbate. There are some reactions utilizing ammonia (NH_3). These include many metal halides such as $NiCl_2$, NaBr, LiCl, $FeBr_2$ etc. They tend to have significantly elevated temperatures (i.e. 150 °C or higher) and pressures (10 bar and higher) of operation [29]. These developments and the research in this area is at a very early stage and there are significant draw backs in terms of safety, conditions and materials used for domestic utilization.

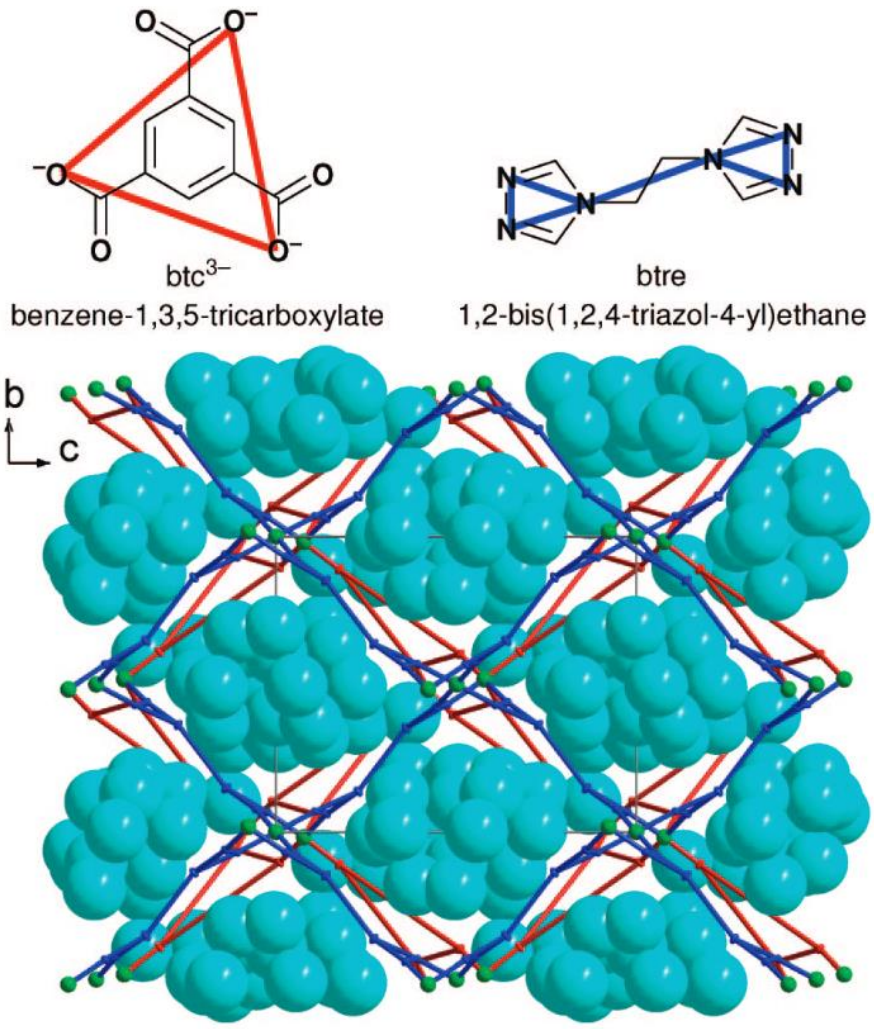

Figure 20 - Schematic drawing of a metal organic framework showing two ligand types (red and dark blue) and nickel atoms (green) with oxygen atoms (light blue) filling the empty space in the structure [32] .

A new class of sorbate recently gained attention in academia; metal organic frameworks (MOFs), an example in Figure 20. These materials are solids, and their structure is that of metal ions being held together by organic species. They also have strong bonds and ordered

geometries. They have been investigated for adsorption for gas storage, typically hydrogen, although their suitability for heat storage is now under investigation [32]–[34].

These materials appear to have superior energy density and comparable water loading characteristics under similar temperatures (95 / 140 °C desorption and 30 -40 °C adsorption) while retaining cycle stability [29].

There have also been investigations into a wide range of composite materials especially with salt hydrates, e.g. $CaCl_2$ and other salts in zeolite, silica gel and other frameworks [35], [36]; however, this area is at an early stage of research.

1.2.2.4 Thermochemical Heat Storage

Thermochemical heat storage utilizes the enthalpy of reaction for a given chemical reaction in order to store heat (it can also make use of the material's specific heat capacity). These processes make use of reversible exothermic (gives out heat) and endothermic (requires heat) reactions [15]. The amount of heat stored is dependant entirely on the given reaction and the bond strength being broken and made.

There are several chemical methods available to store energy including dilution (adding and removing water from a salt solution), hydration (adding and removing water from a solid crystal material), solution (crystallising or solvating a salt) and reaction (making and breaking down of chemical substances). An example equation for a reversible chemical reaction which releases energy with a forward bias is seen below.

$$A + B \overset{\pm \Delta E}{\Longleftrightarrow} C \tag{2}$$

Thermochemical heat storage is an active process requiring chemical reactors and heat exchangers, in order to drive charge and discharge processes. With reversible equilibrium reactions, a separation step is needed to remove the products of a reaction from each other in order to drive the position of the reaction to the forward one, favouring more products.

Temperature levels during charge and discharge are highly dependent on the reactions used. This is due to implementations restricting the usage of reactions to those in the correct temperature range. There is a broad range of available temperatures, with salt-hydrate solutions around 70°C to ammonia breakdown at 400 - 700°C. Figure 21 gives a range for some different types of thermochemical storage.

The important characteristics for these systems are chemical compatibility, stability, toxicity, reversibility, cyclability, corrosion, cost of materials, balance of plant, efficiency, energy density, lifetime, storage time, temperature range and many others.

For the purposes of clarity, any chemical processes that involve the absorption or adsorption have been covered in the previous section and any further examples will not be of the absorption or adsorption type.

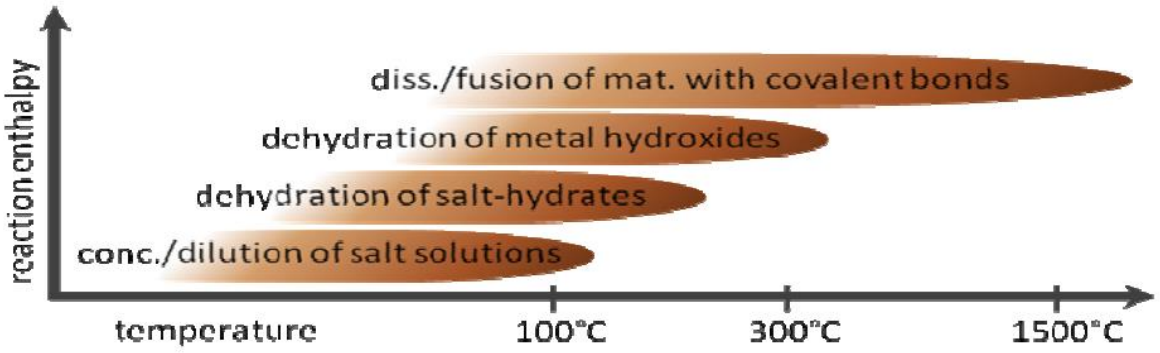

Figure 21-Range of temperatures versus reaction enthalpy of several types of thermochemical storage [37].

1.2.2.4.1 Calcination / Carbonate Systems

$$MCO_{3(s)} + \Delta H_r \leftrightarrow M_{(s)} + CO_{2(g)} \quad (3)$$

Calcination/ Carbonate based systems have two types, (both driven by CO_2 partial pressure and high temperatures to produce calcite and cerrusite.) The general reaction form for these systems can be seen above in equation 3.

Calcite based systems operate at temperatures between 973 to 1273K between partial pressure of 0 – 10 bar. The enthalpy of chemical reaction for this process is 178 $kJmol^{-1}$.

Investigated during the 1970s, this type of system has numerous downsides such as a low cycle efficiency of 10 -30% and energy densities only 10% of the theoretical 35.3 $kWhm^{-3}$ [38] were achieved due to the utilization of sub-micron particles to avoid passivation of the surface [39].

During the 1980s, the reaction was then operated in a fluidised bed and rotary kiln with similar conditions leading to efficiencies between 10 -40%, though the rotary kiln achieved only 60% material conversion in comparison with 100% in the fluidised reactor [40].

The major advantages to this type of system are the use of known industrial processes without the need for a catalyst, no by-products, simple product separation, high material energy density and low cost.

The disadvantages to this system are the issues with agglomeration and sintering of the solid product, poor reactivity (difficulty with conversion %) and accessing and storing the CO_2.

Cerrusite (lead carbonate) based systems are similar to calcite based systems. They also use CO_2 but can tolerate a wider temperature range, between 573 – 1730K, in a packed bed [41]. This type of reaction was originally used in concert with heat pumps and the calcite based system [42]. The operating partial pressure for this reaction is, however, dramatically reduced to between 0 -1 bar.

This system again benefits from high theoretical energy density, easy product separation, requires no catalyst and has no by-products. Unlike calcite systems, this chemical reaction has poor reversibility and requires access to and storage of CO_2 with a toxic product.

1.2.2.4.2 Metallic Hydrides

$$MH_n + \Delta H \leftrightarrow M + n/2H_2 \quad (4)$$

This type of chemical process stores heat energy via the reversible process of producing metal hydrides. The general reaction form can be seen above in equation 4.

The main materials utilized and investigated are lithium, calcium and magnesium. These systems use high temperatures (523 – 723K) for magnesium, 1223 – 1373K for calcium and lithium, and large partial pressures of hydrogen (1 to 100 bar) [43].

One specific interest is the production of magnesium hydride. This particular reaction is suitable due to the reversibility, lack of by-products, easy product separation and operational temperatures (200 - 500°C), seen in Figure 22. However, this reaction does have drawbacks due to slow reaction kinetics, necessary chemical doping, high operating pressures and the need to store hydrogen gas [40].

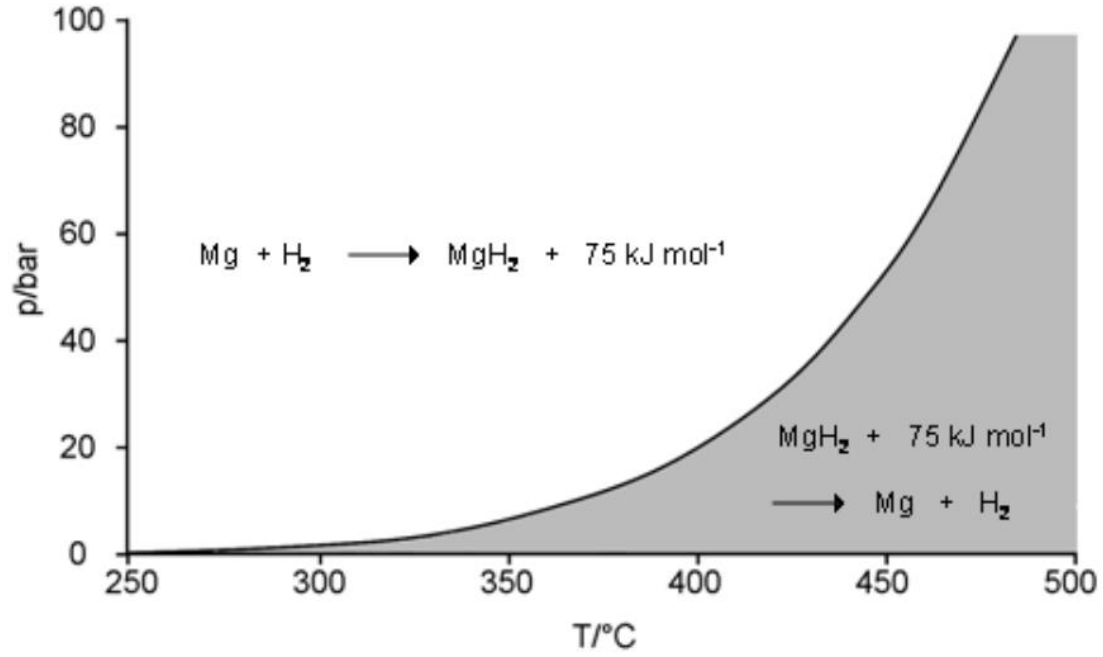

Figure 22 - Dissociation pressure curve of MgH_2. [44]

Originally studied for hydrogen storage rather than heat, research took place into using hydrides with heat pumps to assist in heat transfer [45] and thermal energy storage in concentrated solar power [46].

The Max-Plank institute designed and produced 3 prototype systems, a steam generator (Figure 23), solar thermochemical plant (Figure 24) and a solar cooking/cooling device [44].

The steam generator had a volume of 20 L and consisted of a semi-permeable tube to supply H_2 into magnesium powder with nickel powder. The helical tube contains the pressurised water flow and serves as the heat exchanger. Heat can be supplied via the external casing from ribbon heaters to drive the desorption process.

This device was capable of delivering a maximum power of 4 kW at temperatures and pressures up to 450°C and 50 bar. Unfortunately the research published no efficiency data.

The further solar-thermochemical plant essentially gathered solar radiation to generate electrical energy with a Stirling engine. The design took account of the periods with weaker or no solar radiation by using a similar MgH_2 based storage device operating between 623 – 723K to provide the heat to the Stirling engine. The design was tested in the laboratory and in limited field tests to establish the functionality of the design. The researchers did not however supply any output from these investigations and identified shortcomings of the installation were identified and measures to correct these proposed.

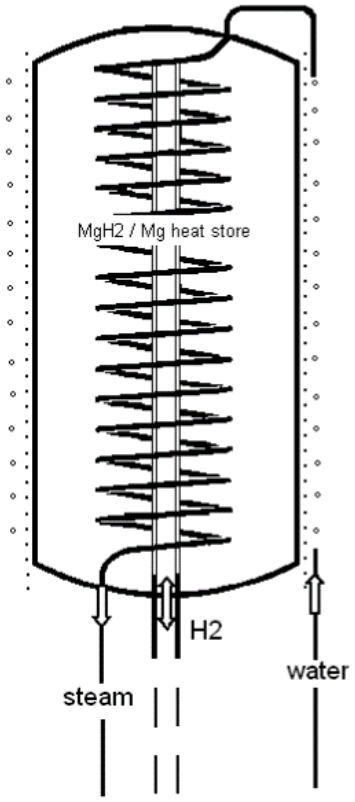

Figure 23 - Diagrammatical representation of a steam generator based on MgH_2 based thermochemical heat storage.

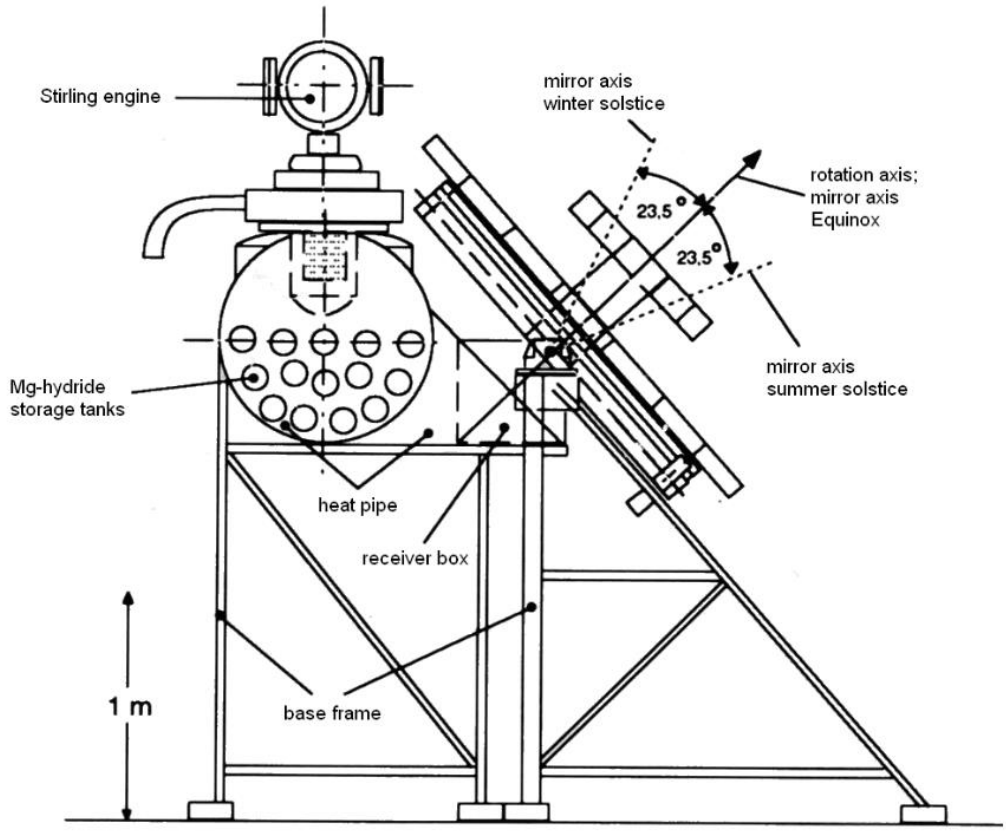

Figure 24 - Schematic diagram of the cross section of the prototype solar power station utilizing a MgH_2/Mg heat store, Stirling engine and fixed focus solar concentrator.

1.2.2.4.3 Other systems

Due to the nature of thermochemical storage being a more recently investigated and diverse field of study, there is a large number of potential chemical reactions that would be suitable for heat storage which will not be covered in this document.

Such examples of these are:

- Ammonia based systems – Ammonium hydrogen sulphate, NH_3 synthesis.
- Organic systems – methane reformation, dehydrogenation and thermal dissociation.
- Hydration reactions – covered in sorption based storage.
- Reduction and oxidation – peroxides.
- Dilution of salt solutions.

Further detail and an excellent comparison of such can be found in Pardo et al. [40].

1.2.2.5 Latent / Phase Change Heat Storage

Latent heat storage, also known as phase change heat storage utilizes the change in phase of a material and the specific heat capacity in order to store heat energy. These phase changes are normally solid to liquid or liquid to gas; however solid to solid changes in crystal type PCMs can also be utilized. The relationship between energy, phase change (enthalpy of fusion), specific heat capacity and change in temperature can be seen below in equation 5.

$$E = MC_p\Delta T + M\Delta H_{fusion} \quad (5)$$

As a function of this energy storage within the latent heat of the material, all of the energy is stored at the particular temperature of the change in phase. This accordingly confers an advantage to applications that use/need small temperature ranges and can reduce heat losses.

Latent heat storage can be utilized in active applications, such as latent heat storage with forced air in roof spaces or in passive applications such as within walls or under floor [47].

In order to charge the material, it requires heating until it undergoes a phase change. Discharging will occur when the temperature of the PCM's surroundings goes below the temperature of the phase change, reverting to the original phase releasing heat.

Latent heat storage is used in a similar manner to conventional heat storage but has the advantage of a fixed temperature point with a larger enthalpy. With the correct selection of a

phase change material, it will have a higher energy density with a lower thermal loss for a given storage application. In addition, when compared to a sensible heat store, they have a higher exergy and thus more work can be recovered from the system before requiring recharging.

They are generally used diurnally but can also be used seasonally; however like conventional storage, the longer the store is left before discharge the further the efficiency drops. Due to the fact higher (or lower) temperatures are not required to store more energy and their higher exergy, the heat loss associated with this storage is decreased for an equivalent amount of conventional sensible storage.

Historically, the main component of most latent storage systems has been water-ice for the use of cooling. This has many forms from ice slurries, ice on coils etc… however further materials are used and are typically categorised as organic e.g. paraffin or inorganic, eutectics or hydrated salts [48]. A few of these materials are listed in Table 1 below:

Table 1- Comparison of a few possible phase change materials [2][49][48][50][51][47]

Material	**Melting Temperature (°C)**	**Heat of Fusion (kJ/kg)**	**Density (kg/m^3)**
H_20	0	333	998
RT5	7	156	860
RT27	28	179	870
RT54	55	179	900
$AlCl_3$ + NaCl (66-34)	93	201	n.a
KNO_3	333	366	2110
NaCl(56)-44$MgCl_2$	430	320	n.a

Most literature classifies phase change materials under **organic** (hydrocarbon based) or **inorganic**.

Inorganic materials cover a larger temperature range and typically have similar enthalpy per mass with organic PCMs but have higher enthalpies per volume due to their higher densities.

Examples of well-known organic phase change materials include paraffin wax, other linear alkanes, glycols, sugar alcohols, fatty acids which can be seen in Figure 25 compared by melt temperature and melting enthalpy.

These organic materials typically show good storage densities with respect to mass and volume and typically change phase congruently with little sub-cooling. Vapour pressures are usually low, while chemical compatibility is usually excellent and they rarely react with common reagents.

Unfortunately, these materials typically have significant volume expansion, although this may not be critical depending on how soft the materials are, leading to lower forces on expansion. In addition, their thermal conductivity tends to be poor and these materials are combustible (although they are not inflammable.) Sometimes paraffin waxes are blended to obtain different material properties. Fatty acids do however show less chemical compatibility compared to glycols, alkanes and alcohols due to the acid functional group.

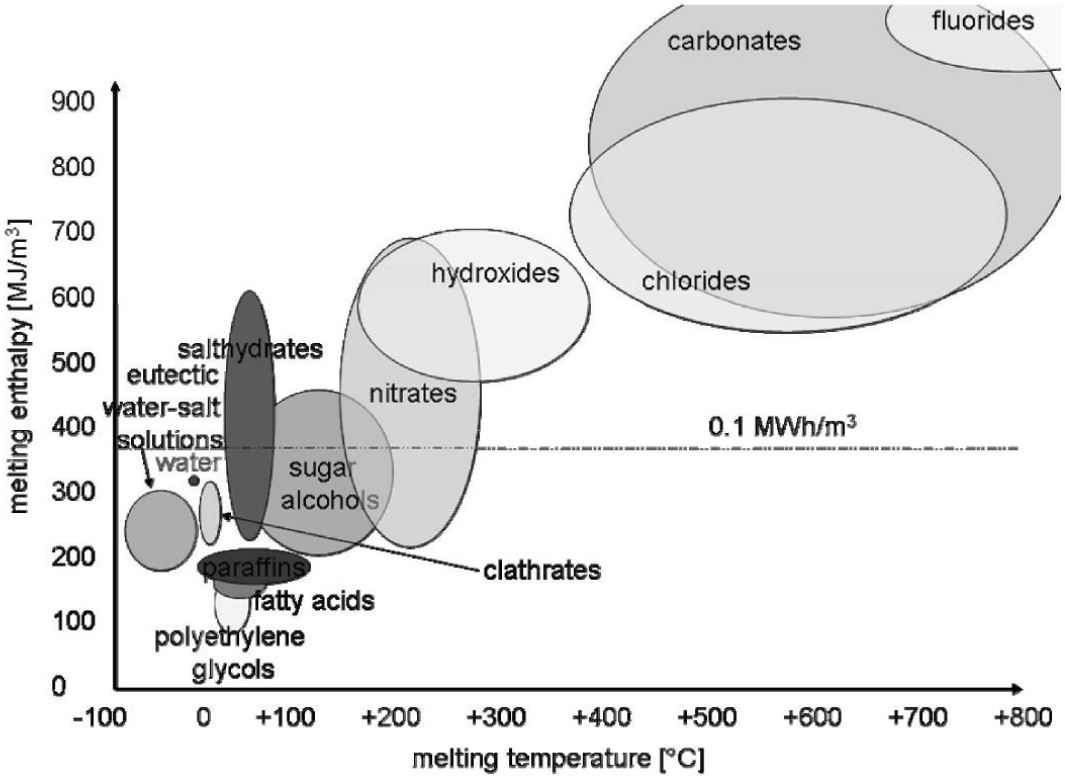

Figure 25 - Classes of materials that can be used as phase change material showing typical melting temperature range and enthalpy [52].

Examples of well-known phase change materials in the inorganic category are water and sodium acetate trihydrate (commonly found in hand warmers.)

It is important to note that in the case of phase change for water, the enthalpy is used for cooling purposes rather than heating as is typical in most organic PCMs. In addition, numerous water-based eutectics e.g. NaCl are also used for sub-zero temperature cooling.

Further water-based salt hydrates are also used in the temperature range of melting between 5 - 130 °C; however these materials suffer from subcooling and phase separation which causes cycling stability issues.

Toward the higher end of melting temperature, 300 – 800+ °C, salts are used as PCMs and have significantly increased melting enthalpies, thermal conductivities and energy storage densities. They also have a very low vapour pressure and have very little sub-cooling. These materials are promising but are a design and health and safety concern in domestic scenarios due to their extreme temperature and chemical properties.

One further class, outside of inorganic and organic and not as popular, is **clathrates**, crystalline structures where molecules are enclosed. When the lattice is formed with water these are clathrate hydrates: when formed with water and the enclosed molecules are gas, these are gas hydrates.

Gas hydrates typically have melting temperatures between 0 - 30° and usually enclose noble gases, chlorofluorocarbons or alkanes. These are however difficult to utilize as these materials are not stable at ambient pressure, though several exceptions and other forms with non-polar liquids or organic salts enclosed, exist.

Latent heat storage began to receive far more attention in recent decades for many applications, such as thermal management in electronics [53], buildings, military vehicles [54] and also within energy storage for applications such as solar thermal power generation [55].

PCMs have also been applied in a number of ways, for example as an additive to conventional gypsum wallboards, diurnal passive heat storage systems utilizing ceiling space [56] or underfloor shape stabilized plates [57]. Stalin et al. [58] also investigated the use of phase change materials in a perforated plate above a ceiling fan for air cooling. All of these systems typically utilize near room temperature organic PCMs, however some of the materials operate at temperatures approaching 65 °C [59].

1.2.2.5.1 Molten Salt

Molten salts or inorganic salts are most widely implemented for thermal storage in thermal concentrating plants. They have a high density and energy density, very low vapour pressures and can operate at high temperatures 300 ° C. Pure salts are typically based on carbonates, chlorides, nitrates and sulphates; however, some molten salts in use are mixtures or eutectics to dramatically reduce the melting temperatures [60]. The temperature ranges for these

materials is usually between 120 – 1000 °C (seen in Figure 26) but few pure materials have a suitable latent heat capacity [48] .

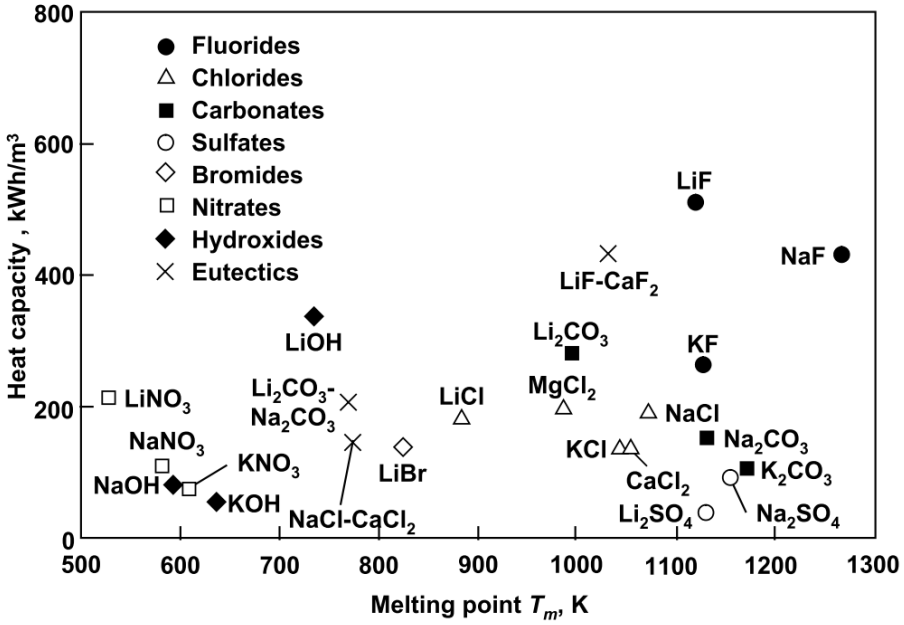

Figure 26 - Melting temperature and heat capacity of various molten salts [61].

The cost of these materials can vary largely with materials like KOH reported as the likely most cost effective [61] where fluoride based salts have a larger heat storage capacity but are less attractive due to concerns with material compatibility and cost [62].

One large system in use to temporally displace energy production is the molten salt system developed and used at the AndaSol solar production facility in southern Spain, Figure 27. It stores 1350 MWh of thermal energy, or 9 hours of 50MWe full load production [63] [64].

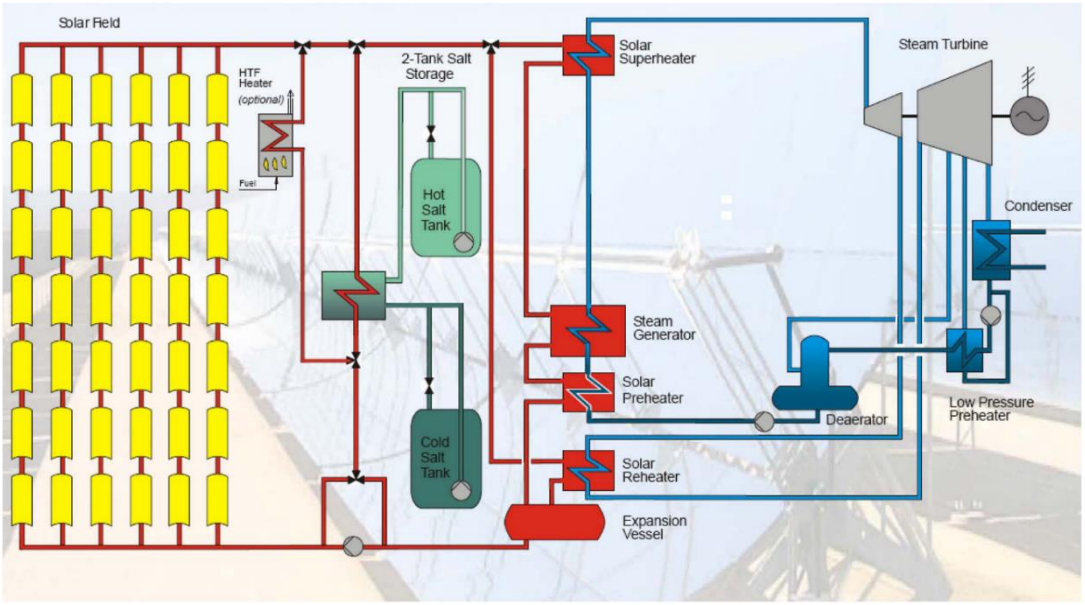

Figure 27 - Schematic diagram of AndaSol solar plant with concentrated solar collection and molten salt thermal storage [26].

This facility utilizes a synthetic oil heat transfer fluid at 400 ° C to be directed toward the molten salt storage system or the steam generators. The system is designed to produce double the thermal energy required for the electricity required in order to produce sufficient thermal energy for storage and utilization overnight. The molten salt in question is a 60:40 wt.% mixture of sodium and potassium nitrate [26]. Steam is produced at 100 bar and 377 °C from the molten salt cycling between 386 – 292 °C. This means the latent heat of melting is not used in this system.

Figure 28 - Sodium Nitrate PCM Storage test module from [65].

Another system developed at the German Aerospace Centre (DLR) utilized sodium nitrate of 5 kW at a melting temperature of 306 °C [65]. The vessel was 30.8 cm in diameter, 1.4 m high (Figure 28) with 7 internal finned heat exchanger tubes with Therminol VP-1 as a heat transfer fluid. The researchers calculated this system had an energy density of 83.3 kWh/m^3 and power of 42.5 kWm^{-3} (8.51 kWh) though this would be more favourable with larger systems. A typical charge and discharge for this system can be seen in Figure 29.

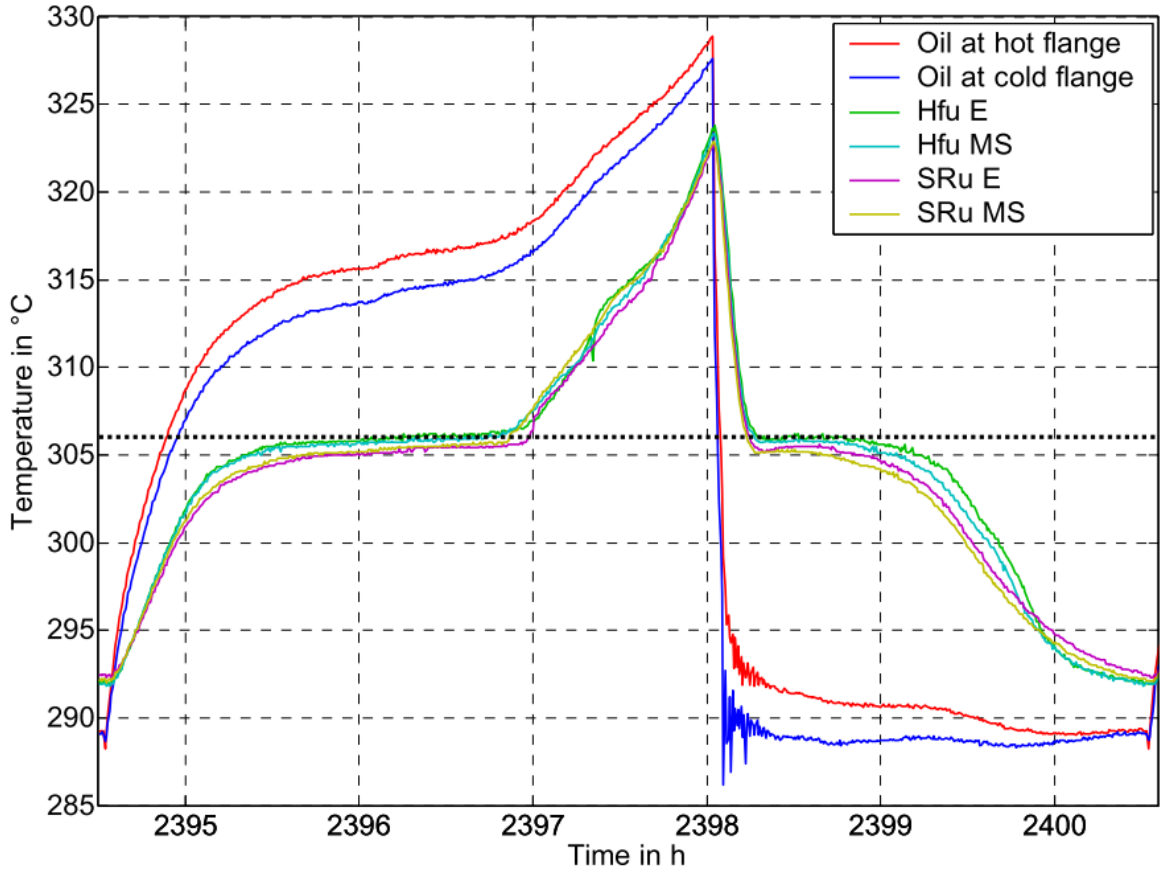

Figure 29 - Typical experimental charge and discharge cycles of sodium PCM storage test module from [65].

The design used fins of expanded graphite or aluminium to assist in heat transfer which were found to achieve the desired power rating and had satisfactory chemical compatibility. Over 4000h and 172 cycles no degradation in the salt or the fins was detected.

1.2.2.5.2 PCM Composites and Additives

Due to the poor thermal conductivity in lower temperature phase change materials and shape forming, research has taken place into addressing these issues with composites and additives.

There have been numerous investigations into the usage of composite PCMs (from shape stabilisation with low-density polyethylene (LDPE) [66] to modelling charge and discharge enhancement using embedded metal foams [67].) In the latter case it was found that the discharge rate was improved approximately 8 times with a porosity of 0.8 using aluminium and

paraffin wax / aluminium and $NaCO_3$. Similar empirical studies have investigated lithium, sodium, potassium and calcium silicate composites [68], copper porous matrixes with N-eicosane [69], concrete with embedded macro-encapsulated steel balls of octadecane [70] and PCM-enhanced cellulose insulation in passive solar walls [71] which have demonstrated improvements from their base materials.

Many investigations into PCM enhancement and reviews of PCM enhancement with additives have taken place, with the introduction of graphite, carbon fibres, metals, graphene etc… [72], [73].

An example of one of these investigations is the development and testing of an n-tricosane phase change material embedded with 10 wt.% graphite fibres. In comparison to pure wax, substantial reduction (1/2) in solidification time was achieved at temperatures from ambient to ~ 115 °C.

Another investigation determined that the addition of 1wt% carbon black and Al_2O_3 nanoparticles had dramatic effects on the thermal conductivity of 2 commercially available organic room temperature melting PCMs [74]. It was found that Al_2O_3 particles penalised the thermal conductivity of both PCMs ~7-8% where carbon black lead to a 35% and 24% improvement in the RT20 and RT25 paraffins while other thermal characteristics were not greatly affected.

These are a few examples of the work in the area of additives/composites and further detail / reviews of this area can be found in Fang et al [72], Mohamed et al [73] and Cao et al [75].

1.2.2.5.3 Pumpable micro-encapsulations / Slurries and Emulsions

Encapsulation is the process of encasing a material in an unreactive material in order to be added to a fluid to form a mixture with the properties of both the carrying fluid and the encapsulated material. The principle of emulsions is to achieve the same outcome by putting a fine dispersion of droplets of a given material which is immiscible and non-soluble in a carrying fluid. A microscopic image of several microcapsule types for PCM storage can be seen in Figure 30.

The idea of encapsulation or slurries of phase change materials into a pumpable form has been researched for some time [76]–[78], the idea being that a microencapsulation suspension/slurry or emulsion (no encapsulation of PCM) or phase change material can dramatically reduce heat losses in pipelines and simplify heat exchanger design to being simple modules of fixed design with multiple units depending on heat demand due to their isothermal heat transfer. Research has shown that emulsions and microencapsulated suspensions have had similar thermal properties [79].

In addition, they have dramatically higher energy storage density [80] than conventional heat transfer fluids while the superior heat transfer qualities of the carrying fluid can be retained [77]. Due to both their energy density and isothermal heat transfer, not only do these slurries/emulsions carry more energy for a given pipeline, but they also lose less energy from the stored heat (dependent on melting point selection.)

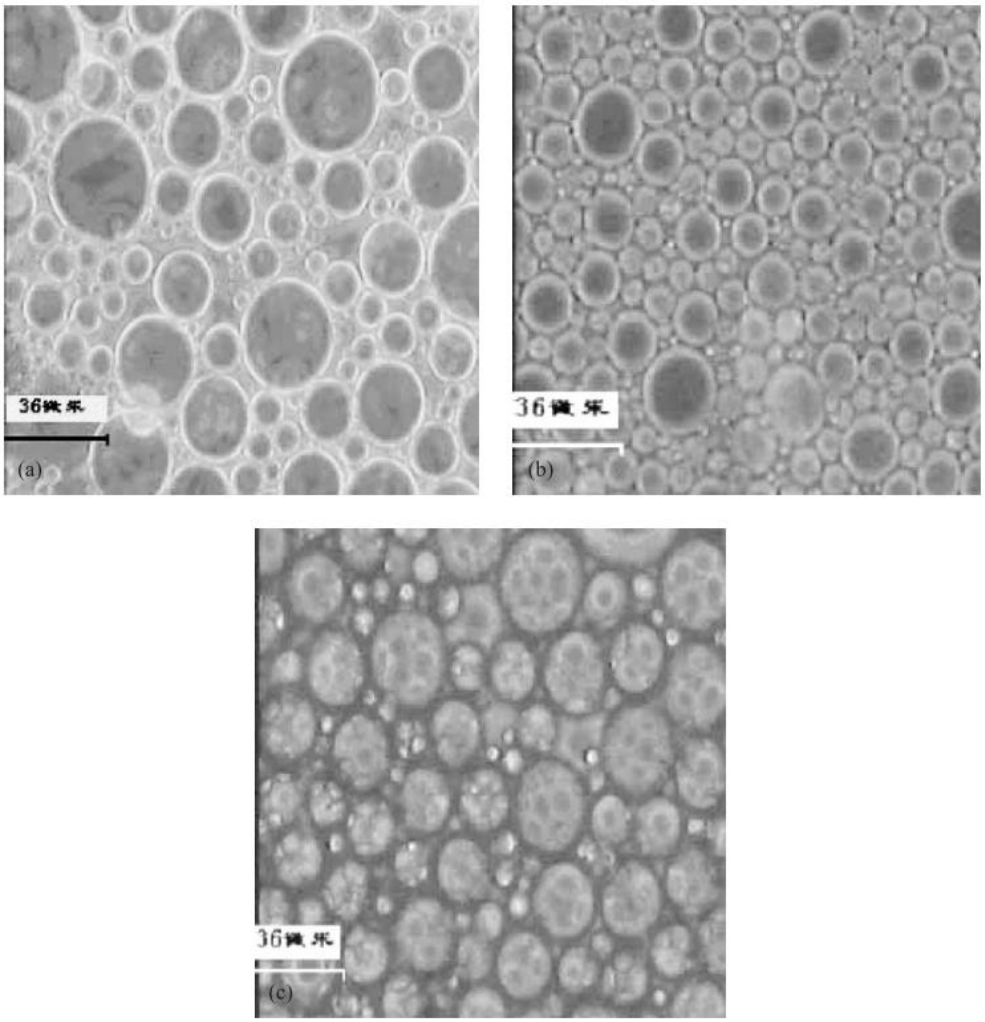

Figure 30 – Phase difference microscope images of microcapsules with (a) polystyrene as the shell, (b) polymethyl-methacrylate as the shell, and (c) polyethyl-methacrylate as the shell [79].

There are disadvantages to these systems however; when at lower temperatures PCMs solidify, but the mixture's viscosity dramatically increases at higher percentages of PCM [79] causing issues with fouling, pumping and phase separation. Emulsion systems typically require an emulsifier to prevent phase separation and to increase the stability of the suspension [81] . It has also been observed that surfactants and particle size can also reduce

drag and the ratio of particle size to heat exchanger pipe diameter can have an effect on heat transfer. Goel et al. [82] determined that wall temperatures were affected being up to 15% lower with the 250 pm microcapsules a when compared to those with the 100 pm microcapsules.

Vorbeck et al. demonstrated that a phase change slurry unit requires 5 times the pumping power for the slurry when compared to water while storing approximately 74% more heat energy (2.7x the pumping energy per unit of heat stored.)

Similar studies investigating the enhancement of thermal properties in emulsions and the effects of increasing viscosity [83] have further confirmed vast improvement in heat storage density and the deleterious effects of high viscosity where PCM ratio exceeds 50wt %.

1.2.2.6 Comparison of Heat Storage Technologies

A concise and robust comparison of the technologies based on their characteristics is shown below in order to understand more easily how the technologies compare.

Table 2 - Comparison of key metrics for various heat storage technologies [16]

Technical performance	**Typical current international values and ranges**		
Energy Input/Output	Solar heat, waste heat, variable renewable energy sources (PV, wind), electricity/heat		
Technology Variants	Sensible Thermal Energy Storage, **STES**	Storage in Phase Change Materials, **PCM**	Thermo-chemical Energy Storage, **TCS**
Storage Capacity (kWh/t)	10 - 50	50 - 150	120 - 250
Thermal Power (MW)	0.001 - 10	0.001 - 1	0.01 - 1
Efficiency, %	50 - 90	75 - 90	75 -100
Storage Period (h,d,w,m)	d - y	h - w	h - d
Cost (€/kWh)	0.1 - 10	ott-50	8 - 100
Technical lifetime, yr	10-30+ (depending on storage cycles, temperature and operating conditions)		
Load (capacity) factor, %	80	80	55
Max. (plant) availability, %	95	95	95
Typical (capacity) size, MW_e	25	0.5	100
Installed capacity, GW_e (GW_{th})	9–10 (all types)	<<1	18 (estimate)
Environmental Impact	Negligible, with GHG emissions reduction, depending on the amount of primary fossil energy saved by using energy storage		
Costs (USD 2008)	**Typical current international values and ranges**		
Investment cost, $/kW	3400 – 4500	6000 – 15,000	1000 – 3000
O&M cost (fixed & variable), $/kW/a	120	250	20 – 60
Fuel cost, $/MWh	N/A	N/A	N/A
Economic lifetime, yr	20		
Total production cost, $/MWh	80 – 110	120 – 300	25 – 75
Market share, %	0.25	Negligible	N/A

1.2.2.7 Heat Transfer Fluid

In most domestic and industrial cases, water or steam is used as a primary heat transfer fluid in both heat generation and storage. This is usually the case due to its ubiquity, low cost, chemical compatibility and high specific heat capacity.

Domestic systems typically use liquid water up to 90 °C where industrial systems can also utilize water at higher pressures to avoid boiling or directly can use heated or superheated steam, this relationship can be seen in Figure 31. When approaching heat exchange fluid temperatures of 200 °C or more it is more common to see the utilization of steam or thermal oils. It is also advantageous in these systems that the storage medium also being the heat transfer fluid avoids further heat transfer losses.

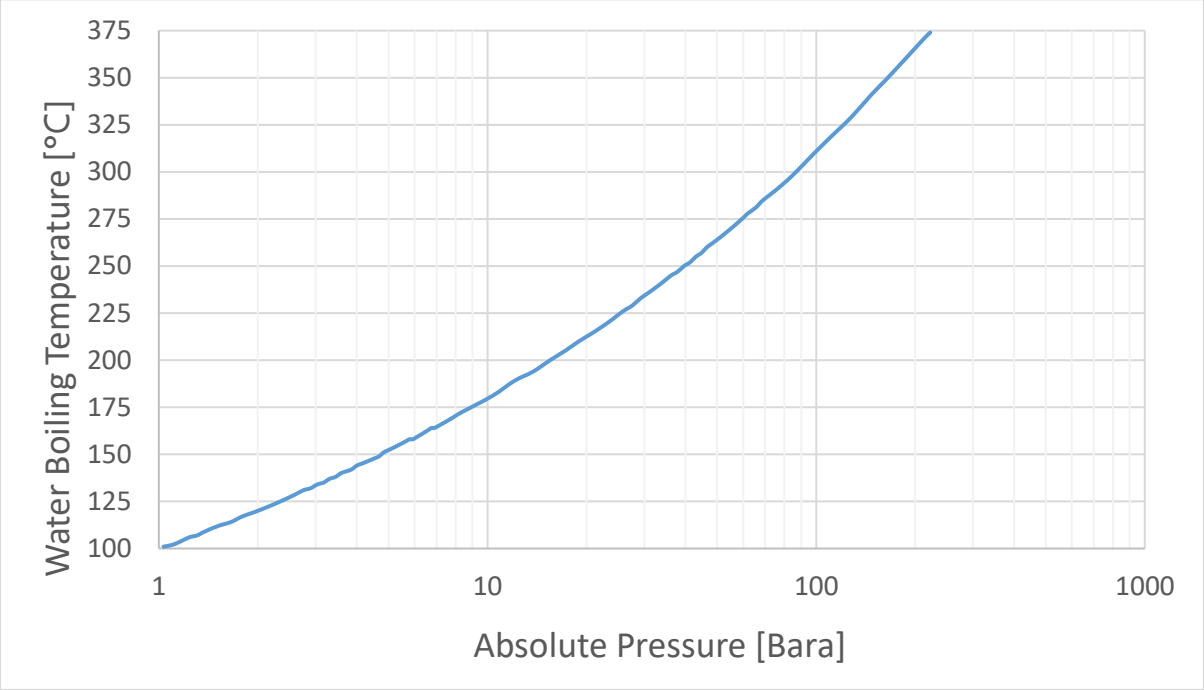

Figure 31 - Boiling temperature of water versus absolute pressure. Source: Data from [84]

Where these systems have heat exchanger fluid come into direct contact or consumption by humans, the temperature of storage must be above 60° C to prevent contamination via Legionella bacteria.

1.2.3 Domestic heat store technical requirements

The choice of storage technology in homes is subject to a number of practical, technical, economic and social factors. One social constraint would be that such systems could reduce quality or access to open space within the home or local community. With respect to several technical requirements, a number are listed below:

- **Operational Temperature Regime** – this determines heating operational range and affects the rate of heat transfer.
- **Heat storage capacity** – both volumetric and density-based metrics important for how large or heavy a system will be.
- **Heat storage duration** – how long a store can retain heat- this varies from system to system but the longer a store holds heat the lower its cycle efficiency becomes. Important with respect to systems design for diurnal, seasonal etc… operation.
- **Partial load operation characteristics** – i.e. how a system operates when not at full load which is likely for discharge.
- **Cycle efficiency** – indicates the wastage of the system, important for running costs.
- **Durability / long term stability** – important for determining the life time of a system and maintenance costs.
- **Materials availability.**
- **Capital cost including installation.**
- **System integration** – how / if / how well can a system be integrated into the home or with other systems.
- **User perception** – important for the popularity and acceptance of the system.
- **Operational methodology** – seasonal systems will have many fewer cycles than diurnal systems. This will have effects on the payback time of a system dependent on many other factors. Seasonal systems therefore would payback less quickly and warrant a lower cost per effective heat storage and/or higher value of recovered heat at a later stage.

To determine the appropriate use cases of a heat storage system, store charge time and power rating calculations were made based on the average values found in Energy Saving Trust. (2008) and a diurnal usage charge. Across the whole sample of their gathered data **for hot water usage only** the mean value of energy used per day in a residential home is 16.8 ± 2.2 MJ/day or 4.67 kWh [9]. This gives a 1.795 kWh duty with the average home heating element duty time of 2.6 hours per day i.e. 1.795 duty kW heater to store a single day of energy. With a different diurnal cycle utilizing a 6 hour charge period this decreases to 0.78 kW.

To see values for storage times exceeding a single day, observe Table 3 below:

Table 3 - Values of stored energy and duty for an average residence by days stored of hot water.

Number of Days to store	Energy for period kWh	Heater Duty (2.6 hours) kW	Heater Duty (overnight 7 hours) kW
1	4.67	1.80	0.67
2	9.33	3.59	1.33

7	32.67	12.56	4.67
10	46.67	17.95	6.67
14	65.33	25.13	9.33
30	140.00	53.85	20.00
60	280.00	107.69	40.00
120	560.00	215.38	80.00
365	1703.33	655.13	243.33

For calculating a more accurate estimate for houses by their type on a yearly basis the BPIE (Buildings Performance Institute Europe) has compiled various statistics [128] including energy use for space heating purposes which can be seen for the UK in Figure 32.

With an owner-occupied average residence size of 109 m^2 this gives an energy use for a post 2002 mid terrace as year as 11205 kWh or 30.7 kWh per day.

This is 35.4 kWh per day total heat energy in total adjusting Table 3 to the following Table 4.

At present the main motivators for the utilization of any form of stored heat in the home by consumers are the Economy 7 and Economy 10 tariffs offered by suppliers drawing attention to 1 day storage.

For an average property with electrically heated hot water, a tank of 100 – 200 litres is typically used. The average of 4.67 kWh a day translates to 80 litres of water heated from 10 to 60 ° C. This disparity in tank sizing is due to the diluting effect the introduction of new cold water into the tank has.

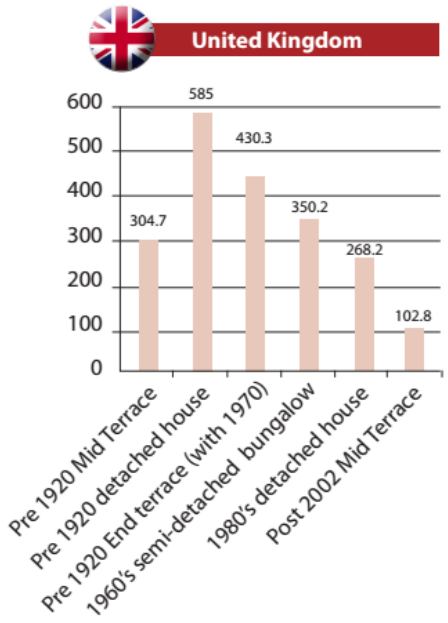

Figure 32 - Average heating consumption levels in final energy use (kWh/m^2a) of family homes by construction year. [128]

Table 4 -Values of stored energy and duty for an average residence by days stored of heat, hot water + space heating

Number of Days to store	*Energy for period kWh*	*Heater Duty (2.6 hours) kW*	*Heater Duty (overnight 7 hours) kW*
1	35.37	13.60	5.05
2	70.74	27.21	11.79
7	247.58	95.22	41.26
10	353.69	136.03	58.95
14	495.17	190.45	82.53
30	1061.07	408.10	176.85
60	2122.14	816.21	353.69
120	4244.28	1632.42	707.38
365	12909.69	4965.26	2151.61

For the given owner-occupied property utilizing 35.37 kWh for both central and hot water heating, this would translate to 608 litres of water heated from 10 to 60 ° C (without the effect of dilution which could easily double this value.) Calculations show 36.4% of a tank is useable with a supplied minimum temperature of 40 ° C from a storage temperature of 60 ° C with a cold water inlet at 5° C.

These magnitudes of stored hot water can be reduced by storing at higher temperatures; however in the latter case storage of water between 10 and 90 ° C only reduces the amount of water required to 380 litres (without effect of dilution), a still typically un-manageable amount for most residents and would require a thermostatic mixing valve to suit legal regulations on the temperatures allowed in building pipework. This large amount of water is the reason why most storage tank heaters only provide hot water rather than space heating.

In contrast, storing a similar amount via phase change of beeswax would necessitate 480 kg or 631 litres with no dilution effect, an amount easily stored underfloor where the same property (area 109 m^2) could store 1090 litres with a 1cm thick layer.

1.3 Literature Review

Latent heat storage technology offers a unique option for decoupling domestic heat production and consumption. With the energy being stored in the change of phase, significantly more energy is stored and represents a means effectively and efficiently to store significant heat for residential applications while being able to meet residential size, form, safety and temperature range requirements. With this in mind, phase change materials give a unique opportunity for original research.

In order to situate the research presented in this thesis, further investigation into the area of phase change material literature has been performed and has been classed into several discrete sections below including phase change storage: within building fabric, packed beds, integrated systems and numerical modelling.

1.3.1.1 General Reviews of phase change storage for domestic use

Further general reviews on the area of phase change material research in the built environment or for domestic heating and cooling can be found in Whiffen et al. [85] [86], Akeiber et al [87], Sharif et al. [88] and Farid et al. [89].

Whiffen et al. [85] Part I initially presents the motivations, existing technologies, empirical analysis methods and general methodology of PCM system design, PCM selection and examples of existing PCMs. It subsequently covers typical containment / application methods, heat transfer issues (low thermal conductivity and enhancement) and brief exploration of costs.

Part II [86] introduces specific applications of PCM including wallboard and concrete composites, passive cooling ceilings / ceilings and air conditioning. It demonstrates the difference between PCM and conventional building materials as seen in Figure 33 and Figure 34.

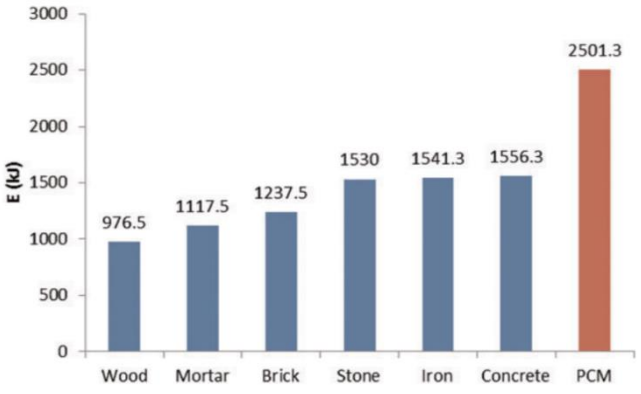

Figure 33 – Comparison of energy stored and released during a 24 hr period

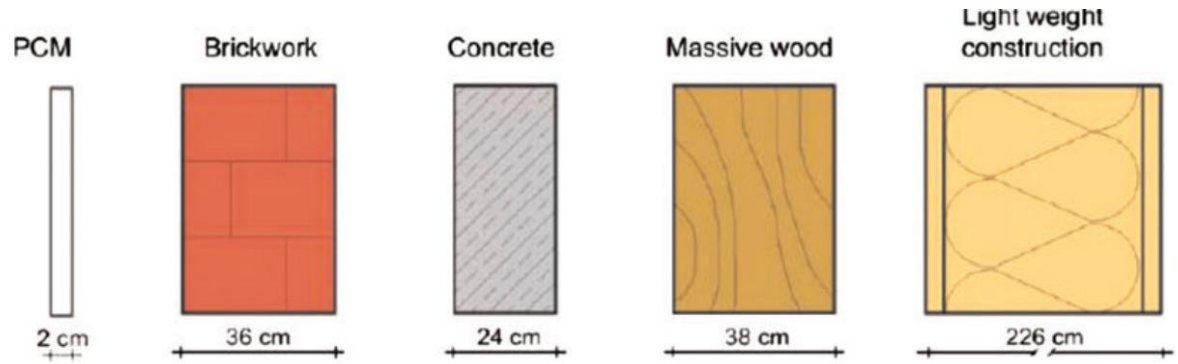

Figure 34 - Comparison of thickness required to store 5700 kJ over 10 K [86].

The paper goes on to discuss the technical limitations of PCMs, such as the limited thermal conductivity and limitations with usage cycles that do not allow full phase change, in addition to modelling limitations due to assumptions leading to wide variation in modelling outcomes. This paper finishes with a brief discussion of the industrial and economic barriers to entry of the technology e.g. lack of proven systems and models / lack of economic motivation with current energy prices.

Akeiber et al [87] offers similar content but with a focus on utilization for building cooling in hotter climates than the UK. The paper reviews PCMs being applied in walls, roofs, windows and floors which were usually thermally advantageous over conventional building materials. It also noted that 60% of previous studies used organic PCMs of which paraffin was the most popular (46% of studies.)

Sharif et al. [88] reviews studies that investigate PCMs for use for heating and domestic hot water systems. It covers the integration of PCMs in water and air solar collectors noting that the various integration methods resulted in superior thermal and energy characteristics including overnight performance.

The review also covers studies that investigated the use of encapsulated PCMs in solar thermal storage tanks in order to increase the energy stored. These studies clearly demonstrated significant increases in energy density, exergetic efficiency, temperature and amount of hot water supplied with various inorganic and organic PCMs in a wide variety of capsule geometries.

Similar studies are reviewed that use large PCM slabs in ducts and packed bed PCM stores which resulted in similar outcomes, in addition to the effect on results of important metrics such as capsule size, inlet temperatures, mass flow rate etc… which had large effects on solidification time, outlet temperature, energy density and efficiency.

Farid et al. [89] covers much the same as the preceding reviews but also includes a brief section on fire retarding treatments for PCM integrating building materials. It is notable that

there are few studies in this area given the prevalence in utilization of organic PCM materials. The paper concludes that in particular, PCM enhanced wallboards offer an attractive, cheap solution to enhancing the thermal storage of a building for little additional cost but that few studies have been undertaken (as of 2014) with “few general rules pertaining to the thermal dynamics of PCM wallboard” available [89].

1.3.1.2 Phase Change Storage within building fabric

Various researchers have engaged with research into the viability of phase change storage inside of building fabric. Sub-sections of the building fabric that have been investigated include within walls, encapsulated in plasterboard, within roofs, ceilings, ceiling fans, windows and floors.

The potential for PCM integration into wallboards has had significant investigation in recent years. Biswas et al. [90] developed and investigated a “nano-PCM” composite wallboard experimentally and numerically. Using gypsum powder (80 wt %) and a mixture of n-heptadecane with expanded graphite in a 92 to 8 ratio respectively wall boards were fabricated for experimental characterisation in a natural exposure testing facility in Charleston South Carolina.

A numerical 2D model was developed using Comsol and thermophysical properties of the utilized materials. This model was validated, and then used to perform annual simulations. The validation was successful and the researchers reported excellent agreement between their model and the experimental data.

Subsequent annual simulations showed an insulating effect compared to a normal gypsum wall, showing between 4 – 44 % reduction in heat gains and losses dependant on wall orientation with a stronger insulating effect on heat losses.

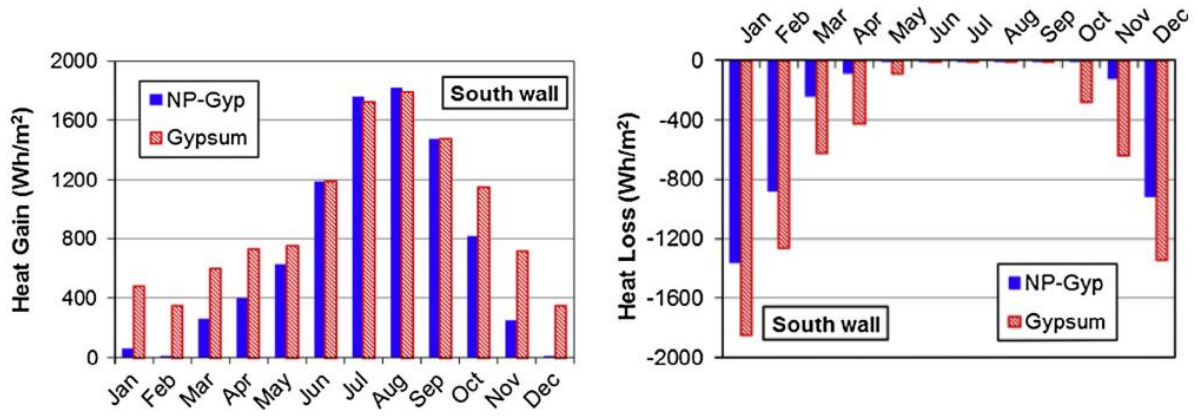

Figure 35 -Calculated monthly heat gains and losses through the south wall, with 20–23.3 °C room temperature set points [90].

It was shown that while the use of PCMs reduced overall electrical energy consumption significantly in winter months, it also significantly increased the load factor (the ratio of the peak electricity consumption to average electricity consumption over a certain time period) depending on the temperature set points, Figure 35.

Fateh et al. [91] also investigated the effect of PCMs used as wall insulation (Dupont Energain ™), the importance of wall orientation and the melting point of the PCM via a dynamic model with Matlab Simulink of lightweight buildings in a European locale. This investigation determined that significant reductions (60%) in energy consumption can be realised although wall orientation was very important, with the most benefit realised from the southern wall and the least from the northern wall, with more heat transfer through the northern wall. They concluded that without the presence of solar radiation, the effect of peak shaving this energy is no longer happening and the reduction of energy consumption becomes negligible. In addition to the PCM, melting temperature was determined to be an important characteristic with enhanced energy consumption reductions when this temperature is close to the temperature variation in the building.

Further experimental studies such as Lee et al. [71], [92] have reported similar conclusions.

Researchers have also investigated ceiling based PCM systems for cooling with Stalin et al. [58] briefly investigating the potential for a coupled ceiling PCM-fan based cooling system numerically determining the viable PCMs for a system, taking ~ 2 hours to reach a comfortable temperature for a room of 4 people in Madurai, India.

Turnpenny et al. [56] developed an overnight charging latent heat cooling system consisting of ducted fan aerated heat-pipes connected to / immersed in Na_2SO_4, Figure 36. Both a numerical model (one dimensional, assuming no sub-cooling or density change and written in Fortran) and experiments were generated. The results of changing flow rates of air were investigated and comparisons with the model drawn. Unfortunately the model predicted twice the value for heat transfer in most cases though there was good agreement with predicted and measured temperatures. This over-prediction was attributed to the assumption of only conductive heat transfer and the tendency of the real PCM to melt over a temperature range rather than a single value.

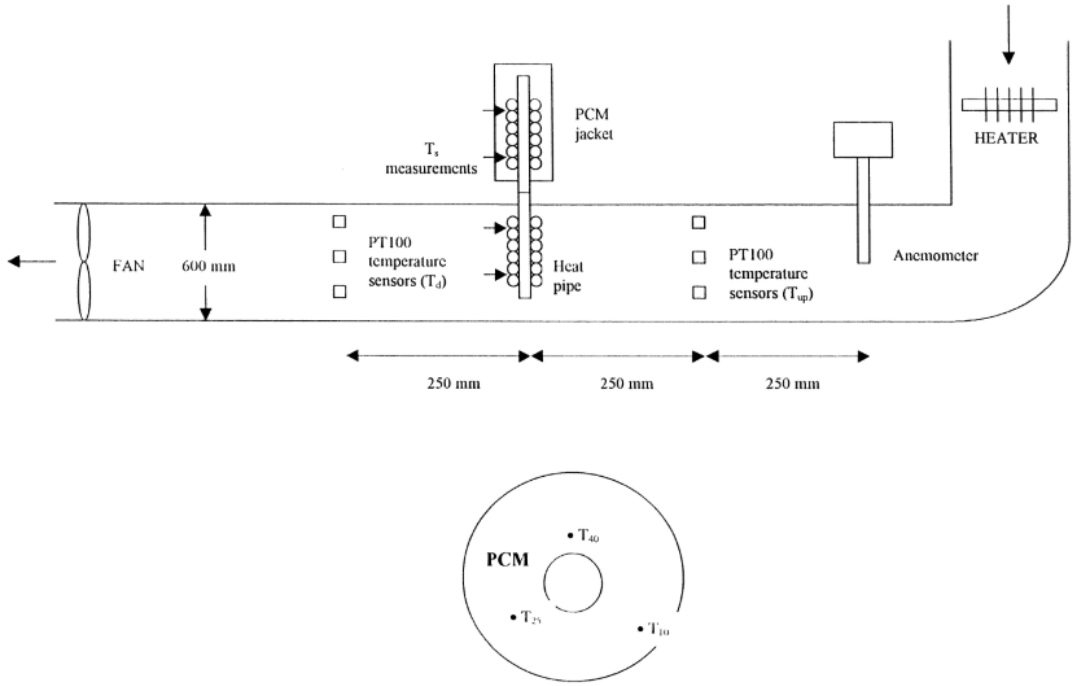

Figure 36 - Schematic plan view of experimental rig and cross-section of PCM container from [56]

Several researchers have also investigated the potential for underfloor phase change heat storage. Ansuini et al. [93] investigated a radiant floor prototype with an integrated layer of PCM and custom designed steel matrix to act as a thermal diffuser as shown below in Figure 37. In addition a 2D numerical model with intermittent water flow was developed alongside a room scale model to determine the impact on room comfort. The design was intended for a Mediterranean climate with a grain encapsulated paraffin based PCM with a melting point of 27 °C and used thermostatic baths to supply the two temperature controlled plates above and below the radiant floor.

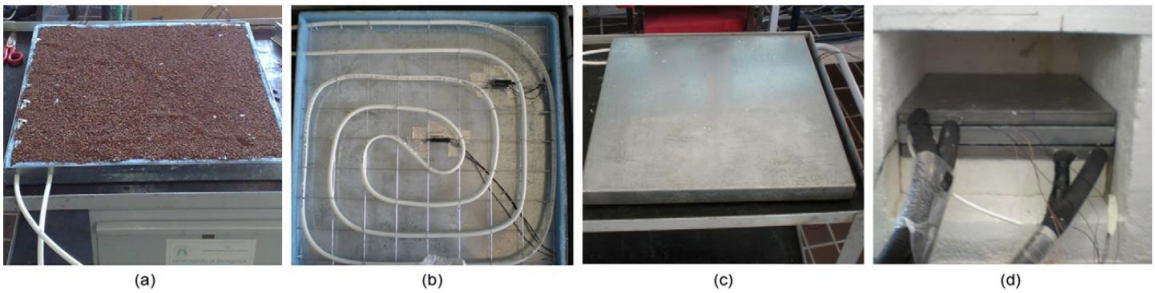

Figure 37 – Experimental setup from [93]: (a) the metal container with the pipes and the supporting metal net, (b) the specimen filled with the granular PCM, (c) the closed specimen, and (d) the specimen before closing the testing chamber.

The numerical model was initially found to be sub-optimal and temperature profiles differed significantly from measured due to voidage in the PCM grains and the presence of air

between the radiant floor and the temperature controlled plates. The comparison however did indicate a thermal stratification effect with melted upper layers of PCM forming greater thermal resistance to heat flow to lower levels – this precipitated the usage of the steel matrix to combat this effect which was demonstrated. A further 2D numerical model was developed, accounting for this matrix, which showed good agreement with measured results and was compared to another 2D simulation of a conventional radiant floor with no phase change material present.

A comparison between these models during winter heating and summer cooling demonstrated the isothermal nature of phase change materials resulted in an advantageous 4 K decrease in surface temperature during summer and vice versa – the PCM resulted in poorer performance than a standard radiant floor during winter due to the same effect. Further room scale simulation showed the results of this system during summer, mid-season and winter.
During summer temperature peaks were 1.5 K lower than the conventional system, required 25% less cooling water, in addition to retaining heat during the night time which aids in room comfort levels. Mid-season, the systems were compared with heating and cooling turned off for the radiant floor and again showed more time at a comfortable level and a lower surface temperature. During winter, the systems effectively performed in the same way.

Inaba et al. [94] also numerically investigated and validated a melting phase change material slurry in a rectangular enclosure heated from below and cooled from above and found that comparing a model with and without phase change – heat transfer coefficients increase with phase change occurring and that higher concentrations of phase change material in the slurry suppress heat transfer due to viscous effects.

Belmonte et al. [95] also investigated a coupled phase change floor with a chilled ceiling using Trynsys, using environmental data from Versailles, during the months of June and September. Like the former paper, it concluded that the success of a system depended heavily on the selection of PCM melting point and latent heat which had direct ramifications on comfort levels and energy consumption. It showed that most advantageous PCM melting temperature for reducing cooling load was close to or slightly above the temperature set point of the building.

Xia & Zhang [96] experimentally investigated a dual layer radiant floor system using PCMs in a heating and cooling layer as seen in Figure 38.

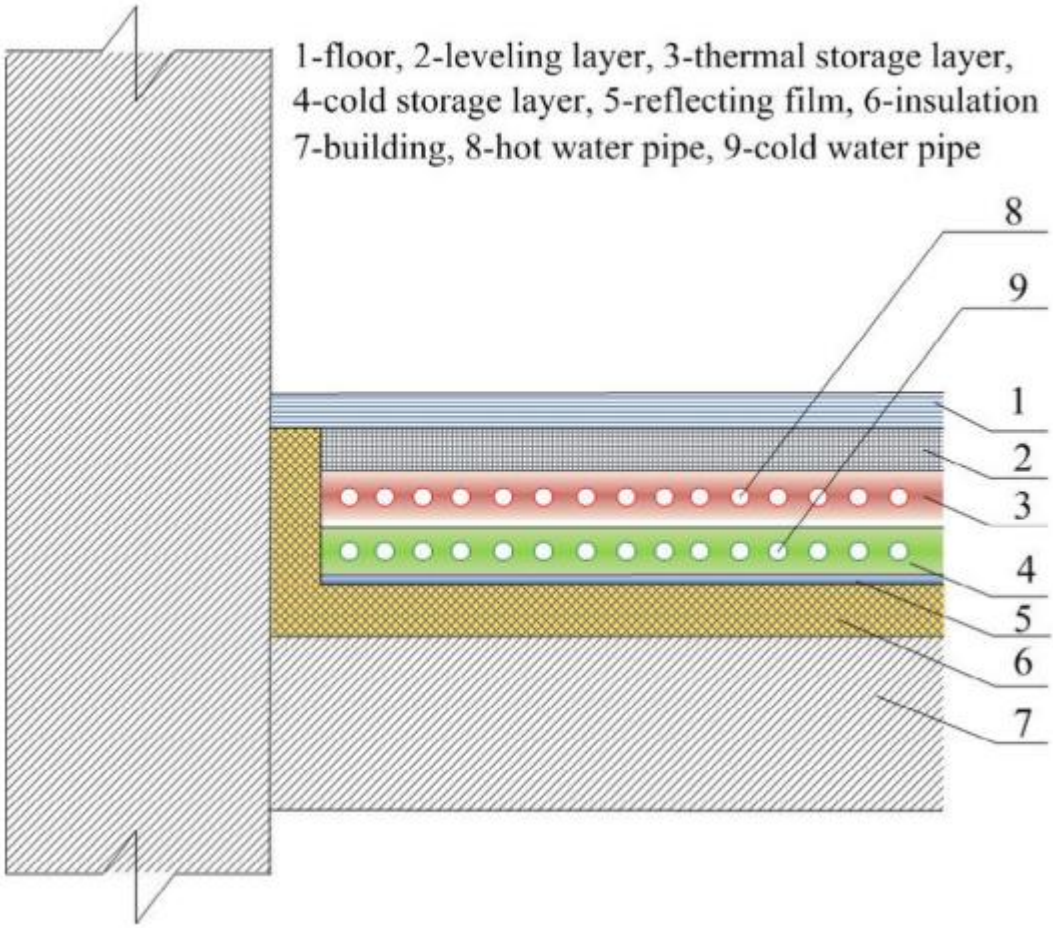

Figure 38 - Structure of double-layer radiant floor system with phase change material from [96].

They experimentally investigated which situation was more optimal, the cold PCM being the upper layer and vice versa. Water for heating and cooling was supplied from off peak electrical heaters / coolers at a fixed flow rate at various temperatures. The configuration with the cold PCM at the bottom resulted in a larger air temperature and larger change in air temperature when compared to the reverse configuration. It was found that the conditions used were sufficient to maintain comfort in winter and summer during heating mode. An earlier similar numerical only investigation was undertaken by Jin & Zhang [97] that showed large increases in energy release (up to 41.1 and 37.9%) during heating and cooling processes compared to a radiant floor without PCMs.

1.3.1.3 *Reviews of Numerical Modelling* of *Phase Change Materials*

Numerical modelling of phase change materials has been of great interest to researchers for some time and previous sections have discussed a few examples of such. In addition, due to the numbers of numerical and experimental investigations, several review papers have been compiled discussing the lengths and breadths of this area of research.

Dutil et al. [98] presents the Stefan problem, from which numerical methods for the solution of phase transitions are derived, the fixed grid approach and subsequent finite volume, finite element method. The subsequent section of this review presents a comprehensive collection of models utilizing several problem formulations including several types of geometries, packed beds, finned designs, porous materials and slurries.

Most importantly, this review discusses issues with these models and their validation – in particular that most modern research is relying less on experimental validation and **that there was little quantitative validation against other research compared to qualitative comparison**. In addition, these more recent studies there is more of a reliance on commercial modelling program and **discussions that related to stability, convergence and grid independence are decreasing.**

They also warn about the risk of extrapolation from the number of numerical and experimental studies as convection effects can be extremely sensitive to the geometry and phase change material viscosity and thermal conductivity. They also noted the lack of investigation of pumping power in several studies where the usage of higher viscosity phase change materials would have significant effects.

Verma, Varun and Singal [99] compiled a review comparing numerical models based on the first law of thermodynamics and the second law of thermodynamics, almost all of which are based on the former. The important difference between these models is the reliance in the former on energy compared to the latter's reliance on entropy. It is also of note that while the former has been clearly verified with experimental results, the latter have not and still require substantiation.

Gracia and Cabeza [100] provides a general overview of the studied models for packed beds including single phase, Schumann's, concentric dispersion and continuous solid phase models. Single phase models are discussed as being unpopular due to their assumption that the PCM and heat transfer fluid are at the same instantaneous temperature.

Schumann's model, despite being 2 phase was identified as still being limited due to a lack of consideration of conduction within the fluid and solid phases. This model has however been used to investigate packed beds where these conditions were not a limitation.

The computational expense for each model type was also presented and a series of general modelling conclusions were presented, including the particle size being a dominant parameter and multiple type of PCM packed beds presented higher energy transfer rates and thus power.

Al-abidi et al. [101] presents a comprehensive review of the utilization of computational fluid dynamic modelling for studying phase change materials. The program Ansys Fluent is

discussed, how it formulates the problem and the available pressure and density based solution methods. The review lists a series of self-developed models and then moves on to cover the numerous examples of models generated using the Fluent program found in the literature.

They observed several conclusions from their review including the successful application of this program to different situations, the availability of other program such as Comsol and StarCCM, that in many situations the 2D models agree well with 3D models and the **utilization of this program is not only feasible due to the accurate results but that the program offers optimisation tools to "achieve maximum efficiency while saving time and money."**

1.3.1.4 Importance of calibration of the mushy constant

One key parameter in several of the models found in the literature is the mushy constant, a parameter which governs how quickly velocities are reduced to zero in the mushy phase (partially solid, partially liquid) utilized in the enthalpy-porosity technique in the Ansys Fluent program.

This parameter has not been often discussed or the effect of changing its value explored in the majority of modelling research observed during the literature review process. Of the few papers which have investigated this variable it has been found to have a large effect on modelling output.

Kheirabadi and Groulx [102] investigated the effect of changing this value while modelling lauric acid using Comsol Multiphysics 4.4 and Fluent 15.0 and **found higher values of mushy constant directly correlate with longer melting times and lower values result in "unphysical predictions of melt front development."**

In addition to these discoveries they found that values of mushy constant and chosen time step value were not independent and that to get similar melting front development with varied time step sizes requires variation in the mushy constant. **They identify that further efforts are needed to investigate these phenomena in different geometries and with different materials.**

Kuma and Krishna [103] investigate the effect of varying this constant on the thermo-hydraulics of gallium and similarly concluded that varying the mushy constant value had the same effect on the melting rate and melting front geometry which can be seen in Figure 39.

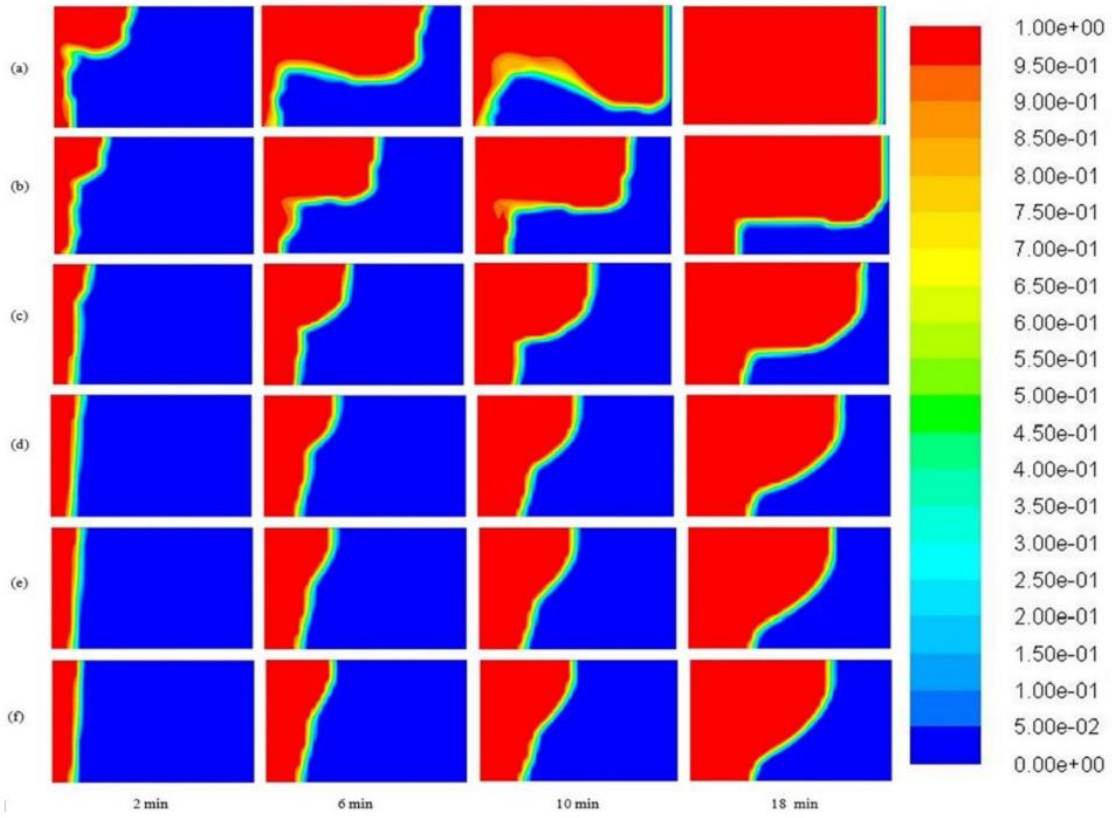

Figure 39 - Melt fraction contours for different values of mushy constant from Kuma and Krishna [103]: (a) 10^3, (b) 10^4, (c) 10^5, (d) 10^6, (e) 10^7, (f) 10^8.

It is important to note however, this is **one of many studies with an extremely low mesh resolution** at only 3000 cells as a result of mainly phase dependant properties.

Pan et al. [104] investigated unconstrained melting of Calcium Chloride Hexahydrate and found again that not only was the mushy constant an important variable for getting good agreement between experimental and modelling data but also that calibrating was essential and the optimal value for mushy zone constant appeared to be related to the driving temperature difference.

1.4 Motivations

As has been previously discussed, thermal energy storage as a subclass of energy storage is expected to play a primary role in the UK's target to reduce greenhouse gas emissions in line with the UK Climate Change Act by 2050.

Latent heat storage / phase change storage has several demonstrable advantages over conventional / sensible thermal storage but has a complex heat transfer process which is difficult to investigate or model due to complex phenomena in addition to time dependency. Further complexity in these situations arises due to geometry choices and heat source orientation.

Of the literature reviewed there appear to be several areas for improvement not limited to limited empirical verification, lack of critical investigation of mushy zone constant variation, decreasing discussion or verification of time and mesh independence. Critically, there are few studies directly investigating time dependent heat transfer models of varied configuration intended to represent an underfloor storage system while modelling or investigating the impact of important temperature dependent thermo-physical material properties. There also appear to be few studies analysing time dependent local variation in non-dimensional parameters such as Peclet number.

The current study intends to model and experimentally detail the transient phase change process in two materials and to understand the various non dimensional parameters, the convective heat transfer coefficient and their relation to geometrical configuration / correlation to solid-liquid interface characteristics. Understanding the above will improve understanding and assist in the development of models / designs for phase change storage systems, in addition to determination of the value of modelling over exploratory experimental work.

Due to limitations in experimentation and large body of work in melting alone, study of solidification process has not been investigated.

1.5 Aims and Objectives

This PhD on "High Density Heat Storage for Homes" has two general objectives. The first is to establish the feasibility of providing this kind of service, primarily for the support of low carbon heat supply. This includes ascertaining the size and form constraints, the technical and economic potential of different technologies and the methods available to integrate them into existing heat production systems. The second is to develop a high-density heat storage technology, methodology or material/s suitable for utilization within the home. These requirements are split into the following constituents:

1. Conduct a thorough investigation into the thermal properties of 2 PCMs in order to determine the required thermo-physical properties.
2. Conduct a thorough investigation into the heat transfer phenomena of two PCMs during a melt process in various configurations intended to represent an ideal underfloor heat storage system utilizing experimentation and modelling.

The focus of this thesis is on the detailed investigation of beeswax and paraffin wax and the processes during melting and the outcome should improve understanding of the heat transfer processes of a physical melt and the various factors which affect modelling these materials numerically.

The geometries modelled represented two heating methods expected to be utilized in underfloor heating systems, one with a flat plate bottom plate heater and the other with submerged pipework either located centrally or adhered to the bottom surface.

The geometries experimentally investigated reflect only the former flat plate heater configuration and were investigated utilizing visual and thermal imagery in addition to a matrix of submerged temperature sensors.

This should contribute knowledge with respect to not only the generation of models but also the validation and investigation into the efficacy of thermal, visual and temperature sensor-based model validation.

1.6 Publications

Investigating organic phase change behaviour with thermal photography

James K.W. Moore, Denis Cumming, Solomon Brown,

Energy Procedia,Volume 151,2018,Pages 52-56,ISSN 1876-6102,

https://doi.org/10.1016/j.egypro.2018.09.026.

1.7 Thesis Outline

Chapter 1 (this chapter) introduces the topic and content of the thesis including the motivations and problem definition. This section also includes the general background of thermal energy storage technologies and the literature review.

Chapter 2 contains the numerical modelling theory which underpins the modelling of the subsequent chapters, including discussion of the Stefan problem, how the CFD modelling program Ansys Fluent implements this and the modelling parameters used.

Chapter 3 investigates the experimental determination of and literature sourcing of the thermo-physical properties of the chosen beeswax and paraffin wax phase change materials. This chapter also experimentally investigates the materials' selection for an experimental vessel intended to characterise the melt processes of beeswax and paraffin wax.

Chapter 4 numerically investigates and compares the two phase change materials in a 2D 2.5cm square domain with heating provided by a bottom mounted isothermal hot plate intended to represent an ideal underfloor heating system. This chapter also investigates the effects of an inverted configuration with a top mounted isothermal hot plate for beeswax only. Key parameters, both dimensioned and dimensionless, are discussed.

Chapter 5 numerically investigates additional pipe heated models intended to represent an underfloor heating system. The investigated conditions include varying the pipe placement in the domain from the middle to the bottom surface and the effect of varying the spacing between the bottom's mounted pipes with beeswax only. Comparisons of the modelled geometry via dimensioned and dimensionless parameters are discussed.

Chapter 6 numerically investigates the effect of varying a key modelling parameter, the mushy constant value for the beeswax PCM in two configurations – one using the same isothermal heated bottom plate domain from Chapter 4 and the other using the bottom mounted pipe with 2.5cm spacing domain from Chapter 5.

The same dimensionless and dimensioned parameters are discussed and compared for both geometries with reference to this differing geometry and the results of changing the mushy constant.

Chapter 7 details the experimental investigation of the melting process of beeswax and paraffin wax in a 5cm vessel for validation of two 5cm CFD melting models. It also details experimentation with a larger 15cm vessel with a matrix of temperature sensors not only to validate the equivalent CFD model but to also determine the efficacy of using visual and thermal photography alongside the temperature sensor matrix for investigating a phase change melt in beeswax.

Chapter 8 summarises the overall conclusions to this thesis from each chapter and recommendations for further work.

Chapter 9 is the bibliography and contains the references utilized in this thesis.

Chapter 10 contains the appendices, referenced additional pieces of work, additional descriptions of key terms and additional system constraints not considered in the main body of work.

2 Numerical Modelling Theory

Modelling a phase change is an example of a “free boundary” or “moving boundary” problem, where the evolving interface where phase change occurs is an unknown and forms part of the solution. Originally this class of problem was first investigated by Lamé and Clapeyron in 1831 to determine crust thickness from a cooling liquid. The problem class was generalised by Josef Stefan in 1889 when he released 4 papers on various real phase change problems [105].

The Stefan problem has a few assumptions:

1. No volume change in either phase during phase change.
2. The temperature of phase change is fixed.
3. Each phase is homogenous and isotropic.
4. Heat transfer to the liquid phase is via conduction only.

Coupling the Stefan problem with the Stefan condition, a fixed grid and enthalpy method this type of problem can be approached numerically and programmatically.

$$\lambda\rho\left(\frac{ds(t)}{dt}\right) = k_s\left(\frac{\delta T_s}{\delta t}\right) - k_l\left(\frac{\delta T_l}{\delta t}\right), \tag{6}$$

The Stefan condition is stated above where λ is the enthalpy of melting/fusion, ρ is the density (liquid or solid phase is unstated), s(t) is surface position, k is thermal conductivity, t is time, and T is temperature. Subscripts **s** and **l** refer to solid and liquid phases [98].

The application of a fixed grid allows for the avoidance of discontinuities and numerical instability by creating a “Mushy Zone” between the solid and liquid phases, although this has effects on the performance of the model as the thickness of this zone and the quality of the discretization will have effects.

Within the Fluent software there are several governing equations used in the models which are given below. These governing equations related to mass, momentum and energy conservation:

$$\frac{\partial\rho}{\partial t} + \nabla\cdot(\rho\vec{v}) = 0 \tag{7}$$

$$\frac{\partial}{\partial t}(\rho\vec{v}) + \nabla\cdot(\rho\vec{v}\vec{v}) = -\nabla P + \nabla\cdot\overline{\tau} + \rho g + F \tag{8}$$

$$\frac{\partial}{\partial t}(\rho H) + \nabla \cdot (\rho \bar{v} H) = \nabla \cdot (k \nabla T) + S \tag{9}$$

The aforementioned source term S is the Darcy's law damping term, which is added to the energy equation due to the phase change effects on convection and is defined as:

Where *H* is total enthalpy, ρ = density, *S* = is the source term and $\bar{v}$ = fluid velocity.

$$S = C(1-\gamma)^2 \frac{\bar{v}}{\gamma^3 + \in} \tag{10}$$

Where $\in = 0.001$ and is a small constant used to avoid dividing by zero, C is the mushy zone constant which describes the kinetic process within the mushy zone which is typically defined between 10^4 and 10^7 [106].

$$h = h_{ref} + \int_{T_{ref}}^{T} C_P \Delta T \tag{11}$$

Where *H* is defined as:

$$H = h + \Delta H \tag{12}$$

Where C_P is specific heat, h_{ref} is the reference enthalpy at reference temperature T_{ref} , ΔH is the latent heat content tracking between being fully solid and liquid, L is the latent heat of the PCM where γ is the value of liquid fraction during a phase change between the temperatures T_l ($T_l > T$, fully liquid) T_S ($T < T_S$ fully solid) and T (temperature.)

This gives:

$$\gamma = \Delta H \,/\, L \tag{13}$$

Where:

$$\gamma = \begin{cases} 0 & \text{if} \quad \mathrm{T} < T_S \\ 1 & \text{if} \quad \mathrm{T} > T_L \\ (T - T_S)/(T_L - T_S) & \text{if} \quad T_L > T > T_S \end{cases} \tag{14}$$

Convective heat transfer is the mode of heat transfer which takes place in the fluid (gas or liquid) phase and is dependent on gravity, material thermo-physical properties, fluid flow behaviour and the temperature difference between the bulk of the fluid and the temperature of the fluid at the solid-liquid interface / heated surface.

Heat transfer in a solid takes place via conduction only, where in a fluid heat transfer can take place via both conduction and convection depending on bulk fluid motion.

Convection increases the rate of heat transfer by virtue of removing heated material from the heated surface to be replaced with cooler fluid and moving heated fluid to the solid-liquid interface. This results in a greater temperature gradient and thus energy transfer.

The convective heat transfer coefficient can be calculated from the following equation and is a property of a given configuration rather than of the heated fluid which is experimentally or numerically determined.

$$q = Ah_c(\tau_S - \tau_\infty) = \frac{\tau_S - \tau_\infty}{1/Ah_c} \quad (15)$$

Where q = the heat transferred per unit time, A = heat transfer area, h_c = convective heat transfer coefficient, τ_S = temperature at the surface and τ_∞ = temperature in the bulk of the fluid [107]. As no heat transfer areas are available in the subsequent models, the length of the heat transfer surface is used instead.

The value of heat transfer coefficient is highly dependent on the many variables which can affect convection such as geometry, surface finish, laminar or turbulent flow, fluid thermo-physical properties such as density, viscosity, conductivity and bulk fluid velocity.

With these practicalities considered, numerical simulations have been undertaken using the Ansys Fluent 17.1 – 19.4 software package [108] and has accounted for the thermodynamic properties of both phases, and which are considered temperature dependent.

In this work, the Enthalpy-Porosity technique [109][110][111] is used to simulate melting. Instead of tracking, this method utilizes the quantity ‘liquid fraction’ which indicates what fraction of a given mesh element is in liquid form. This value is computed every iteration and is determined by an enthalpy balance and gives rise to a “mushy zone” in which the value for liquid fraction lies between 0 and 1 (neither fully solid nor liquid.) This area is modelled as a quasi-porous region where the porosity decreases as the material fully solidifies. When fully solid, there is zero porosity (i.e. no pores containing fluid) and velocities are extinguished.

The mushy zone constant is an important parameter as it determines how fast the solidifying materials transitions to zero velocity. The larger the mushy zone constant, the quicker the transition and large values may result in oscillatory behaviour in the solution.

Important characteristics of the subsequent models include the time required to melt fully, flow patterns and presence of the differing phase change materials and are investigated via the utilization of dimensionless number and variable analysis e.g. Reynolds, Rayleigh numbers etc.

Post processing of the results generated by the Ansys Fluent program have taken place using the Ansys CFD-Post program with corrected equations for calculation of 2D variables when necessary.

For the numerical solution of the model's **double precision** and the **SIMPLE** pressure-velocity coupling was utilized. This was in conjunction with the first order upwind differencing scheme for energy and momentum. The **PRESTO** scheme was selected for pressure correction and convergence values were set at 10^{-3} for the mass and momentum, and 10^{-6} for energy. **Solution control under-relaxation factor values were set 0.5 for pressure, 0.05 for liquid fraction update and 0.5 for all other factors unless mentioned otherwise.** This is in line with recommendations from the Ansys Fluent manual [106] for simulations with high Rayleigh number flow / natural convection. In addition, these conditions were selected due to the increased measured agreement found between different modelling choices and experimental data found in [112]. The **laminar viscosity model** was utilized in all models. The maximum number of iterations for each time step was set to 2000 unless specified otherwise.

The first order implicit transient formulation was used although the second order implicit transient formulation was also investigated but found to generate significantly more unstable solutions and require significantly more computational time.

Simulations were conducted on numerous computers which are detailed below: a given investigation will state which computational resources were utilized. The Super Compute cluster resources of Sheffield University were utilized and the change from one cluster to another was due to the retirement of the ICEBERG cluster.

PC 1

A Viglen Omnino desktop equipped with a single Quad Core 2.30GHz Intel i5-2500T and 16GB of DDR RAM running the 64-bit Debian 8/9 operating system.

PC 2 and 3

2 HP ProLiant SL160z G6 equipped with two Quad Core 2.13GHz Intel Xeon E5506 CPUs and 40GB of DDR3 RAM running the 64-bit Debian 8/9 operating system.

Super Compute Cluster 1 – ICEBERG.shef.ac.uk

Node machines are either 2 x Octa Core 2.60 GHz Intel Xeon Processor E5-2650 v2 with 64GB DDR3 memory or 2 x Hexa Core 2.66 GHz Intel Xeon Processor X5650 with 48GB of DDR3 memory running the 64-bit Scientific Linux operating system.

Super Compute Cluster 2 – SHARC.shef.ac.uk

Node machines are Dell PowerEdge C6320s with 2 x 2.40GHz Intel Xeon E5-2630 v3 with 64 GB of DDR4 RAM running the 64-bit Centos 7.x operating system.

3 Determination of phase change material thermo-physical properties and preliminary experimental investigation

In subsequent modelling work, in order to achieve accurate models, the conditions and thermo-physical data for materials must be input correctly. Therefore in order to validate a given model, the same thermo-physical properties of the investigated materials must be determined and utilized in order to do so.

Two of the most important thermo-physical characteristics for such a model are the temperature dependant density and the enthalpy of phase change (latent heat of melting). This section details the determination and results of investigations to determine these metrics for beeswax and paraffin wax.

Both beeswax and paraffin wax were supplied from Sigma Aldrich CAS numbers 8012-89-3 (bleached wax) and 8002-74-2 (paraffin wax 58-62 °C ASTM D 87.)

3.1 Density determination

Density for fluids is typically determined using graduated cylinders; however in this case the submerged probe methodology detailed in [113] was used due to the requirement to assess the density at varied fixed temperatures for both ease of use and accuracy. This methodology utilizes Archimedes' principle to indicate the density of a liquid by submerging a known volume probe suspended from a wire and measuring the mass deviation between not submerged and fully submerged at a fixed height.

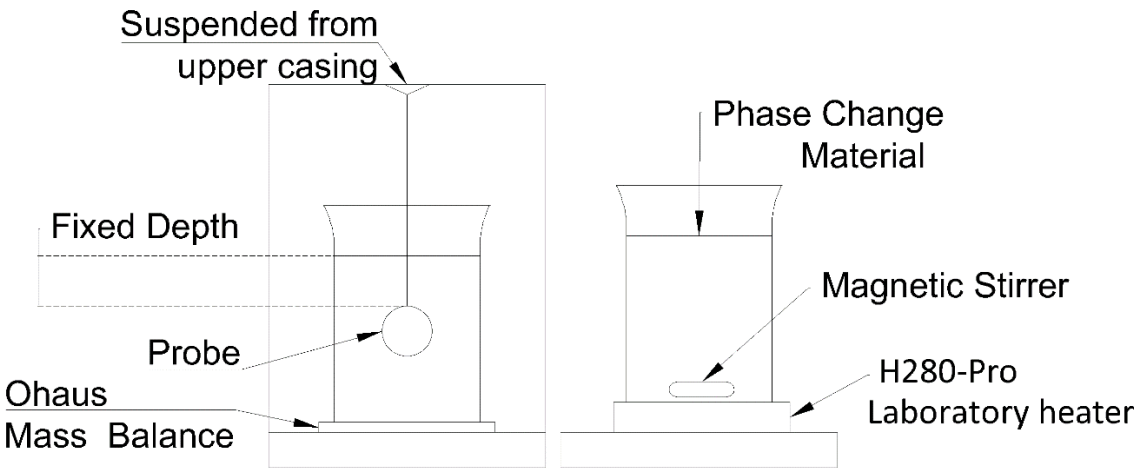

Figure 40 - Diagram of setup used for density determination experimentation.

This technique requires that: 1 – the probe is of a higher density than the fluid, 2 – the probe and wire are submerged to the same height under the fluid surface repeatedly and 3 - that the probe weight is fully taken via the wire suspending it. Under these conditions, the density of the fluid material is related to the change in observed mass over the probe volume [113]:

$$\rho_F = \frac{\Delta m}{V} \tag{16}$$

To determine the experimental values for variable density for beeswax and paraffin wax, a PVC sphere of average diameter 12.783 mm was countersunk drilled and glued so as to be suspended from 0.25 mm polyamide based fishing wire. Wire volume was considered to be negligible and fixed depth probe measurements were taken with heating, mixing and temperature control provided by a MS-H280-Pro laboratory heater. The temperature range was 45 – 80 °C and mixing RPM fixed at 1000 RPM. Mass deviation was calculated with an Ohaus Discovery analytical balance (Model DV2125CD).

Several values were determined for the density of water at different temperatures. When compared to literature values for water density, error was found to be under 2.25%.

Table 5 shows experimentally determined values for beeswax and paraffin wax density. These density values are an extremely important parameter due to their potential to significantly affect convection effects due to changes in buoyancy. The magnitude of density change in the liquid phase gives rise to convection with larger density changes leading to increased advective effects.

Table 5 – Density – experimental temperature data of beeswax and paraffin wax.

Temperature (°C)	Density (kg/m^3)	
	Beeswax	Paraffin Wax
60	N/A	782.48
65	857.20	773.46
70	813.55	771.29
75	807.75	766.83
80	806.73	759.25

The values determined in Table 5 demonstrate a good agreement with values found in literature [114]–[117].

3.2 Melting Enthalpy determination

In order accurately to characterise these materials, it is necessary to use a relatively slow rate of heating due to phase change materials typically having low conductivity and a large latent heat enthalpy.

Differential Scanning Calorimetry (DSC) is a thermo-physical analysis technique which determines a power required for a given temperature increase in a sample. Given a well-controlled temperature ramp rate, peaks and troughs in a power signal can be integrated in order to find the area under the curve and thus the energy consumed for a given temperature change. An example signal can be seen in Figure 41.

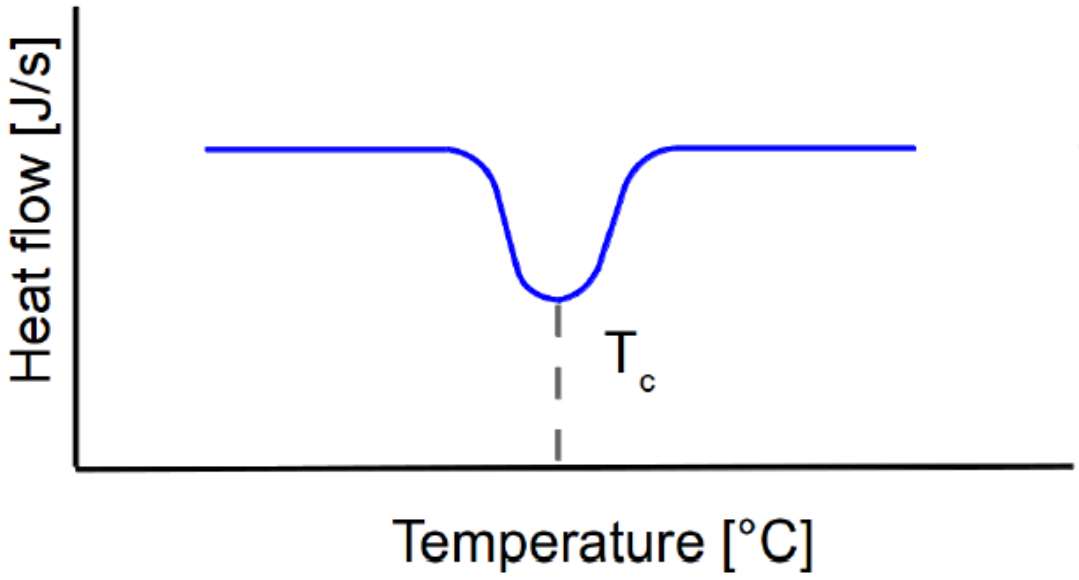

Figure 41 – Example power (heat flow) signal showing exothermic peak. [118]

Given a phase change transition is typically an order of magnitude larger value than the specific heat capacity of a material, these appear as large sharp power signal peaks or troughs around a specific temperature (the melting temperature.) Other thermo-physical properties can also be attained such as specific heat capacity and heat of crystallization.

For this investigation, measurements were made using a Mettler Toledo DSC 1 STAR System with aluminium 40µl sample pans (ME-26763). The heating rates selected for characterisation

were 5 and 10 ° C per minute between 10 -75 ° C. This system is a heat flux DSC where the power values are determined via comparison to a reference pan. A schematic of a heat flux DSC can be seen in Figure 42.

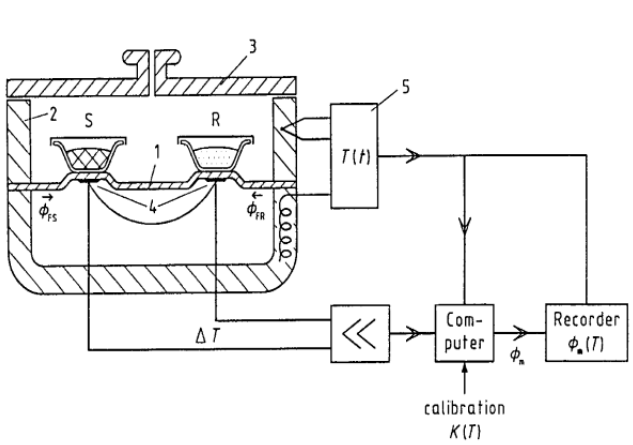

1 Disk.
2 Furnace.
3 Lid.
4 Differential thermocouples.
5 Programmer and controller.
S Pan with sample substance.
R Pan as reference
Φ_{fs} Heat flow rate from furnace to sample pan.
Φ_{fr} Heat flow rate from furnace to reference pan.
φ_m Measured heat flow rate.
K Calibration factor.

Figure 42 – Schematic diagram of heat flux type DSC [118].

Masses were calculated with an Ohaus Discovery analytical balance (Model DV2125CD). The utilization of these rates and sample masses was chosen as [119] indicates that the latent heat sensitivity increases with: "increased heating rate or sample mass is caused by a much larger heat flow signal associated with a very small corresponding increase in signal noise."

Data was processed using the Origin Pro 8.5.1 software utilizing manual peak finding and area calculation via integration to find the values for latent heat enthalpy. Values for both melting and solidification were found to be in good agreement for most experimental runs. Those where a good agreement was not found were re-run until there were 3 successful runs for each material. The values for all runs of both solidification and melting were then mean averaged for each material to give the values in Table 6.

Table 6 - Experimentally determined mean average values of latent heat of melting for paraffin wax and beeswax.

Material	Latent heat (KJ/kg)
Beeswax	242.9
Paraffin wax	208.7

An example differential scanning calorimetry plot of paraffin wax can be found in Figure 43.

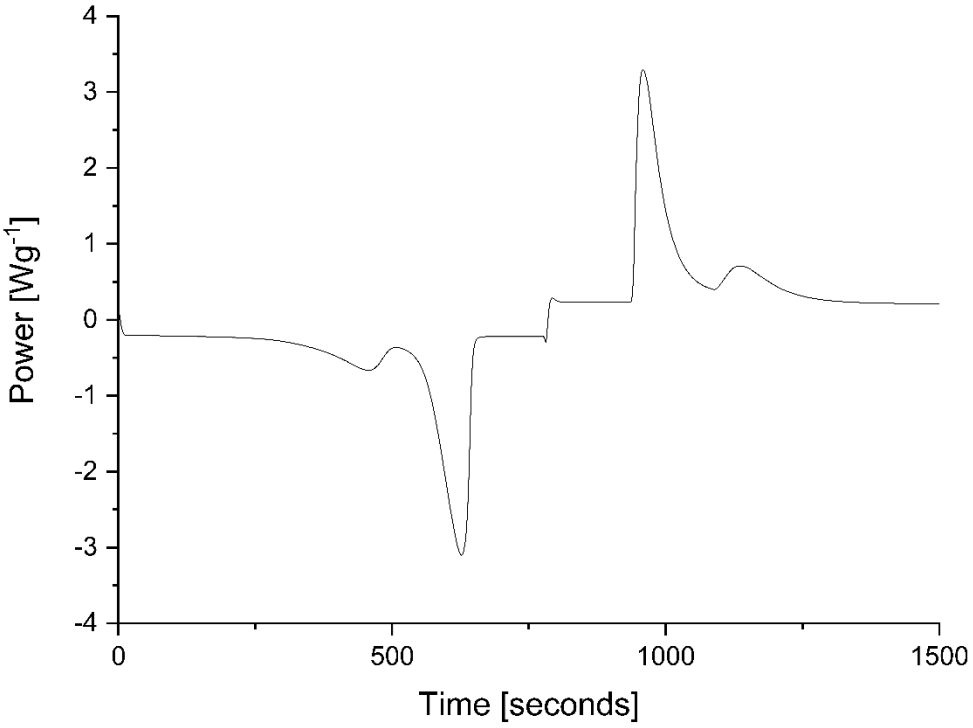

Figure 43- Differential scanning calorimetry plot, time versus power for paraffin wax at 5° C per minute between 10 -75 ° C.

Like the values determined for density, these showed good agreement with literature values found in [115], [117], [120], [121].

3.3 Literature sourced thermo-physical properties

The thermo-physical properties of paraffin wax and beeswax (not empirically determined and used in modelling) are listed in Table 7 and Table 8 with values taken from [115] [117] [122] Where appropriate, linear interpolation of temperature dependant values for material characteristics has taken place for modelling.

Table 7 – Thermo-physical properties of beeswax and paraffin wax.

Property	Beeswax	Paraffin Wax
Specific heat (J/kg.K)	4760	2450
Thermal Conductivity (W/m.K)	0.41	0.37
Solidus Temperature (°C)	60	60
Liquidus Temperature (°C)	62.95	60.81

Table 8 – Viscosity-temperature data of beeswax and paraffin wax.

Temperature (C°)	Viscosity (P)	
	Beeswax	Paraffin Wax
60	0.11	0.0689
65		0.0613
70		0.0548
75		0.0493
80	0.05	0.0446
90		
100	0.03	

3.4 Preliminary investigation of thermal and visual imaging analysis of a phase change melt process for experimental vessel materials' selection

In order both empirically to validate generated models and choose the best materials for a larger experimental setup intended to do so, this section covers the creation of a small experimental test vessel intended to quantify not only both the utility of a set of materials for thermal camera imagery and visual camera imagery analysis but also to quantify the melt process of both paraffin wax and beeswax generating some preliminary results.

This section describes the methodology and design of the test vessel followed by analysis of the thermal and visual imagery generated during this initial experimental testing.

This section of work has been taken from the published paper "**Investigating organic phase change behaviour with thermal photography"** detailed in section 1.6.

3.4.1 Methodology / Vessel Design

In order to determine the best construction materials and make a preliminary investigation into phase change material melting and solidification experiments a small test vessel was constructed as seen in Figure 44.

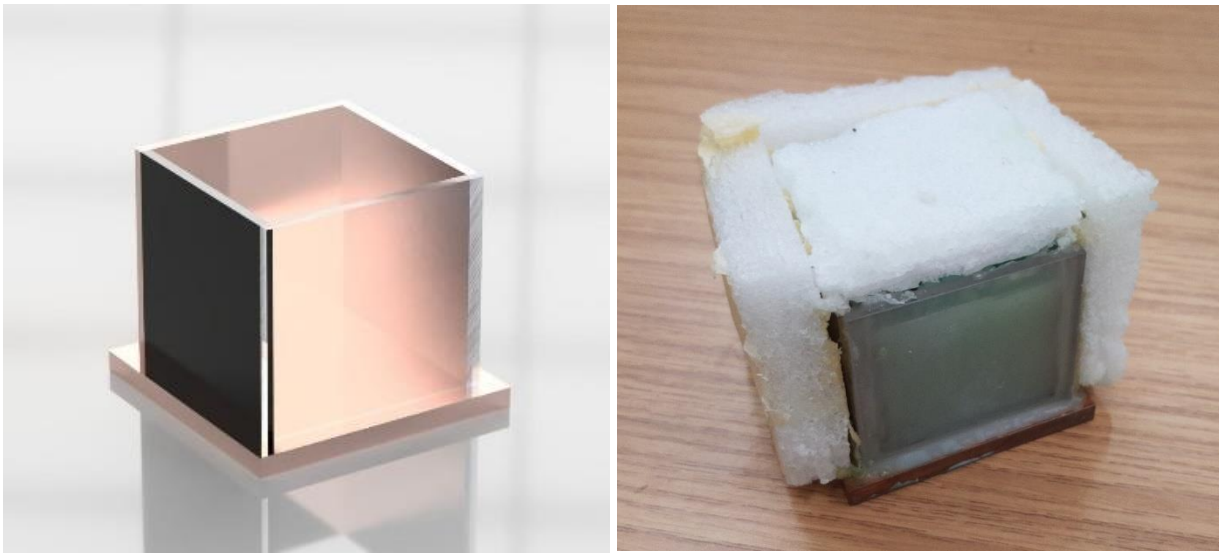

Figure 44 – CAD rendered image and picture of preliminary test vessel composed of 4 materials: copper, aluminium, infra-red transparent PMMA and polycarbonate.

This vessel was composed of a 1 cm thick copper base and single 0.5cm walls made of polycarbonate, IR transparent PMMA (Bay Plastics LTD), copper and aluminium. Both paraffin wax, beeswax and the efficacy of each face material type were quantified under thermal imaging.

The choice of IR transparent PMMA and polycarbonate was made due to the materials' thermal insulating properties and transparency in the IR spectrum (both) around 750nm and visible light (polycarbonate.)

The metals copper and aluminium were selected to determine whether indirect imaging of the box surface temperature would give rise to useful thermal images via conduction from the contained PCM materials.

In order to closely match the model, isothermal 80°C heat was supplied to the base from an IKA C-MAG HS 7 lab top heater during the melting process. This was subsequently turned off for the solidification process. In addition, each face (with exception of the imaged face and base) was insulated with 15mm of polystyrene.

For comparative imagery an FLIR SC-Series thermal camera (SC640) and PLAYSTATION Eye ™ webcam were operated to take images at a pre-set interval of 5 minutes. The SC640 was operated in camera controlled timed shot. Both the SC640 series camera and PLAYSTATION Eye ™ webcam have a resolution of 640 x 480 pixels.

The PLAYSTATION Eye ™operated in a similar fashion, with a Raspberry Pi 2 utilized to operate an identical simultaneous 5 minute interval.

3.4.2 Results

The results from thermal and visual photography were processed to understand which materials were best suited for which imaging type and to get some preliminary results on the isothermal melting process of paraffin wax and beeswax.

3.4.2.1 Visible light Imagery

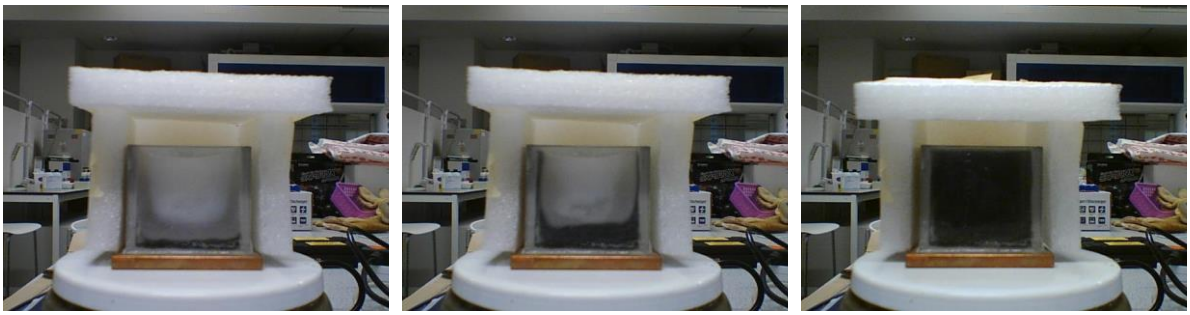

(a) (b) (c)

Figure 45 - Visual imagery of paraffin wax melting at (a) 30 minutes; (b) 60 minutes; (c) 103 minutes duration observed from transparent polycarbonate wall. Figure 45 (a-c) present images through the transparent *polycarbonate* wall of the paraffin wax melt at 30, 60 and 103 minutes respectively.

Figure 45 (a) clearly demonstrates the melting process has begun with the melted portion visible as the darkest region. The solid-liquid interface recesses upwards with time, as can be

seen in Figure 45 (a) and (b). From observation of the melt process, the total melting time for both beeswax and paraffin wax was determined to be 157 and 103 minutes respectively.

A U-shaped profile is partially visible in Figure 45 (b) which can be attributed to significant conduction through the adjacent metal walls leading to more rapid melting when compared to the PMMA or polycarbonate faces.

This outcome is important to account for in the event of validation studies utilizing numerical modelling and is a limitation of this vessel due to investigating the 4 different materials. Convection currents and their directions have not been captured using visual photography and were also not visible to the human eye.

Imaging of solidification was attempted but it was found that heat losses through the imaged face lead to premature solidification occurring on that face. This leads to an image not representative of reality.

It is also expected that this premature solidification phenomena is working in reverse during the melt phase, where the exposed face has the last material to melt and appears to show a sudden increase in melting rate toward the end of the melt process.

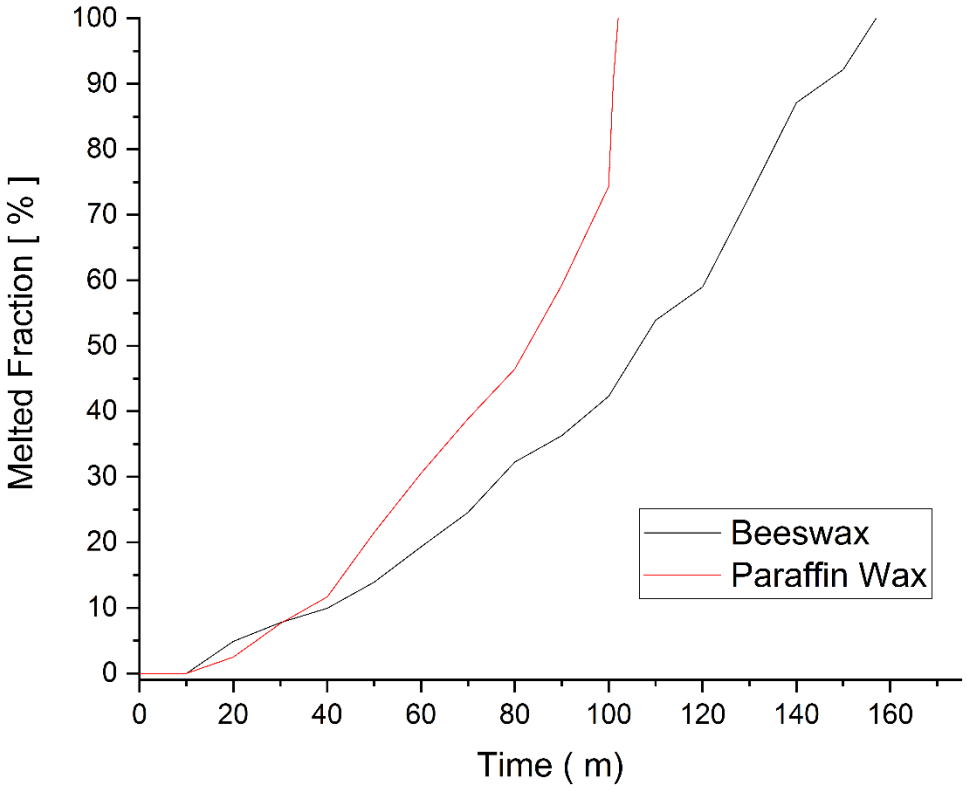

Figure 46 - Melting time track of beeswax and paraffin wax.

Figure 46 shows a comparative plot of paraffin wax and beeswax melting progress versus time which was generated via manual masking and pixel area calculations using the software ImageJ.

Initially beeswax shows a faster rate until around 40 minutes where paraffin wax overtakes with an increasing rate of melting. Despite beeswax having a higher thermal conductivity(0.41 compared to 0.37 $Wm^{-1}K^{-1}$) than paraffin wax, the remaining thermo-physical properties including an increased density, almost double the specific heat capacity and a 25% higher enthalpy of melting, are the likely causes in part for the additional 45 minutes until melt completion.

The paraffin wax melting track in Figure 46 also shows a rapid increase in melting rate at the very end of the melt process and it is believed that this is attributable to the exposed face retaining the final solid material until the last part of the melt process due to the heat losses through this face. This would lead to an apparent sudden rate increase as the last solid material melts and rapidly becomes transparent, appearing to show a rapidly moving solid-liquid interface when the majority of material behind the solids on the imaged face has already melted. The beeswax melt process does not however appear to show a similar trend, which may be being masked by the much longer melting process, allowing a more favourable equilibrium to be found for imaging.

3.4.2.2 Thermal Imagery

Thermal images were taken for both IR transparent (polycarbonate and PMMA) and opaque materials (copper and aluminium) which can be seen in Figure 47 and Figure 48. It was hoped that metal surfaces would have sufficient conduction from the internal material in order to confer the melt structure via re-radiation. Figure 47 clearly demonstrates the nil efficacy of using metal walls for this purpose; this was the case during a melt or solidification process. This is likely to be caused by a large portion of the thermal energy of the wall being directly conducted from the heat source rather than the contained material. This effect may be minimised using a thermally insulating gasket and may be worth further investigation.

Contrastingly, the PMMA and polycarbonate walls demonstrate indications of the solid-liquid interface which allows for interface tracking much like the visual imaging. Unfortunately, further detail such as thermal gradients from convection currents are not realised. In addition, it is noted that the same limitations for visual imaging are present in thermal imaging such as surface blemishes.

It was thought that with an increased level of insulation on both non-imaged and imaged faces and a larger test vessel, further detail and improved image quality may yet be realised. While

adding insulation to the imaged face presents a challenge it was believed that such a process with a moving actuated insulation via stepper motor was possible.

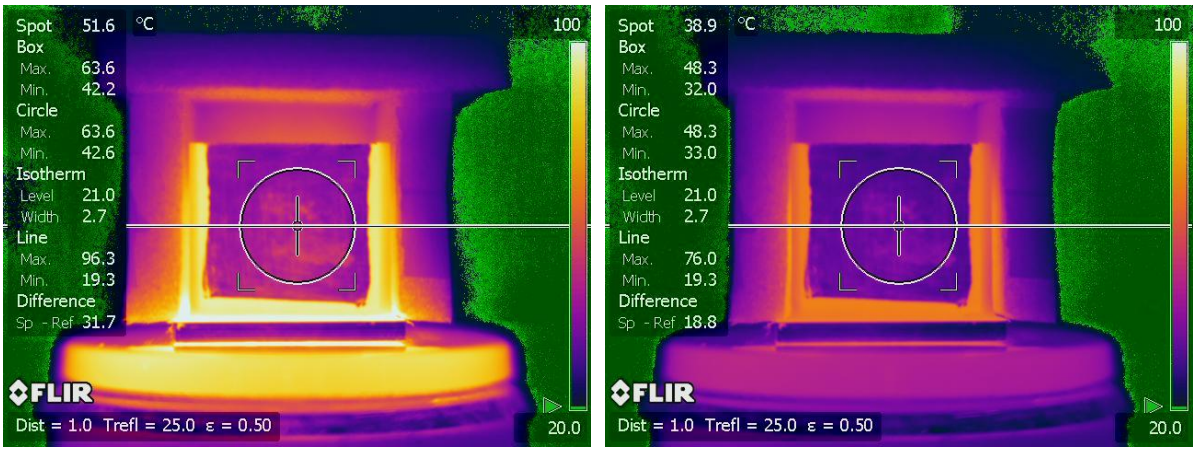

(a) (b)

Figure 47 - Thermal imagery of copper wall during beeswax solidification at (a) 1 minute; (b) 20 minutes duration.

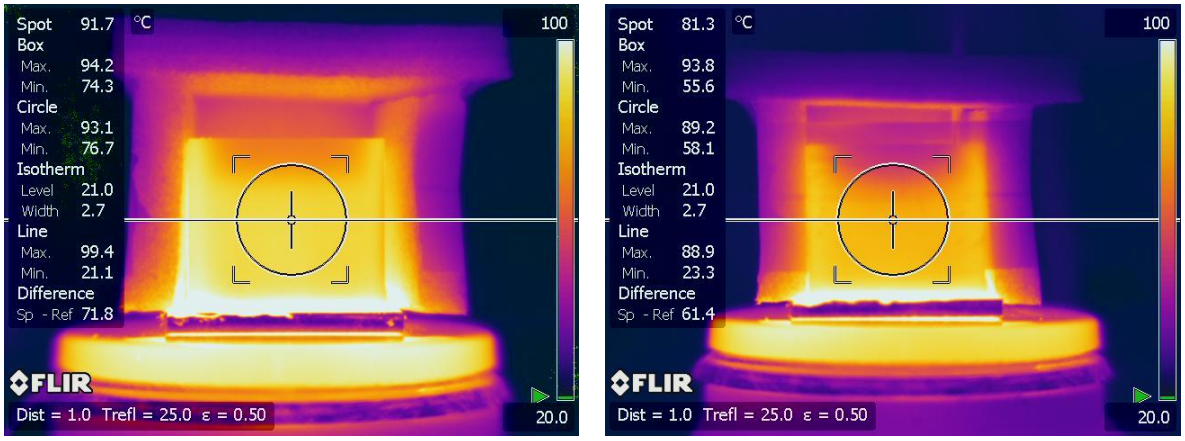

(a) (b)

Figure 48 - Thermal imagery of (a) IR Perspex wall (b) polycarbonate during beeswax melt process at 169 minutes duration.

3.4.3 Conclusion

This brief investigation into suitable materials for the utilization of visual and thermal photography, for analysis of a phase change melt process, has found that with the correct materials (polycarbonate) a track of the solid-liquid interface can be generated for both visual and thermal photography.

Unfortunately, further detail than a simple interface track such as convection currents and their directions has not been realised, likely due to transparency in melted material for visual imaging and insufficient resolution and insulation for the thermal imaging.

It has also been demonstrated that using a highly conductive wall such as copper and imaging of re-radiated thermal energy from the contained material for analysis is not effective, likely due to significant conduction from the heat source rather than the contained material. This effect may be minimised by utilization of a thermally insulating gasket and may be worth further investigation despite the manufacture of such a configuration being complex.

Further to the nil efficacy of metal walls in this experimentation it has been found that both thermal and visual imaging are insufficient for solidification analysis due to heat losses through the imaged wall leading to premature solidification on this colder surface.

In future work it may be possible to improve the quality of thermal and visual imaging via the utilization of more non-removable insulation on non-imaged walls and with the addition of a moving stepper motor actuated insulated cover for the imaged face during periods where imaging is not taking place. This would significantly reduce the heat losses from this face which should improve the quality of thermal imaging and potentially allow for efficacious imaging of the solidification process.

One identified limitation of this experimentation is the lack of isotropy due to large amounts of thermal conduction from the heat source through the metal walls and losses through the imaged face which leads to a non-linear melt profile with material melting on the metal walls first. Subsequent numerical validation studies would have to account for this or the test vessel would have to be redesigned.

4 Investigating paraffin and beeswax in a 2D infinite width plate configuration

This chapter contains the first exploratory modelling undertaken to represent an underfloor heating system with a 2D 2.5cm square domain. The configuration chosen is one of an isothermally heated flat plate with a layer of the chosen phase change material 25mm thick with an infinite width. The infinite width is achieved via the usage of matching walls which allow flow to pass from one to the other.

This is intended to represent a thin layer of phase change material heated electrically from below with significant amounts of insulation between the storage and the floor above in a typical room.

Initially a comparison of the two chosen materials, paraffin wax and beeswax, is made to determine the differences in a commonly investigated material (paraffin wax) and a less ideal renewable material.

This is followed by a brief investigation of the effect of the reversed configuration with top heating for beeswax to determine the effect of forcing a wholly conductive heat transfer regime.

4.1 Introduction – 2D simulation with bottom heating

The first section of this chapter develops and discusses the generation and results of the investigation of a small 25mm x 25mm 2D CFD model in a bottom isothermally heated normal gravity configuration (bottom heated) for both beeswax and paraffin wax

4.1.1 Computational Domain and Initial and Boundary Conditions

In order to compare the beeswax and paraffin wax PCMs for underfloor heating at 25 mm dimensioned 2D square domain are used. Figure 49 shows a schematic of this geometry. The two vertical matched walls are connected to each other to allow crossflow and thus form a layer of infinite width. Heat is supplied by an isothermal 80 °C bottom wall.

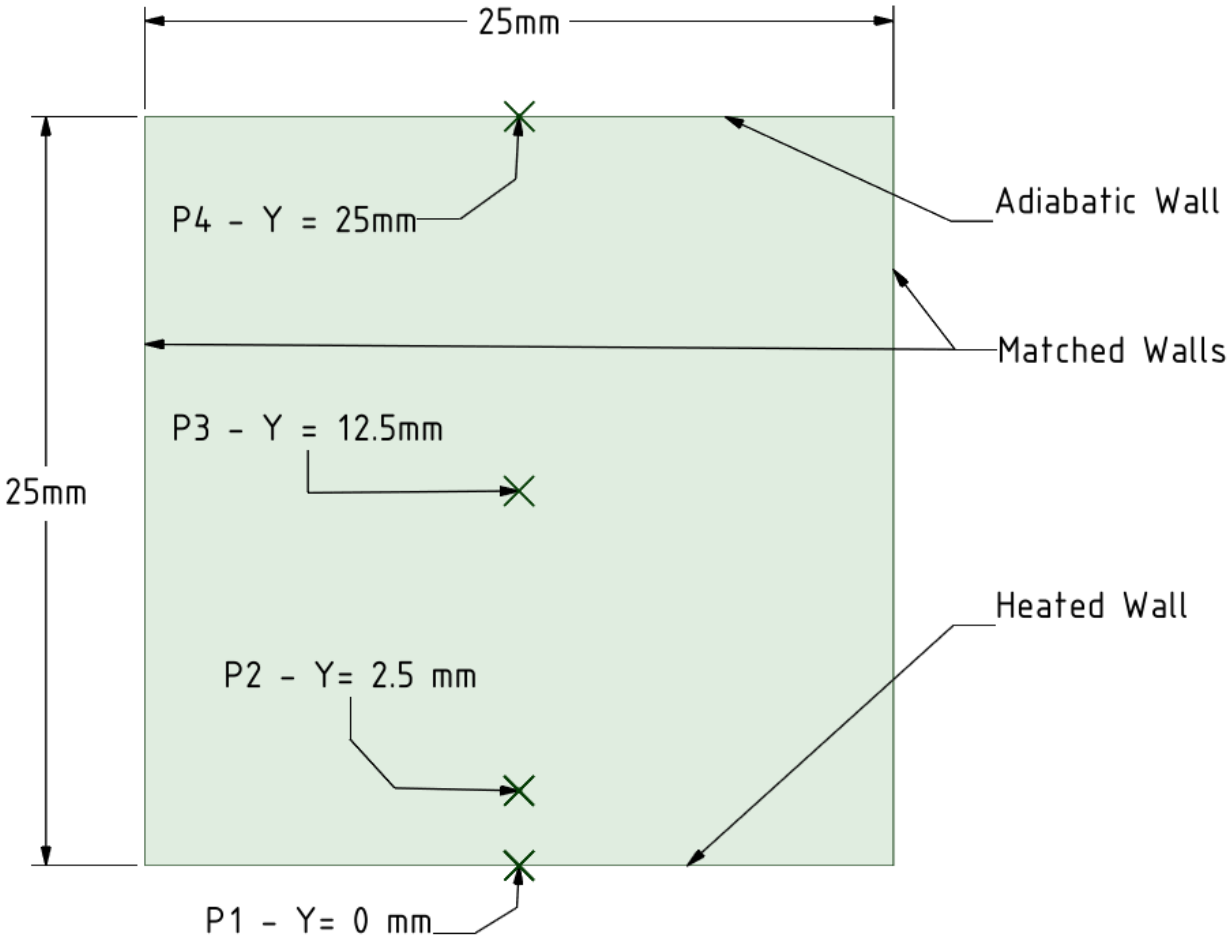

Figure 49 – 2D 25mm square computational domain used for investigation to compare beeswax and paraffin wax. Sample points P1 – P4 shown at x=12.5mm y= 0mm, y= 2.5mm, y= 12.5mm and y=25mm.

These models were computed using Ansys 17.2 and utilized the following assumptions: (1) the top wall is adiabatic to represent ideal insulation; (2) flow is Newtonian and incompressible; (3) flow is laminar and under the effects of gravity; (4) joule friction heating is negligible; (5) physical properties are temperature dependant and accounted for using the linear multi-point data entry method for materials' properties ; (6) heat transfer occurs by conduction and convection only; (7) volume change is ignored; (8) three dimensional convection is ignored.

The following initial and boundary conditions are applied:

- Bulk temperature - 25 °C.
- Bottom wall - 80°C.
- Top Wall – adiabatic.

- Side walls are matched and allow flow to pass in between.
- X velocity – 0 ms^{-1}.
- Y velocity – 0 ms^{-1}.
- Gauge pressure – 0 Pa.
- Gravity – on, set at -9.81 ms^{-2}

At time $t \geq 0$ the mushy constant value is set as:

$$C = 100{,}000$$

4.1.1.1 Solution Method and Controls:

For the numerical solution of the model the previously given methods and controls were utilized and PC 1-3 were utilized for computations (details of machine hardware and solution methods/ controls given in chapter 2).

4.1.1.2 Thermo-physical properties:

The thermo-physical properties of paraffin wax and beeswax are listed in chapter 3 with values in Table 6, Table 7 and Table 8. Where appropriate, linear interpolation of temperature dependant values for material characteristics has taken place.

4.1.2 Results and discussion

In this section, the results of the mentioned models are presented, discussed and compared in terms of the melt, heat rate and relevant dimensionless numbers. In each of the above cases presented, the models with 40,000 cells in mesh resolution were used for the analysis.

4.1.2.1 Evolution of Melt (Time)

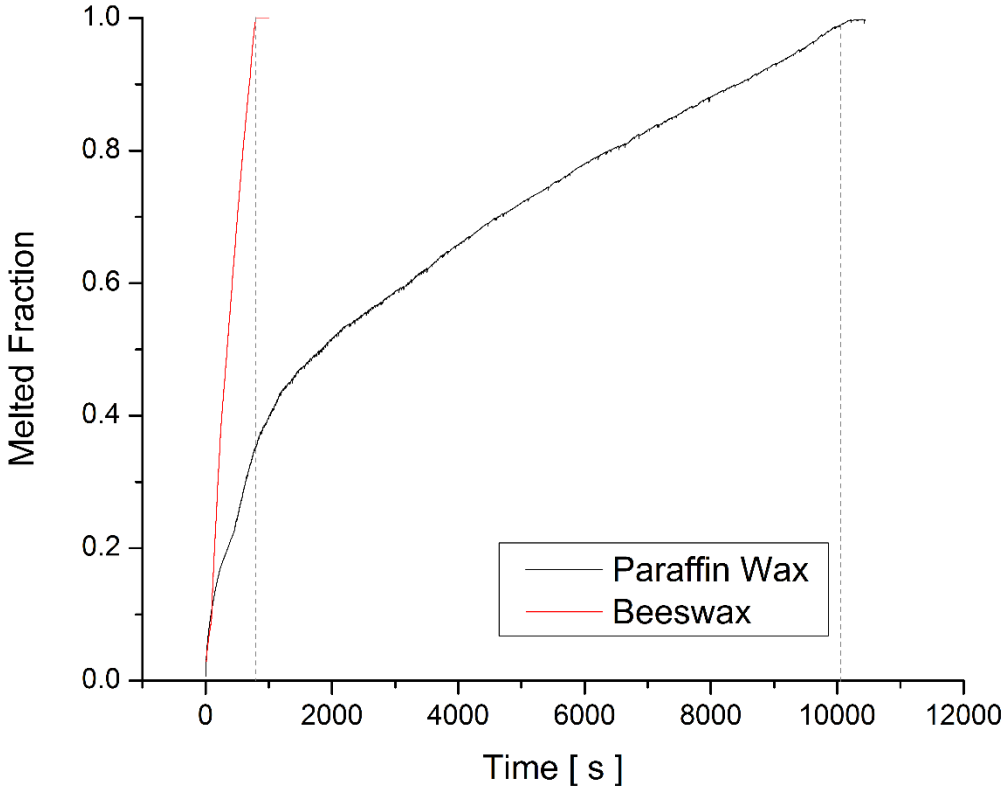

Figure 50- Melted fraction for paraffin wax and beeswax during melt process.

Figure 50 shows the computed surface average volume fraction of liquid for both paraffin wax and beeswax. As can be seen, the progress of beeswax melt shows a fixed higher melting rate until the full melt has completed at 800.0s compared to paraffin wax.

The progress of the melt and the time required for the phase transition of the full volume are important characteristics for a PCM, particularly as this indicates how much and how quickly a PCM can store energy. Here the melt time has been computed using a surface average and has been deemed to be fully melted at 99.0% melted or higher. This has shown a melting time of 800s for beeswax and 10062.5s for paraffin wax respectively.

Paraffin wax demonstrates an initially more fluctuating start, between ~ 0 – 2000 s, before settling into a slightly noisy, almost linear, slowly decreasing melting rate until completion at 10062.5s. It is of note that both materials have a very similar liquid volume fraction until ~100 s where beeswax retains a faster melting rate. During the first ~2000 seconds, the paraffin wax shows two exponentially decreasing melting rates, changing regime at ~450 seconds to the subsequent increased melting rate, attributable to the onset of convection at this time.

Figure 52 and Figure 51 show the contours of liquid mass at various times throughout the melting process for the paraffin wax and beeswax respectively. As can be seen in Figure 52 with increasing time the melting progresses with an extension of the liquid domain proceeding to the top of the domain. This progression is observed to become less parallel to the top wall with time which may complicate subsequent validation.[1]

Figure 53 shows the melting process follows similar behaviour and shows the calculated streamlines of velocity of paraffin wax at various times through the melting process. It was found that during the early stages, while the magnitude of melted liquid remains small (thin layer), conduction is dominant as buoyancy forces are unable to overcome viscous forces. This was also true for the beeswax although for a shorter timescale.

This figure also illustrates the formation of Rayleigh–Bénard convection cells (between 500 – 1000s) in a multi-cellular flow pattern with alternating clockwise and counter-clockwise rotation. As the time of melt increases and the liquid domain increases in size, the convectional flow continues to develop with increasing velocity. As this occurs, the convection remains multi-cellular, however the total number of cells reduces until only one remains. During the transition to, and after the formation of only one convective cell, some instability is observed with temporary additional cells forming and dissipating.

A similar flow development is observed in beeswax: a much quicker initial formation of convection at after ~100s with Figure 51 demonstrating three convection cells at 200s, collapsing into one larger cell as the melt progresses. The beeswax flow also demonstrates less instability in cell formation likely due to stronger convection flow.

It is of note that despite large differences in several thermo-physical properties, melt time and other variables, both beeswax and paraffin wax share very similar melt contour shapes although the formation of the convection cells is significantly slower in paraffin wax.

[1] Validation to take place via visual and thermal photography – processing of imagery without a straight interface will complicate interface tracking.

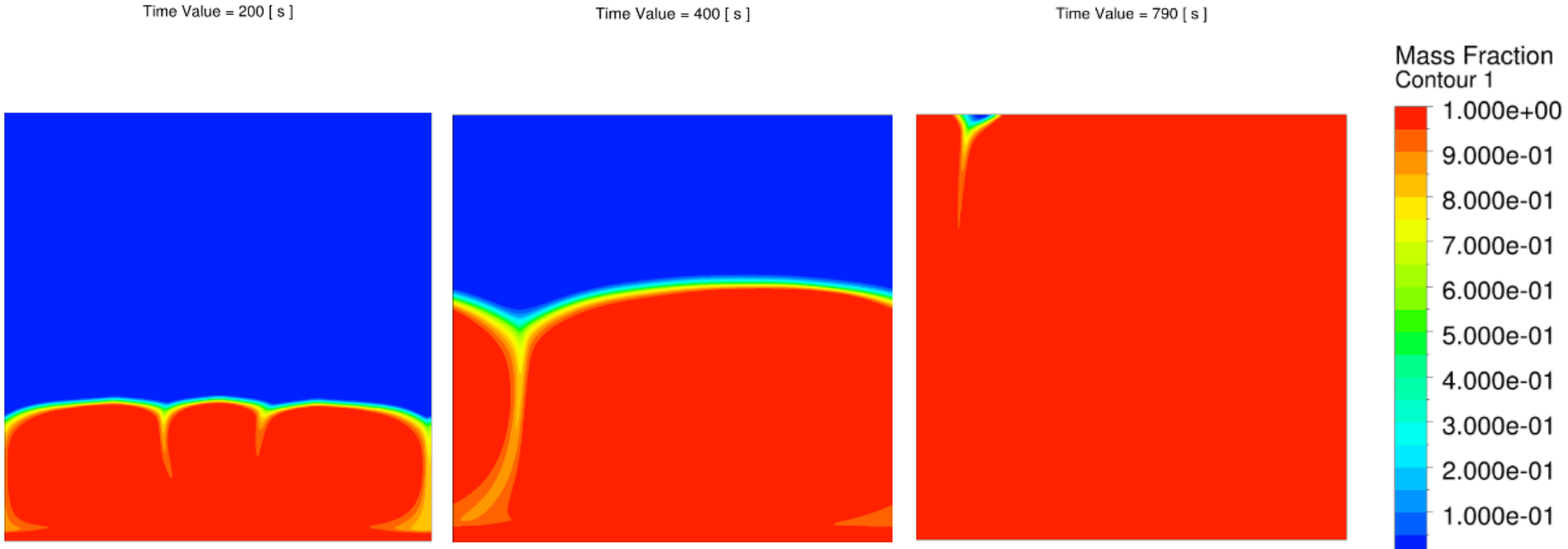

Figure 51 - Contours of liquid mass fraction in beeswax at 200s (a), 400s (b) and 790s (c).

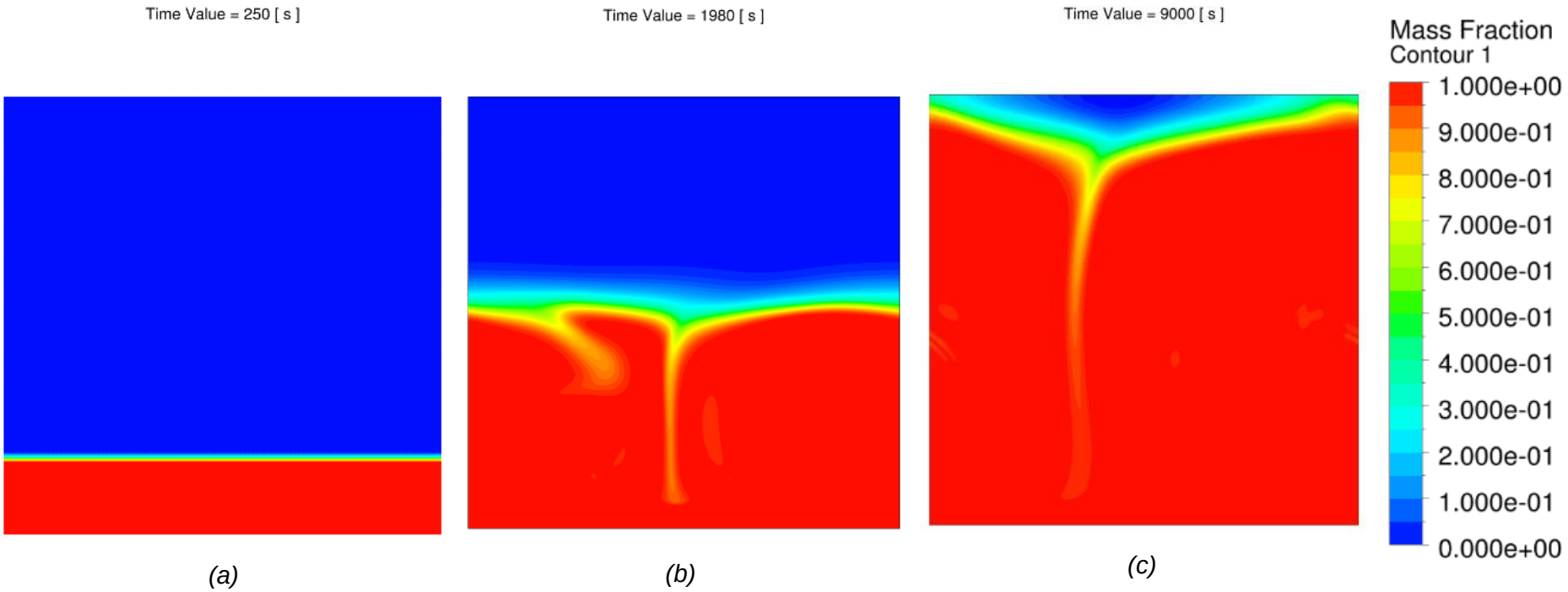

Figure 52 - Contours of liquid mass fraction in paraffin wax at 250s (a), 1980s (b) and 9000s(c).

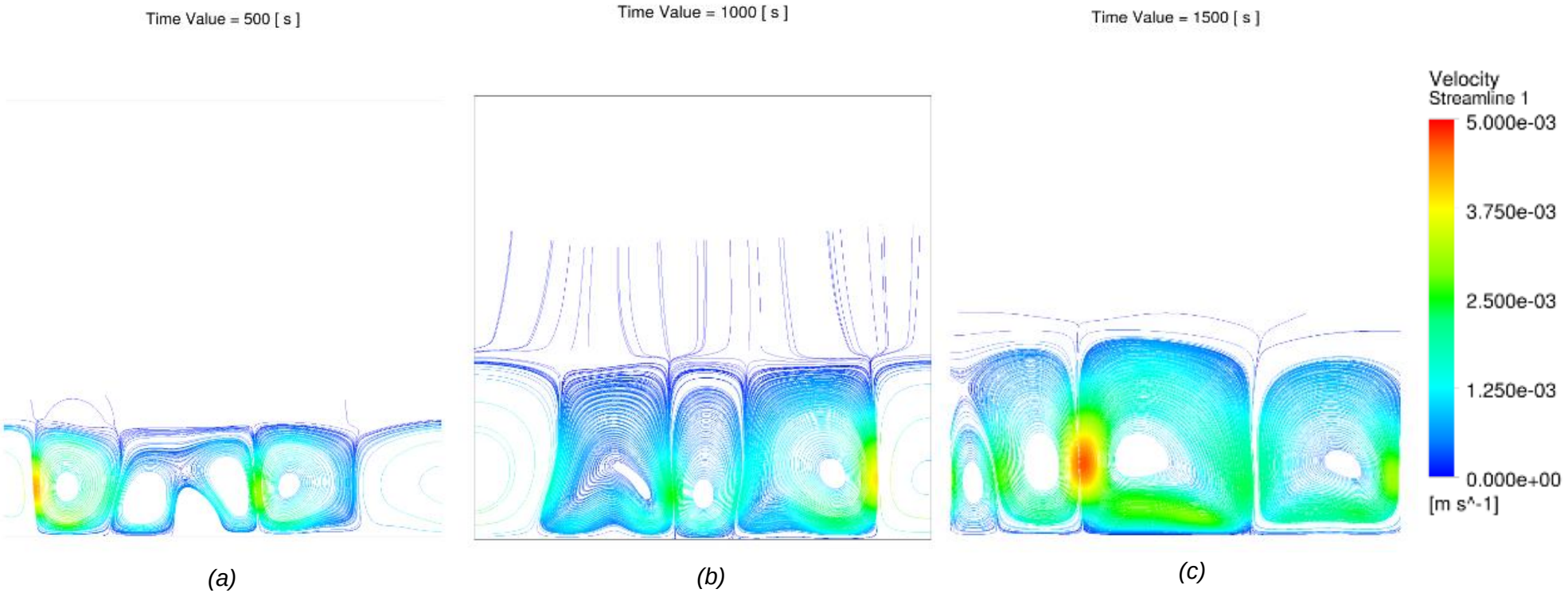

(a) *(b)* *(c)*

Figure 53 – Development of velocity streamlines of paraffin wax at 500s (a), 1000s (b) and 1500s (c) demonstrating developing convective cells.

With the latent heat storage of beeswax approximately 40% larger than the paraffin wax, in addition to its specific heat also being approximately 100% larger, beeswax is clearly the superior PCM for both total energy storage and heat storage rate for this configuration. Due to the larger values for specific and latent heat, this indicates a significantly better rate of heat transfer. This is a particularly interesting result as the thermo-physical energy values are elevated, as is the viscosity. It is likely that the extended time that paraffin wax remains conduction dominated with reduced heat transfer rates compared to convective heat transfer is responsible.

4.1.2.2 Heat transfer power and convective heat transfer coefficients

Figure 54 and Figure 55 illustrate the average heat transfer power of beeswax and paraffin wax which demonstrate very different behaviour between the two materials. Paraffin wax initially starts with a very high transfer power attributable to initial conductive transfer with decreasing heat transfer rates as the temperature gradient decreases. This occurs from around 8700 Wm^{-1} to 1400 Wm^{-1} until convection starts within the liquid domain ~500 –

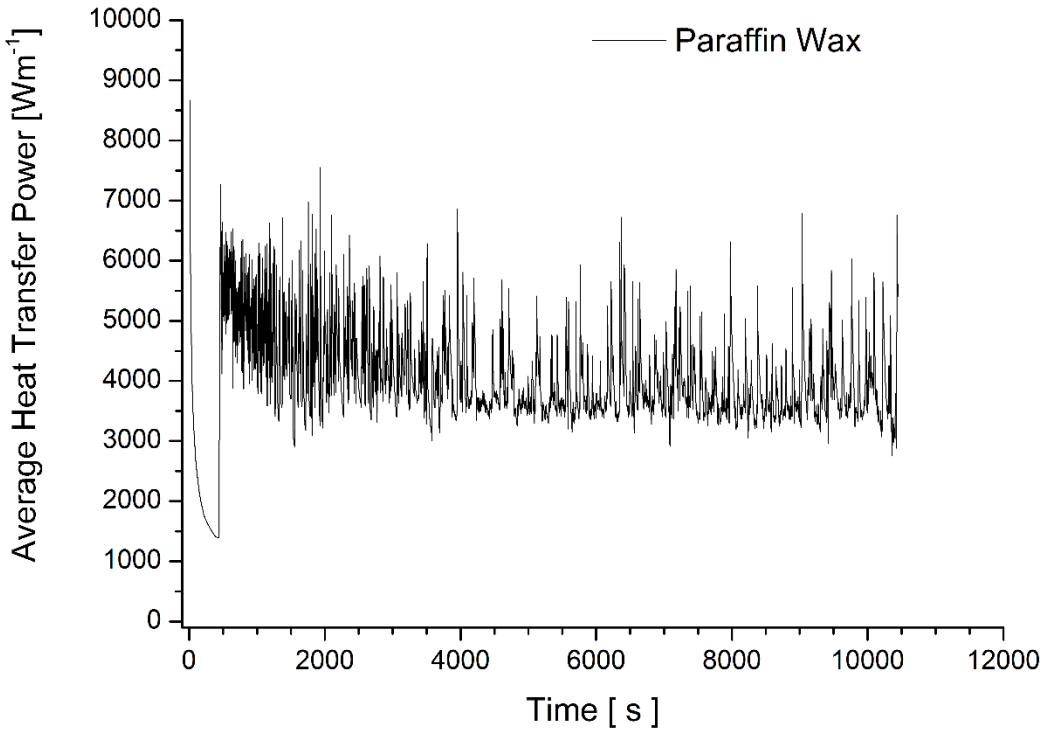

Figure 54- Paraffin wax average heat transfer power during melt process.

1000s. The onset of convection in the paraffin wax then increases the heat transfer rate to between 3000 and 7000 Wm^{-1}.

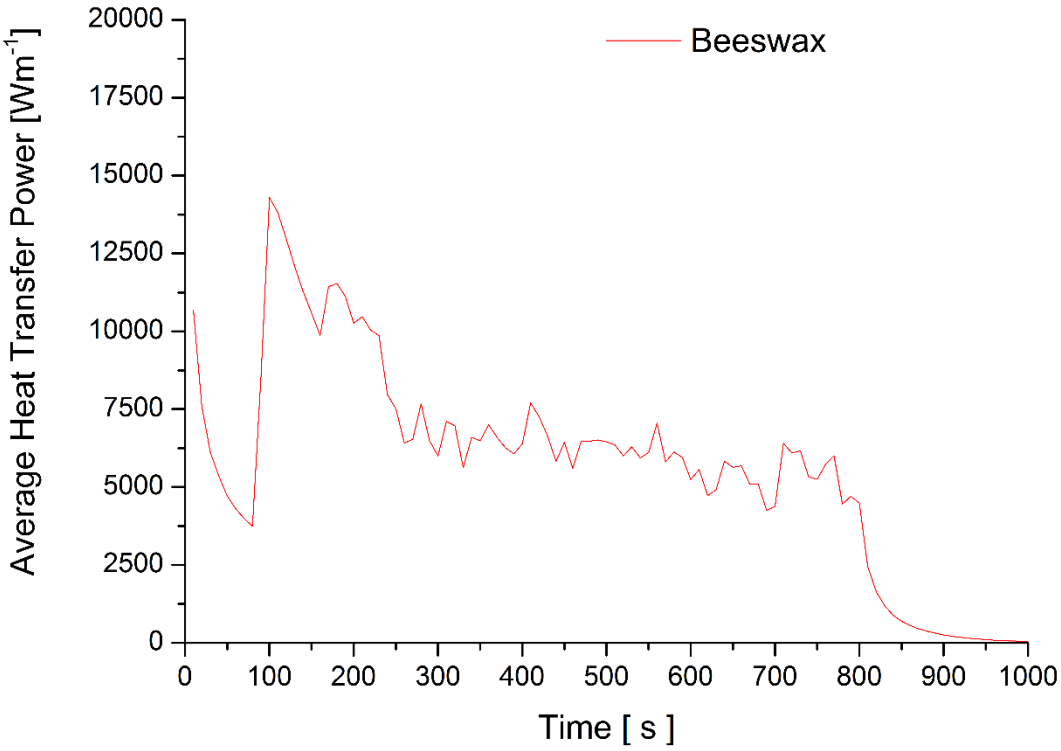

Figure 55 - Beeswax average heat transfer power during melt process.

Beeswax demonstrates similar initial behaviour with an initial spike to ~10500 Wm^{-1} which decreases to ~3800 Wm^{-1} at 80s. This is attributable to a conductive process with a decreasing temperature gradient as the material warms. At this point a convective flow pattern begins to establish itself and rapidly increases the transfer rate to above the initial transfer, reaching a value of 14300 Wm^{-1} and subsequently decreasing and oscillating between 5000 – 8000 Wm^{-1} until melt completion.

The much larger heat transfer power for beeswax would seemingly indicate a superior characteristic in terms of heat transfer, particularly when observed in context of the smaller melt time and higher latent and specific heat compared to paraffin wax.

As expected, the comparison on convective heat transfer coefficients in Figure 56 closely follows the same trends as the power graphs with large initial values rapidly decreasing and subsequently increasing with the onset of convection.

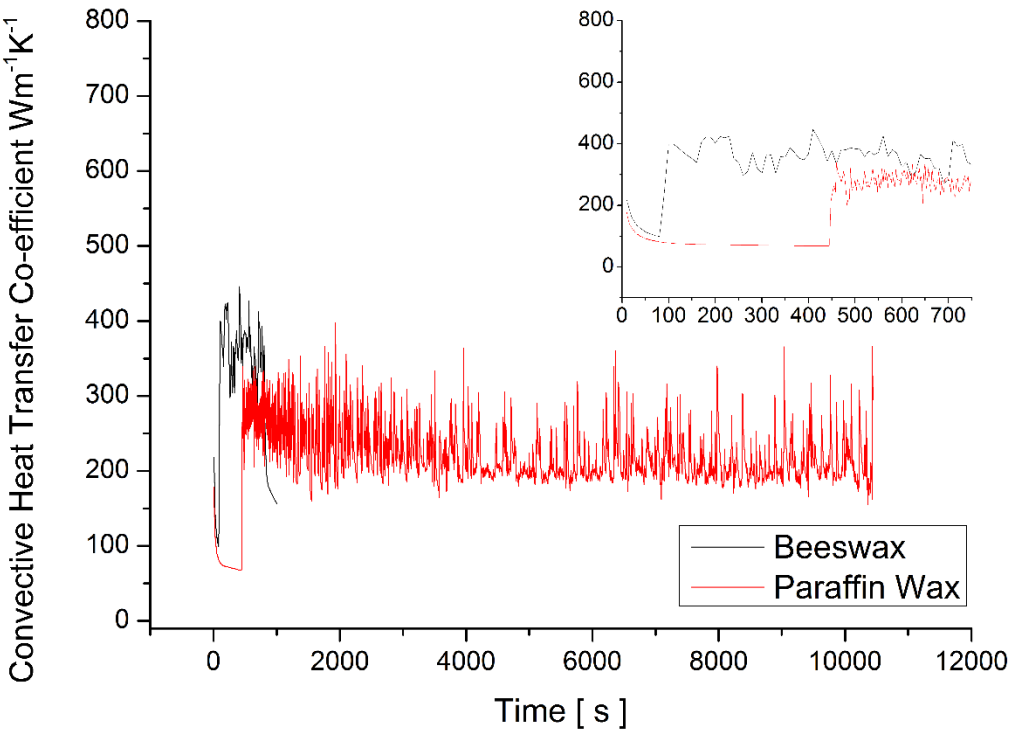

Figure 56 - Convective heat transfer coefficient comparison of beeswax and paraffin wax.

Beeswax again demonstrates an earlier onset and much larger value during the convection process, spiking to ~400 $Wm^{-1}K^{-1}$ and oscillating between ~400 - 300 $Wm^{-1}K^{-1}$ with a slight decreasing trend until melt process completion. Paraffin wax follows this same trend but with a longer time until convection begins with values oscillating between a wider range of ~350 - 200 $Wm^{-1}K^{-1}$ until melt completion.

It is clear that the more rapid melting in beeswax is as a result of very rapid onset of convection and higher initial but decreasing values.

The noisier signal from paraffin wax when compared to beeswax is likely related to weaker ongoing convection causing less stable convection in comparison to the significantly stronger convection ongoing with beeswax. This stronger convection in beeswax is re-iterated in the further dimensionless number analysis.

4.1.2.3 Rayleigh Numbers

Rayleigh number analysis is undertaken to assess to what extent convection is occurring in each material during the melt process. For this analysis the Rayleigh number and Grashof numbers are defined as follows [3]:

$$Ra = GrPr \tag{17}$$

$$Gr = \frac{g\beta(\tau_S - \tau_\infty){L_h}^3}{\nu^2} \tag{18}$$

Where $\beta_{Beeswax}$ =0.004170747, $\beta_{Paraffin\ wax}$ = 0.001247723 and L_H =0.025 (m) but would usually be the ratio of horizontal plate area to plate perimeter in 3 dimensions. In this case it has been assumed to be the 2D hot surface length [4]. Figure 57 and Figure 58 show the Rayleigh number as a function of time for the paraffin and beeswax respectively. It's clear from Figure 57 that the beeswax melt is in th e convective regime (Ra > 1700 [123]), initially at a larger value of 4.5×10^6 at the hot surface and 2.5×10^6 at the points further in the Y dimension. Paraffin wax (Figure 58) is similarly within the convective regime initially starting at ~ 0.75×10^6 on the hot surface ~ 0.625×10^6 at the remaining points.

As the melt develops for both materials, these values initially decrease quickly before forming a small linearly decreasing value. The sudden decrease and adjustment to this linear decreasing trend can be attributed to rapid changes in both kinematic viscosity and density upon initial heating.

As Rayleigh number can be interpreted as a dimensionless number, which measures the relative importance between the effects of buoyancy and those of viscosity with thermal conduction, it is expected to decrease over the melt process and rapidly decrease when the melt process is complete.

Convection is clearly visible in both melt processes due to both the Rayleigh numbers and by observation of the liquid mass fraction contours as well as the flow pattern. Figure 51, Figure 52 and Figure 53). The larger values of Rayleigh number in beeswax also agree with a more vigorous convective process which is later confirmed via Peclet contour analysis.

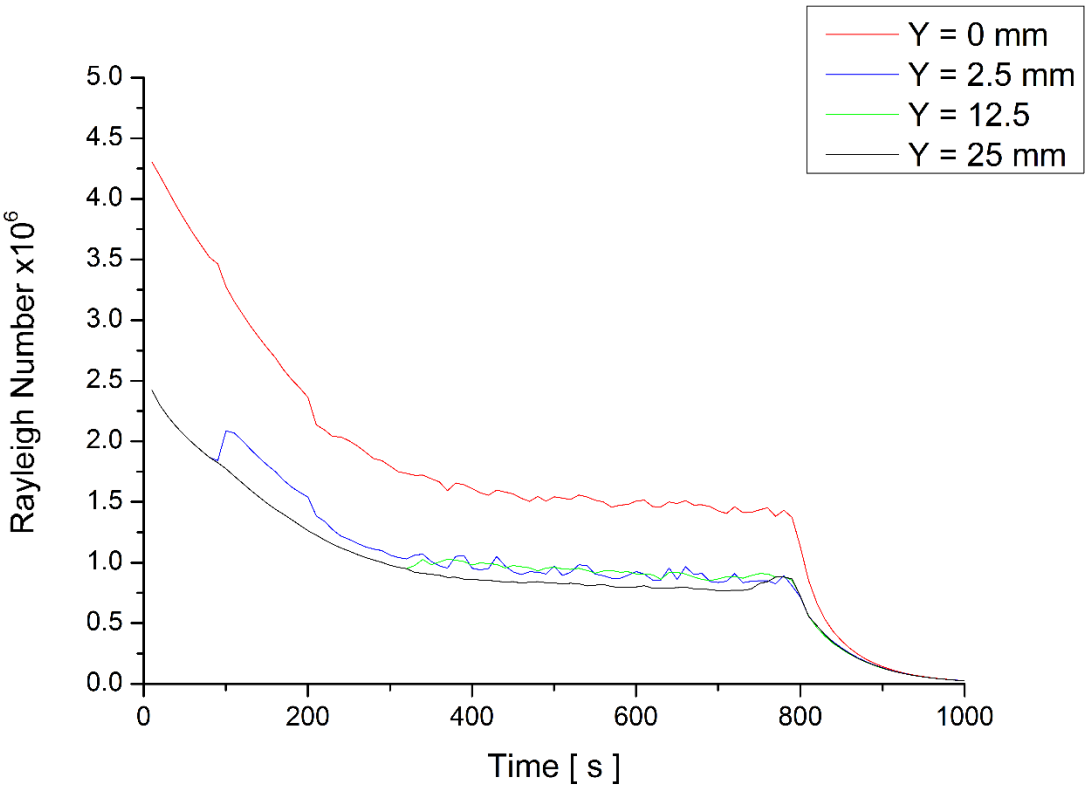

Figure 57 – Rayleigh number analysis at points P1 (12.5, 0) mm, P2, (12.5, 2.5) mm, P3 (12.5, 12.5) mm and P4 (12.5, 25) mm for the ongoing melt process in beeswax.

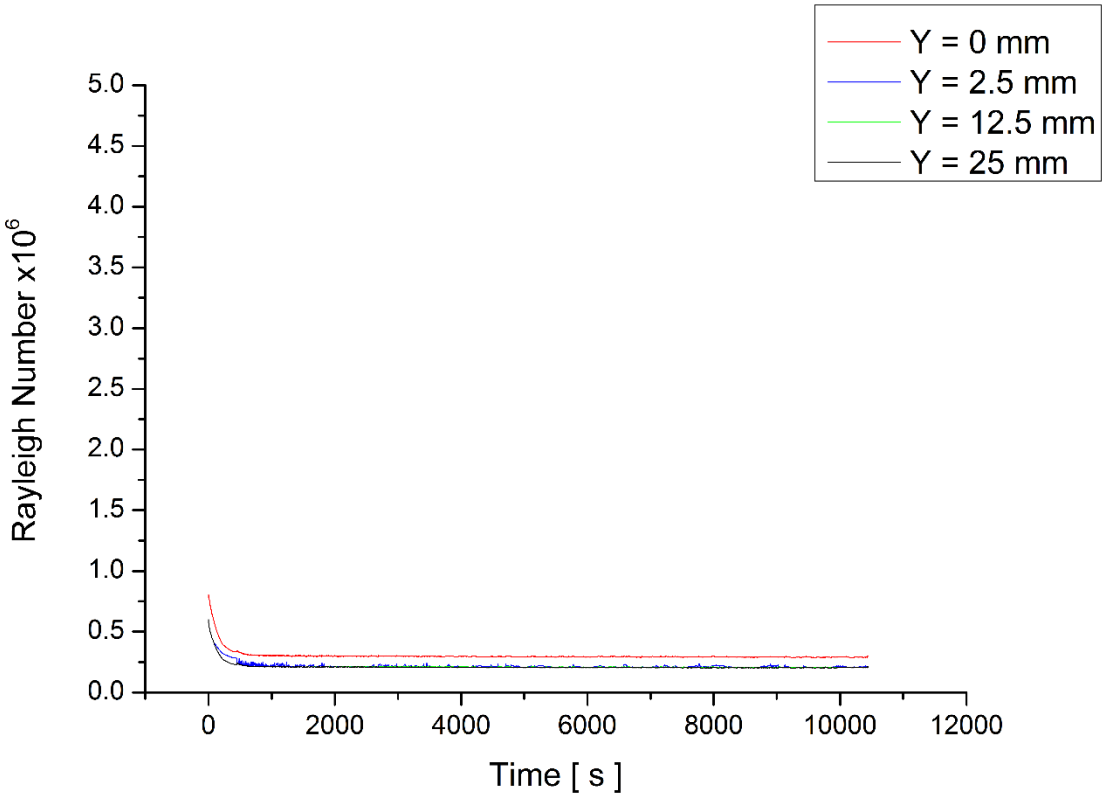

Figure 58 - Rayleigh number analysis at points P1 (12.5, 0) mm, P2, (12.5, 2.5) mm, P3 (12.5, 12.5) mm and P4 (12.5, 25) mm for the ongoing melt process in paraffin wax.

This initiation of convection is coincidental with an increase in power transfer in Figure 54 and a decrease in Rayleigh number observed in Figure 58 for paraffin wax and Figure 55 and Figure 57 for beeswax. The magnitude of Rayleigh number in both materials by average and by contour indicates that the convection is taking place, but not within a turbulent regime (transition occurs near 10^7 [124]). Turbulence convection, if present would have been advantageous for heat transfer.

4.1.2.4 Peclet Numbers

Peclet number analysis was undertaken in order to quantify the ratio of heat transfer conducted and convected in the fluid/bulk. This is shown in Figure 59 for beeswax and Figure 60 for paraffin wax.

$$Pe = RePr \tag{19}$$

Where *Re* is the Cell Reynolds number in the CFD-Post Software.

This Reynolds value is calculated using cell variable values in comparison with cell size. This is a relative comparative Reynolds number dependent on the cell size and thus will vary from simulation to simulation depending on the meshes used. In this case the meshing for all simulations gives the same cell sizes allowing for a valid comparison. This is also the case for further chapters modelling simulations.

As shown in Figure 59, throughout the entire melting process, the contours of Peclet number and average values across the surface for beeswax show the presence of vigorous convection, with Peclet numbers of 1.5 to 5 visualised. This is expected for a convection dominated heat transfer process.

In contrast, as shown in Figure 60, paraffin wax has much lower Peclet numbers between 0 to 0.28. This shows a significantly lower ratio of convection to conduction. The overall heat transfer is, however, conduction dominant even across and despite the fully formed Rayleigh–Bénard convection cells. Both figures clearly show the presence of convective cells.

It is likely that convection dominance is highly advantageous, with the beeswax melting 10x quicker than the paraffin wax with a Peclet value up to 15x larger despite the thermo-physical

values of beeswax being considerably larger, leading to the increased amount of energy stored.

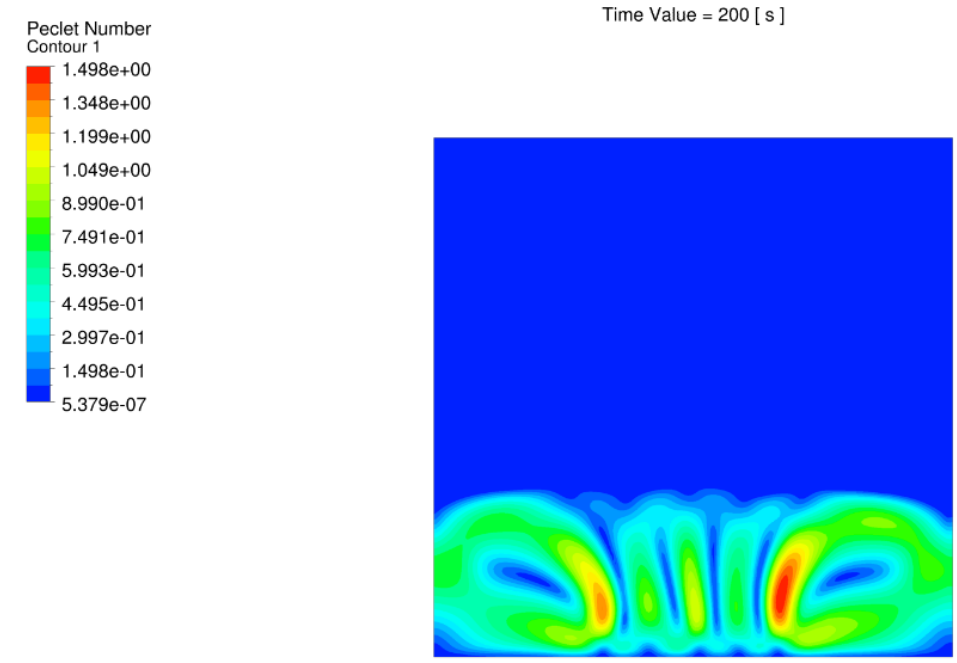

(a)

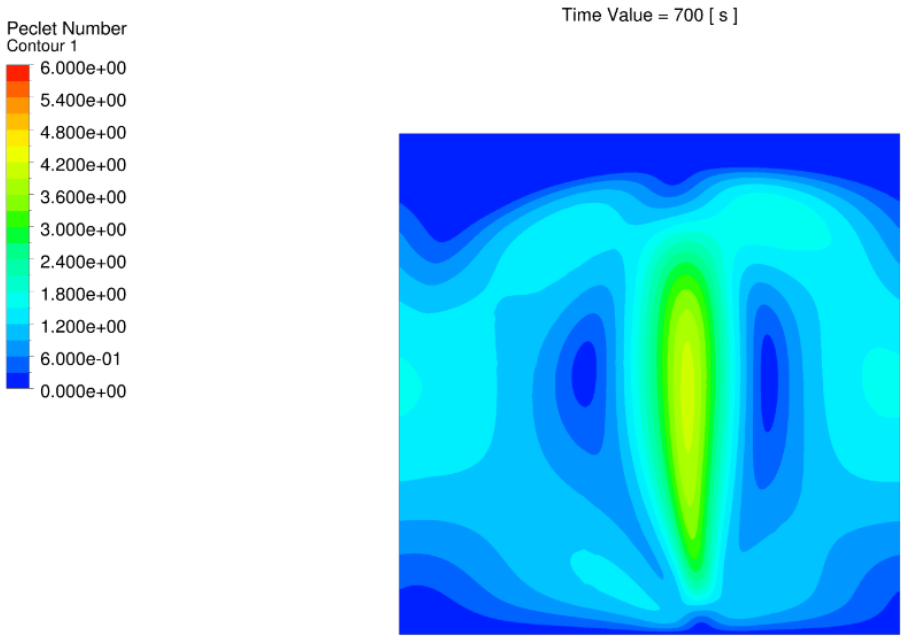

(b)

Figure 59- Contours of Peclet number for beeswax at (a) 200 s and (b) 700s.

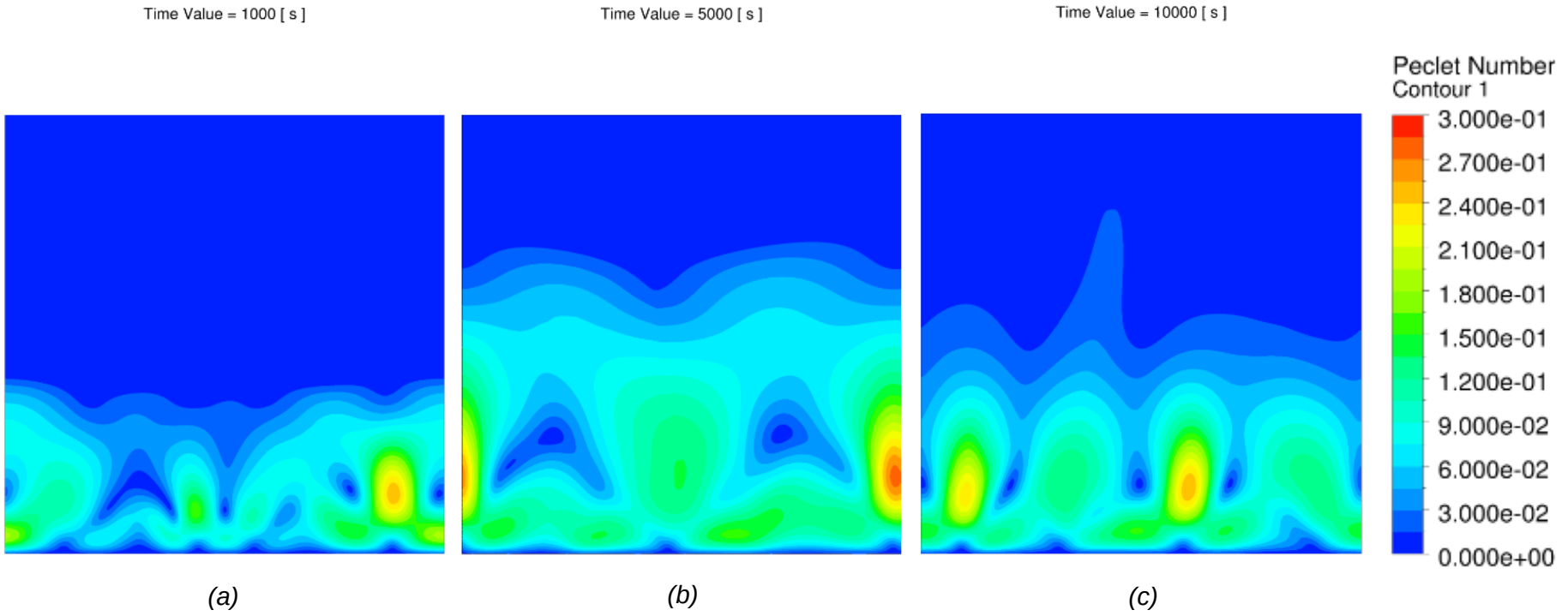

Figure 60 - Contour plot of Peclet number for paraffin wax at 1000s (a), 5000s (b) and 10000s (c).

4.1.2.5 Nusselt Numbers

As the specified configuration is one of bottom heated horizontal plates, coupled with the values of Rayleigh number, the Nusselt number correlation utilized is the following [107]:

$$Nu = 0.54\, Ra^{1/4} \tag{20}$$

Where:

$$(\tau_s + \tau_\infty)/2$$

$$1.0 < Ra < 1 \times 10^{10}$$

Nusselt number analysis was undertaken in order to quantify the ratio of heat transfer conducted and convected from the hot surface. Average values from the heated surface for each material can be seen in Figure 61.

The plot shows a similar trend to the Rayleigh (Figure 58 and Figure 57) and power (Figure and Figure 55) plots with a larger initial value decreasing before convection begins but has no subsequent increases, rather smoothly decreasing to a fixed value for the remaining duration of the melt process in both beeswax and paraffin wax. The tail off in beeswax is directly attributable to the melt process completing and the temperature starting to increase.

The average Nusselt number plot for both materials shows the values agree with the Peclet analysis; convection is on-going. Beeswax shows a larger value 15 – 11.5 throughout the majority of the melt process. Paraffin wax demonstrates a lower initial value before dropping to a fixed value ~10.5. These values, coupled with observation of the contours of Peclet number, show that convection is weaker for paraffin wax both at the heated surface and in the bulk.

Given the larger thermo-physical values for beeswax, it is storing more energy and doing so at a larger rate. Given the larger Nusselt value associated with beeswax, a higher ratio of convection to conduction seems to be highly advantageous.

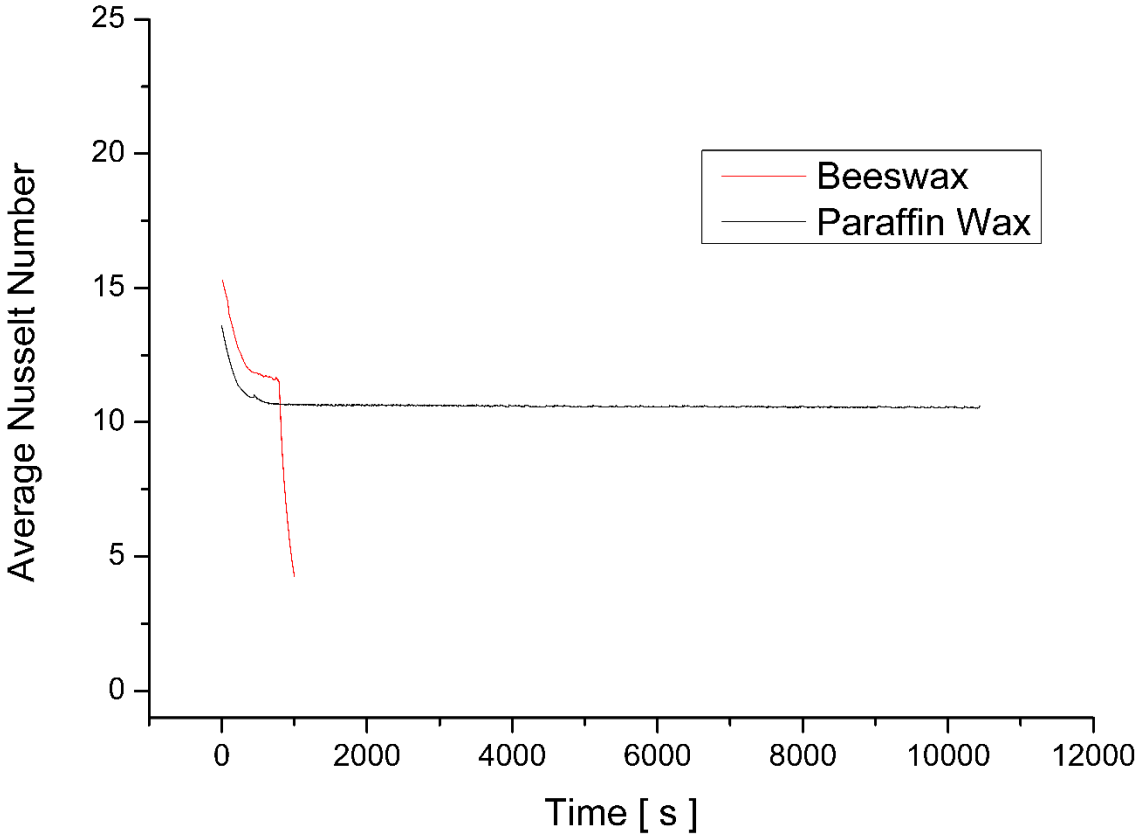

Figure 61 –Average Nusselt number versus time for beeswax and paraffin wax during melt process.

Values for Nusselt number calculated via the convective heat transfer coefficient values follow the same curve profile for this variable and also show similar values ~ 25 – 10 but a different curve profile (consult Figure 56 as the profile is identical at the range of values specified) which could indicate that Equation 20 is not appropriate for analysis in this case.

4.2 Introduction – 2D simulation of beeswax with top heating

In order to further investigate the effect of convection on beeswax for underfloor heating, the previous investigation on beeswax is replicated with the same conditions excepting the force of gravity being inverted. This will reflect a system with the heated plate installed at the top surface and will show the effect of forcing the PCM to melt wholly under a conductive regime.

Figure 49 from the previous study shows a schematic of the geometry used. The configuration is the same: two vertical matched walls are connected to each other to allow crossflow and thus form a layer of infinite width. Heat is supplied by an isothermal 80 °C bottom wall (due to inversion of gravity this now functions as the top wall.)

4.2.1 Computational Domain and Initial and Boundary Conditions

These models were computed using Ansys 17.2 and utilized the same assumptions as previously made in this study: (1) the top wall (not heated) is adiabatic to represent ideal insulation; (2) flow is Newtonian and incompressible; (3) flow is laminar and under the effects of gravity; (4) joule friction heating is negligible; (5) physical properties are temperature dependant and accounted for using the linear multi-point data entry method for materials properties ; (6) heat transfer occurs by conduction and convection only; (7) volume change is ignored; (8) three dimensional convection is ignored.

The following initial and boundary conditions are applied:

- Bulk Temperature - 25 °C.
- Bottom Wall - 80°C.
- Side walls are matched and allow flow to pass in between.
- Top Wall – adiabatic.
- X Velocity – 0 ms^{-1}.
- Y Velocity – 0 ms^{-1}.
- Gauge Pressure – 0 Pa.
- **Gravity – on, inverted and set at +9.81 ms^{-2}**

At time $t \geq 0$ the mushy constant value is set as:

$$C = 100{,}000$$

4.2.1.1 Solution Method and Controls:

For the numerical solution of the model the previously given methods and controls were utilized and PC 1-3 and Super Compute Cluster 2 were utilized for computation (details of machine hardware and solution methods/ controls given in chapter 2.)

4.2.1.2 Thermo-physical properties:

The thermo-physical properties of beeswax used in this study are identical to those used in the previous study and can be found in chapter 3: Table 6, Table 7 and Table 8.

4.2.2 Results and discussion

In this section, the results of the inverted gravity model are presented, discussed and compared in terms of the melt, heat rate and relevant dimensionless numbers. The same model as previously, with 40,000 cells in mesh resolution, was used for the analysis.

Please note, Figure orientation is the same as the previous section! Gravity is inverted rather than the model rotated to allow for easier comparison.

4.2.2.1 Evolution of Melt (time)

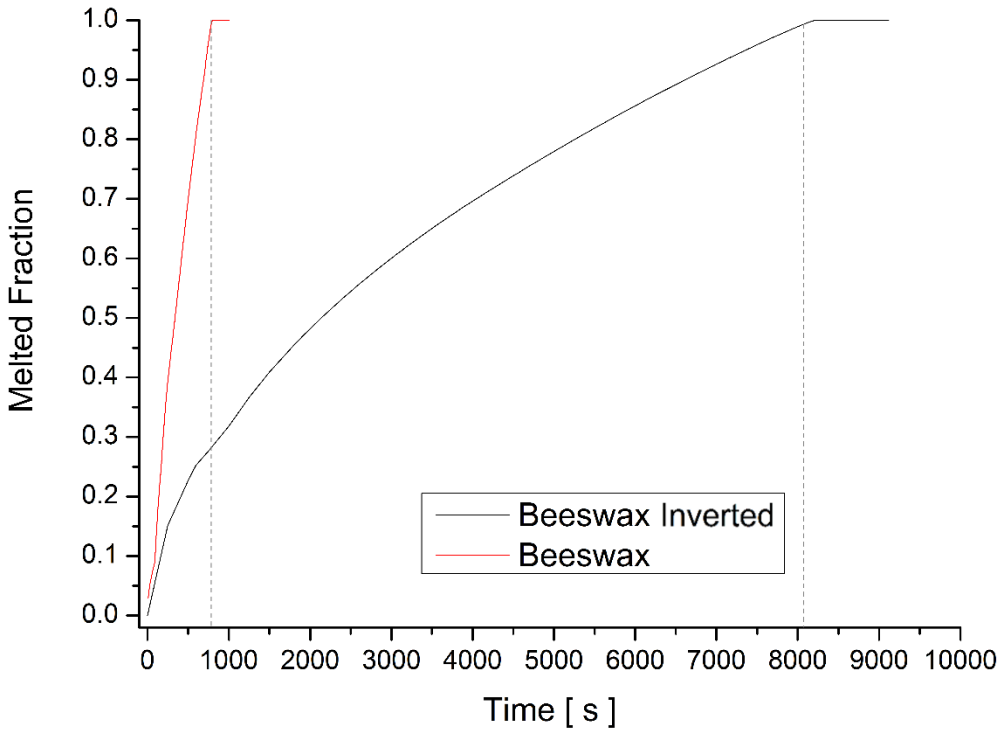

Figure 62- Melted fraction progression comparison between normal beeswax configuration and inverted configuration.

The melt fraction has been computed in the same way as the previous study and Figure 62 clearly demonstrates a dramatic increase in the amount of time required to attain melt completion for the inverted configuration. Melting completion in the inverted configuration has taken 8040s compared to 800 seconds in the former configuration.

Unlike the standard configuration with a higher rate and a steadier, almost linear rate of melt, the inverted configuration demonstrates a larger initial rate of melting followed by an apparent exponentially decreasing melting rate until completion. This decreasing rate is related to conduction dominance and is attributable to increasing thermal resistance as the temperature gradient decreases over time.

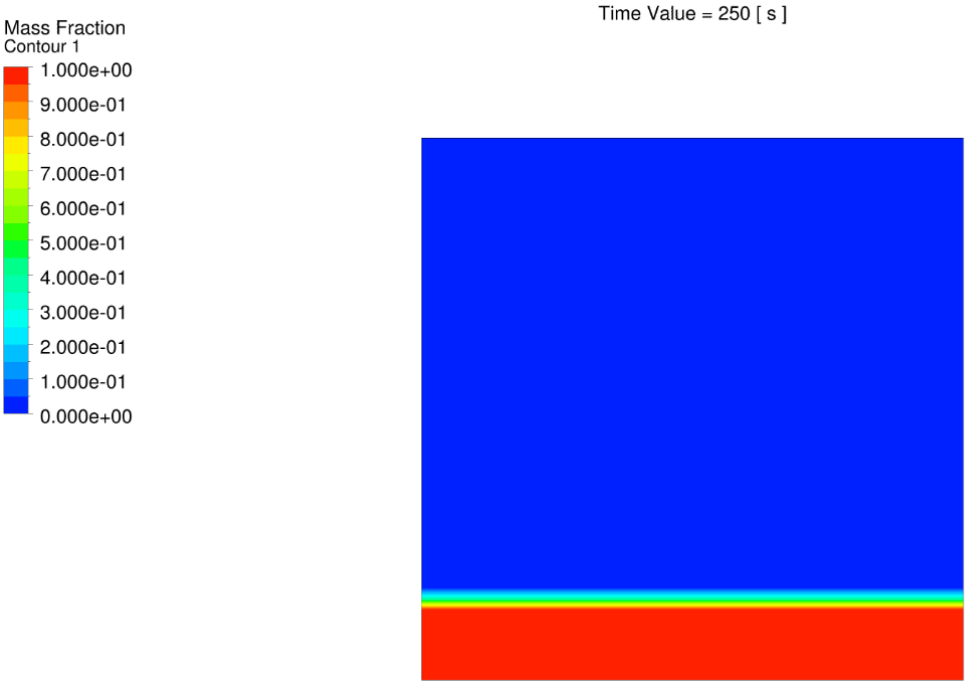

Figure 63 - Contours of liquid mass fraction for inverted beeswax configuration at 250s.

Further indications of conduction dominance are found in Figure 63 and Figure 64, contours of liquid mass fraction. The standard configuration (Figure 51 and Figure 52) the flow patterns clearly demonstrate the formation of Rayleigh–Bénard convection cells and the liquid-solid interface becomes less parallel to the top surface over time. In contrast, the inverted configuration remains highly parallel throughout the melt process indicating a lack of convection and a wholly conductive process.

Figure 65 shows a comparison between the heat transfer power in the standard and the inverted configuration and reveals a dramatically lower power of heat transfer for the inverted configuration, spiking initially to ~23000 Wm^{-2} before exponentially decreasing to ~ 325 Wm^{-2} at the conclusion of the melt process. Again, this decreased peak and average value, in

addition to the exponentially decreasing rate, are highly indicative of a conduction dominant process.

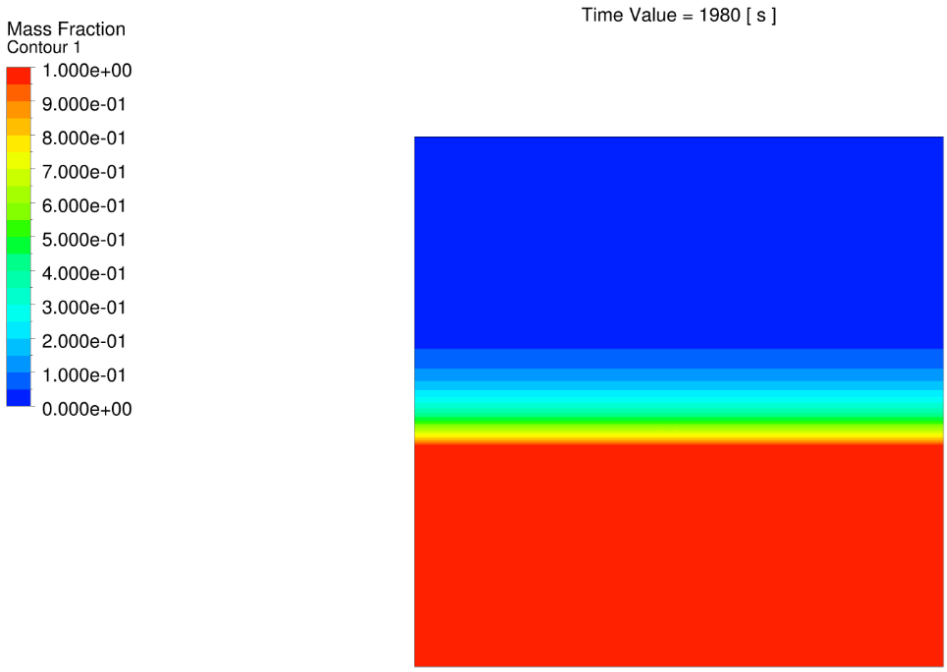

Figure 64 - Contours of liquid mass fraction for inverted beeswax configuration at 1980s.

4.2.2.2 Heat transfer power

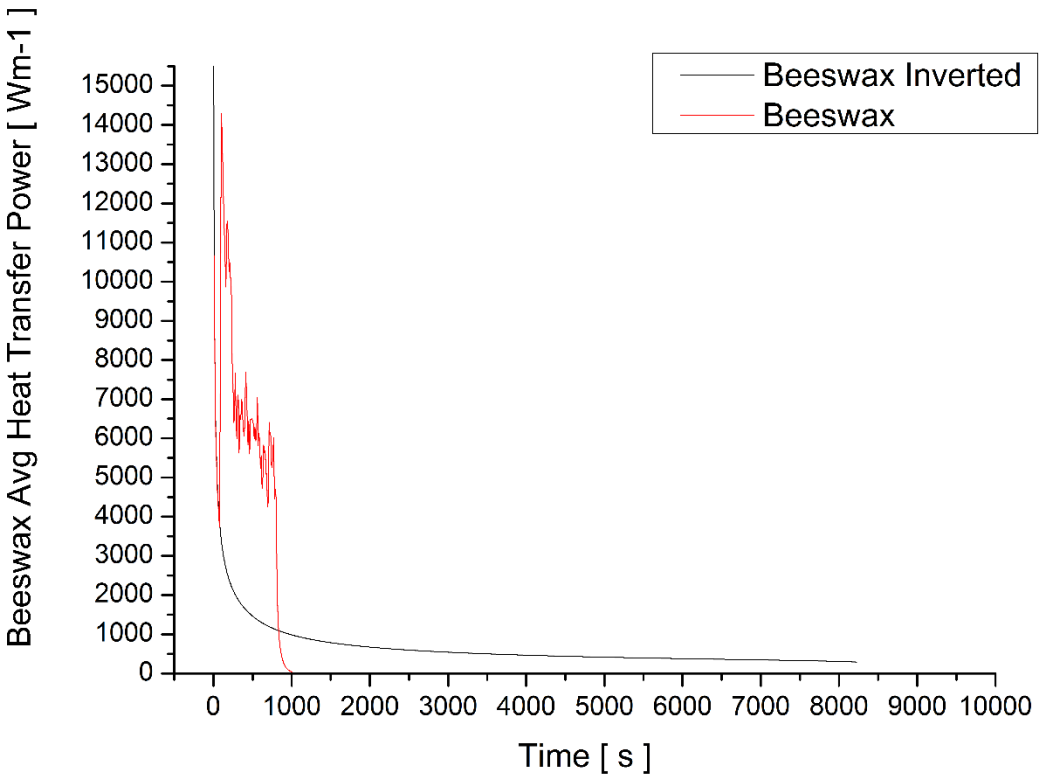

Figure 65- Average Heat Transfer Power comparison between normal beeswax configuration and inverted configuration.

In contrast, the standard configuration (Figure 55) spikes to nearly ~15000 Wm^{-2} decreasing to an oscillatory power signal between 5000 – 10000 Wm^{-2}. This shows the standard configuration to have ~13x greater heat transfer power at the lowest recorded heat transfer values for both configurations. As expected, the inverted configuration shows no noisy signal due to conduction dominance.

4.2.2.3 Rayleigh Numbers

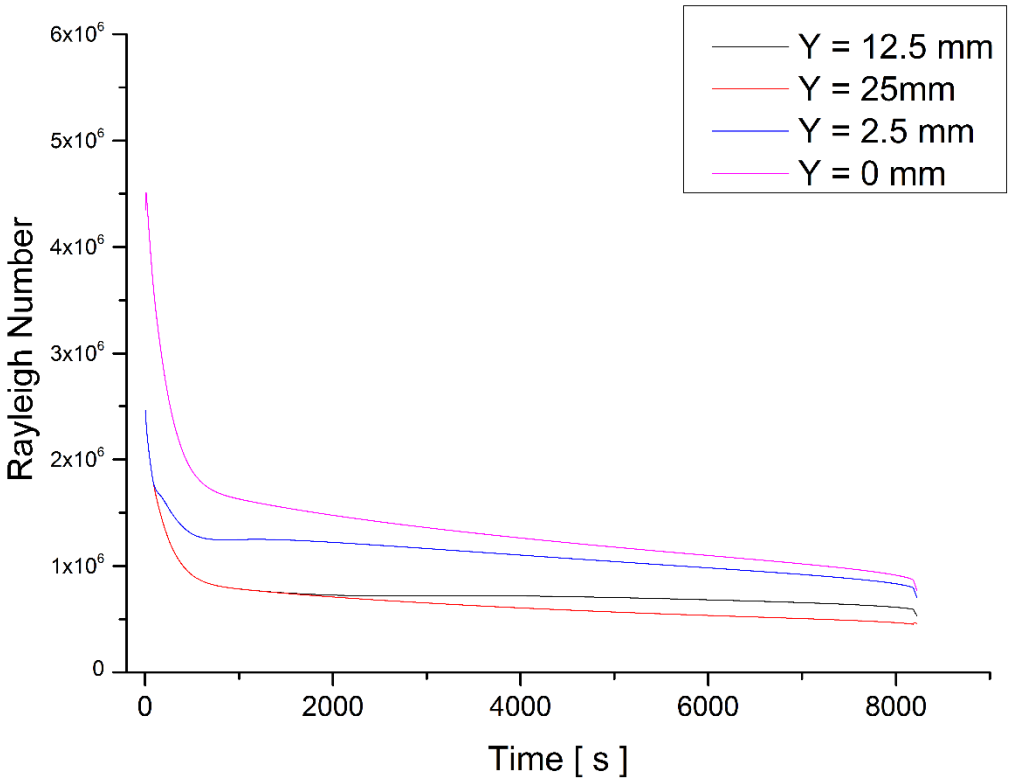

Figure 66 - Rayleigh number analysis at points p1 (12.5,0) mm, p2, (12.5,2.5) mm, p3 (12.5,12.5) mm and p4 (12.5,25) mm for the ongoing melt process for beeswax in the inverted configuration.

Figure 66 shows an extremely similar plot to Figure 57 in both shape and values. This is not unexpected due to the formulation of the Grashof and Rayleigh numbers and the increased smoothness of Figure 66 in comparison can be attributed to conduction dominance. As this has been determined to be a fully conductive dominant process this figure has been shown for completeness but does not represent any meaningful analysis.

4.2.2.4 Peclet Numbers

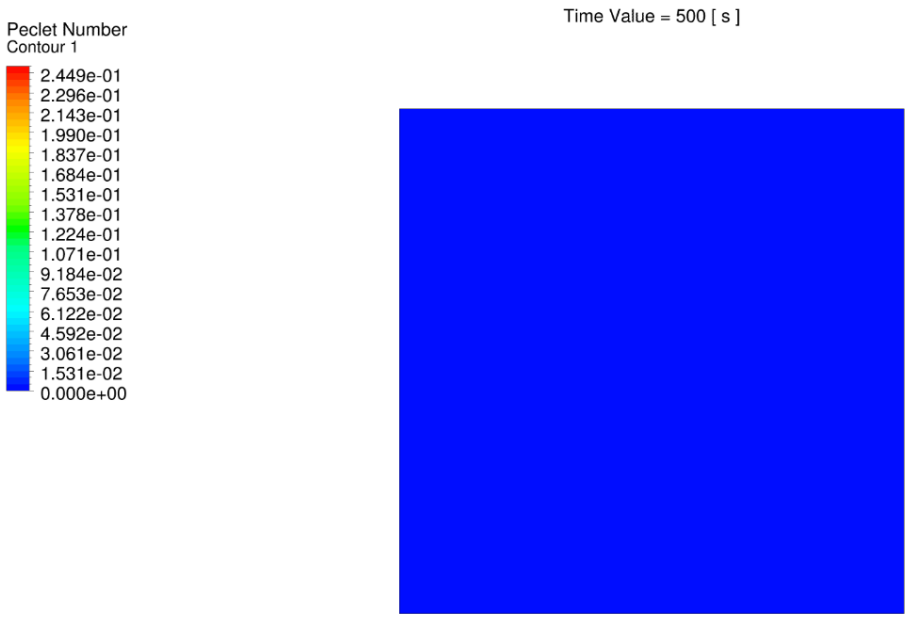

Figure 67- Peclet Number contour plot of inverted beeswax configuration at time 500s.

Peclet number analysis for the inverted configuration is simple and contrasts highly with the standard configuration imagery found in Figure 59, where values up to 5 are seen. Figure 67 clearly demonstrates a complete lack of convection throughout the computational domain with values of Peclet number barely exceeding zero. This indicates total conduction dominance and these values are reflected in all contour plots generated throughout the melt process.

The range of this contour plot is set between the maximum and minimum values of Peclet number found during the entire melt process with the maximum found in a small number of cells.

4.2.2.5 Nusselt Numbers

A Nusselt number comparison in this case is unnecessary as by definition, the value for Nusselt number in the inverted configuration is 1 due to full conduction dominance.

4.3 Mesh and Temporal Dependency

Mesh generation for this 2D domain was one of unstructured quadrilaterals with adjustment to maximum face size to change the number of generated cells.

In addition to the simulations described above, in order to ascertain the grid and temporal independence of the simulations above, a convergence study was undertaken and indicated independence on characteristic melt time at 20,000 cells and 0.25s for the beeswax and paraffin wax. For these, the error in the beeswax melt time between 20,000 and 40,000 cells was 0.16% and between 20,000 and 10,000 cells 2.41%, while in the paraffin wax independence was indicated at 20,000 cells with a 4.12% error between 20,000 and 40,000 cells during the convective study. The conductive study with inverted gravity uses the same 40,000 cell mesh.

A temporal study was also undertaken for beeswax with time steps of 1, 0.5, 0.25 and 0.2, 0.1 and 0.05s in which melt times were found to be 906, 830, 841, 838, 989 and 900 s respectively. Similar closely grouped melt times were found for paraffin wax ±10%.

Additional monitors of both temperature and velocity were placed at several points within the computational domain as additional convergence criteria.

4.4 Conclusion

The present study has investigated the modelling and results of melting paraffin wax and beeswax at 80 °C on an isothermal plate of infinite width intended to represent an ideal underfloor heating system with bottom and top heated configurations.

Several observations were made using dimensionless number and variable analysis. Key observations were convection dominance in beeswax with standard gravity associated with a significantly reduced melting time of 800s for beeswax compared to paraffin wax 10062.5s. This is a particularly interesting result given the thermo-physical properties of beeswax are significantly larger than paraffin wax which means the beeswax melt is not only storing more energy, but is also doing so at a rate significantly larger than paraffin wax.

Both beeswax and paraffin wax show discrete Rayleigh–Bénard cells with a ratio of heat transfer by convection to conduction of up to 1.5 in beeswax and 0.28 in paraffin wax.

Beeswax has larger values of latent heat and specific heat by approximately 40% and 100% respectively. This indicates that convection is advantageous in these conditions for beeswax and the higher ratio of conduction to convection in paraffin wax, likely as a result of its decreased density change, has conferred a significantly slower rate of melting.

In addition, a further model of beeswax with gravity inverted to damp convection conclusively shows convection is advantageous as this process was fully conduction dominant and increased the melting time by almost 10x.

It is clear that for these models a much higher mesh resolution is needed than in comparable literature which is thought to be as a result of using additional temperature dependent properties rather than primarily phase dependent properties and formulaic density approximations.

Future work to comparing similar 2D models for experimental validation can be found in Chapter 7.

5 Investigating various 2D pipe heated geometries with beeswax

5.1 Introduction

A further investigation into the geometrical configuration of an underfloor heat storage system has been undertaken via the generation and modelling of a pipe heated domain of various x dimensional widths and pipe mounting locations.

This investigation is split into two sections, one comparing the melt process of 4 domain widths with a single 10mm diameter pipe as a heat source.

The second section investigates the effect of mounting the pipe in two locations: on the bottom wall or centrally in the domain.

5.2 Computational Domain and Initial and Boundary Conditions

In order more fully to investigate the effect of convection on beeswax for underfloor heating, further models intended to represent a current, potential underfloor heating system with heat provided by a 10mm pipe were generated.

Placement heights of the pipe have been varied between being **centrally located** in the domain and located at the **bottom surface**. Spacing between the pipes in the domain has also been varied by increasing the x dimensional length between 25, 50, 75 and 100mm.

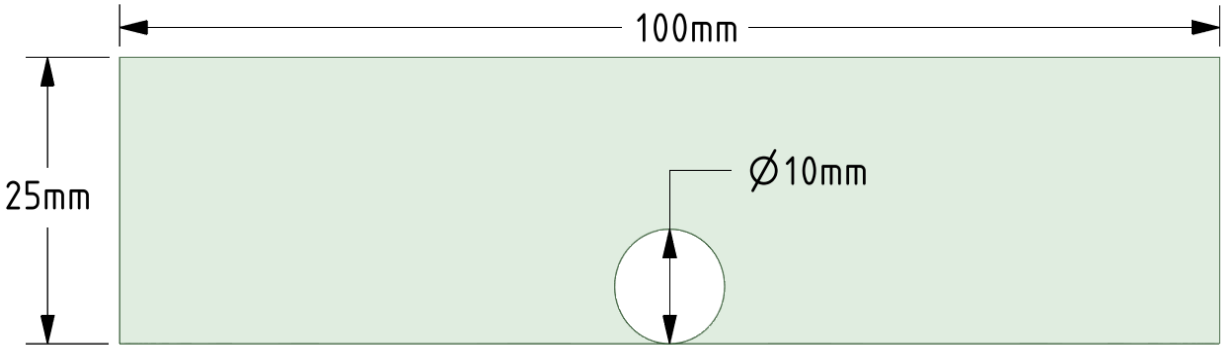

(a)

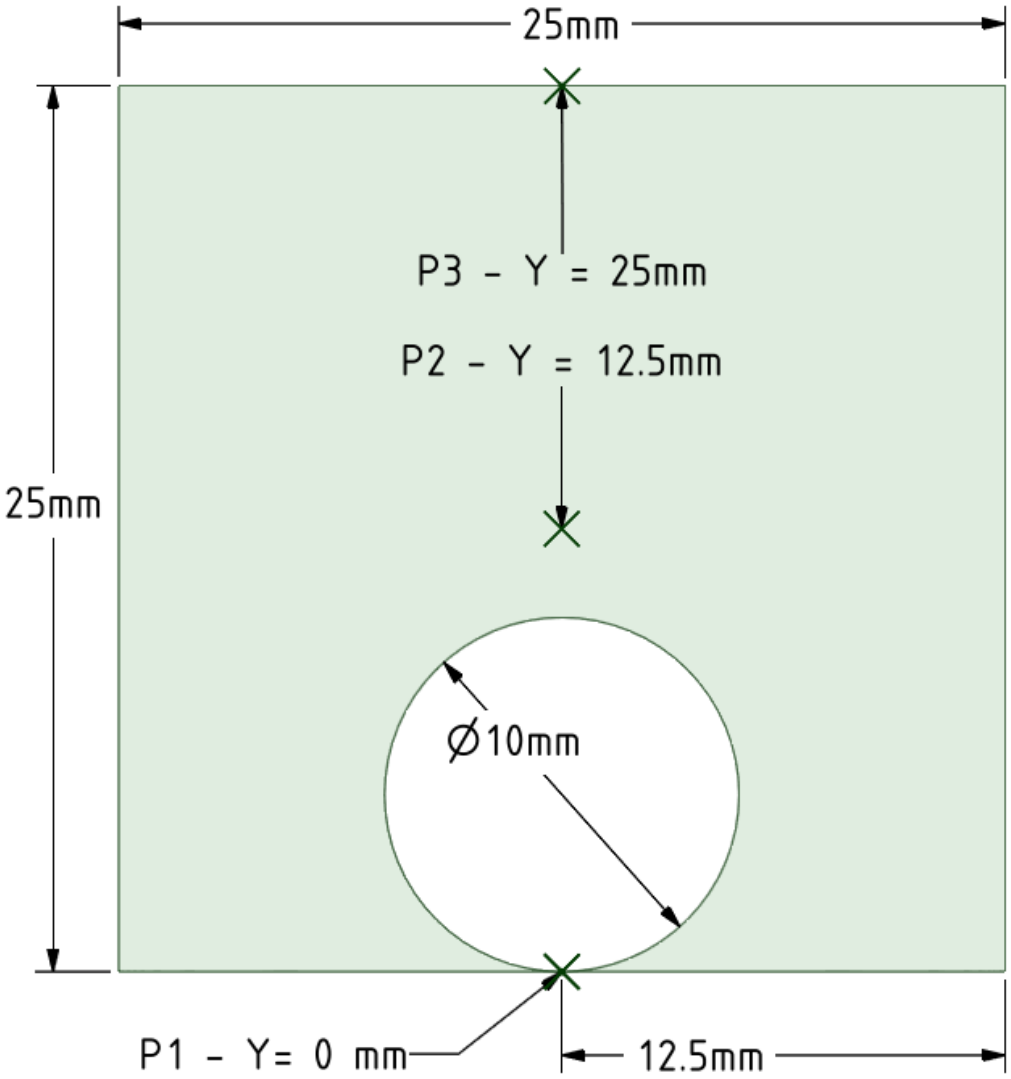

(b)

Figure 68 - 2D rectangular computational domains with varied x dimensions (a) 100 mm (b) 25mm and pipe placement on the bottom surface for investigation of underfloor pipe heated storage utilizing beeswax.

Figure 68 shows a schematic of the geometry used. The two vertical matched walls are connected to each other to allow crossflow and thus form a layer of infinite width. It is important to note that with the pipe configuration **this still results in a layer of infinite width and repeating pipes spaced by the domain width**. Heat is supplied by an isothermal 80 °C pipe surface.

These models were computed using Ansys 18.2 and utilized the same assumptions as previous models are made in this study with some modification:

The top and bottom wall is adiabatic to represent ideal insulation; (2) flow is Newtonian and incompressible; (3) flow is laminar and under the effects of gravity; (4) joule friction heating is negligible; (5) physical properties are temperature dependant and accounted for using the

linear multi-point data entry method for materials properties; (6) heat transfer occurs by conduction and convection only; (7) volume change is ignored; (8) three dimensional convection is ignored.

The following initial and boundary conditions are applied:

- Bulk Temperature - 25 °C.
- Pipe wall temperature - 80°C.
- Top and bottom walls – adiabatic.
- Side walls are matched and allow flow to pass in between.
- X Velocity – 0 ms^{-1}.
- Y Velocity – 0 ms^{-1}.
- Gauge Pressure – 0 Pa.
- Gravity – on, set at -9.81 ms^{-2}

At time $t \geq 0$ the mushy constant value is set as:

$$C = 100{,}000$$

5.2.1 Thermo-physical properties:

The thermo-physical properties of paraffin wax and beeswax are listed in chapter 3 with values in Table 7 and Table 8 and previously experimentally determined densities listed in chapter 3 in Table 6. Where appropriate, linear interpolation of temperature dependant values for material characteristics has taken place.

5.2.2 Solution Method and Controls:

For the numerical solution of the model the previously given methods and controls were utilized and PC 1-3 and Super Compute Cluster 2 were utilized for computation (details of machine hardware and solution methods/ controls given in chapter 2).

5.3 Results and discussion – Variation of X Dimension length

In this section, the results of the varied x dimension length pipe models are presented, discussed and compared in terms of the melt, heat rate and relevant dimensionless numbers. The same model settings as previously used in the bottom wall heated configuration with mesh l;curvature compensation turned on were utilized resulting in 55,000 cells in the base case,

with proportionally increased numbers of cells for each larger domain, was used for the analysis.

5.3.1 Evolution of Melt (time)

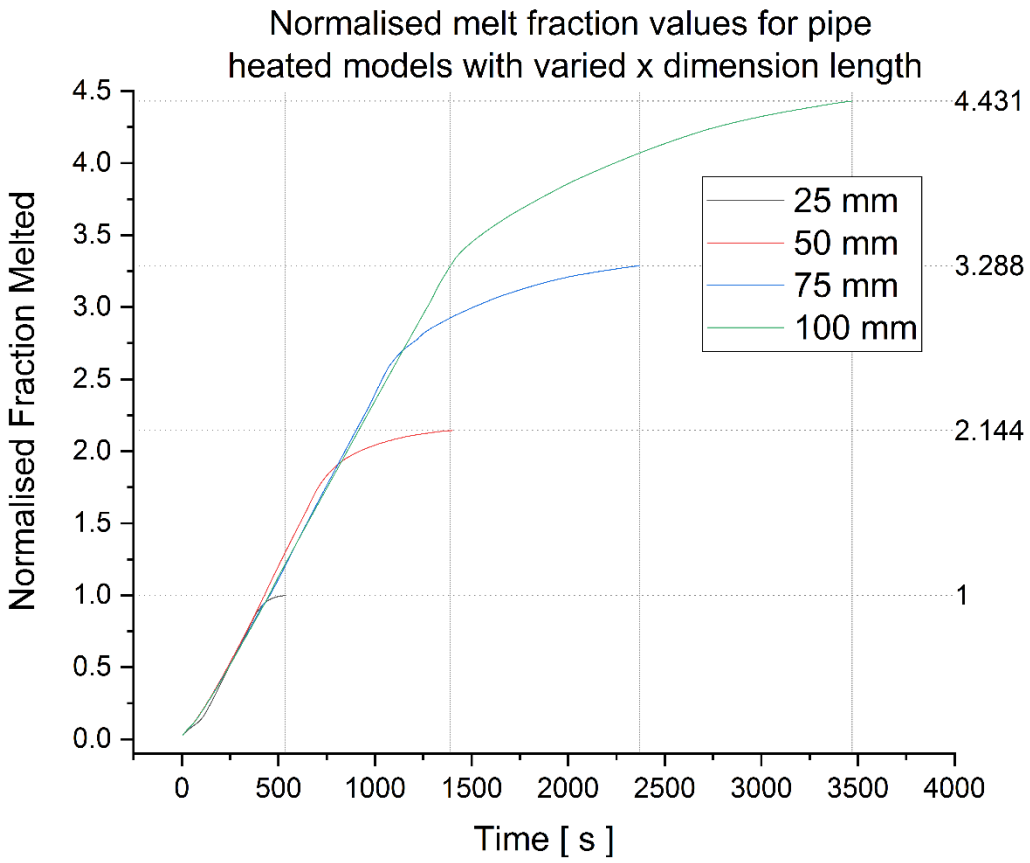

Figure 69 - Normalised melt fraction over time curves for varied x dimension models.

Figure 69 has been normalised by the relative volume to be melted in each model (546.46 mm^2, 1171.46 mm^2, 1796.46 mm^2 and 2421.46 mm^2 giving a ratio of 1, 2.144, 3.288 and 4.431 respectively.) As can be seen, the time of melts are as follows: 25mm at 535s, 50mm at 1390s, 75mm at 2370s and 100mm at 3470s which reflects a non-linear increase in time related to the volumetric increase in material. The time of melt expected for a volume related linear relationship would be 1147s, 1759s and 2370s for 50mm, 75mm and 100mm respectively.

Comparing the melt time of the 25mm pipe model to the previous chapter models shows the pipe configurations superior melt time compared to the flat plate configuration (535s and 800 seconds respectively.) This should be expected as the pipe model has both a larger heat transfer surface (25.7% larger at 31.42 mm versus 25mm) and a reduced amount of material to melt due to the presence of the pipe (the flat plate has ~15% more material). The 25mm

pipe model agrees well with linear factoring of ratio of heat transfer surface and reduced material result: a predicted melting time of the pipe model of approximately 544 seconds.

It is easily seen that the latter stages of every varied x dimension model slow down dramatically as convection can no longer melt portions directly adjacent to the pipe as easily as above. At this point conduction takes over as the melting method for these adjacent areas causing the flattening of each curve at the end of the melt process. The increasing amount of conductive melting for each wider domain is the likely cause for this non-linear increase of melting time and the flattening effect of this conduction dominated melting can be seen in the latter portions of each model's melt process clearly in Figure 69 and Figure 70. Additionally, this can be seen in the power and Nusselt figures.

Figure 69 shows that initial melting rates from 0-100s are very similar, although as a melt is ongoing, the larger volume models will attain the previous smaller model's 100% charge faster, due to ongoing convection related melting where in contrast, the previous models will be dominated by conductive melting at the same time. This can also be seen in Figure 71.

The initial conduction for all models reaches a rate of ~ 0.22 % s^{-1} in Figure 71 followed by a reduction in rate associated with increasing thermal resistance as the material heats. The onset of convection can be seen as the peak in all models around 0.2 -0.3 % s^{-1} after the initial decreasing in rate and a trend of a reduced peaking rate is seen for increasing domain width.

The sudden rate increase at ~330 seconds for 25mm, ~600s for 50mm and subsequent models appears to be associated with the convective melt process reaching the top surface. As heat cannot move through the adiabatic top surface this is not unexpected.

Convection related melting is indicated by noisy sections and the following smooth sections are indicative of rising conduction dominated melting. This can also be seen in the average Nusselt values decreasing (Figure 81) and in Peclet diagrams when values are less than 1.

The sudden rate increase for 75mm at 1225 seconds appears to be related to a short lived Rayleigh cell instability but may indicate model convergence issues. This same time period shows an unstable rapidly varying average Peclet number on Figure 80.

All models developed similar structures and flow rates. This structure consists of one large convective cell directly over the heated pipe with the width of the convective cell widening with the increasing domain width as can be seen in Figure 75 and Figure 76. Initial stages of the melt show the convective cell structure progressing toward the top surface with little sideways melting which can be seen in Figure 72 and Figure 73.

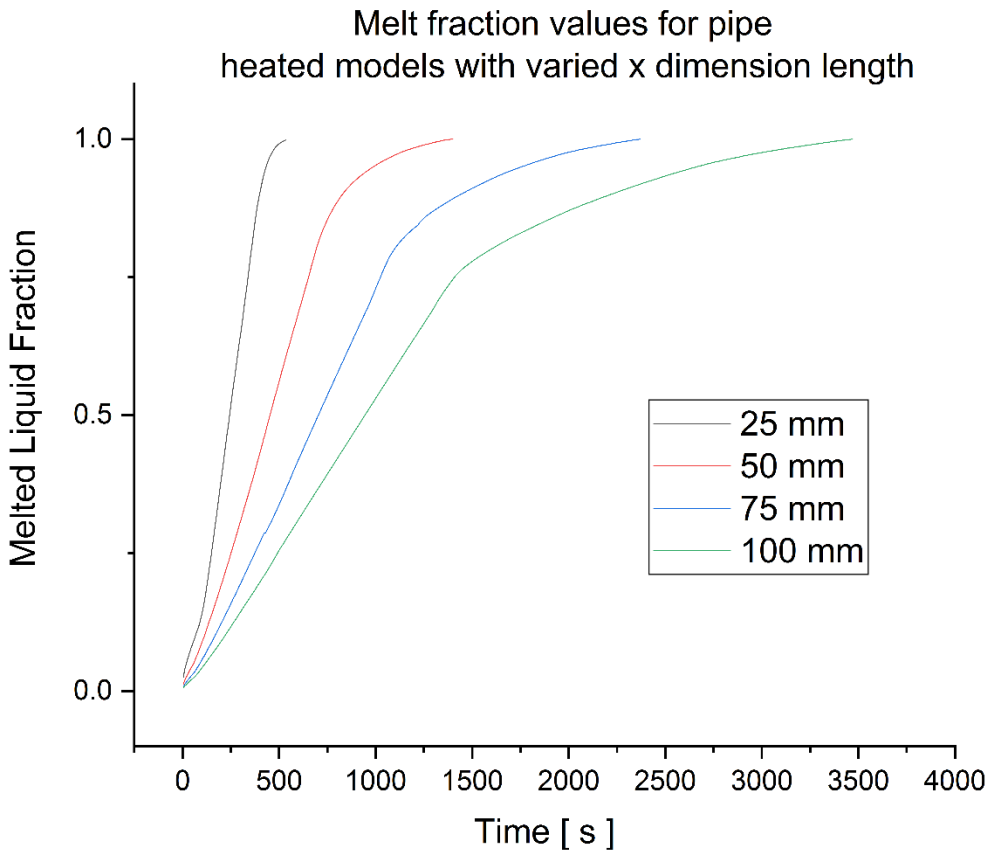

Figure 70- Melt fraction over time curves for varied x dimension models.

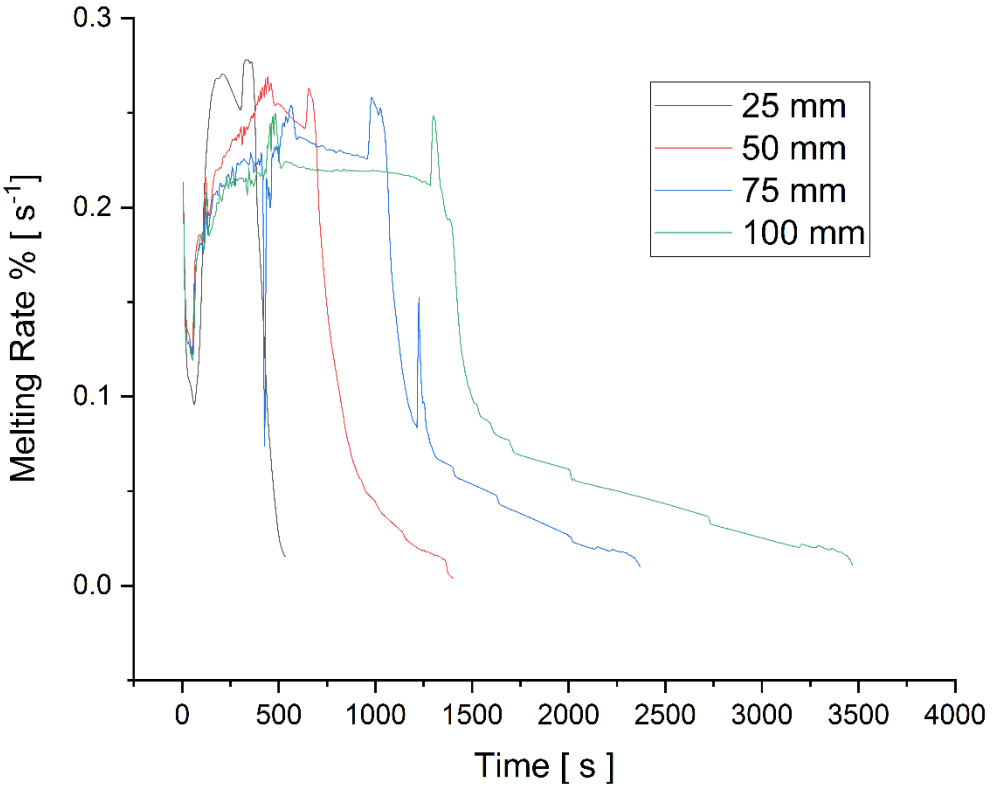

Figure 71 - Melting rate curves for varied x dimension models.

Once the melted material reaches the top surface, the convective cell then starts to widen and melt all material above the pipe which can be seen in Figure 75. The final stage of the melt process is characterised by a slow conductive melt process directly sideways from the pipe to melt the remaining material. Figure 74 is shown to demonstrate the cell flow structure, a central rising flow with two adjacent falling flows.

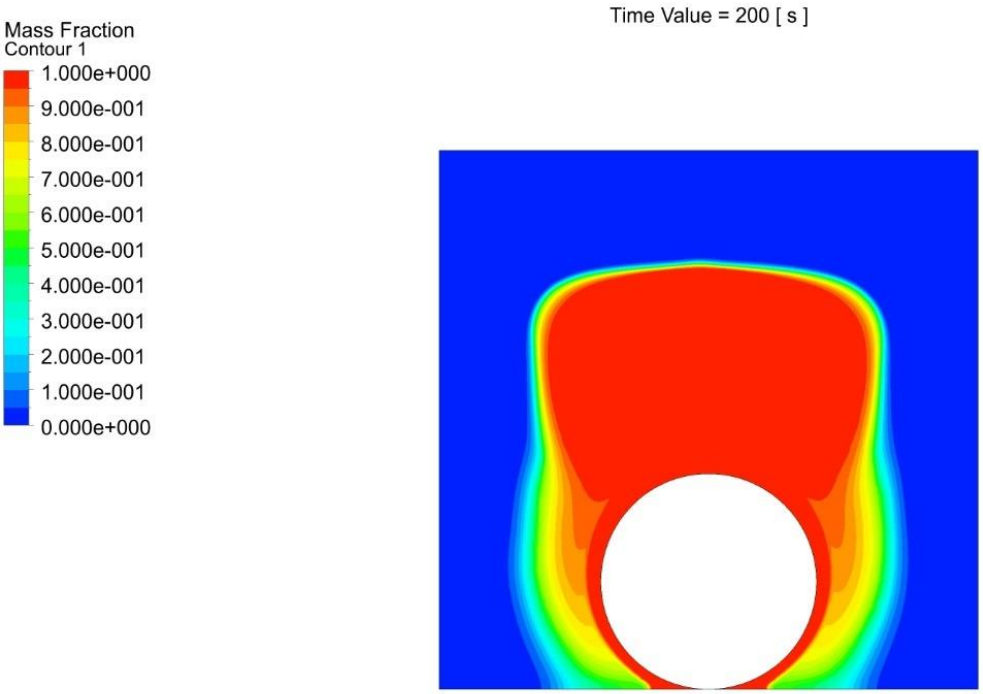

Figure 72 - Contours of melt fraction for 25mm x length bottom mounted pipe model at 200s.

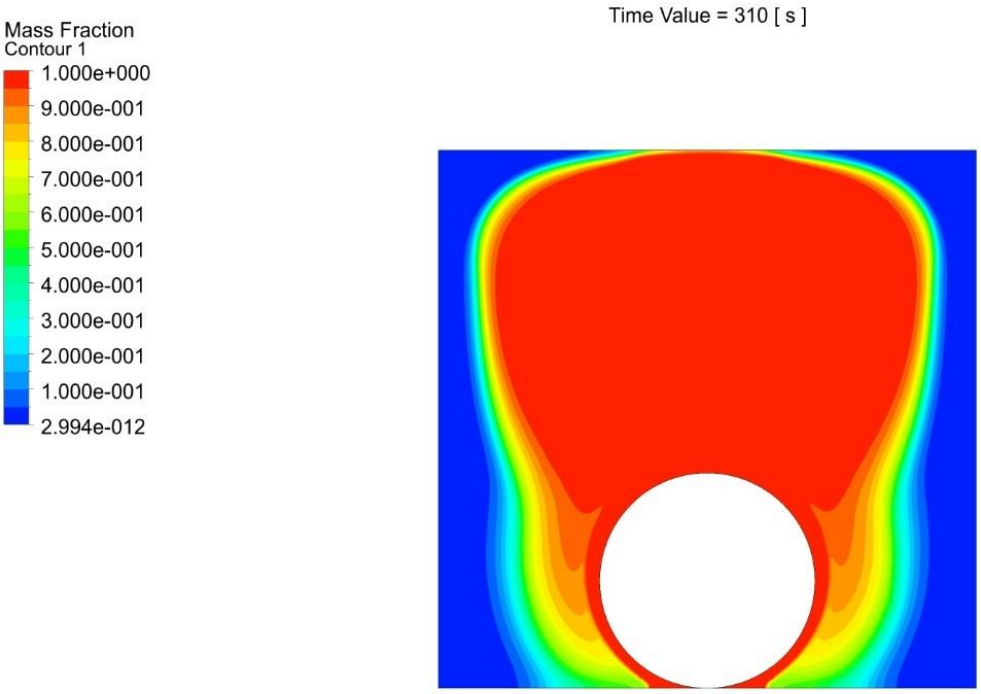

Figure 73 - Contours of melt fraction for 25mm x length bottom mounted pipe model at 310s.

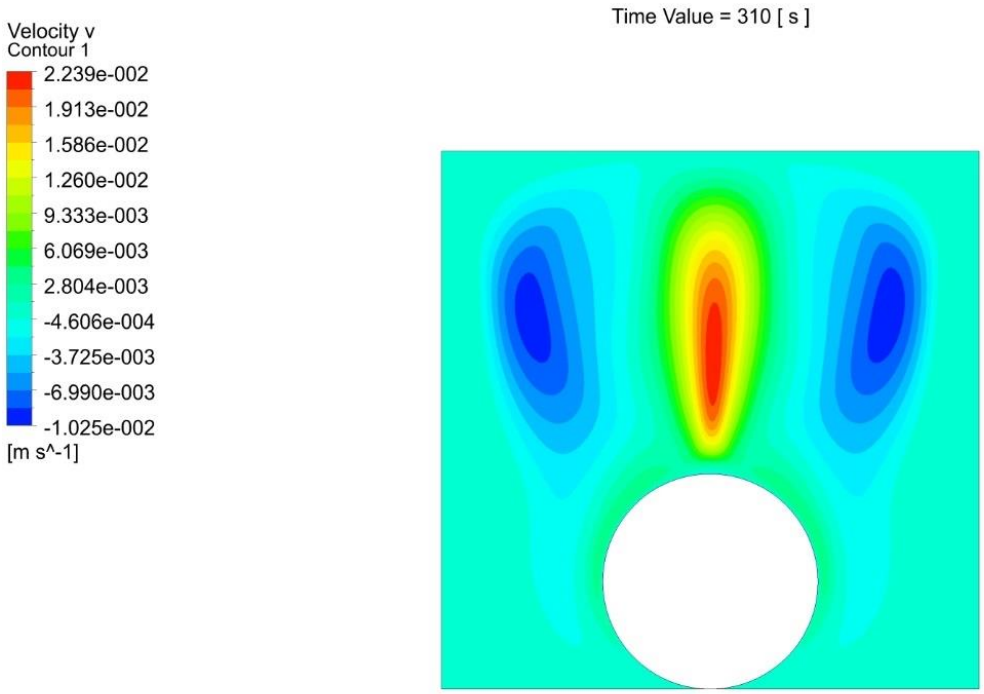

Figure 74 - Contours of Y velocity for 25mm x length bottom mounted pipe model at 310s.

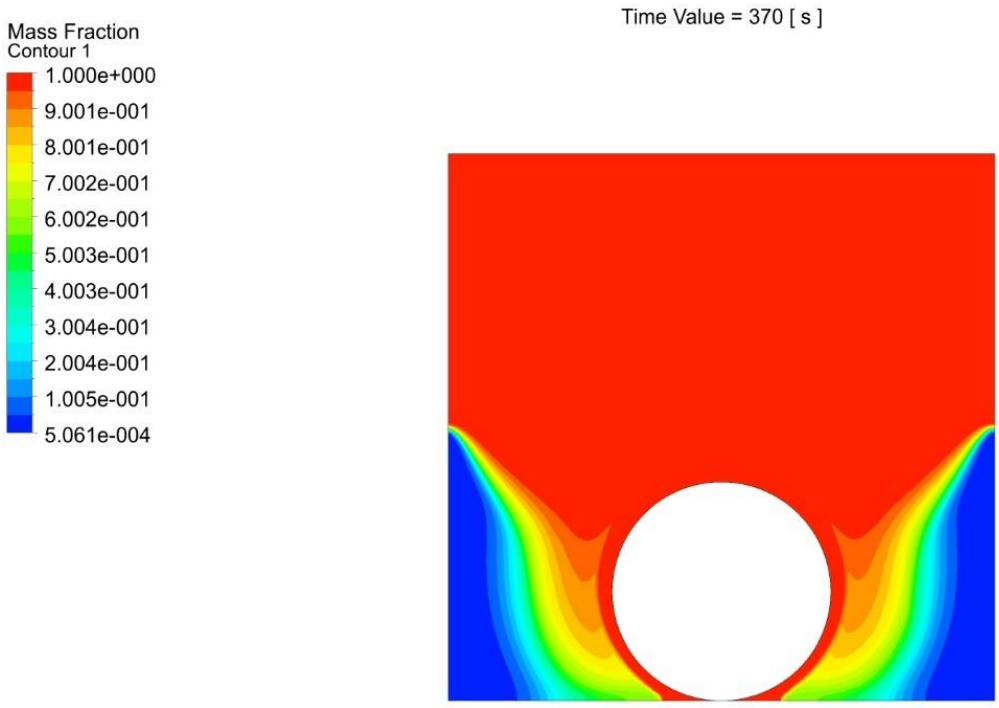

Figure 75 - Contours of melt fraction for 25mm x length bottom mounted pipe model at 370s.

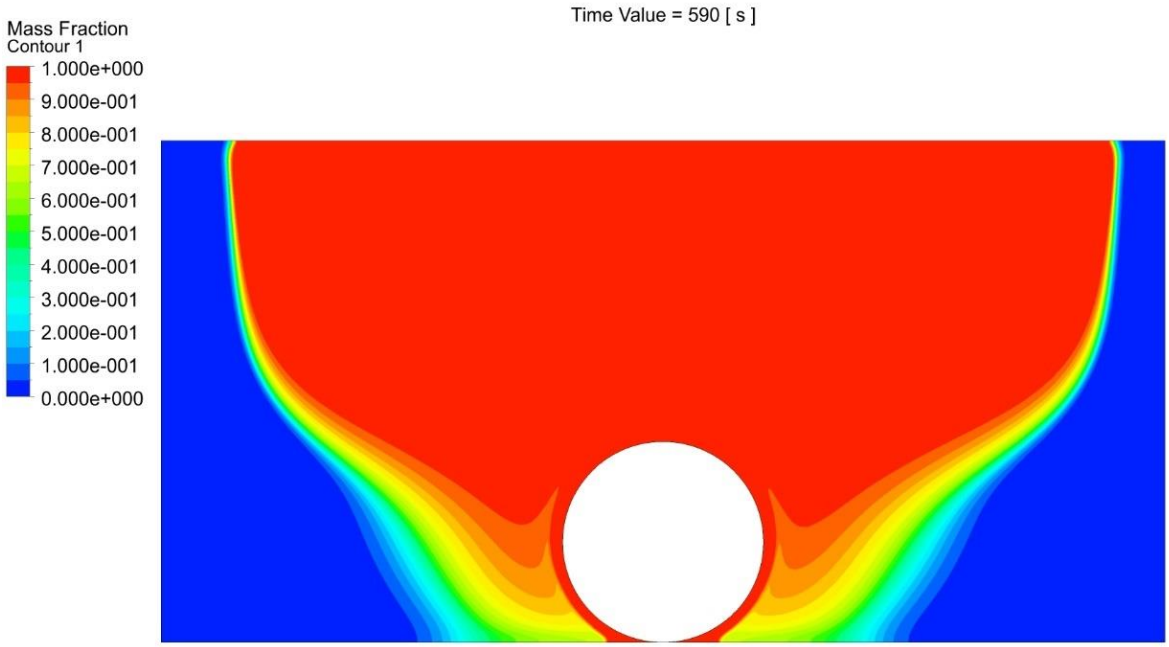

Figure 76 - Contours of melt fraction for 50mm x length bottom mounted pipe model at 590s.

5.3.2 Heat transfer power and convective heat transfer coefficient

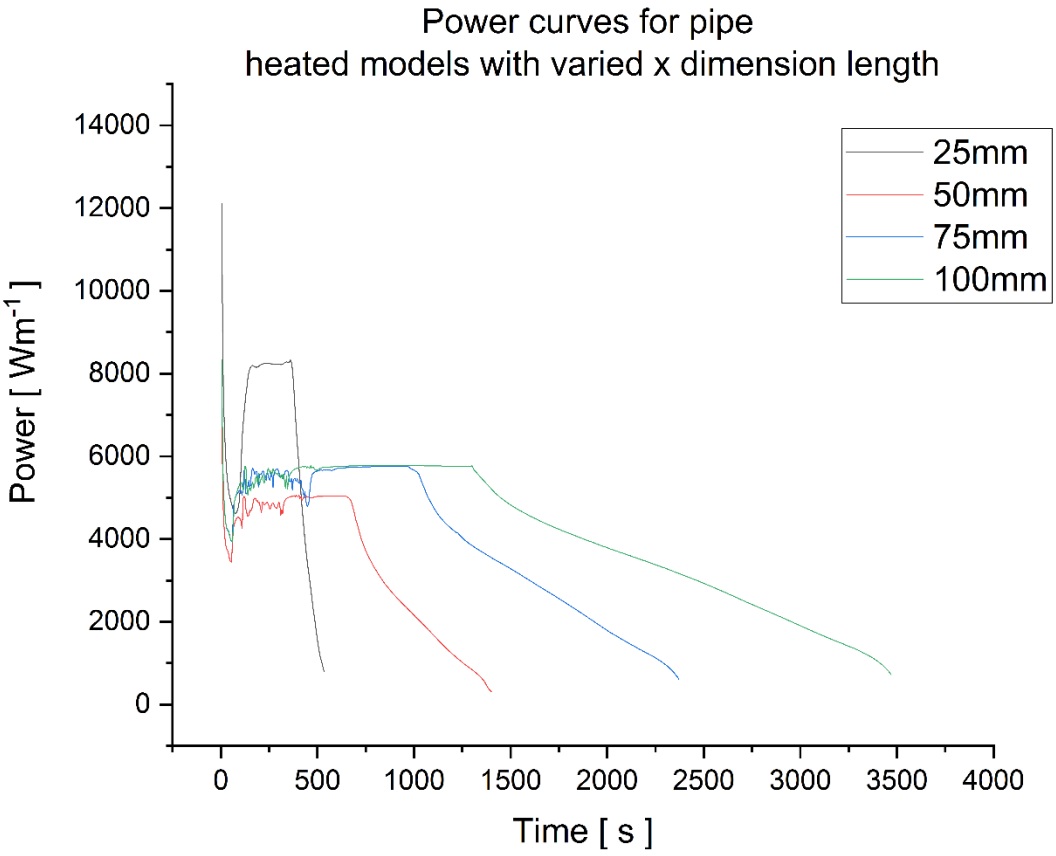

Figure 77 - Power curves over time for varied x dimension models.

For this analysis the CFD Post software has been used to calculate and average power value from the entire pipe interface with the phase change material.

Figure 77 shows a pattern of the smallest domain volume giving the highest power, 50 mm the lowest power and 75 mm being slightly larger than 50mm. This is an interesting result as this implies that the geometrical configuration results in a complex interplay of both thermal transfer and flow. This may also be attributed to reduced amounts of conduction due to the smaller domain with relatively more convection.

A very similar pattern for each model is observed with a large initial conduction driven value around 12000 Wm^{-1} which then drops to a minimum as thermal resistance increases as material heats. This is followed by the onset of convection then increasing the value again. The peak value is largest for 25mm ~ 8200 Wm^{-1}, 75mm ~5700 Wm^{-1}, 100mm ~5700 Wm^{-1} and 50mm ~4700 Wm^{-1}. The curve is a little noisy during the convective portions before the curve flattens with melting becoming gradually more conduction dominant. This is then followed by a smooth linearly decreasing section which is attributable to a conductive melt as the remaining material at this point is adjacent to the pipe leading to little convective melting. This decrease is associated with the increasing thermal resistance in conduction processes as the adjacent material warms and in this case melts. The elongation and flatter decreasing tail sections of these configurations is associated with the increasing domains width as this results in more material and time to melt in addition to more adjacent material that must melt.

The convective heat transfer coefficient curves in Figure 78 show a similar pattern to the power curves with an initial spike to ~ 250 $Wm^{-1}K^{-1}$ for the 25mm configuration and 150 $Wm^{-1}K^{-1}$ for the other configurations. This initial spike is followed by a rapid decrease and then a subsequent increase associated with the onset of convection. All configurations have this onset around 50 seconds with a rapid increase, smooth for 25mm and a little noise for the other configurations. The values peak at ~735, 400, 410 and 390 $Wm^{-1}K^{-1}$ for 25, 50, 75 and 100mm respectively.

The convective process shows a noisier signal where in contrast, conductive heat transfer becomes more dominant in the later smooth decreasing section of the curves and is associated with melting material adjacent to the heated pipe.

The perceived stretching along the time axis of the larger x-dimension models in the smoother more conduction dominated sections of the curves, is again associated with increased domain width and increasing amounts of material adjacent to the heated pipe to be melted by a more conductive dominant process.

A very interesting feature of this figure is that the 50mm model demonstrates the lowest second peak convective heat transfer value. It is believed that may be due to the greater

distance between the pipes leading to sub-optimal flow guidance, without the relative decrease in competition for heat transfer between adjacent pipes in the larger x-dimension models.

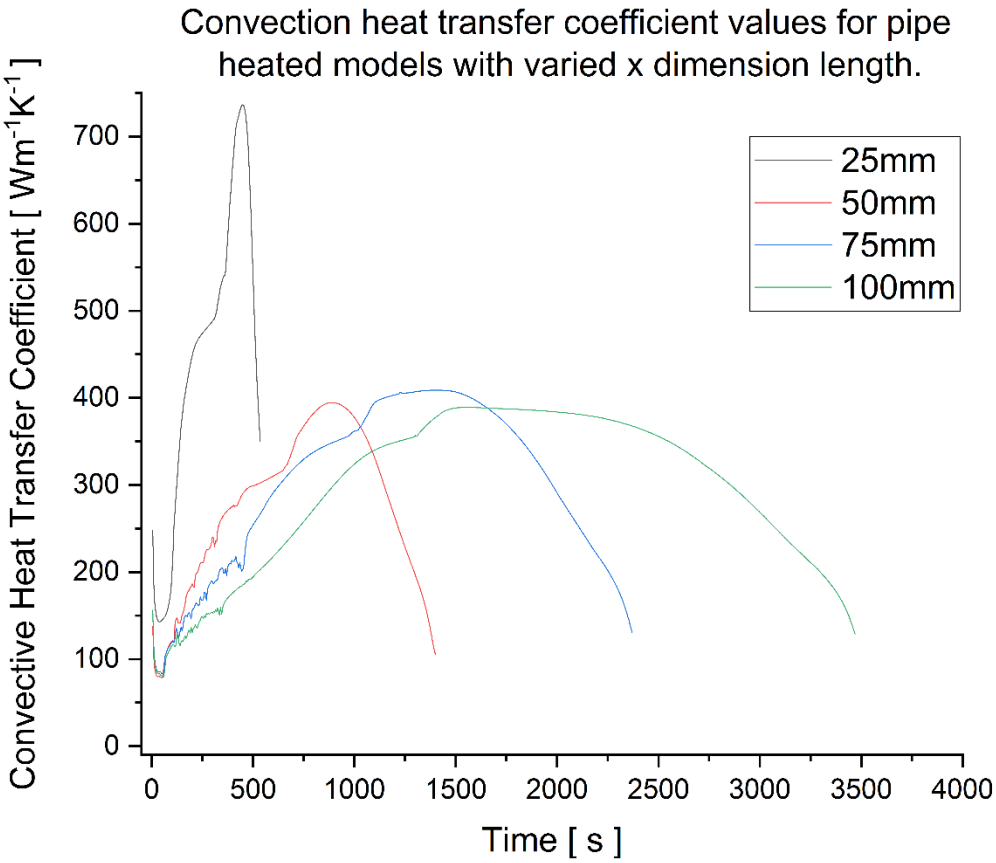

Figure 78 - Convective heat transfer coefficient curves for varied x dimension models.

With the larger domains there are significantly larger volumes of material in the bulk which will reduce the bulk temperature over the melting process. In addition, with the larger domains a single pipe has access to significantly more material to convect between itself and a neighbouring pipe which may lead to the slightly increased value of heat transfer coefficient for the 75mm and 100mm configurations.

5.3.3 Rayleigh Numbers

For this analysis, the average Rayleigh number has been calculated as follows [3]:

$$Ra = GrPr \tag{21}$$

$$Gr = \frac{g\beta(\tau_S - \tau_\infty){L_h}^3}{\nu^2} \tag{22}$$

Where $\beta_{Beeswax}$ =0.004170747 and L_H =0.010 (m) but would usually be the ratio of horizontal plate area to plate perimeter in 3 dimensions. In this case it has been assumed to be the 2D hot surface length [4].

The CFD Post software has been used to perform these calculations and then determine the average value across the whole pipe surface. This is intended to give a better comparison when considering the latter investigation of differing pipe positions.

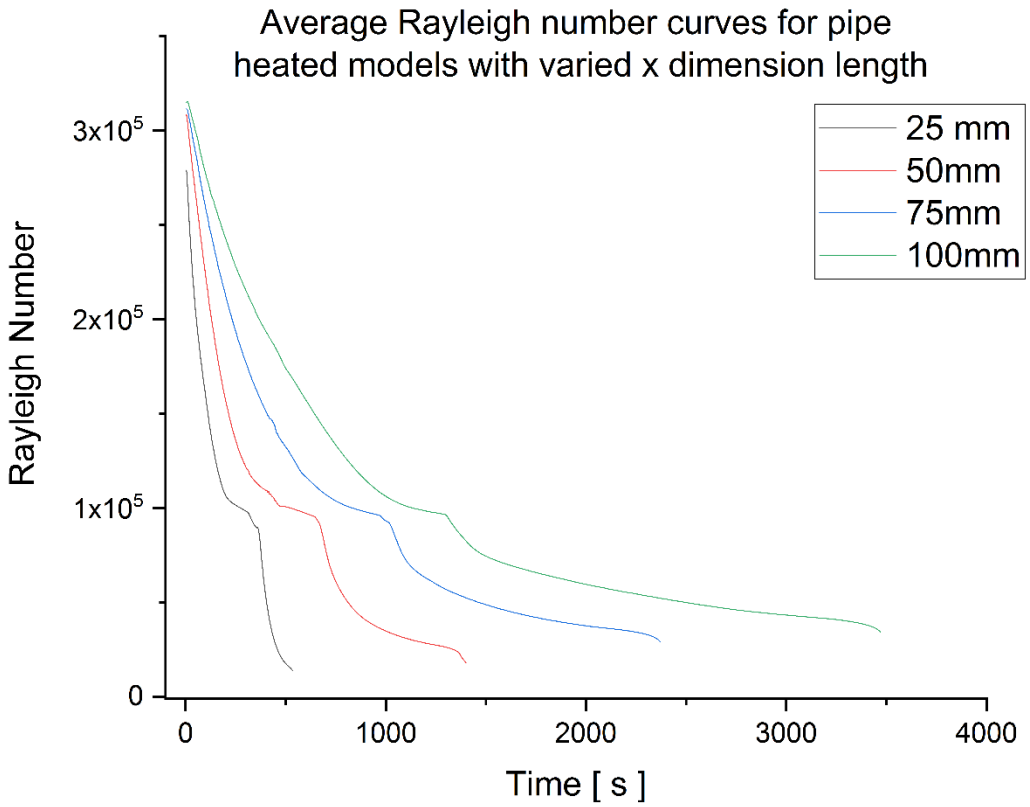

Figure 79 - Average Rayleigh number curves for varied x dimension models.

Figure 79 shows the average Rayleigh number values for the varied domain width models and has a number of interesting features. Where 50mm,75mm and 100mm have an initial value around $3x10^5$ the 25mm model has a value of $2.8x10^5$. These values are significantly above the critical value (Ra > 1700 [123]) indicating convection.

Each model shows a distinct decreasing value before a slight plateau (around $1.5\ x10^5$) where convection is ongoing, followed by another now exponentially decreasing value, until melt completion. This latter regime is associated with material adjacent to the pipe now primarily melting via conduction.

As the domain width increases, the curves of these models are stretched along the time axis to their increased total melting time. This is likely due to the significant increase in material to melt with both convective and conductive melt regimes elongating.

Another feature of these curves is a very similar range of values, with the exception of the increased value at completion, compared to smaller domains for larger domain widths. This again is expected to be as a result of larger amounts of melted material now undergoing convection having had a longer time scale to develop. The turbulent regime (transition occurs near 10^7 [124]) like previous models is again, not present.

Compared with the Rayleigh values found in the previous chapter for the flat plate configuration, it is seen that the value has decreased by an order of magnitude. This is interesting as the lower the value indicated, the further away it is from the turbulent convective regime, indicating this geometrical configuration is the cause.

When comparing the Rayleigh curves with other figures such as power, Peclet and Nusselt number curves, there is a good agreement with features.

5.3.4 Peclet Numbers

For this investigation, the Peclet number has been calculated using the CFD Post software and then an average value across the whole domain has been calculated for each time step.

$$Pe = RePr \tag{23}$$

Figure 80 shows that all models start at an initial value of zero, then rising to different peaks of 0.432, 0.291, 0.263, 0.235 for 25mm, 50mm, 75mm and 100mm respectively. These different values are likely a result of the increased volume of material with the domains reducing the average.

All curves follow a similar pattern with noisy peaks associated with the convective process before values smoothly exponentially decrease due to conductive melting with exception to the 25mm configuration.

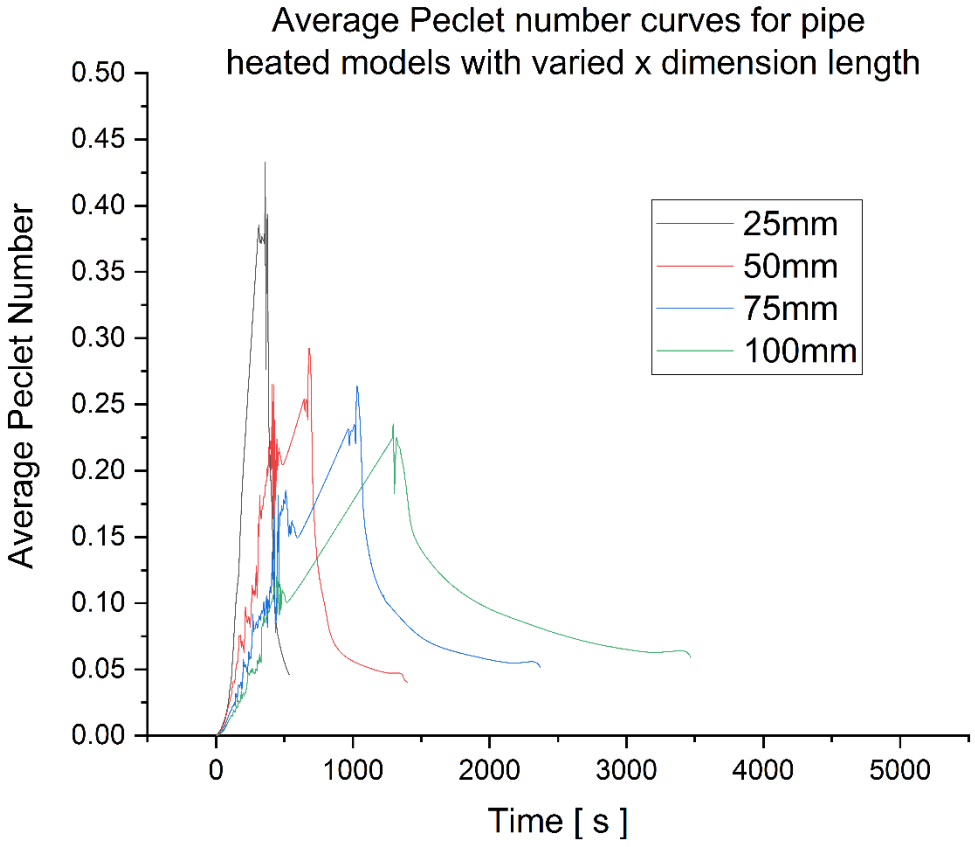

Figure 80 - Average Peclet number curves for varied x dimension models.

This smooth decrease is due to the melting material adjacent to the hot pipe melting primarily by conduction, with wider domains associated with more material conductively to melt, both decreasing the peak while flattening and lengthening the curves as they decrease. It is noteworthy that the wider domains finish their melt with a larger Peclet number; however this is almost certainly attributable to larger bodies of liquid material convecting when the melting process completes.

5.3.5 Nusselt Numbers

As the specified configuration is one of a heated pipe, coupled with the values of Rayleigh number, the Nusselt number correlation utilized is the following [3]:

$$Nu = \frac{2C_{cyl}}{ln\left(1 + \frac{2C_{cyl}}{0.772C_{lam}\,Ra^{0.25}}\right)} \tag{24}$$

Where:

$$C_{lam} = \frac{0.671}{\left[1 + \left(\frac{0.492}{Pr}\right)^{9/16}\right]^{4/9}} \tag{25}$$

$$C_{cyl} = 0.8$$

$$1 \times 10^{-10} < Ra < 1 \times 10^{10}$$

In addition, for this analysis the average values have been calculated from the whole pipe surface.

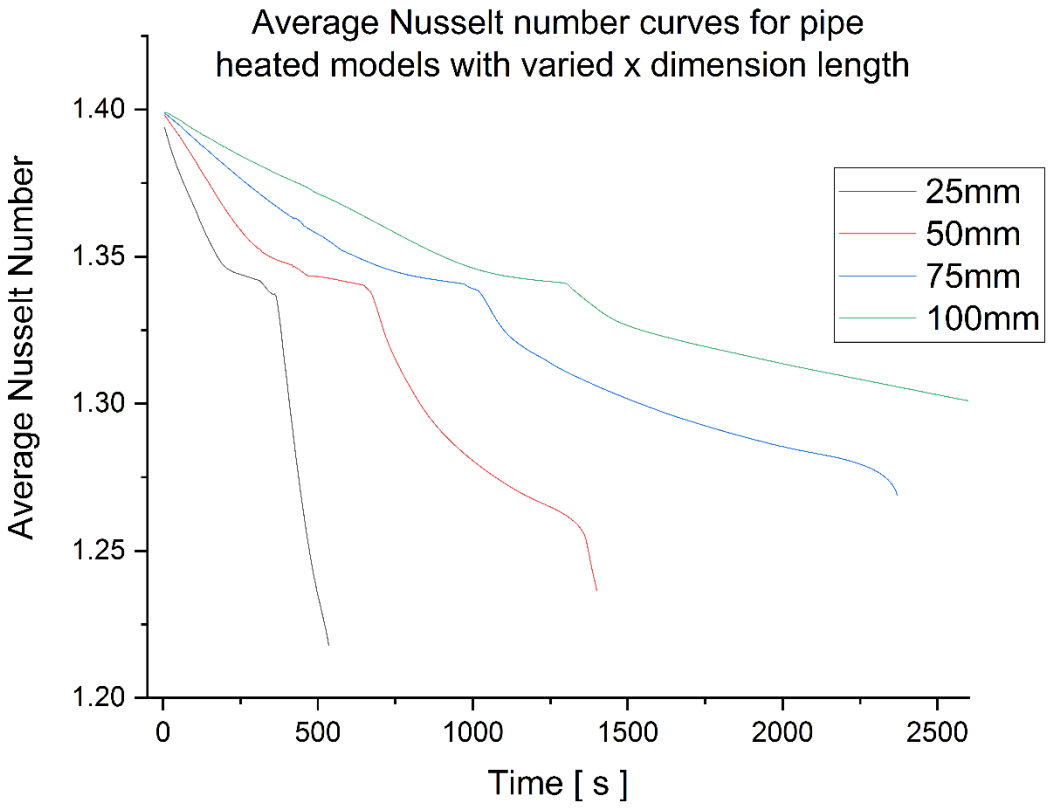

Figure 81 – Average Nusselt number curves for varied x dimension models.

Figure 81 shows curves of average Nusselt number and agrees well with the other dimensionless analysis – convection and conduction dominant areas can be seen by the discrete value reductions.

All varied width models begin with values ~ 1.40 before they steadily decrease and plateau around 1.35. For the 25mm model it then shows a slight decrease is visible from 200 seconds to 345s before the rapid decrease indicating the start of increased conduction associated with the melting of material directly sideways from the pipe until completion at 535s. A similar pattern is found in the other models; however the curve is stretched over their full melting times. This increase in melting time and stretching is associated with increasing amounts of material adjacent to the heated pipe and thus time to be melted using conducted heat travelling sideways, in addition to more material available for convection to take place.

Nusselt number values calculated using the convective heat transfer coefficient for these models are found to be in the range of 2 - 18 and follow the same curve profiles as the plot of convective heat transfer coefficients. This may indicate that the approximation used (Equation 24/25) may not be appropriate for this case.

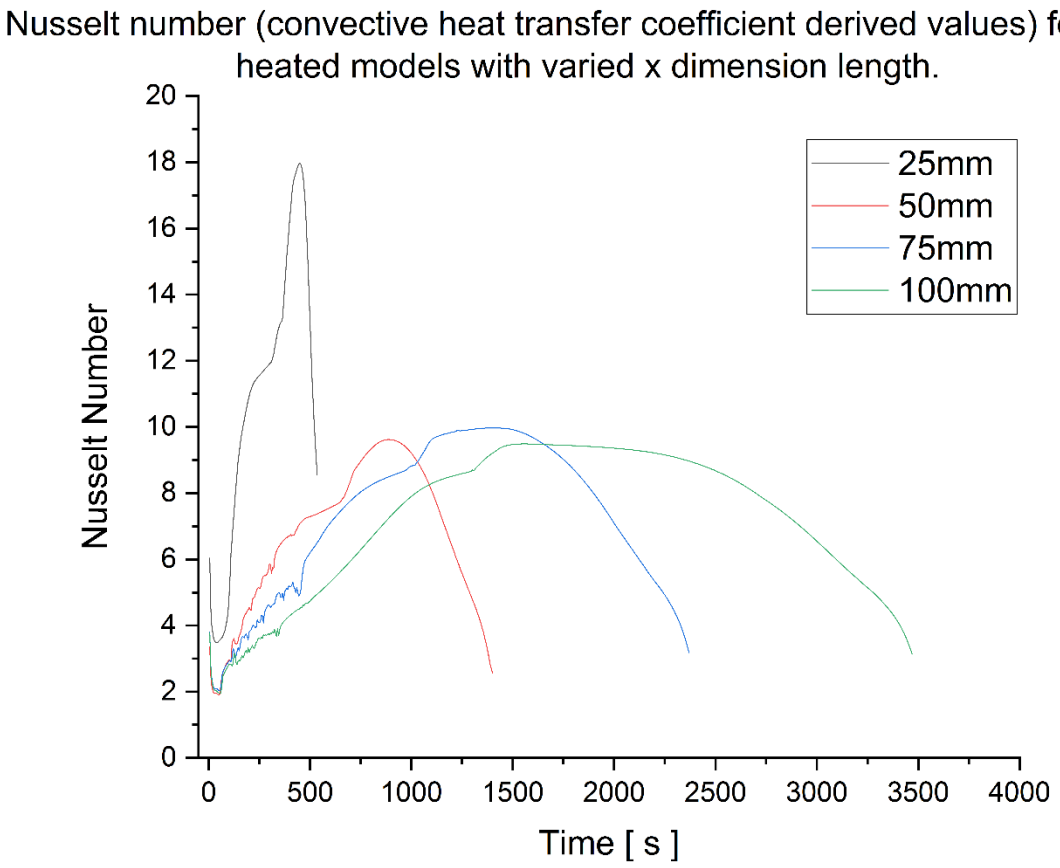

Figure 82 – Heat transfer coefficient derived Nusselt number curves for varied x dimension models.

5.4 Results and discussion – Variation of pipe location

In this section, the results of the pipe models are presented, discussed and compared in terms of the melt, heat rate and relevant dimensionless numbers. The same model as previously, with 55,000 cells in mesh resolution, was used for the analysis.

5.4.1 Evolution of Melt (time)

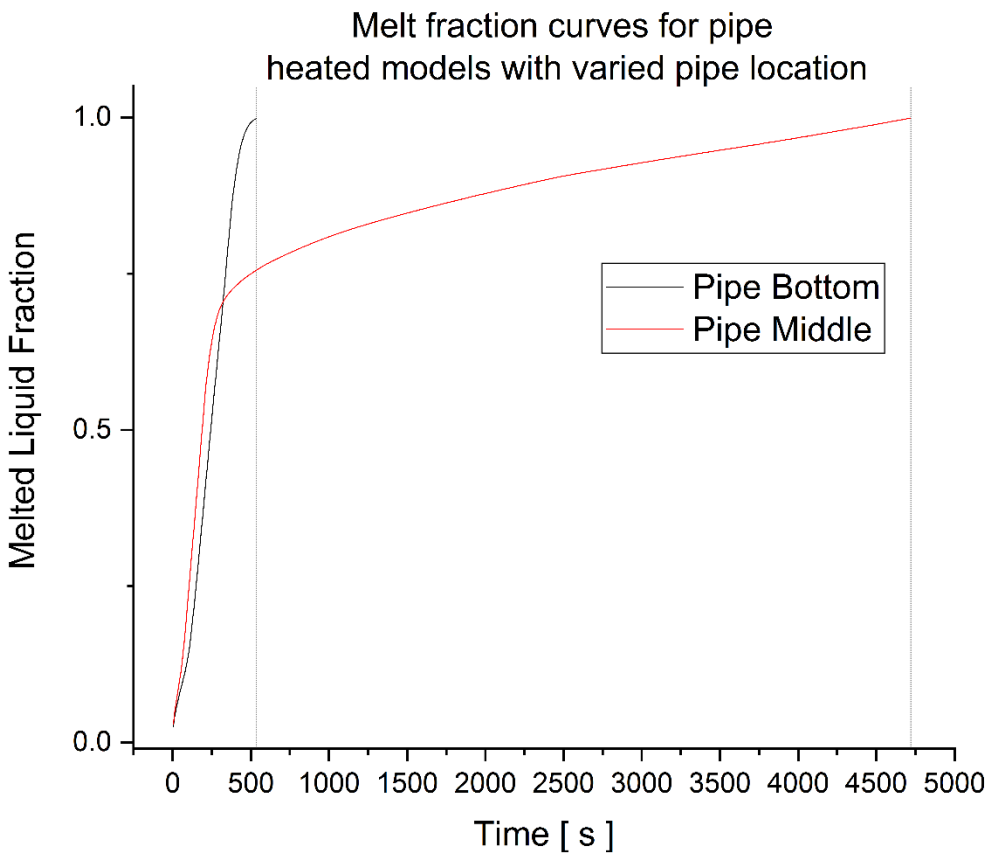

Figure 83 – Melt fraction curves for varied pipe location models.

The melt time is determined as 535s and 4720s for the bottom and middle configurations as seen in Figure 83. It is clear that the geometrical placement within the domain is a critical factor in the performance of the system and that locating the pipe at the bottom of the domain is advantageous as a result of prolonged convection across the whole melt process. This contrasts with the middle configuration where the material below the pipe is melted via conduction only.

The onset of convection is not easy to see in Figure 83; however the transition to conduction dominant melting for the middle configuration is indicated by the exponentially decreasing curve shape. Resolving the onset of convection is more easily seen in Figure 84.

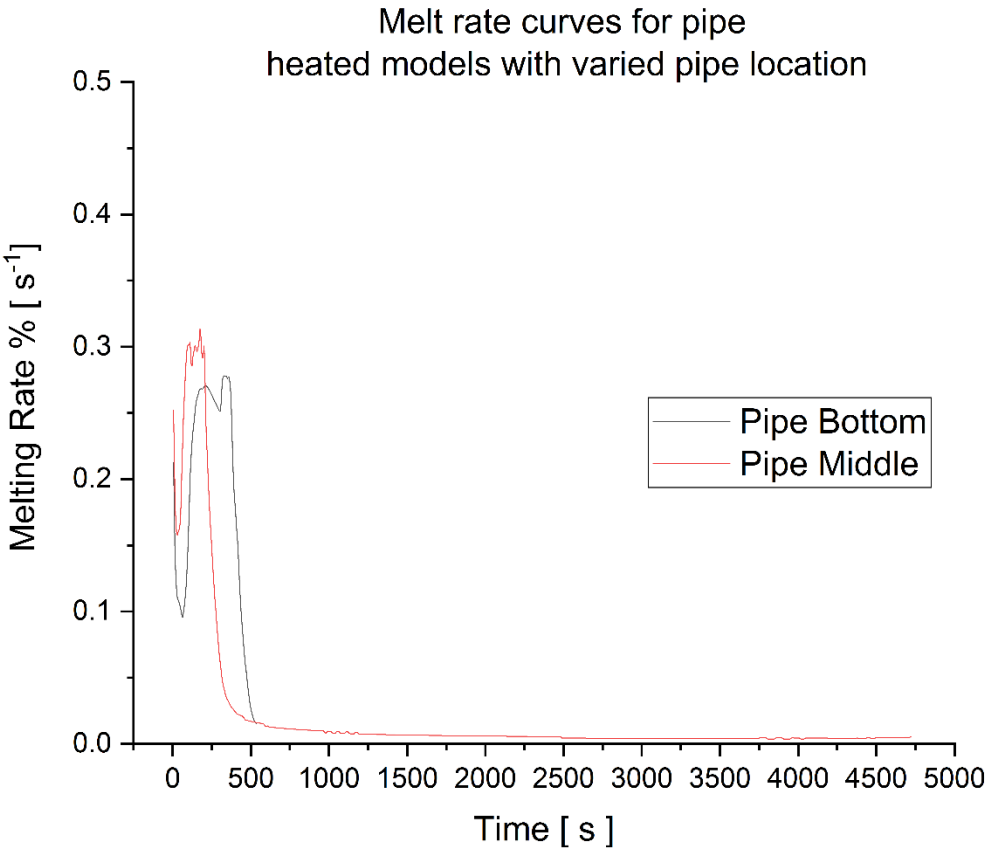

Figure 84 - Melt rate curves for varied pipe location models.

Figure 84 shows that initial rates are very similar, with initial values of ~0.2 % s^{-1} for the pipe at the bottom and ~0.25 % s^{-1} for the pipe situated in the middle. This is not unexpected as conducted heat from the middle pipe will be distributed to more material. Subsequently, both configurations reduce dramatically, to ~ 0.16 % s^{-1} and 0.1 % s^{-1} for the middle and bottom configuration respectively, again with more material available for heat to be directly conducted into, the larger value for the middle configuration is expected. For both, convection then begins and increases the values significantly, at 60s and 30s for the bottom and middle configuration respectively. The delayed onset for the bottom configuration is expected due to flow restriction at the bottom of the pipe reducing the magnitude of convection. The middle configuration then peaks around 0.3 % s^{-1}, higher than the bottom configuration at 0.27 % s^{-1} again likely as a result of the flow restriction.

The behaviour for these models then deviates significantly, with the middle configuration maintaining a consistent value near 0.3 % s^{-1} while convection is ongoing but with a

subsequent dramatic rate reduction due to the melting becoming conduction dominant while material to the sides and beneath the pipe is only melted via conduction.

In contrast, the bottom configuration maintains a mainly convective process for the remainder of its melt process with the decrease and sudden peak at 345s attributable to the melted material in the convective cell finally reaching the top surface and beginning to spread out. This is also seen in the middle configuration at 160s and again is not unexpected as the top wall is adiabatic. The relative lack of a conductive melting dominant section in the bottom configuration results in a much faster melt time, less inhibited by the slow rate of conductive melting due to more convection being able to take place from the lower placement of the pipe.

Like the previous section, the latter stages of every model slow down dramatically as convection can no longer melt portions directly adjacent as easily as those above and conduction takes over as the melting method for these areas causing the flattening of each curve at the end.

The flow formation for the middle configuration is quite different than the bottom configuration as the central location acts as a buffer to the formation of the cell directly above and results in a single cell forming to the sides of the heated pipe. This can be seen in Figure 85, Figure 86, Figure 87 and Figure 88 compared to the bottom configuration in Figure 72, Figure 73, Figure 74, Figure 75 and Figure 76.

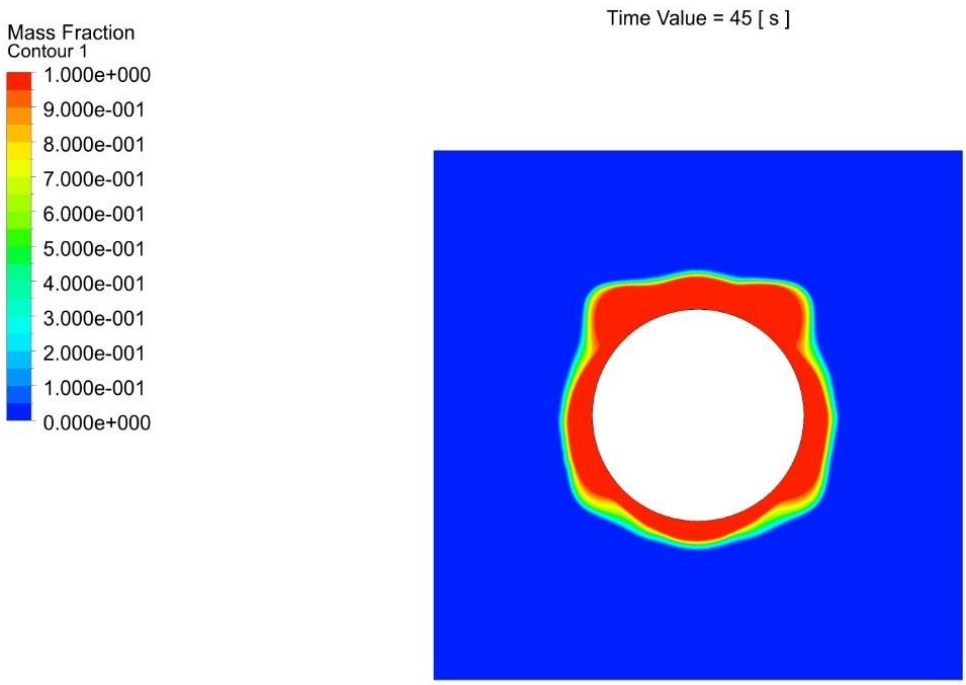

Figure 85 - Contours of melt fraction for middle mounted pipe model at 45s.

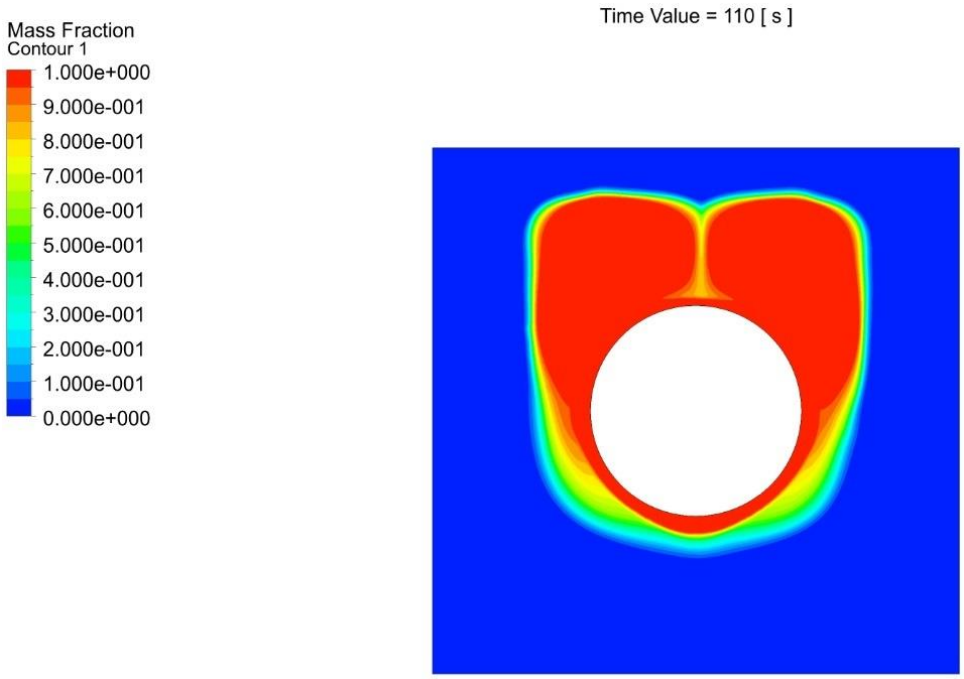

Figure 86 - Contours of melt fraction for middle mounted pipe model at 110s.

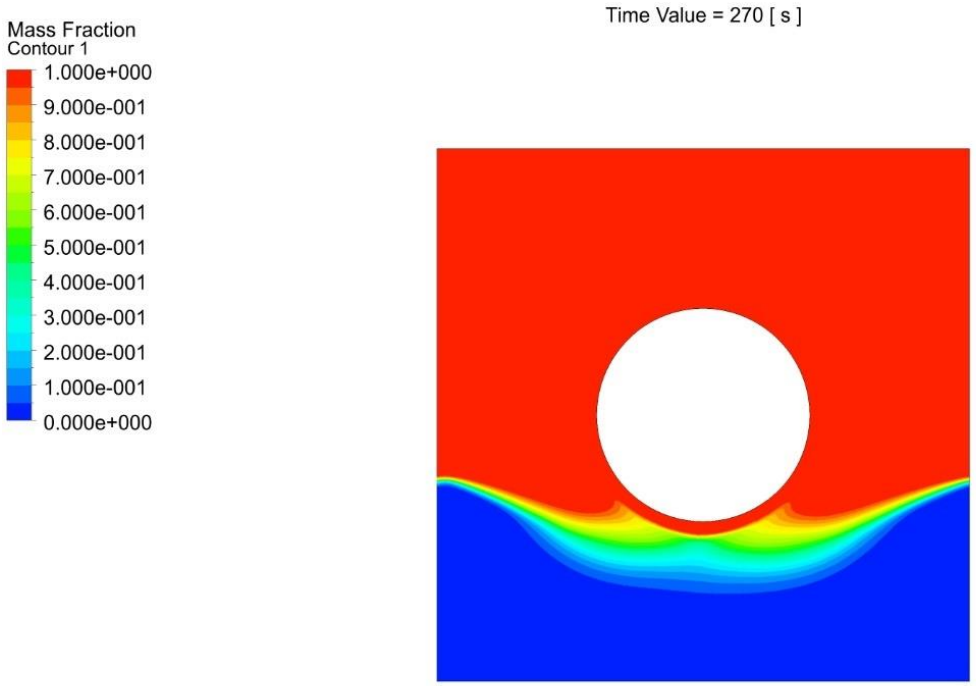

Figure 87 - Contours of melt fraction for middle mounted pipe model at 270s.

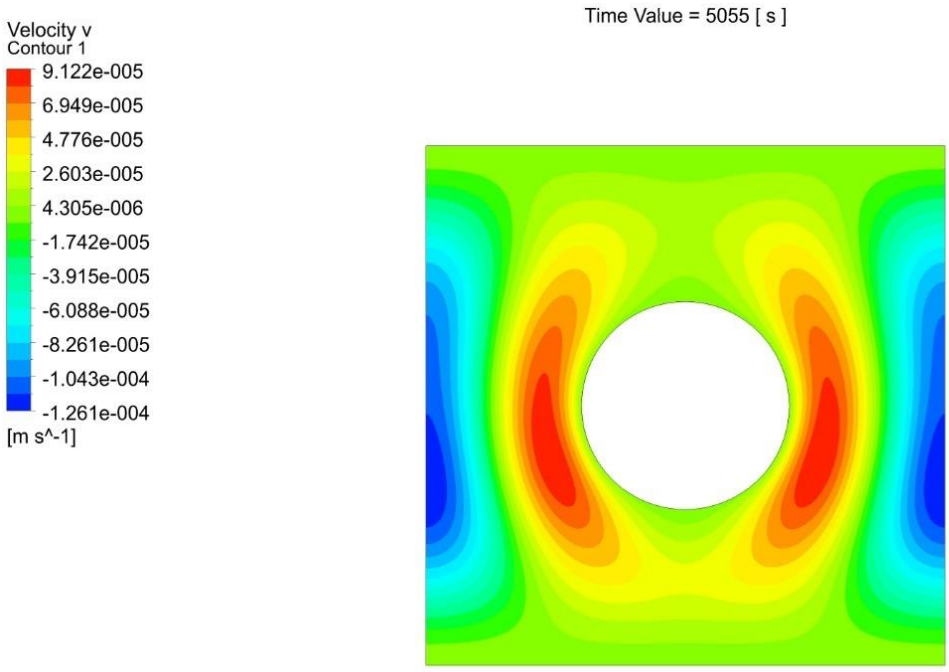

Figure 88 - Contours of Y velocity for middle mounted pipe model at 5055s.

5.4.2 Heat transfer power and convective heat transfer coefficient

Figure 89 shows the power curves for both models and the middle configuration has the largest power which is, however, not sustained due to the convecting material being unable to melt material below the hot pipe.

It is no surprise that a similar pattern to the previous Figure 77 is observed with a large initial conduction driven value around 17000 Wm^{-1} for the middle configuration and 12000 Wm^{-1} for the bottom configuration. This is likely due to conducted heat from the middle pipe being better distributed to more material.

These values then drop to ~8000 Wm^{-1} and 4600 Wm^{-1} (middle and bottom configurations respectively), followed by convection starting and increasing the value again. This value is largest for the middle configuration ~ 11000 Wm^{-1} and with the bottom configuration reaching ~ 8200 Wm^{-1}. Again, this value being increased for the middle configuration is not unexpected due to more advantageous conduction to more material but also to improved flow characteristics from not being sited at the bottom.

Both curves are a little noisy during the convective portions before the melting process becomes conduction dominant and the signal smooth.

The convective portions are followed by a smooth linearly decreasing section which is attributable to a conductive melt as the remaining material at this point is adjacent or **below**

the pipe leading to little convective melting. This decrease is also associated with the increasing thermal resistance in conduction processes as the material warms and melts.

This middle configuration is unlike the bottom configuration which only shows this reducing rate briefly at the end of the melt process as only material adjacent, not adjacent and below the pipe, needs to be melted via conduction. As a result of the mount location, the majority of the melt for the bottom configuration has taken place via convection which has resulted in the dramatically reduced time of melt.

The convective heat transfer curves in Figure 90 Figure 90 – Convection heat transfer curves for varied pipe location models.

show a similar pattern to Figure 78, with middle and bottom configurations showing large initial conductive spikes to ~365 $Wm^{-1}K^{-1}$and 250 $Wm^{-1}K^{-1}$ and both then rapidly decrease to ~265 and 145 $Wm^{-1}K^{-1}$ before the onset of convection. This can be seen as the increase to ~685 and 735 $Wm^{-1}K^{-}$ after the initial decrease for both configurations. These peak values are associated with the end of the convective melting process with only material adjacent or below the pipes. The small plateau / slight decreases then rapid increases at 125s and 280s for the middle and bottom configurations respectively, coincide with the melted material reaching the top surface of the domain. There is subsequent rapid decreasing rate to ~0 $Wm^{-1}K^{-1}$ for the bottom configuration until melt completion and similar rapid decreasing rate to a plateau of below 140 $Wm^{-1}K^{-1}$ in the middle configuration. Both are characteristic of when conductive melting becomes the dominant heat transfer process.

The continuing almost exponentially decreasing value to 0.03 $Wm^{-1}K^{-1}$ for the middle configuration is a result of increasing thermal resistance to conduction as the now fully liquid domain continues to increase in temperature.

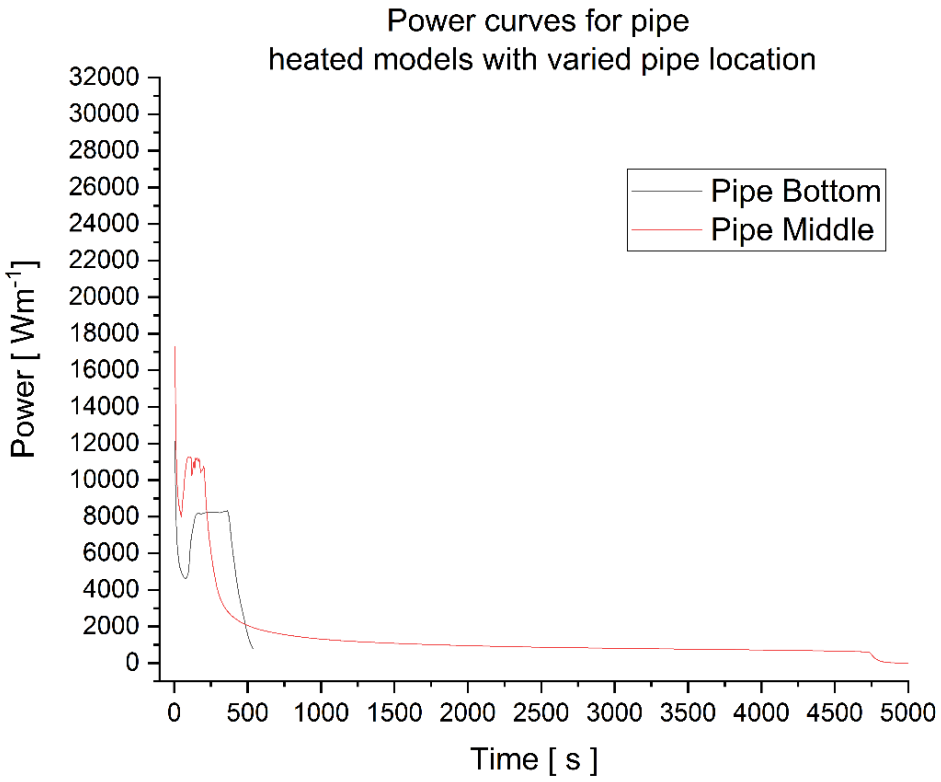

Figure 89 – Power curves for varied pipe location models.

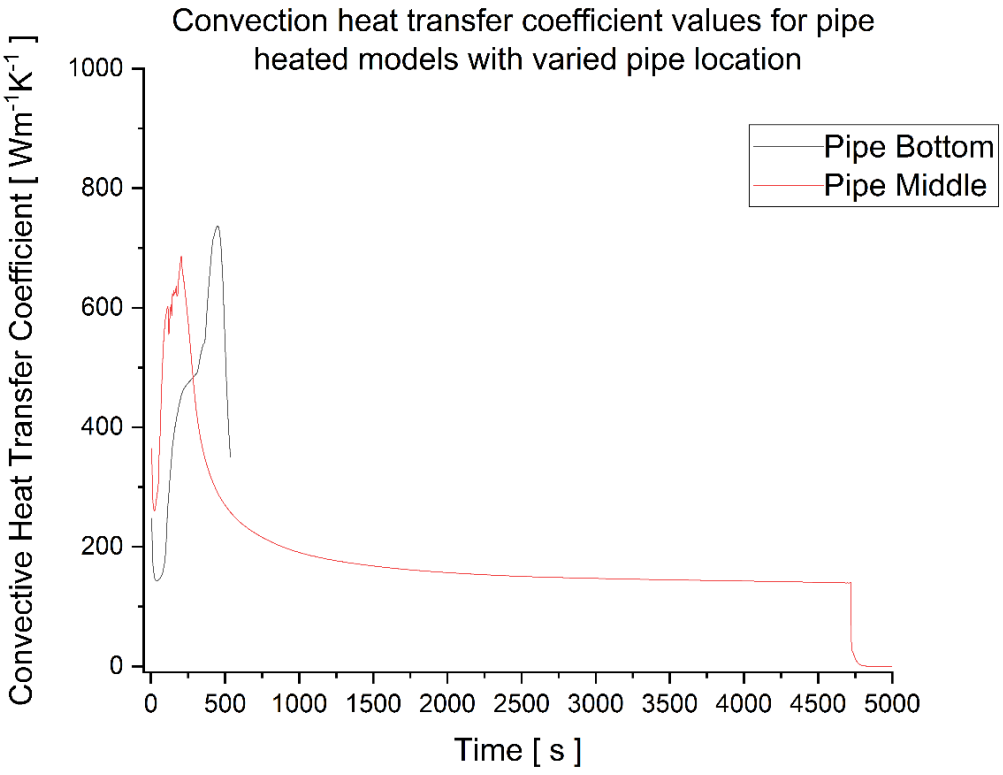

Figure 90 – Convection heat transfer curves for varied pipe location models.

5.4.3 Rayleigh Numbers

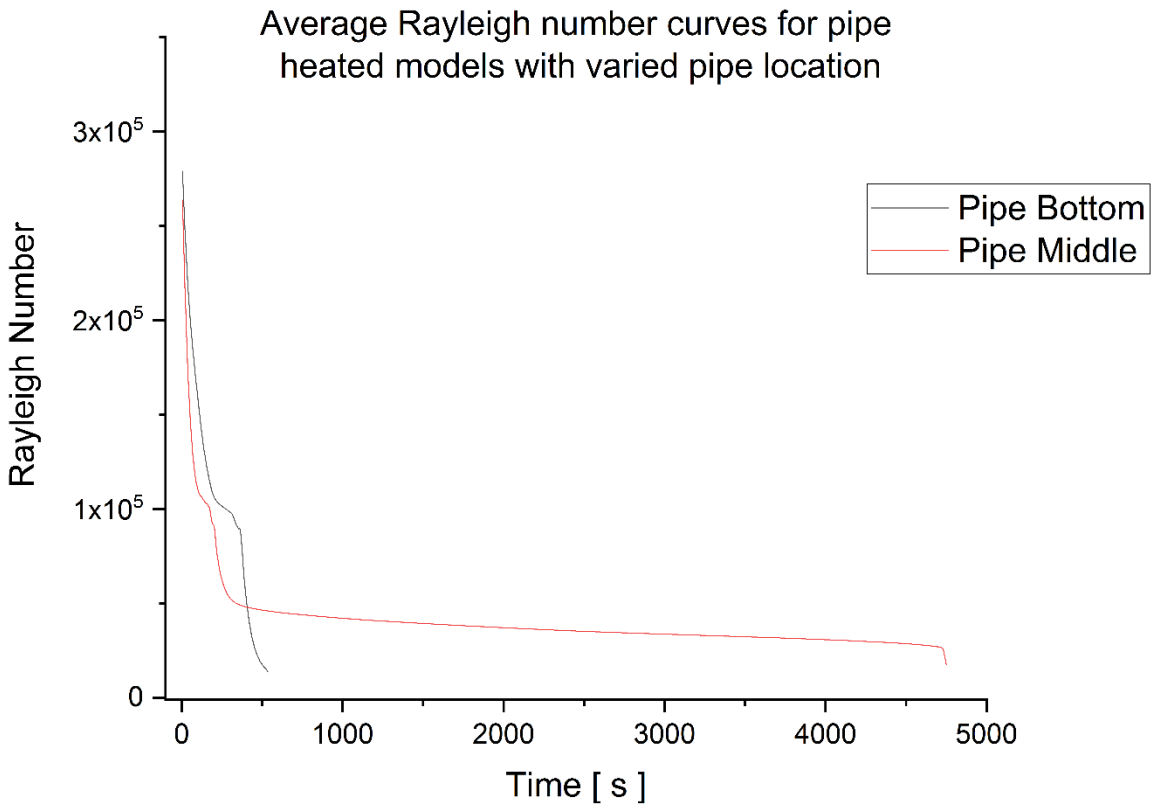

Figure 91 - Average Rayleigh number curves for varied pipe location models.

Figure 91 shows the average Rayleigh number values for the varied domain pipe placement models and some different features compared to Figure 79.

Like the previous curves in Figure 79, there is very similar range of values between the two models until the conductive melting begins to dominate.

The previous pattern of a distinct decreasing value before a slight plateau around 1.5 x10^5 has now changed for the middle configuration. Where the bottom configuration plateaus briefly before again decreasing exponentially to melt completion, the middle configuration shows a dramatically increased amount of time in the conductive melting regime, as demonstrated by the large amount of time in a second plateau around 0.5x10^5. This is as a result of the placement of the pipe leading to significant amounts of material below it only melting by conduction. The values are however still significantly above the critical value (Ra > 1700 [123]) indicating convection which is unsurprising given the material above the pipe.

Again these models are not within the turbulent regime (transition occurs near 10^7 [124]).

When comparing the Rayleigh curves with other figures such as power, Peclet and Nusselt number curves, there is a good agreement with features.

5.4.4 Peclet Numbers

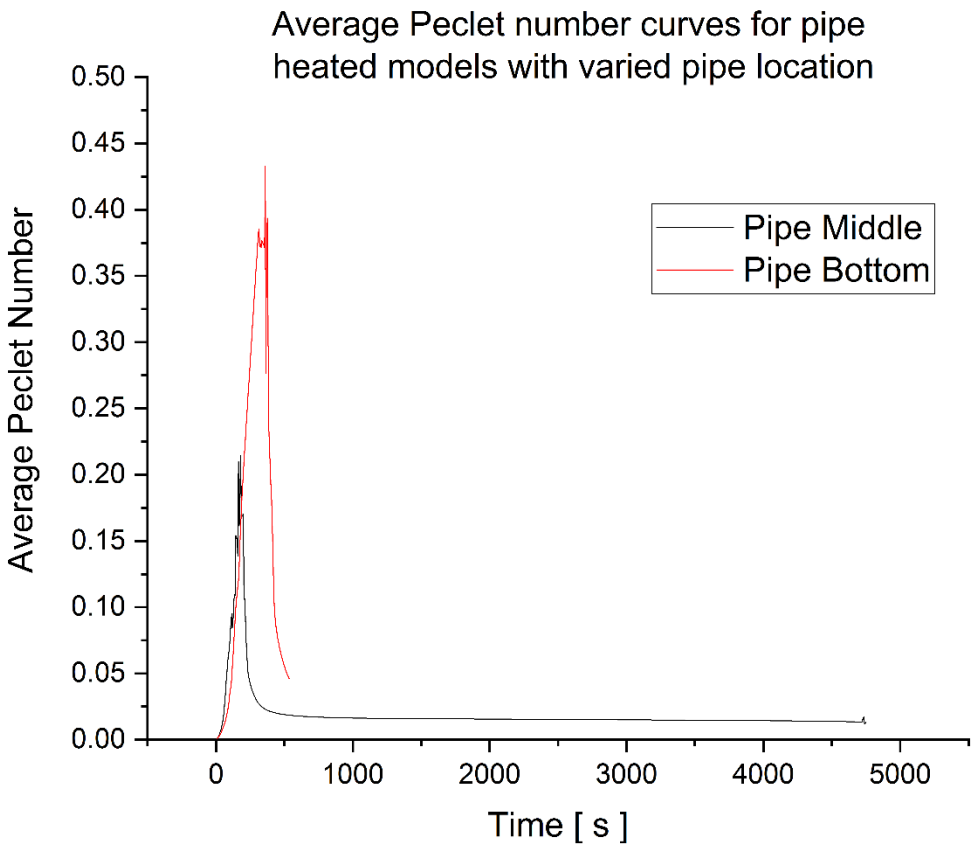

Figure 92 - Average Peclet number curves for varied pipe location models.

Figure 92 shows average Peclet number curves for both configurations in which they start at an initial value of zero. The middle configuration peaks around 0.21 and the bottom configuration around 0.43, more than double the value, indicating significantly more convection over the whole domain at the peak. This is expected due to the pipe being situated at the bottom rather than the middle, allowing for convection of most material in the domain, compared to the middle configuration in which only material to the sides and above it will undergo a convective heat transfer process.

Both curves exhibit slightly noisy peaks associated with the convective process before the value dramatically drops to 0.05 for the bottom configuration at melt completion where the middle configuration decreases and flattens around ~0.015.

5.4.5 Nusselt Numbers

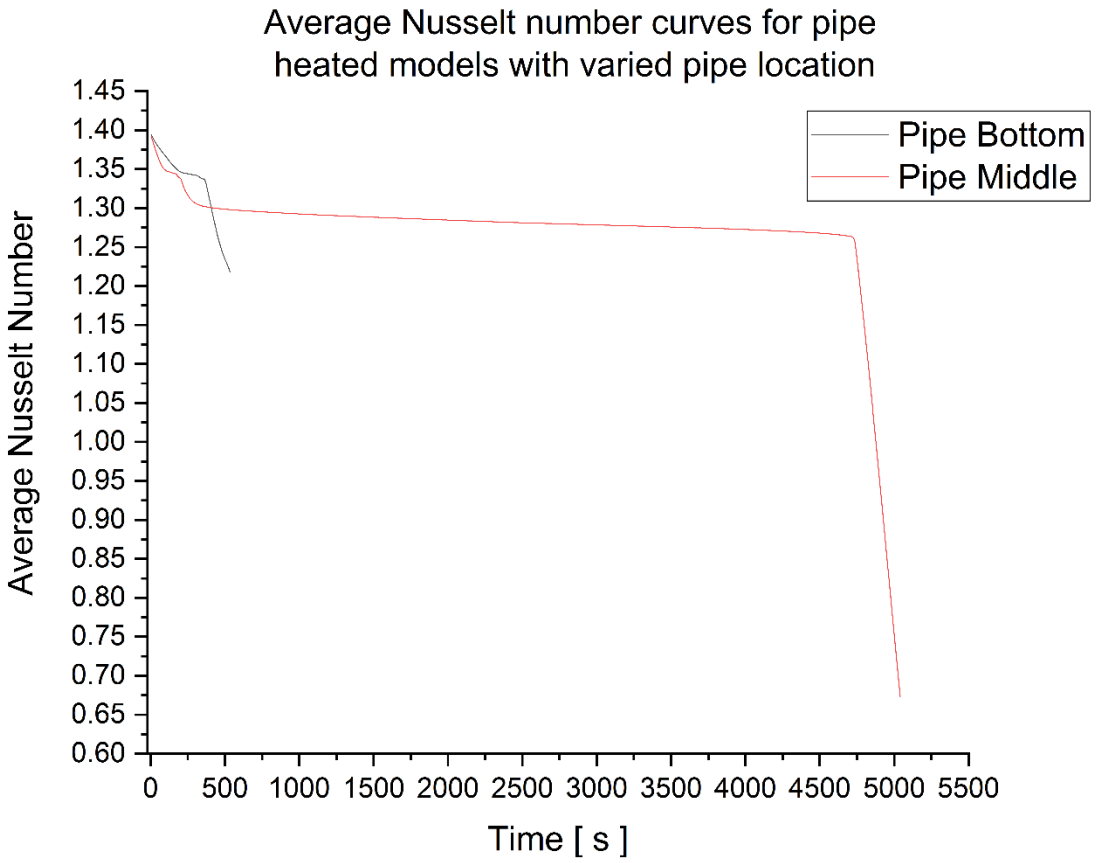

Figure 93 - Average Nusselt number curves for varied pipe location models.

Figure 93 shows the average Nusselt number curves which agrees with other dimensionless number analysis and convection and conduction dominant areas can be seen via the value reductions in both curves.

Both models begin with values ~ 1.40 before both steadily decrease to around 1.35. For the bottom mounted model a slight decrease is visible before the rapid decrease at 365 seconds. This decrease indicates the start of increased conduction associated with the melting of material directly sideways from the pipe. The middle configuration however has two sections: an initial decrease from ~1.40 to around ~ 1.35 at 100 seconds followed by a slightly decreasing value up to 200 seconds where another more rapid decrease takes place. The 100 – 200 second period is where convection is melting the portion above the pipe. Subsequent to 200 seconds is where the process is becoming more conduction dominant as material is melted to the sides and below the pipe until ~4720s when the melt process is finished and the Nusselt number very rapidly tails off to around 0.70.

Nusselt numbers agree well with the previous varied domain width models, the maximum values and values attained during increasing conduction dominance being very similar ~1.3 – 1.35.

As mentioned previously, the Nusselt number values derived from the convective heat transfer coefficient are of an increased value compared to those calculated using Equation 24 [3], which may indicate this approximation is not applicable in this case. The range of values seen in Figure 94, are between 3 – 18 and follow the same profile as Figure 90 – Convection heat transfer curves for varied pipe location models.

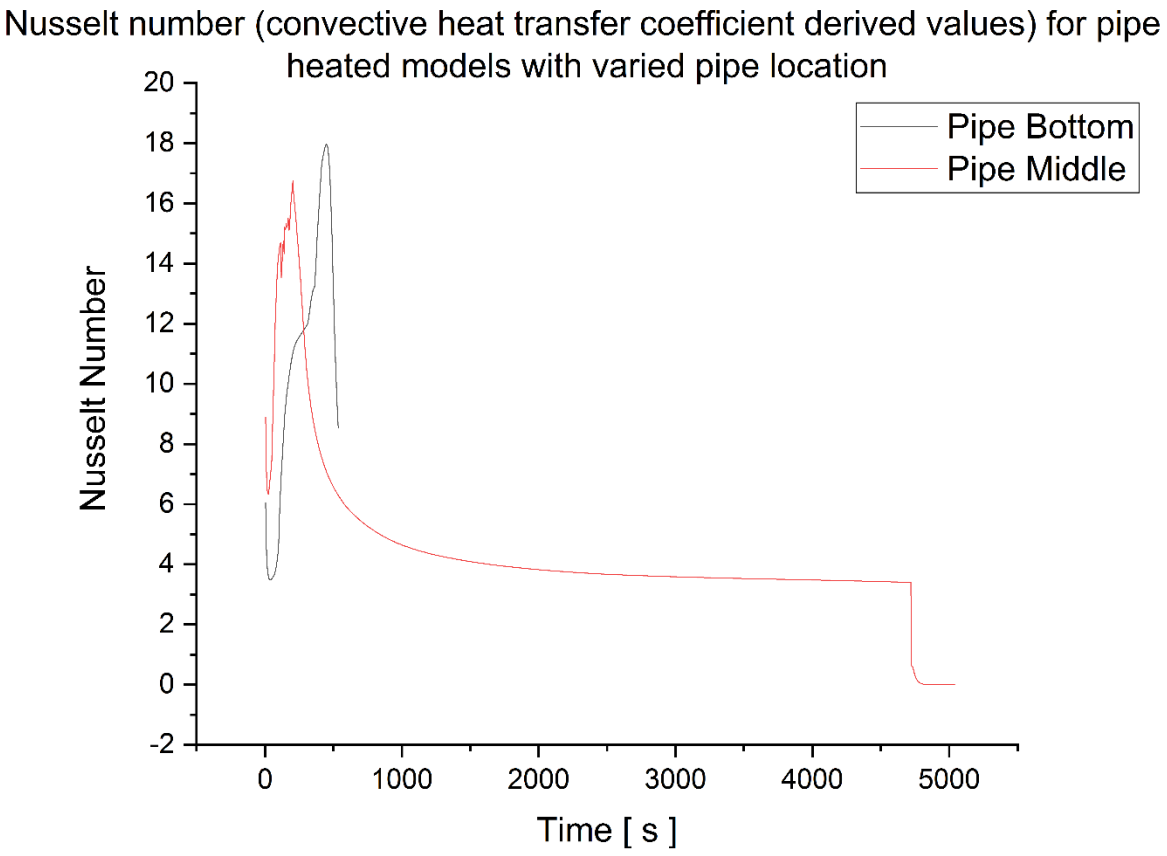

Figure 94 - Heat transfer coefficient derived Nusselt number curves for varied pipe location models.

5.5 Mesh and Temporal Dependency

Mesh generation for this 2D domain was one of unstructured quadrilaterals with adjustment to maximum face size to change the number of generated cells. Proximity and curvature were turned on to account for the curved pipe surface and care was taken to prevent sub-optimal cell generation.

In addition to the simulations described above, in order to ascertain the grid and temporal independence of the simulations above, a convergence study was undertaken and indicated mesh independence on characteristic melt time at 55,000 cells and 0.25s for the 25mm models.

When compared on characteristic melt time, 35,000 cells and 55,000 cells, a deviation of 25 seconds or 0.532% was found.

The larger domains had their mesh resolution settings set the same as the 55,000 25mm models resulting in a proportional linear increase in the total number of cells.

Unfortunately, comparing time steps resulted in a wide range of results for both configurations. 1s, 0.5s, 0.25s, 0.1s and 0.05s were investigated resulting in melt times of 1004s, 535s, 706s, 940s and 1246s respectively for the bottom pipe model. As no clear choice was indicated, 0.25s was chosen as this had been used for the previous flat plate investigations.

Additional monitors of both temperature and velocity were placed at several points within the computational domain as additional convergence criteria for both investigations; however these additional convergence criteria did not clarify an optimal time step.

5.6 Conclusion

This chapter has investigated the effect of changing the location of an isothermally heated pipe at 80° C and the effect on pipe spacing for a melt process in a domain of beeswax.

It is found that by increasing the domain width, the melt time is increased non-linearly with this dimension as a result of increased material being directly adjacent of the heated pipe requiring a slower conductive melting regime. It is also seen that larger domains result in a larger convective heat transfer coefficient likely attributed to a larger volume of material available to convect by virtue of there being a larger distance between pipes. It is also seen that there appears to be a complex interplay between the physical flow and thermal transfer processes with these configurations as the 50mm domain exhibits the lowest power and convection heat transfer coefficient.

Observing melt contours it is shown that each configuration results in the formation of one convection cell at melt completion irrespective of domain width or pipe placement location.

When the pipe location is varied from the middle to the bottom wall it is found that the melting time is significantly affected by the placement of the pipe, with the middle configuration causing a longer period of conduction dominated melting, resulting in a time of melt almost 9 times longer than the bottom configuration.

Analysis of other variables such as average Peclet number, average power and convective heat transfer coefficient also confirm the bottom configuration has significantly higher ratios of convection to conduction. This indicates both that the convection is advantageous but also conveys a much more rapid rate of melting and thus decreased total melt time. It is also seen that increasing amount of conduction attributable to the larger domain widths is undesirable for the same reason.

Conclusively, it would be highly recommended to always mount heating surfaces in such a way that the proportion of phase change materials above the heated surface is maximised.

In future works further attempts to optimize the time step and mesh resolution selection should be made to increase confidence in the model's results. Furthermore, investigation of the potential for convective flow guides to optimise the melting process would be of interest.

6 Investigating the effect of changing the mushy zone constant in 2D flat plate and pipe heated configuration

The importance of the mushy zone constant has been identified in the literature [102]–[104] and the effect of changing the value has large effects on the behaviour of a given melt process. This section details the investigation of changing the mushy constant value in two geometrical situations with beeswax as the PCM. One investigation configuration uses the previously investigated flat plate heater configuration, the other using the previously investigated bottom mounted pipe heated geometry with matching conditions in both.

An investigation in a situation where convection is not dominant is not investigated as the mushy zone constant is a parameter that affects damping to momentum in mushy zone cells with partial fluid-solid and will have little effect on a conductive process with little momentum.

6.1 Computational Domain and Initial and Boundary Conditions

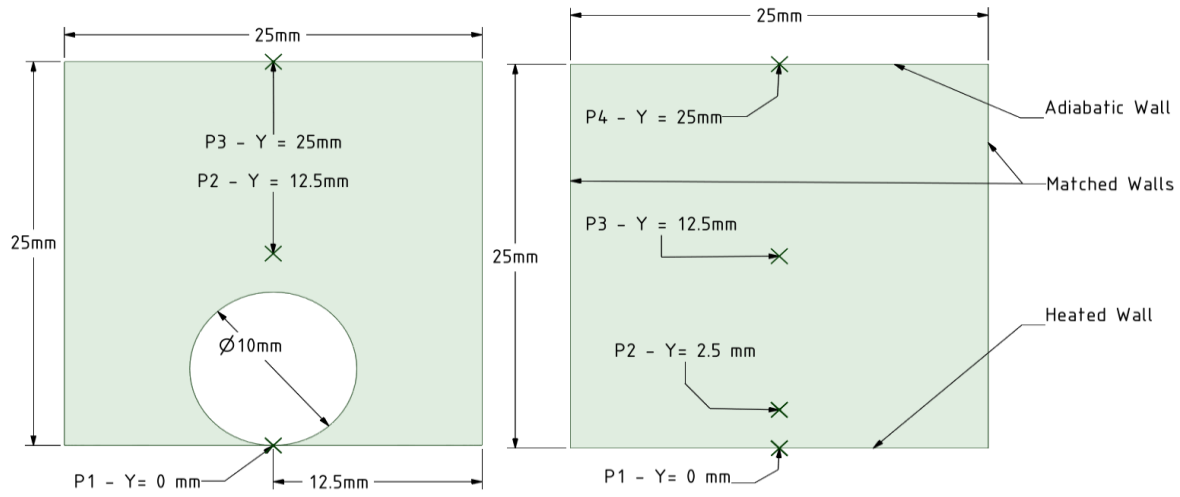

(a)

Figure 95 - 2D 25mm square computational domains used for investigation to compare effect of changing mushy zone constant on beeswax melt process in hot pipe (a) and flat plate (b) configuration. Sample points shown for (a) P1 – P3 shown at x=12.5mm, y = 0mm, 12.5mm and 25mm and (b) P1 – P4 shown at x=12.5mm y= 0mm, y= 2.5mm, y= 12.5mm and y=25mm.

The investigations into the effect of changing the mushy zone use two different geometrical computational domains shown in Figure 95 (a) and (b), with the bulk PCM chosen as beeswax with the same properties as investigated previously. Configuration (a) uses the previously generated and investigated hot bottom pipe configuration from chapter 5, and likewise configuration (b) uses the previously investigated hot flat plate configuration from chapter 4.

These models were computed using Ansys 18.2 and utilized the same assumptions for both situations:

(1) the top wall (and bottom wall for configuration (a)) is adiabatic to represent ideal insulation; (2) flow is Newtonian and incompressible; (3) flow is laminar and under the effects of gravity; (4) joule friction heating is negligible; (5) physical properties are temperature dependant and accounted for using the linear multi-point data entry method for materials properties ; (6) heat transfer occurs by conduction and convection only; (7) volume change is ignored; (8) three dimensional convection is ignored.

The same boundary conditions are applied:

- Bulk temperature - 25 °C.
- Bottom wall / pipe wall - 80°C.
- Side walls matched allowing flow to pass in-between.
- Top wall (and bottom wall for pipe configuration only) – adiabatic.
- X velocity – 0 ms^{-1}.
- Y velocity – 0 ms^{-1}.
- Gauge pressure – 0 Pa.
- Gravity – on, set at -9.81 ms^{-2}

At time $t \geq 0$ the mushy constant value is set as:

$$C = 10^3, 10^4, 10^5, 10^6, 10^7, 10^8$$

6.1.1 Thermo-physical properties:

The thermo-physical properties of the beeswax utilized are listed in chapter 3 with values in Table 7 and Table 8 and previously experimentally determined densities listed in Table 6. Linear interpolation of temperature dependant values for material characteristics has taken place.

6.1.2 Solution Method and Controls:

For the numerical solution of the model the previously given methods and controls were utilized and Super Compute Cluster 2 was utilized exclusively for computation (details of machine hardware and solution methods/ controls given in chapter 2.)

6.2 Results and discussion – Bottom mounted pipe heated Model

In this section, the results of the mentioned models are presented, discussed and compared in terms of the melt, heat rate and relevant dimensionless numbers. In each of the above cases presented, models with 55,000 cells in mesh resolution were used for the analysis.

6.2.1 Evolution of melt (time)

Melt time has been computed using a surface average and has been deemed to be fully melted at 99.9% melted or higher. This has shown a melting time for beeswax of 490, 535, 540, 635, 890 and 1000s for values of mushy zone constant of 10^3 to 10^8 in Figure 96.

This conclusively reconfirms the findings in Kheirabadi and Groulx [102] and Kuma and Krishna [103], that larger values of mushy zone constant result in a longer melt time for a given process. Importantly, this is confirmed in an alternative pipe geometry and the value of melt time can almost double simply by varying this parameter in this configuration.

Another interesting feature is that the melt time values for 10^3, 10^4 and 10^5 (the most commonly used value in literature) are all within roughly 10%. It is difficult to speculate as to why this is the case, although as the mushy zone constant effectively damps the convection process there could be a critical value of mushy zone constant below which variation in output is significantly reduced.

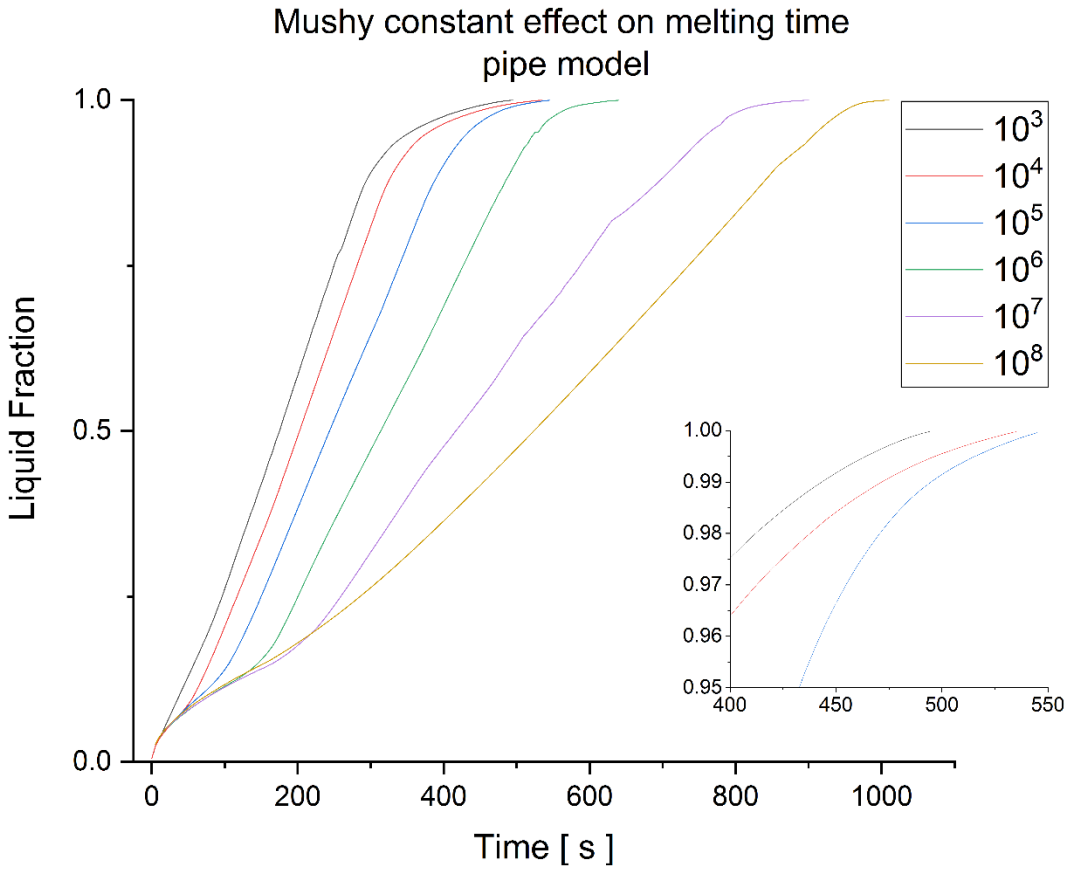

Figure 96 - Melting time curves for pipe heated model with varied mushy constant.

Observing the melt fractions compared with time in Figure 97, it is seen that larger values of mushy zone constant lead to a reduced melt fraction at a given time. It appears that the larger values of mushy zone constant result in slower convection onset and establishment of convective cells, leading to less melted material ascending directly upward during earlier periods of the melt process (Figure 98, Figure 99 and Figure 100) and less melted material proceeding horizontally within established convection cells later in the melt process.

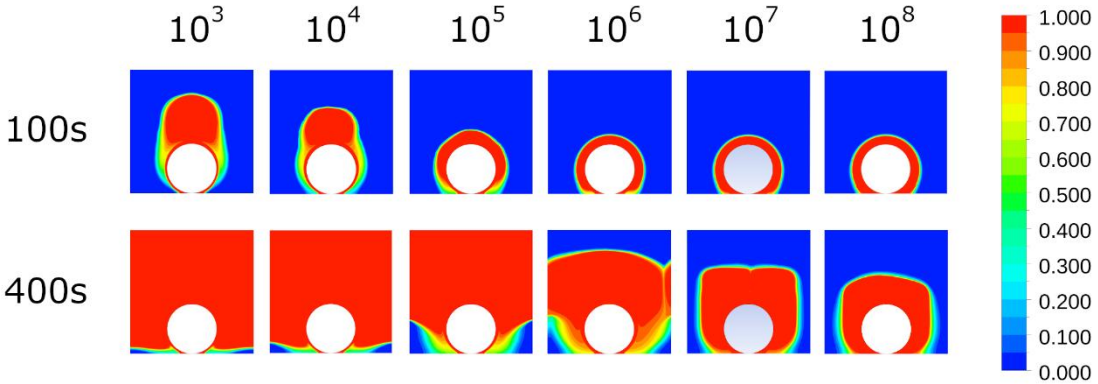

Figure 97 - Comparison of melt contours for Pipe Heated model Mushy constant variation from 10^3 to 10^8 from left to right.

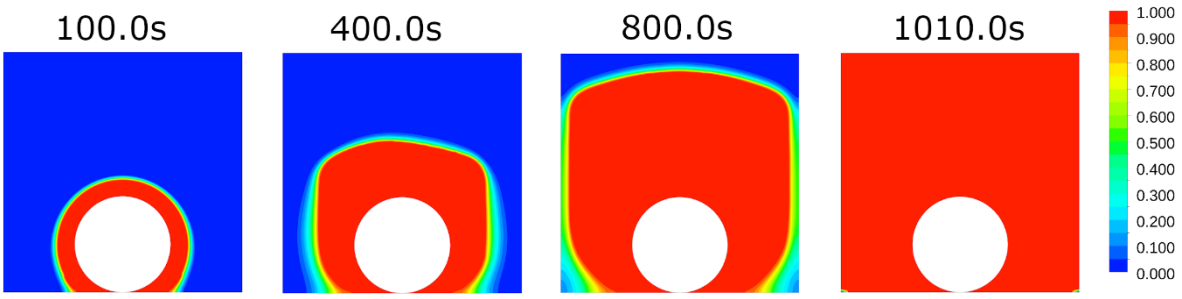

Figure 98 - Melt fraction contours for pipe heated model at mushy constant 10^8 at various times.

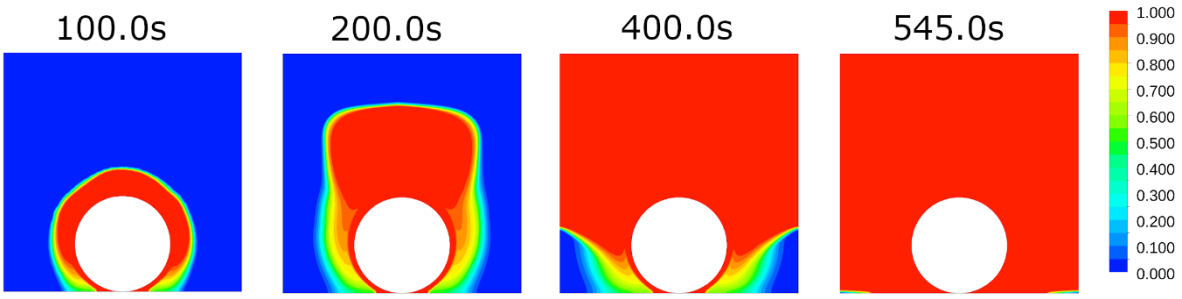

Figure 99 - Melt fraction contours for pipe heated model at mushy constant 10^5 at various times.

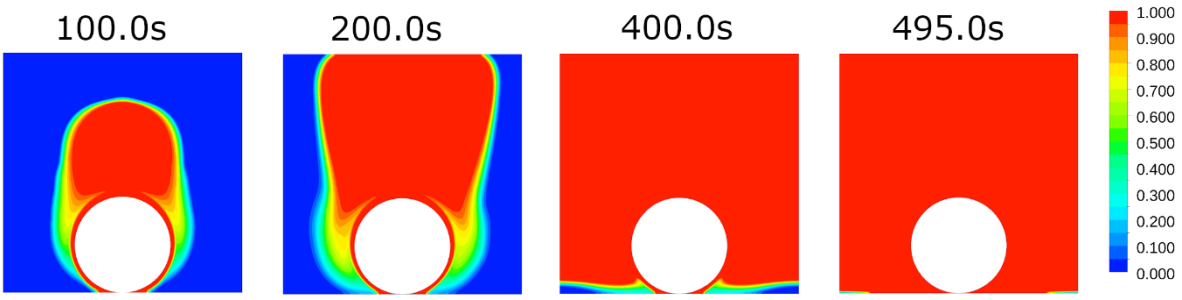

Figure 100 - Melt fraction contours for pipe heated model at mushy constant 10^3 at various times.

In addition, during the early phase of all melts it is seen that conduction dominates with a uniform radial distribution of melted material around the pipe as expected.

Likely as a result of the result of the geometry, all values of mushy constant eventually establish a single convection cell spread to the left and right of the pipe, although the time for this to occur is related to the value of the mushy constant. The larger the mushy constant value, the longer it takes for the convective cell to form from its constituent halves.

6.2.2 Heat transfer power and convective heat transfer coefficient

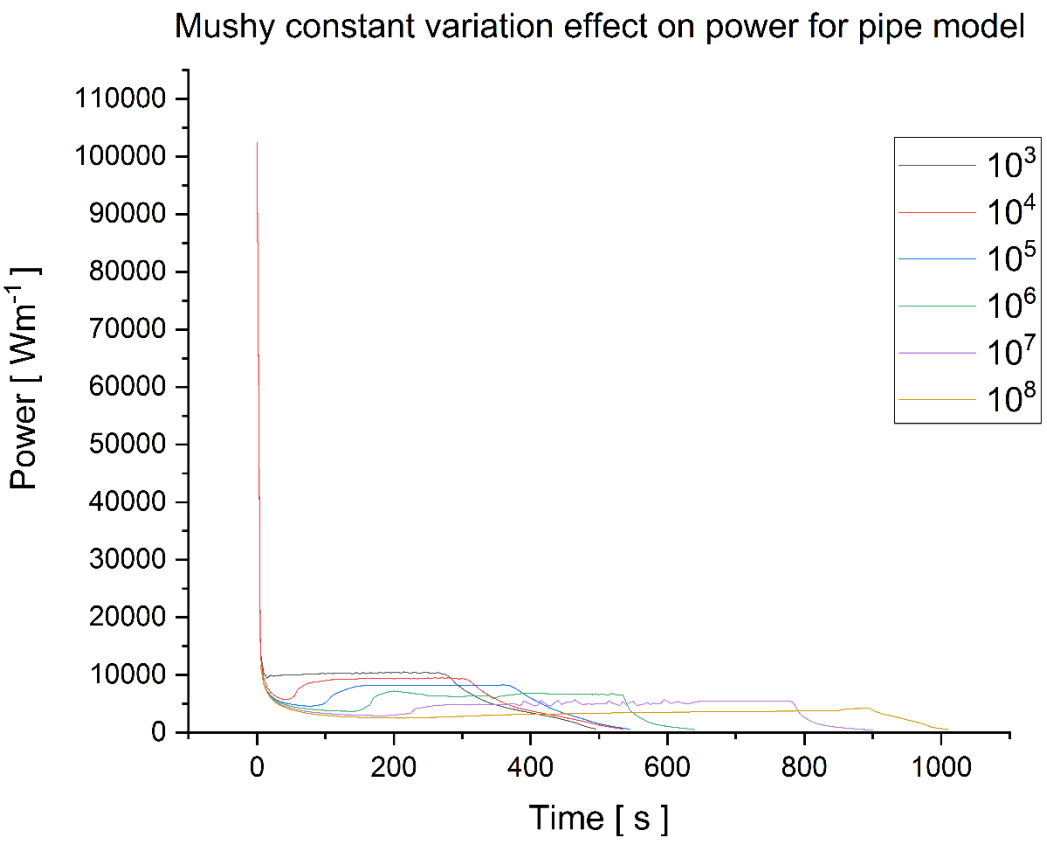

Figure 101 – Power curves for pipe heated model at various mushy constants.

As can be seen in Figure 101 and Figure 102, all models initially reflect a large initial value ~100000 Wm^{-1} and 2000 $Wm^{-1}K^{-1}$ which can be attributed to conduction instantaneously starting. As is expected, larger values of mushy zone constant result in a reduced value of both heat transfer power and the associated convection heat transfer coefficient as a result of the damping effect on convection attributed to larger mushy constant values.

The onset of convection is obvious and seen in all mushy zone constant values with exception to 10^8 in Figure 102 as the reduction in value to a minimum on the curve followed by a sudden increase in value before tailing off around 100 – 300 seconds.

It is expected that this feature is not found for the mushy zone constant curves for 10^8 due to a very slow onset of convection, considering the contrast in melt contours at 100 seconds for Figure 98 and Figure 100.

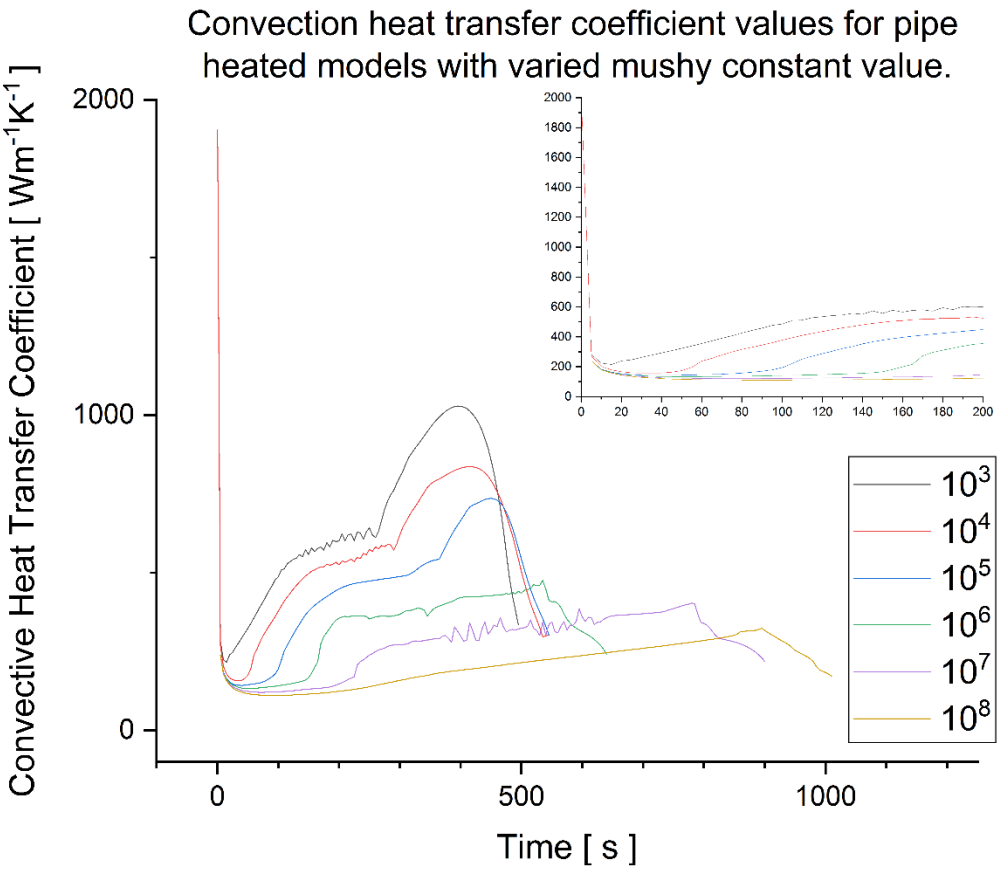

Figure 102 - Convection heat transfer coefficient values for pipe heated model at various mushy constants.

Values for power and convective heat transfer coefficients like the melt times show values more than double when comparing mushy zone constant curves 10^3 and 10^8. The ongoing and maximum peak values for larger mushy constant values are seen to decrease with increasing mushy zone value. These second regimes of increasing convective heat transfer coefficient value, (more easily seen for values 10^3 to $10^{5)}$, are associated with material reaching the top of the domain (where the value plateaus before rapidly increasing) with rapid melting of material at the sides of the domain, (causing the rise up to the peak) with the subsequent rapidly decreasing value associated with the conductive melting of material adjacent to the pipe.

As expected, with an increased melt time for larger mushy constant, the power value curves are lower with larger power transfer associated with lower values of mushy constant.

The model using a mushy constant of 10^7 shows a noisier power signal for reasons unknown; however this may reflect model instability.

6.2.3 Rayleigh Numbers

For this analysis the Rayleigh number and Grashof numbers are defined as follows [3]:

$$Ra = GrPr \tag{26}$$

$$Gr = \frac{g\beta(\tau_S - \tau_\infty){L_h}^3}{\nu^2} \tag{27}$$

Where $\beta_{Beeswax}$ =0.004170747 and L_H =0.01 (m) plate plate, L_H would typically be the ratio of horizontal plate area to plate perimeter iln 3 dimensions. In this case it has been assumed to be the pipe diameter [4].

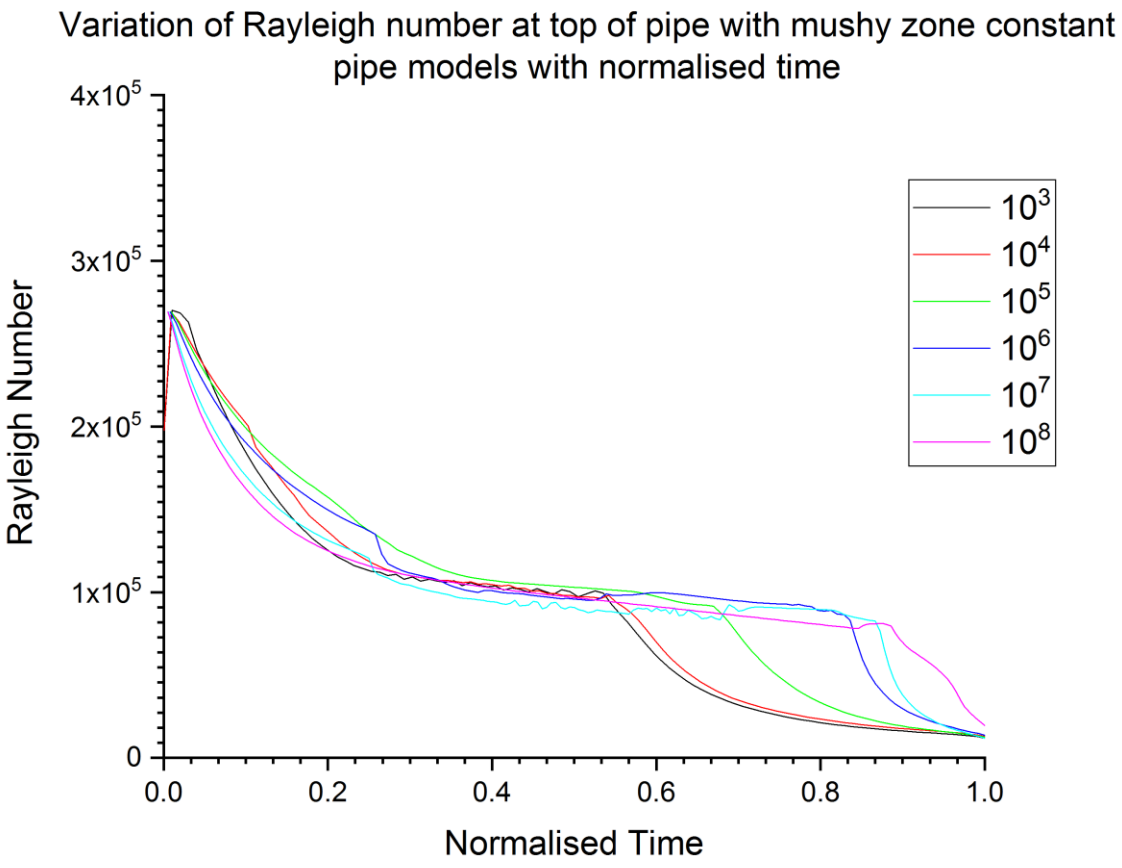

Figure 103 – Rayleigh number values at top of pipe sample point over normalised time for pipe heated models with varied mushy zone constant.

Figure 103 shows the values of Rayleigh number over normalised time at the sample point at the top of the pipe for each model. Each curve follows a similar pattern with a large initial value

around $2.75x10^5$ before reducing to a plateau around $1.1x10^5$ during the main body of convection related melting. This plateau is then followed by an exponentially decreasing value for most models until melt completion.

This figure displays some very interesting features, one of which is that larger values of mushy constant still result in very similar values throughout the majority of the melt process, but larger mushy constant models appear to enter the conductive dominant melting regime much later than smaller values. This is likely as a result of lower values of mushy constant leading to more vigorous convection with flow patterns travelling to the same extent as larger values but with a much more rapid melt. The associated flow patterns can be seen in Figure 98 and Figure 100. This then leaves a larger proportion of the melt process dominated by conduction despite the overall reduction in total melt time which can be seen when inspecting the relative amount of time each model spends in the exponentially decreasing rate regime in Figure 96.

In Figure 103, the model with mushy constant 10^6 has a pronounced drop at 0.22 normalised time; however this does not appear to be an error and is attributed to a change in convective cell shape which can be seen in Figure 104.

The model with mushy constant 10^5 demonstrates the largest value throughout Figure 103 although the reasoning for this is unknown. It may reflect an optimal value with respect to convective thermal transfer and developed flow patterns.

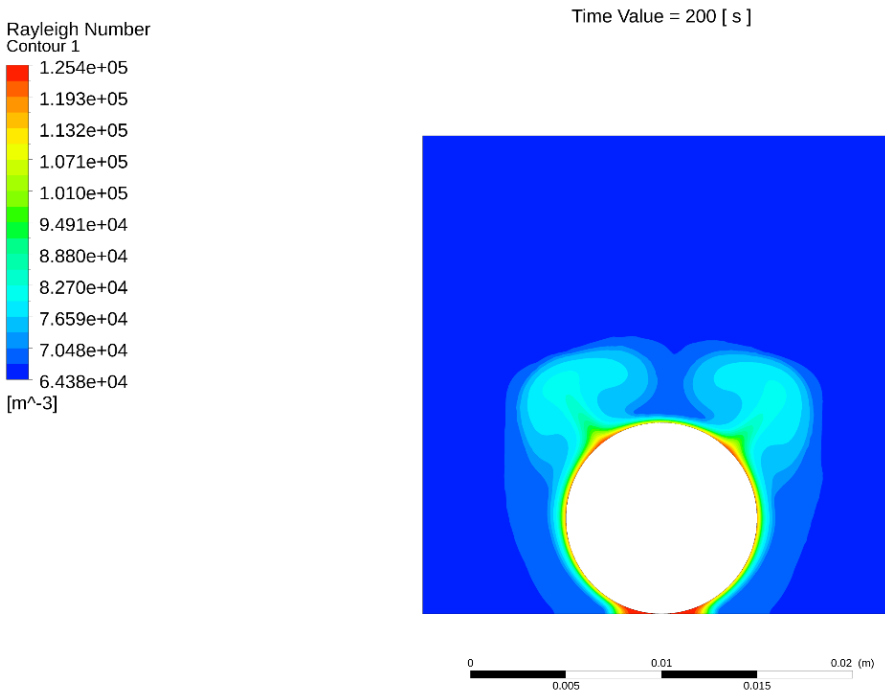

Figure 104 - Contours of Rayleigh number for mushy constant 10^6 pipe model at 200 seconds.

6.2.4 Peclet Numbers

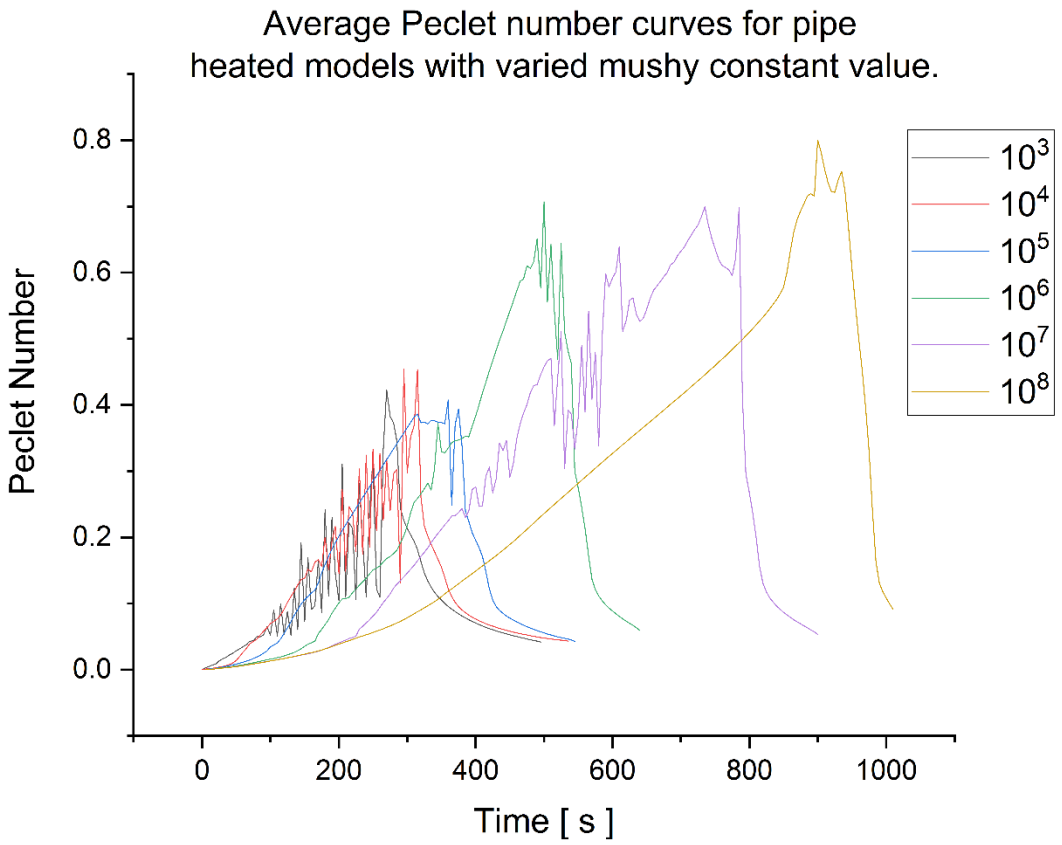

Figure 105 - Average Peclet number curves for pipe heated models with varied mushy constant value.

For this investigation, the Peclet number has been calculated using the CFD Post software and then an average value across the whole domain has been calculated for each time step.

$$Pe = RePr \tag{28}$$

Figure 105 shows interesting curves of average Peclet number with larger values developing at later times in the melt process for larger values of mushy constant. These values increasing over time is not unexpected as the longer time scale allows the convective cells to establish fully and with stability but this is despite the convection damping effect of increasing the mushy constant value.

Starting from an initial value of zero, all models show a smooth increasing value up until the onset of convection, upon which the Peclet value signals become exceptionally noisy. This is

followed by a tail off in values. Values tailing off after melt completion may seem counter intuitive but is not surprising. When the melting process ends, the lack of isothermal solids at the top of the domain reduces the temperature gradient as the convecting material effectively self-mixes the domain, spreading out heat rather than delivering it to the now absent solids. The speed of this decline appears to be faster with increasing mushy constant value which may be attributable to the larger convective velocities established by the larger mushy constant models, e.g. the maximum values of Y velocity attained at melt completion are $1.6x10^{-3}$ ms^{-1} and 2.3 ms^{-1} for mushy constant values of 10^3 and 10^8 respectively (Figure 109 and Figure 110).

The lack of a noisy signal in the 10^8 model is of interest and may be related to its more ordered flow as can be seen in Figure 98 or an artefact of an unstable or inaccurate model as a result of its high mushy constant value.

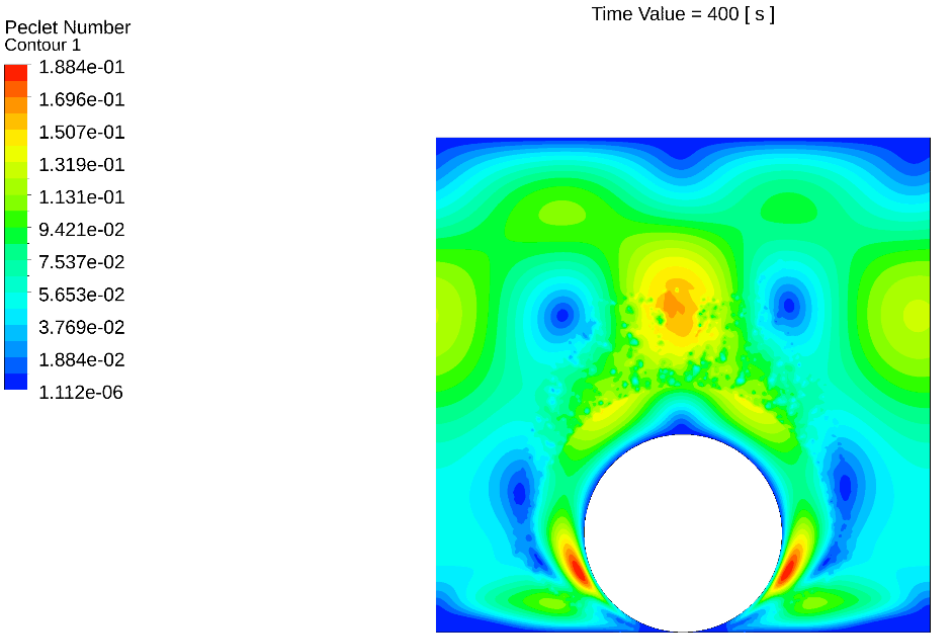

Figure 106 and 107 show contours of Peclet number during the convective melt process prior to completion, clearly showing the large Peclet numbers directly over the pipe as one might expect. They also clearly demonstrate the form of the convection cells within the melted material. These figures also show interesting shapes and increasing ordered channels with increasing mushy constant value.

When compared to Y velocity (Figure 109 and Figure 110) this is easier to see with lower mushy values having much less perpendicular flow around the pipe.

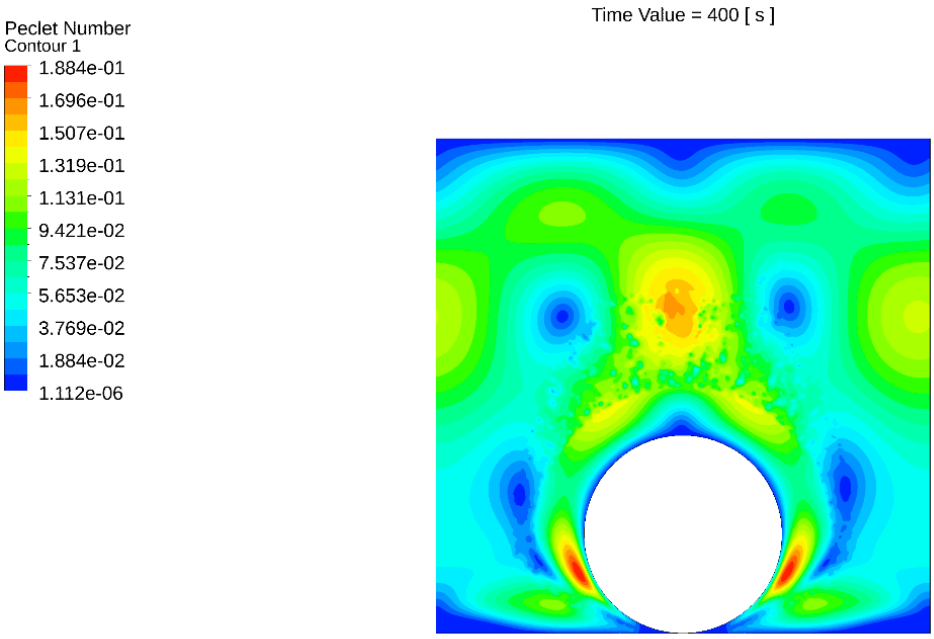

Figure 106 - Contours of Peclet number for pipe heated model with mushy constant set to 10^3 at time 400s.

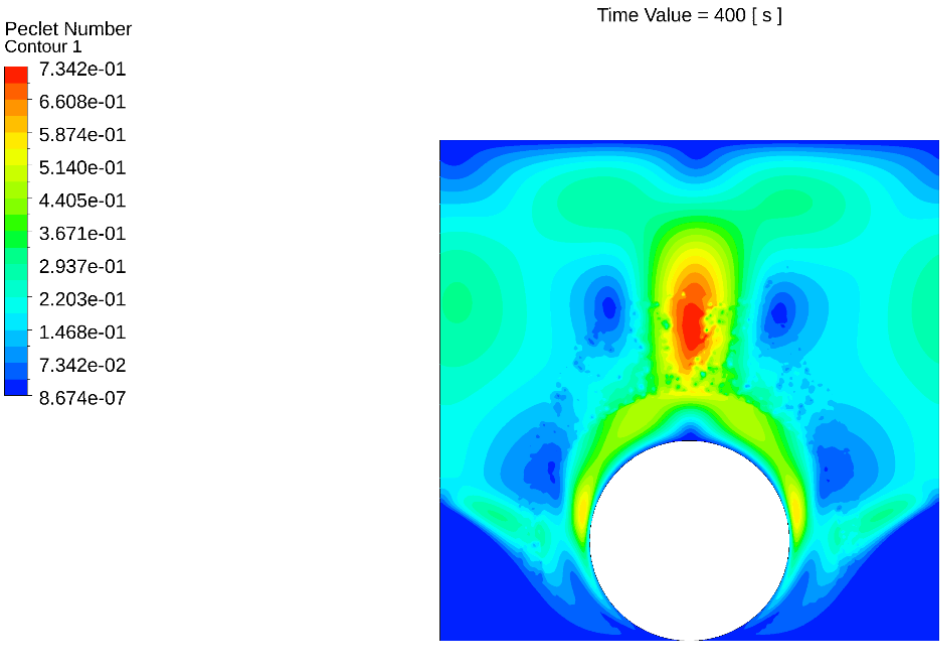

Figure 107 - Contours of Peclet number for pipe heated model with mushy constant set to 10^5 at time 400s.

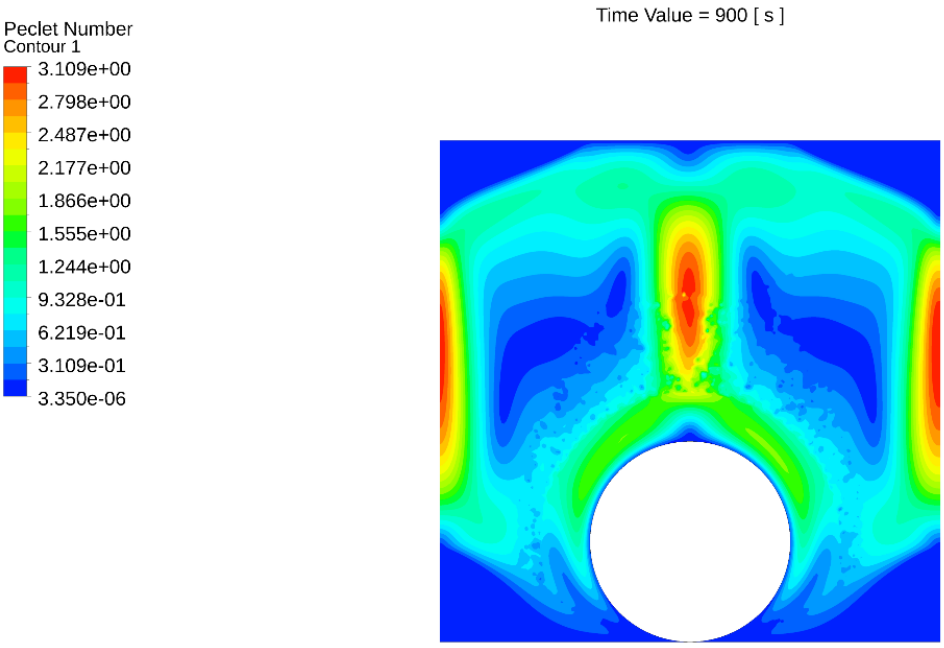

Figure 108 - Contours of Peclet number for pipe heated model with mushy constant set to 10^8 at time 900s.

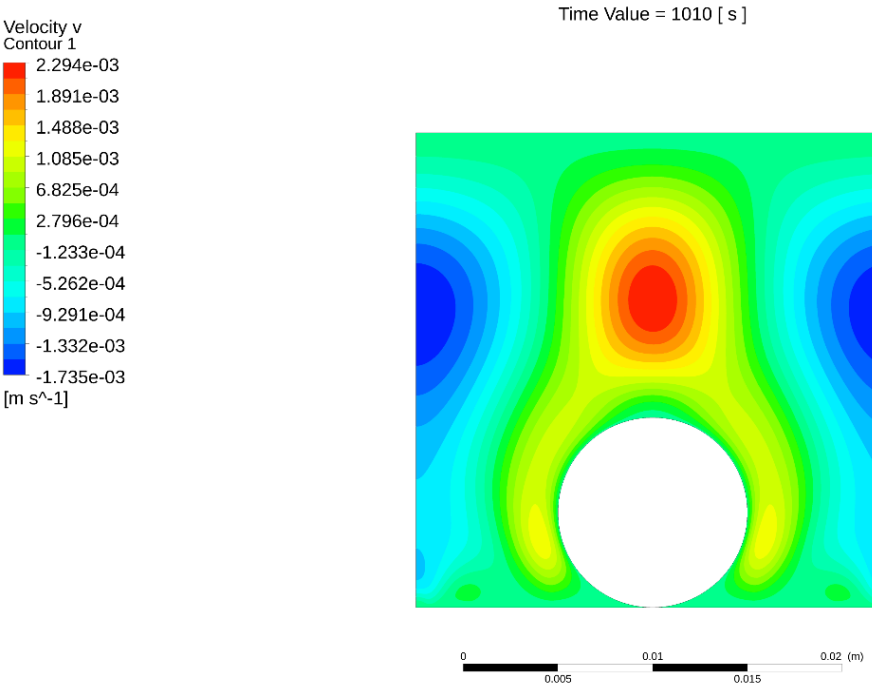

Figure 109 - Y velocity contours for mushy constant value 10^8 pipe model at 1010 seconds.

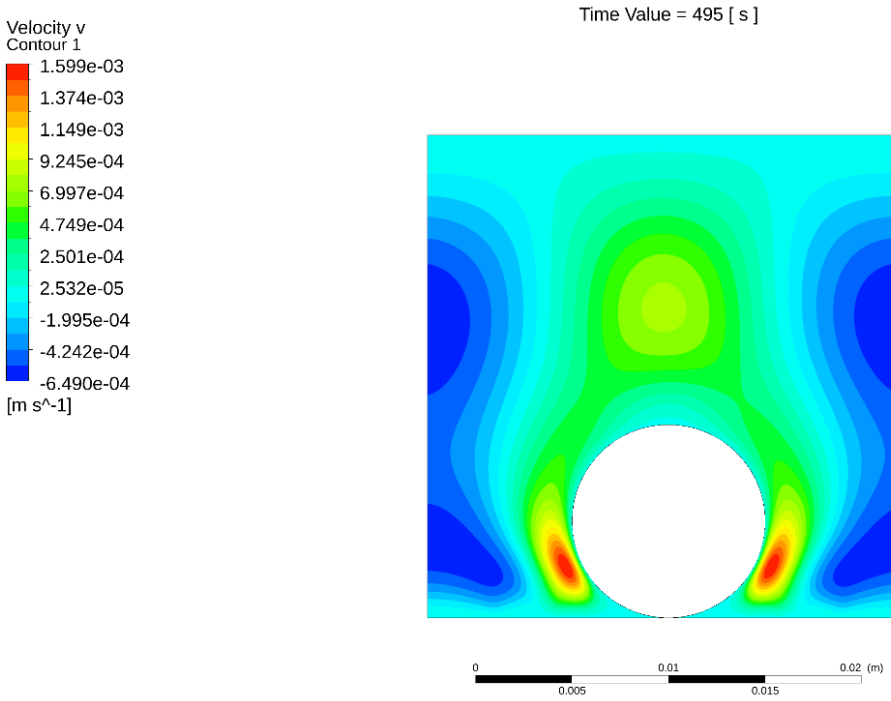

Figure 110 - Y velocity contours for mushy constant value 10^3 pipe model at 800 seconds.

6.2.5 Nusselt Numbers

As the specified configuration is one of a heated pipe, coupled with the values of Rayleigh number, the Nusselt number correlation utilized is the following [3]:

$$Nu = \frac{2C_{cyl}}{ln\left(1 + \frac{2C_{cyl}}{0.772C_{lam}\,Ra^{0.25}}\right)} \tag{29}$$

Where:

$$C_{lam} = \frac{0.671}{\left[1 + \left(\frac{0.492}{Pr}\right)^{9/16}\right]^{4/9}} \tag{30}$$

$$C_{cyl} = 0.8$$

$$1 \times 10^{-10} < Ra < 1 \times 10^{10}$$

Furthermore, for this analysis the average values have been calculated from the whole pipe surface.

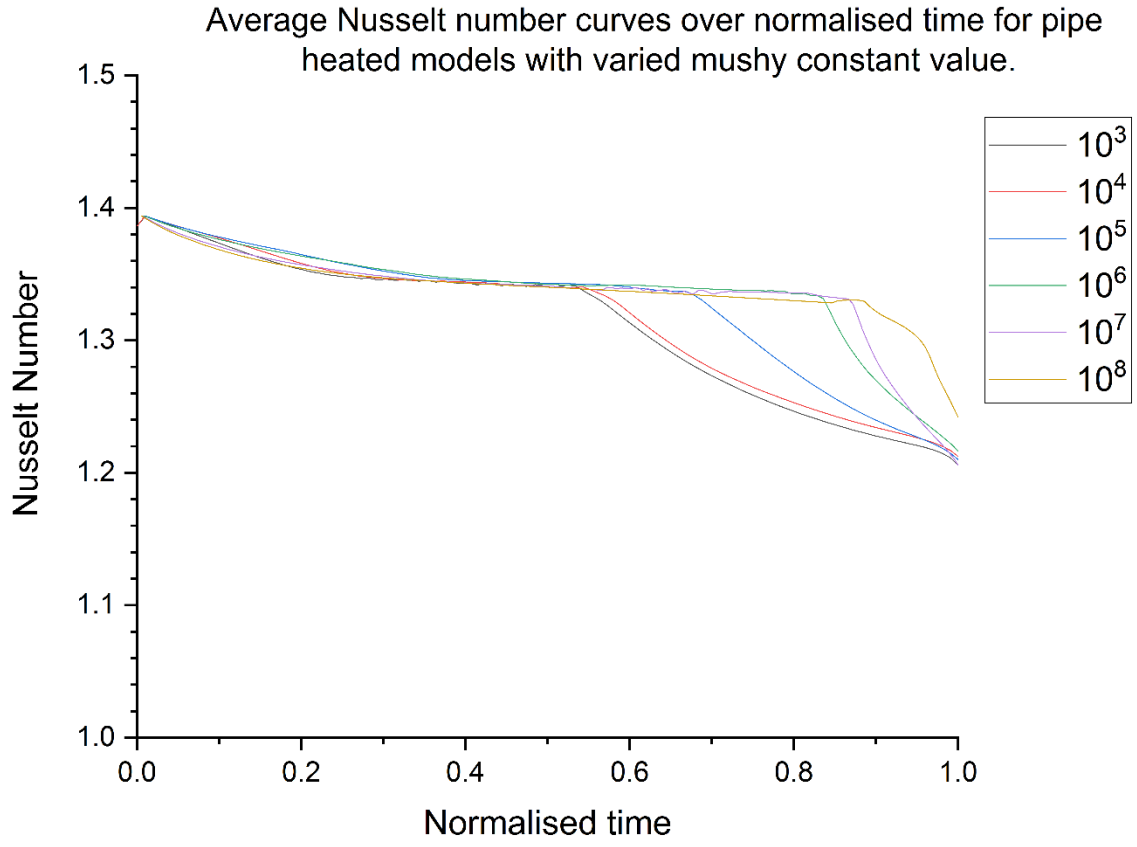

Figure 111 -Average Nusselt number over normalised time for pipe heated models with varied mushy zone constant.

Figure 111 shows the average Nusselt number curves for the varied mushy constant pipe models and shows virtually identical values of Nusselt number across the majority of the normalised time for the models. With values between ~1.4 – 1.2 heat transfer is convection dominant throughout the melting process; however these values decrease earlier for lower values of mushy constant for the same reason this pattern is found in Figure 103. Lower values of mushy constant appear to lead to more vigorous convection but with flow patterns showing advected material travelling to the same extent as larger values of mushy constant but with a much more rapid melt. This then leaves a larger proportion of the melt process dominated by conduction despite the overall reduction in total melt time for the lower value models of mushy constant. As can be seen, these curves agree well with the previous non-dimensional number and variable analyses.

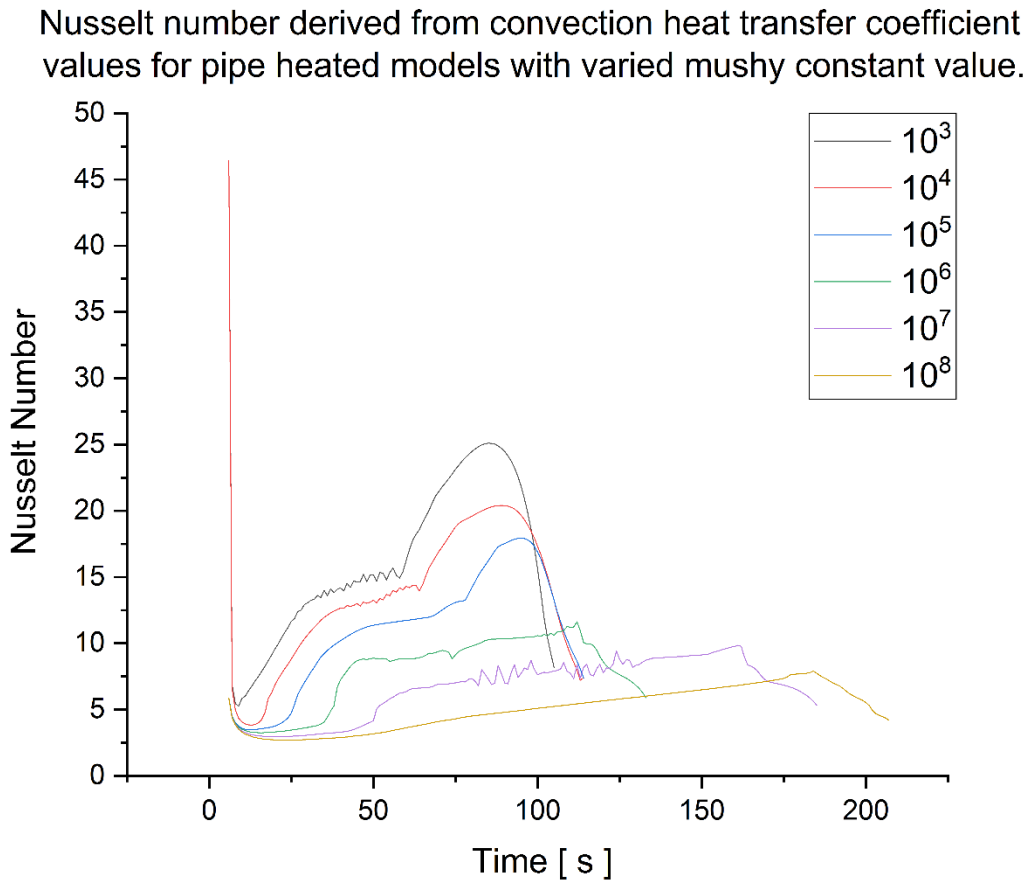

Figure 112 - Heat transfer coefficient derived Nusselt number over time for pipe heated models with varied mushy zone constant.

Like previous pipe model Nusselt calculations, those derived from the convective heat transfer coefficient, (Figure 112) do not agree well with those calculated via Equation 29 which may be under predicting these values.

6.3 Results and discussion – Flat plate heated Model

In this section, the results of the flat plate models with varied mushy zone constant are presented, discussed and compared in terms of the melt, heat rate and relevant dimensionless numbers to each other and the results of the previous pipe models with mushy zone constant variation. In each of the flat plate cases presented, models with 55,000 cells in mesh resolution were used for the analysis.

6.3.1 Evolution of melt (time)

Like the previous pipe model, melt time has been computed using a surface average and has been deemed to be fully melted at 99.9% melted or higher. This has shown a melting time for beeswax of 586.26, 711.26, 841.26, 1416.26, 2256.26, and 2716.26s for values of mushy zone constant of 10^3 to 10^8 in Figure 113.

Like the pipe model, the findings by Kheirabadi and Groulx [102] and Kuma and Krishna [103] are reconfirmed; larger values of mushy zone constant result in a longer melt time for a given process, in this case a flat plate convection configuration. With this comparison in mind however, the time for a full melt to complete is significantly larger for the flat plate configurations, at 10^3 by 96.26s and 10^8 by 1716.26s. This would appear to indicate that the time of melt increase attributable to changing the mushy constant is interdependent on the geometrical configuration and / or heat source.

In addition, mimicking the trend in the pipe configuration, mushy zone constants 10^3, 10^4 and 10^5 for the flat plate models demonstrate much closer melt times than the larger mushy constants; however the variation is closer to approximately 20%. This further indicates that not only is the melt time extended with larger values of mushy constant but that the geometrical configuration or other factors are interdependent, with the mushy constant resulting in these larger relative variations.

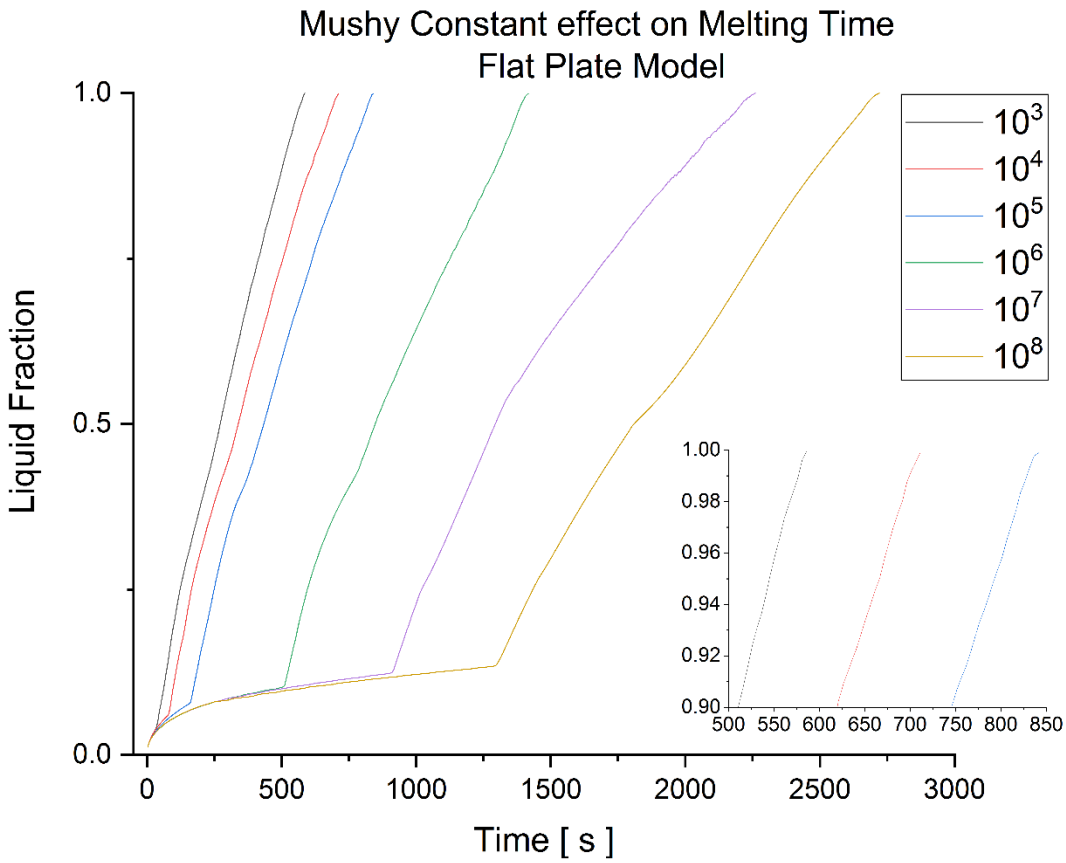

Figure 113 - Melting time curves for flat plate heated model with varied mushy constant.

Observing the melt fractions compared with time in Figure 114, much like Figure 97 it is seen that larger values of mushy zone constant lead to a reduced melt fraction at a given time. Likewise a similar pattern arises as a result of larger values of mushy zone constant as was observed in the previous varied mushy zone constant pipe melts. Observing Figure 114, Figure 115 and Figure 117 it can be seen that the shape and number of the forming convection cells is affected rather than only the shape.

During the early stages of the melt process, the model with a mushy constant value of 10^8 has fewer convective cells with less curvature when compared to those of 10^3 or 10^5. When looking at maximum Y velocities in these melts it is seen that 10^3 reaches 0.04 ms^{-1}, 10^5 reaches 0.032ms^{-1} and 10^8 reaches 0.019ms^{-1}. It may indicate that this curvature may be related to these velocities and that higher velocities result in a higher curvature, a less straight melt interface and more convection cells in the early stages of melt. In contrast, toward the end of the melt process all values of mushy constant finish with only one convective cell.

The time taken for all flat plate melts compared to their associated pipe variant of the same mushy constant is larger in all cases; however, this should be no surprise as the pipe models

have both increased heat transfer surface (31.42 mm versus 25mm) and a reduced amount of material to melt due to the presence of the pipe (the flat plate has ~15% more material).

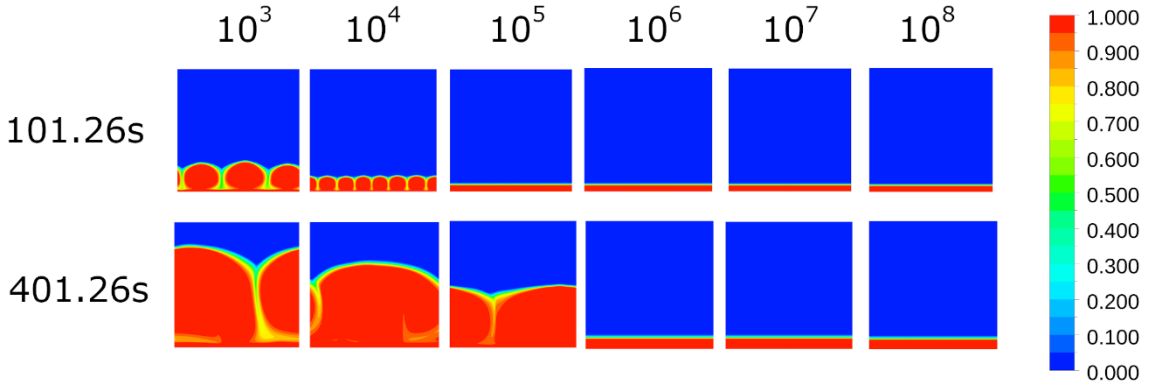

Figure 114 - Comparison of melt contours for flat plate heated model Mushy constant variation from 10^3 to 10^8 from left to right.

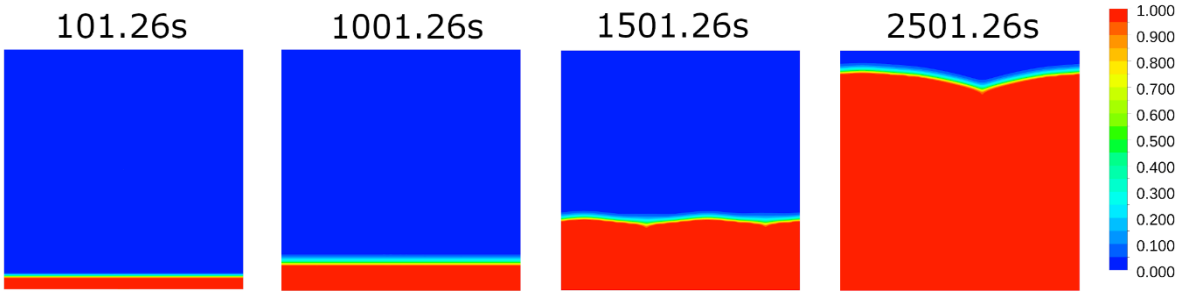

Figure 115 - Melt fraction contours for flat plate heated model at mushy constant 10^8 at various times.

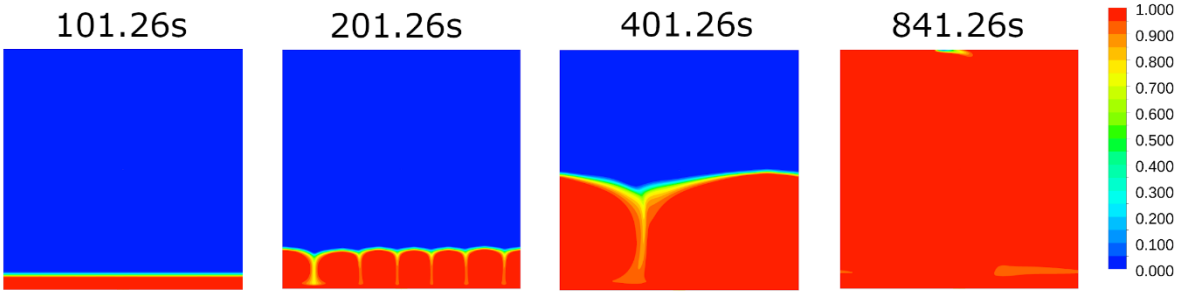

Figure 116 – Melt fraction contours for flat plate heated model at mushy constant 10^5 at various times.

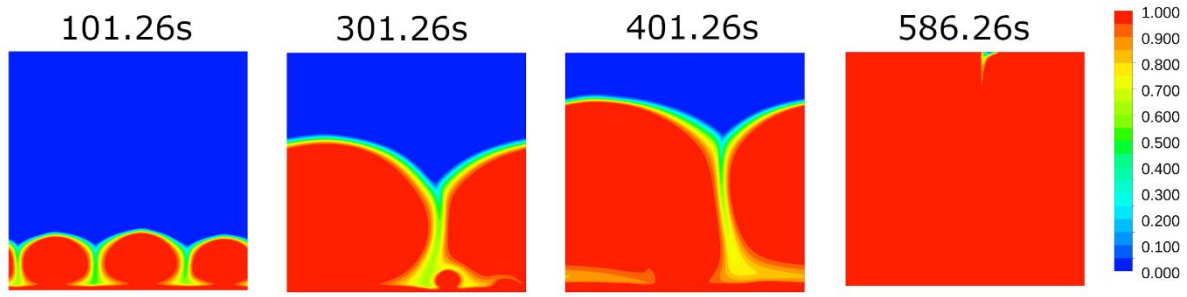

Figure 117 - Melt fraction contours for flat plate heated model at mushy constant 10^3 at various times.

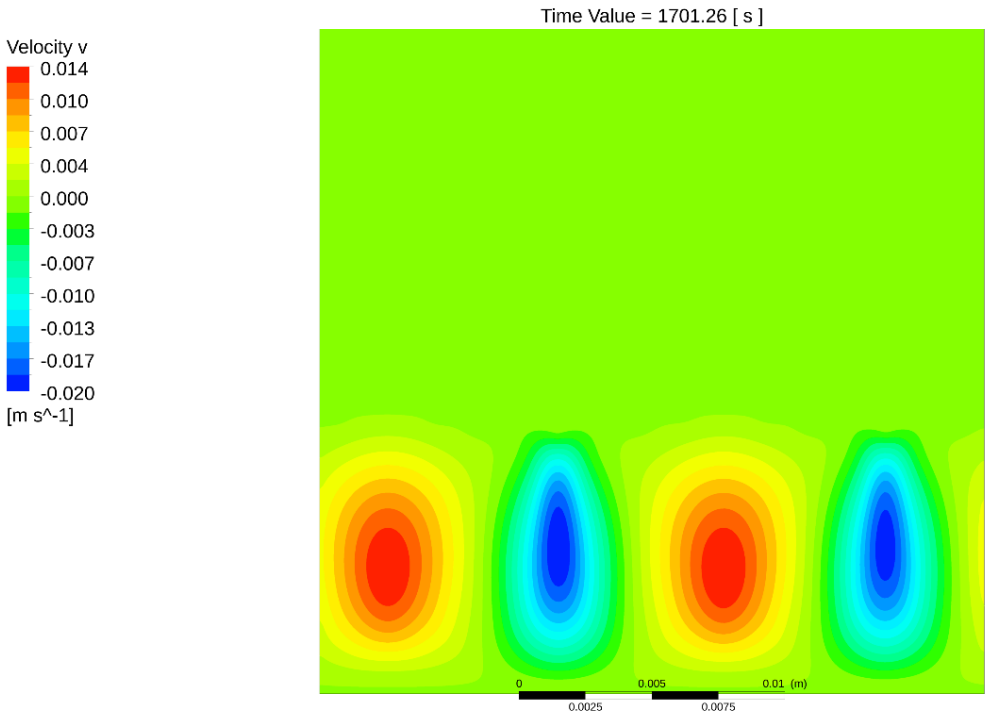

Figure 118 – Y velocity contours for mushy constant value 10^8 flat plate model at 1701.26 seconds.

6.3.2 Heat Transfer Power and convective heat transfer coefficient

Figure 119 and Figure 120 show the power and convective heat transfer coefficient for all models and initially reflect a large initial value ~25000 Wm^{-1} and ~470 $Wm^{-1}K^{-1}$ which can be attributed to conduction instantaneously starting. This is followed by a noisier, convection driven, larger power transfer value with a reducing trend associated with increasing thermal resistance. This is followed by a rapid decrease in power associated with melting completion. Much like the pipe models, larger values of mushy zone constant result in a reduced value of both heat transfer power and the associated convection heat transfer coefficient values (including peak values) after convection has begun.

The onset of convection is seen in all mushy zone constant values in Figure 119 as the reduction in value to a minimum on the curve, followed by a sudden increase in value before tailing off around 100 – 1300 seconds.

Values for power and convective heat transfer coefficients like the melt times show values more than double when comparing mushy zone constant curves 10^3 and 10^8 showing a dependency on the mushy constant, similar when compared to the previous pipe models which approximately doubled in power between the same values of mushy constant.

The extremely noisy power and convective heat transfer signals may be a feature of the flat plate geometry, with increased instability in convection cell formation and development due to a lack of a flow guide or heat source oriented in the Y plane.

The lack of noisy signal in the model of the flat plate with mushy constant value 10^8 is likely attributable to the increased perpendicular flow in as can be seen in Figure 118. It is also possible that this is also demonstrating an unphysical behaviour associated with a lack of model stability or by virtue of the model's geometric configuration and high mushy constant value.

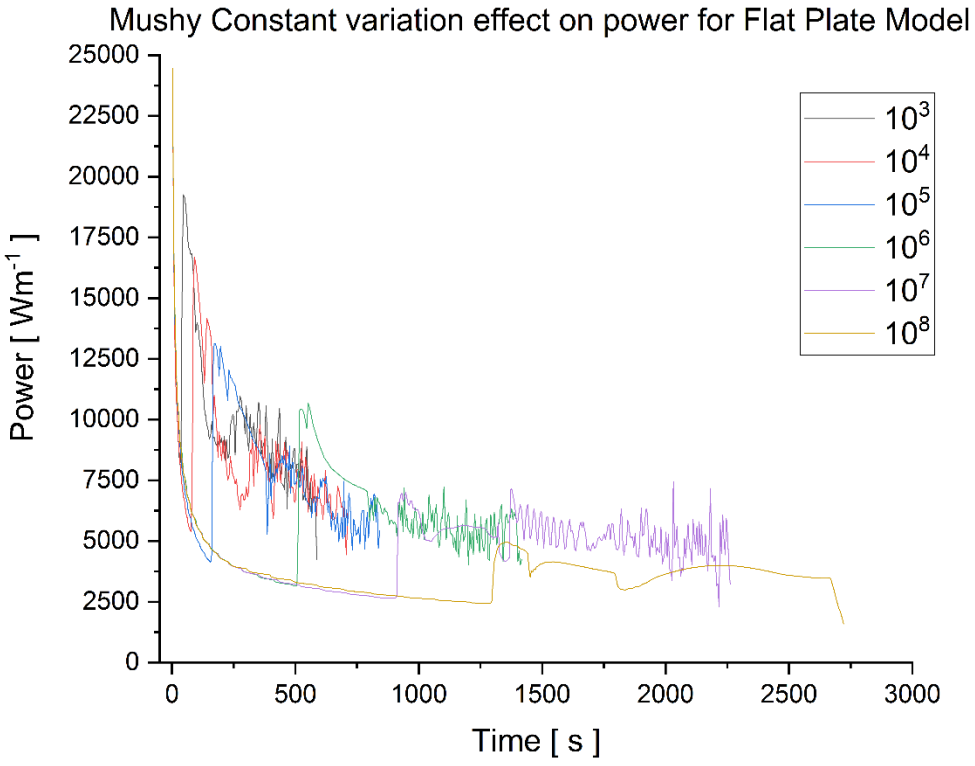

Figure 119 – Power curves for flat plate heated model at various mushy constants.

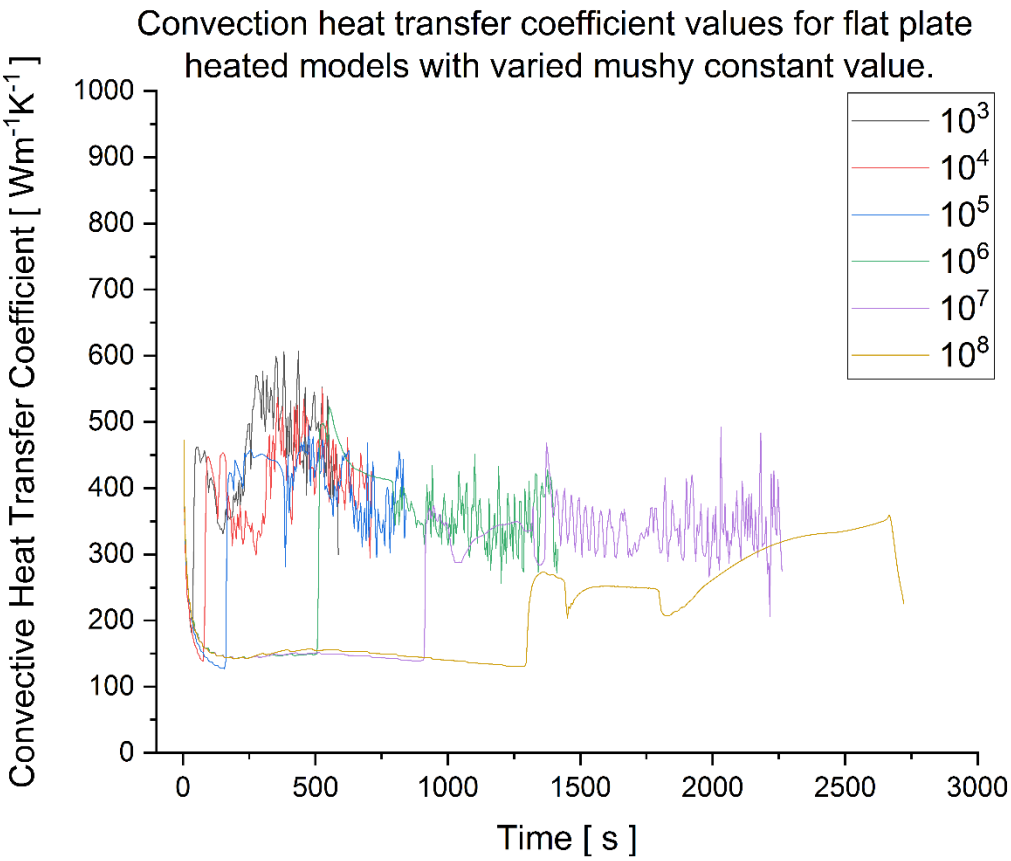

Figure 120 - Convective heat transfer coefficient values for flat plate heated model with varied mushy constant.

The distinct regimes of convective heat transfer coefficient and power value for each mushy constant (more obvious with larger mushy constant values) appear to be related to the number of convective cells reducing and disturbance to flow being caused as flow is disturbed by this process.

6.3.3 Rayleigh Numbers

For this analysis the Rayleigh number and Grashof numbers are defined as follows [3]:

$$Ra = GrPr \tag{31}$$

$$Gr = \frac{g\beta(\tau_S - \tau_\infty){L_h}^3}{\nu^2} \tag{32}$$

Where $\beta_{Beeswax}$ =0.004170747 and L_H =0.025 (m). L_H would usually be the ratio of horizontal plate area to plate perimeter in 3 dimensions. In this case it has been assumed to be the 2D hot surface length [4].

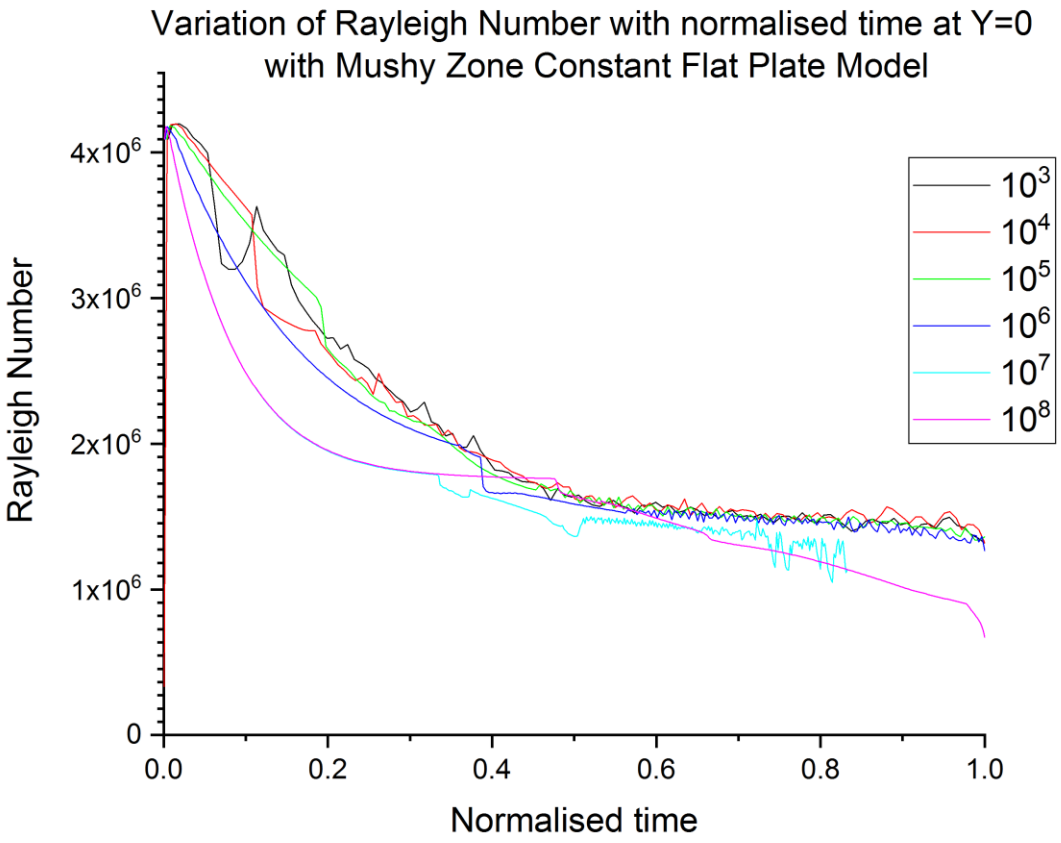

Figure 121 – Rayleigh value samples at centre of flat plate over time for flat plate heated models with varied mushy zone constant.

Figure 121 shows the value of Rayleigh number at a sample point located centrally on the heated flat plate for models of various mushy constants compared with normalised time. All models start with a value around 4.1×10^6 which is significantly larger than the pipe models. It is then seen that each model appears to have a smooth exponentially decreasing value, until the onset of convection, which is denoted by the rapid decrease in value at 0.05, 0.10, 0.20, 0.39, 0.33 and 0.48 for mushy constant values of 10^3 - 10^8 respectively. The onset of convection is also characterised by a subsequently noisy signal.

The off-trend onset of convection time for mushy constant 10^7 is of interest and appears to be a result of the unstable development and movement of the convective cells drifting over the sample point, adjusting the flow structure, causing the Rayleigh number to drift as it is not fixed in a relative position to the forming convection cells.

In addition, the decrease and subsequent increase in Rayleigh number for the model using a mushy constant value of 10^3 could also be an due to the forming and drifting convection cells, or may be indicative of an unphysical process due to this small mushy constant value.

There appears to be a trend that the larger mushy constant models have lower values of Rayleigh number throughout the melting process (which is more pronounced in 10^6 – 10^8 models) which are likely due to the damping effect on convection that these higher values have. This results in a longer time in the more conduction dominated melting and reduces the value of Rayleigh number.

The increased smoothness of the signal from the 10^8 model may be related to the more ordered flow observed in Figure 115, Figure 118 and Figure 125 or could be an artefact of an unstable or inaccurate model as a result of its large mushy constant value.

In order to determine if the flat plate models show a similar rapidly decreasing value as the pipe models at the end of the melt process, additional modelling time steps would be needed.

6.3.4 Peclet Numbers

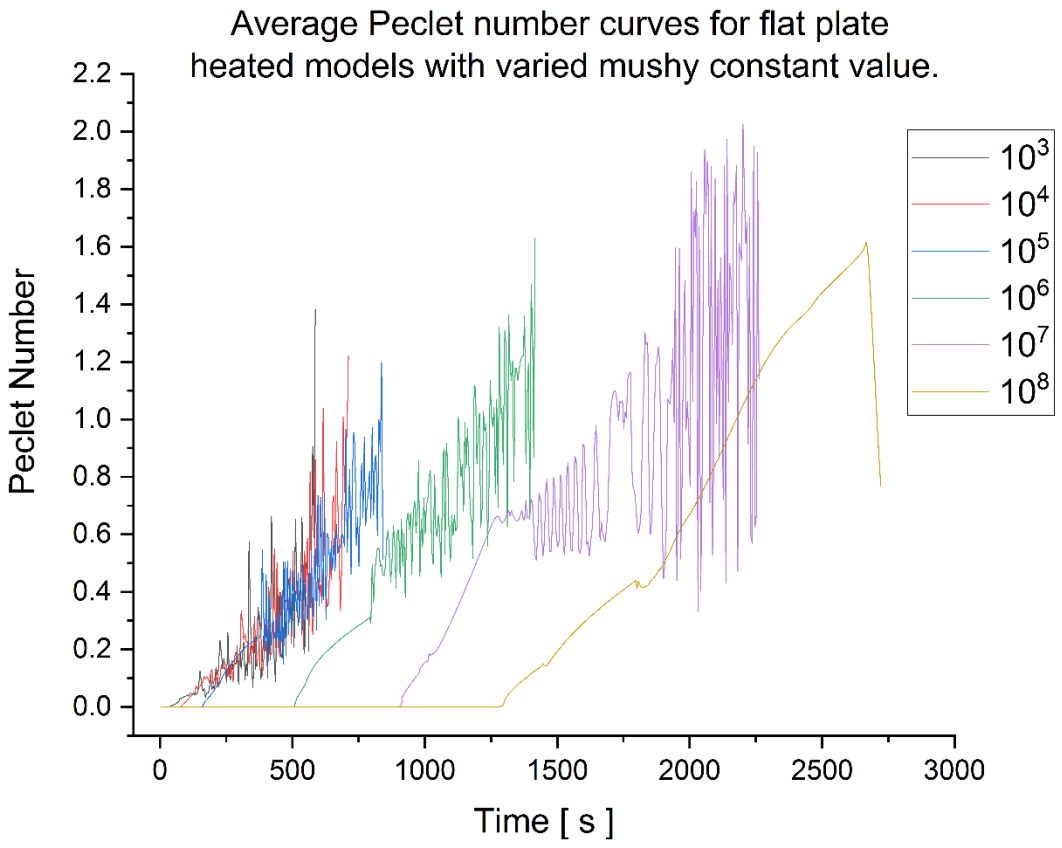

Figure 122 - Average Peclet number curves for flat plate heated models with varied mushy constant value.

For this investigation, the Peclet number has been calculated using the CFD Post software and then an average value across the whole domain has been calculated for each time step.

Figure 122 shows the average Peclet number curves over time for the flat plate heated models of varied mushy constant value. Initially starting at a value of zero, all models develop a much larger value of Peclet number by the time of melt completion, albeit with an extremely noisy signal (more so than the pipe models) which begins with the onset of convection. This increased noise, in comparison to the pipe models, is thought to be caused by the flat plate geometry leading to increased instability in convection cell formation due the lack of a flow guide or heat source oriented in the Y plane when compared to the pipe configurations.

The much larger melt times for increased values of mushy constant are clearly attributable to the increasing delay in the onset of convection as indicated by the longer times at a lower value of Peclet number.

Much like the pipe model configuration in Figure 105, it shows larger mushy constant value models developing larger Peclet values at later times than their quicker finishing lower mushy constant counter parts. This is thought to be as a result of the longer time scale allowing for the convective cells to establish more fully with greater velocity. This is however despite the convection damping effect of increasing the mushy constant value.

Unlike the pipe heated models however the values of Peclet number are not seen tailing off after melt completion due to a lack of extended modelling (with exception to the 10^8 curve).

It is of interest that the curve for the flat plate model at mushy constant value 10^8 has a smooth signal like its pipe model counterpart. Again this may be related to the more ordered flow observed in Figure 115, Figure 118 and Figure 125 or could an artefact of an unstable or inaccurate model as a result of its large mushy constant value.

Figure 123 to 125 show contours of Peclet number which show the convection cells clearly for varied mushy constant values. In particular it can be seen that lower mushy values appear to have much less perpendicular flow around at melt completion.

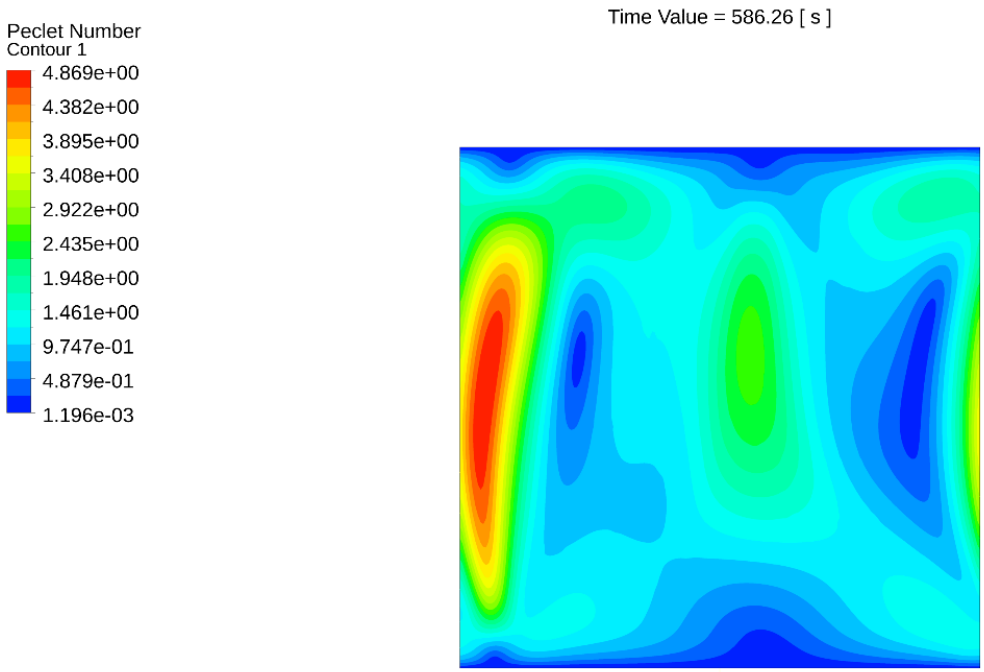

Figure 123 - Contours of Peclet number for flat plate heated model with mushy constant set to 10^3 at time 586.26s.

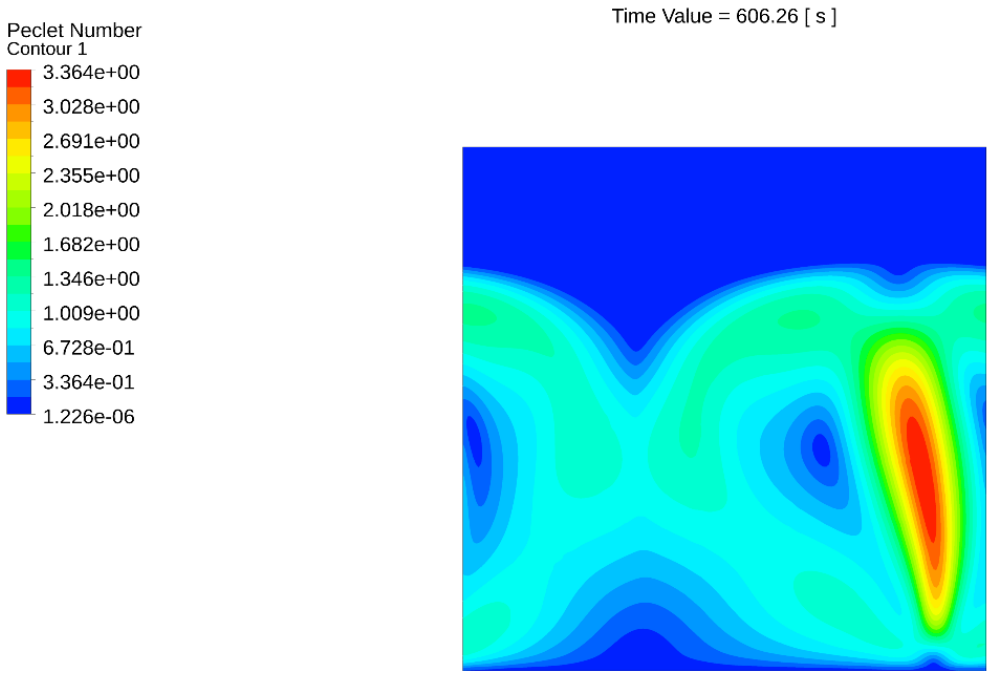

Figure 124 - Contours of Peclet number for flat plate heated model with mushy constant set to 10^5 at time 601.26s.

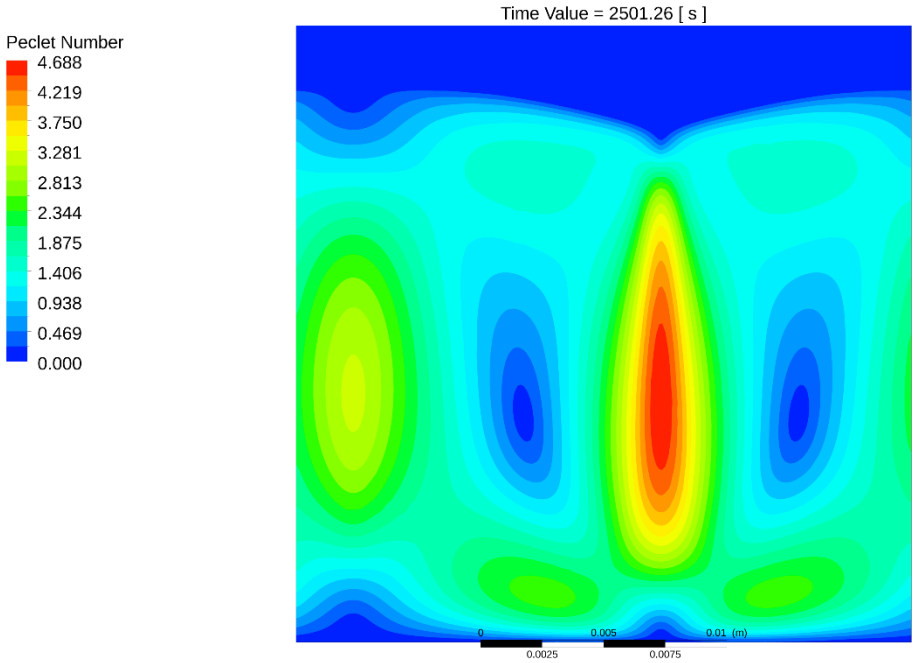

Figure 125 - Contours of Peclet number for flat plate heated model with mushy constant set to 10^8 at time 2501.26s.

6.3.5 Nusselt Numbers

As the specified configuration is one of bottom heated horizontal plates, coupled with the values of Rayleigh number, the Nusselt number correlation utilized is the following [107]:

$$Nu = 0.54\, Ra^{1/4} \tag{33}$$

Where:

$$(\tau_s + \tau_\infty)/2$$

In addition, for this analysis the average values have been calculated from the whole heated surface rather than discrete points.

Figure 126 shows the average Nusselt number curves for the varied mushy constant flat plate models and shows several interesting trends in addition to the dramatically larger value when compared to the previous pipe models. Where the pipe models attain values ~ 1.4 – 1.2 the flat plate heated models vary between ~10.3 and 7. This is associated with the different method of calculation for Nusselt number, but physically this may be explained by the geometry. Where the pipe is effectively 3 types of surface, an upward, downward and perpendicular faces, the flat plate is only one upward face.

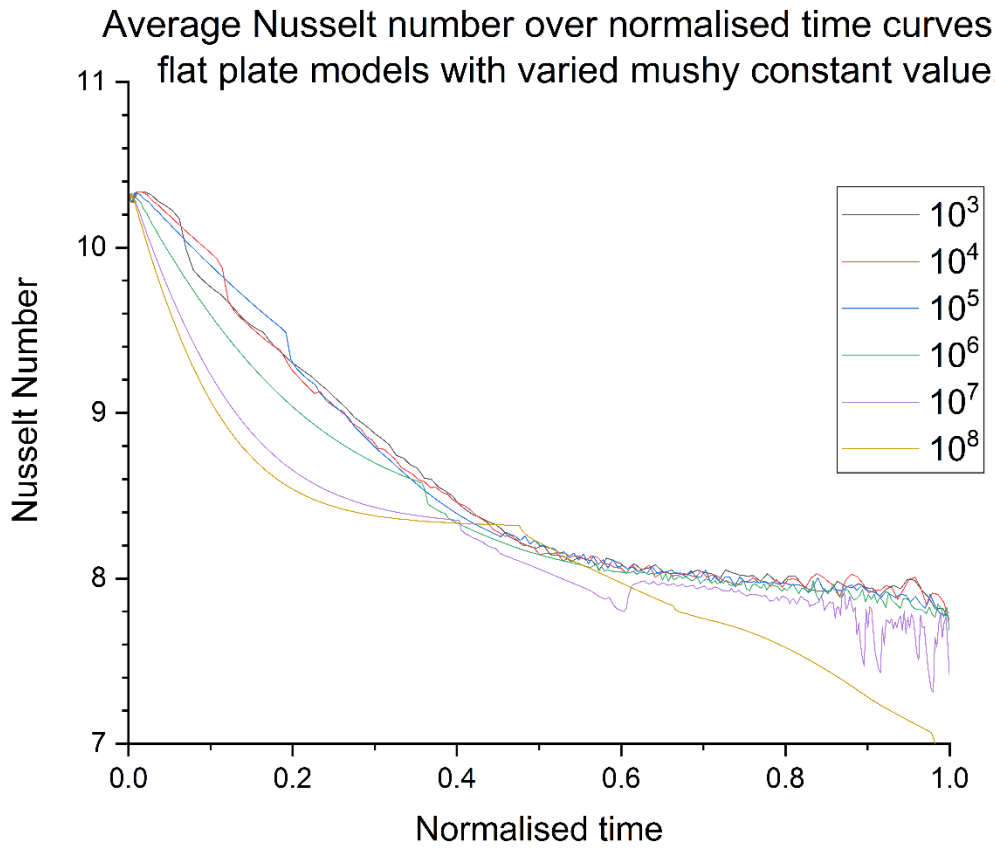

Figure 126 - Average Nusselt number over normalised time for flat plate heated models with varied mushy zone constant.

This figure shows another trend unlike the pipe models: the value of Nusselt numbers show decreasing values for higher mushy constants. The model curves also seem to demonstrate some kind of delayed decrease in value for each, with a sudden drop associated with the formation of convection cells. This can be seen at 0.05, 0.10, 0.2, 0.35, 0.40 and 0.48 for mushy constant models 10^3 to 10^8 respectively. This sudden drop for each appears to indicate the formation / visibility of Rayleigh Bernard cells in the flow patterns. This may be an interesting phenomenon to investigate further as a key indicator of the appearance of cells without contour observation.

It is also seen that mushy constant models 10^6 and above show a much more exponentially decreasing trend before the previously mentioned convection onset, which can be associated by the damping effect of the larger mushy constants, delaying the magnitude and onset of convection giving rise to greater heat transfer via conduction and thus lower Nusselt numbers.

The cause of the noisy signals after ~0.5 on the normalised time axis is not known but may be caused by the same postulated reason for the noisy power signals. It may be a feature of the flat plate geometry and there is increased instability in convection cell formation and

development due to a lack of a flow guide or heat source oriented in the Y plane when compared to the pipe models.

This is further confused by the curve from the flat plate model with a value of 10^8 as it demonstrates no noise at all. This may be related to extremely stable convection occurring, seen in Figure 118 and Figure 125; however this could be an artefact of an unstable or inaccurate model as a result of making the mushy constant value so large.

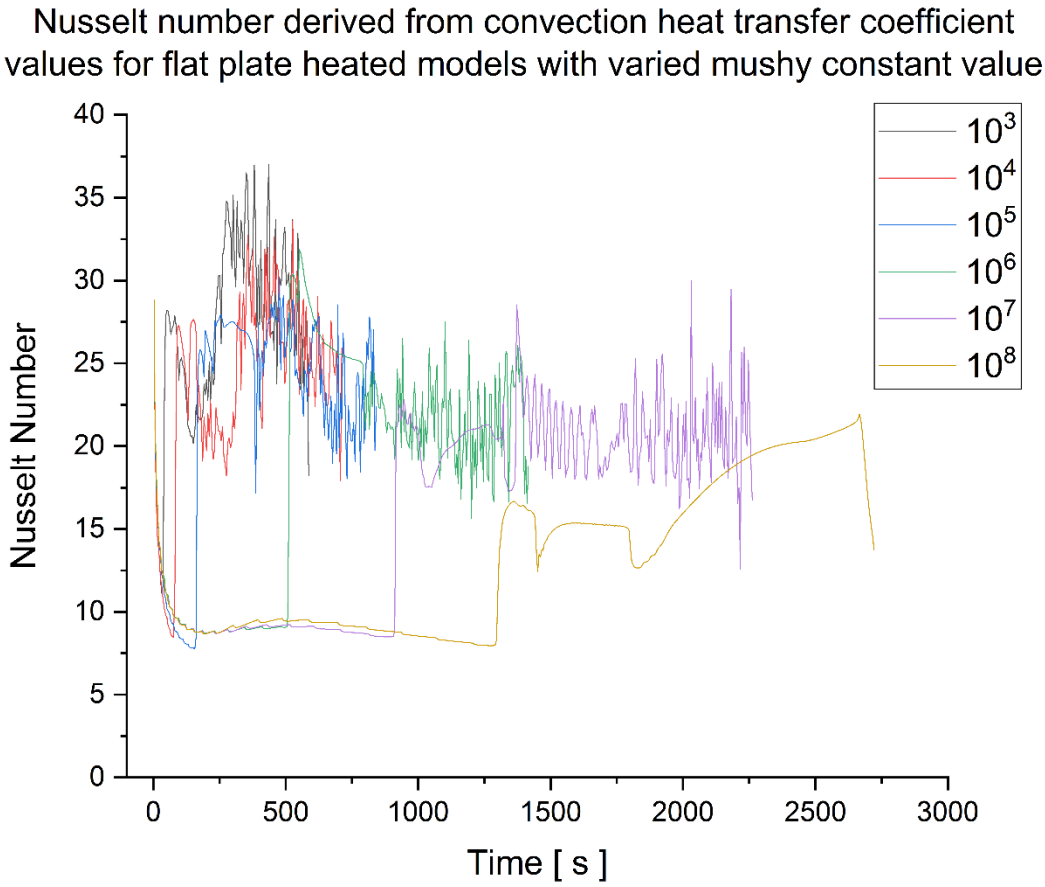

Figure 127 – Heat transfer coefficient derived Nusselt number over time for flat plate heated models with varied mushy zone constant.

Figure 127 show the convective heat transfer coefficient derived Nusselt numbers for the flat plate heated models and has the same curve profiles as Figure 120 - Convective heat transfer coefficient values for flat plate heated model with varied mushy constant. The derived values show a range between 37 – 8, with larger values sustained over the melt process than those in Figure 126 which may indicate that Equation 33 is not accurate.

6.4 Mesh and Temporal Dependency

Mesh generation for this 2D domain was one of unstructured quadrilaterals with adjustment to maximum face size to change the number of generated cells. Proximity and curvature were turned on to account for the curved pipe surface and care was taken to prevent sub-optimal cell generation.

As with the previous chapter, the pipe geometries did not demonstrate an optimal time step choice with 1s, 0.5s, 0.25s, 0.1s and 0.05s investigated, resulting in melt times of 1004s, 542s, 706s, 940s and 1246s respectively. Again, no clear choice was indicated and 0.25s was chosen as this had been used for the previous investigation. The same mesh for the pipe models with 55,000 cells was utilized for this investigation.

The flat plate configuration utilized the previously determined optimal time step of 0.25s (Chapter 4) with an increased mesh resolution of 55,000 cells to match the pipe configuration.

6.5 Conclusions

This chapter has investigated the effect of changing the value of the mushy constant two configurations of the isothermally heated melting process of beeswax, one flat plate heated from below and the other with a pipe mounted on the bottom surface of the domain.

It has been found that like previous research, a larger mushy constant has led to an increased time for melt completion.

Interestingly this effect appears to vary depending on the geometry being investigated, with proportional increases of melt time differing for the pipe and flat plate geometries.

The pipe geometries melt faster than flat plate geometries, as expected, due to the reduced volume of material to melt, the increased heat exchange surface and the different proportional increases of melt time may be related solely to the geometry or only to the total melt time for a given model configuration. Further geometries and configurations would be needed to investigate this phenomenon.

It is seen via variable analysis that the power and convective heat transfer are decreased with increasing mushy constant for both geometries and both contour and variable analysis of the ongoing melts shows the elongation of melt time is related to delayed onset of convection.

Contour analysis also shows that larger mushy constant values appear to result in decreasing curvature of the liquid-solid interface. This is more pronounced for the flat plate configuration and may be related to the increasing mushy constant values correlating with increasing Y velocity at melt completion and/or may lead to increased lengths of time with conduction

dominance during the early melt process. The additional adjacent melted material subsequently undergoing convection.

It is important to note in this study, that it is not possible to conclude a fundamental mushy constant C is inferred due to the geometric sensitivity, with insufficient parametric sensitivity. Convection in a laminar flow regime is strongly dependent of geometry, so inferences about the effect of the mushy constant can only be made within a given geometric context.

In order to explore the effects of the mushy constant further exploration of further geometric contexts to determine to what extent melt results are affected by an interplay between multiple geometries assessed with multiple values of mushy constant.

In addition it is likely that models may need to be temporally and mesh resolution optimised for each mushy constant as higher values of mushy constant appear to correlate with increasing signs of sub-optimal time step setting / mesh resolution.

Determining whether this is the case would require further modelling to investigate conditions of multiple fixed geometry and timestep models with progressively more detailed meshes to ascertain a resolution sufficient for insensitivity in results.

Further to this, investigation of the effect of changing timestep with any mesh independent models found would need to be undertaken.

This proposed body of work could represent many tens of if not hundreds of models.

7 Modelling validation and validation method exploration

In this chapter validation of two models of the isothermal melting process of beeswax and paraffin wax is undertaken in order to determine the accuracy and efficacy of modelling a phase change melt process using the Fluent CFD modelling package.

The first half of this chapter details the experimental investigation of the melt process of paraffin wax and beeswax in the previously utilized 5cm multiple material experimental vessel with an additional automated removable piece of insulation for the imaged face. The investigation utilizes both thermal and visual camera imagery for analysis. This experimental data is subsequently utilized to validate the equivalent 5cm x 5cm 2D CFD models.

The second half of this chapter details the experimental investigation of the melt process of only beeswax in a new 15cm dimensioned open topped box instrumented with an additional matrix of temperature sensors and again utilizing an automated, removable piece of insulation for the faces being imaged by the visual and thermal cameras. This experimental data is then used to validate the equivalent 15x15cm 2D beeswax melt CFD model.

These model configurations are intended to explore the validation of the generated models via important characteristics such as melt contours and melting time. In addition to this, the efficacy of using a thermal camera and a matrix array of temperature sensors is also investigated via the comparison of the data gathered during experimentation.

7.1 Visual Imagery Analysis Methodology

In order to plot a melt progression from visual imagery, a short conversion process and subsequent analysis method is implemented using the software ImageJ. The first step is to rotate (if needed) and crop the gathered visual images to show only the experimental vessel. The second step is to convert the image into an 8-bit monochrome image.

The third step is to utilize the ImageJ thresholding tool to select and binarize the image into only black and white. The final step is to have ImageJ calculate the total pixel area of each image and then the area of the melted material in white. This process is repeated for each image and then the data is output into a comma separated value file.

The processed image files are also saved in order to make comparisons in the results sections below.

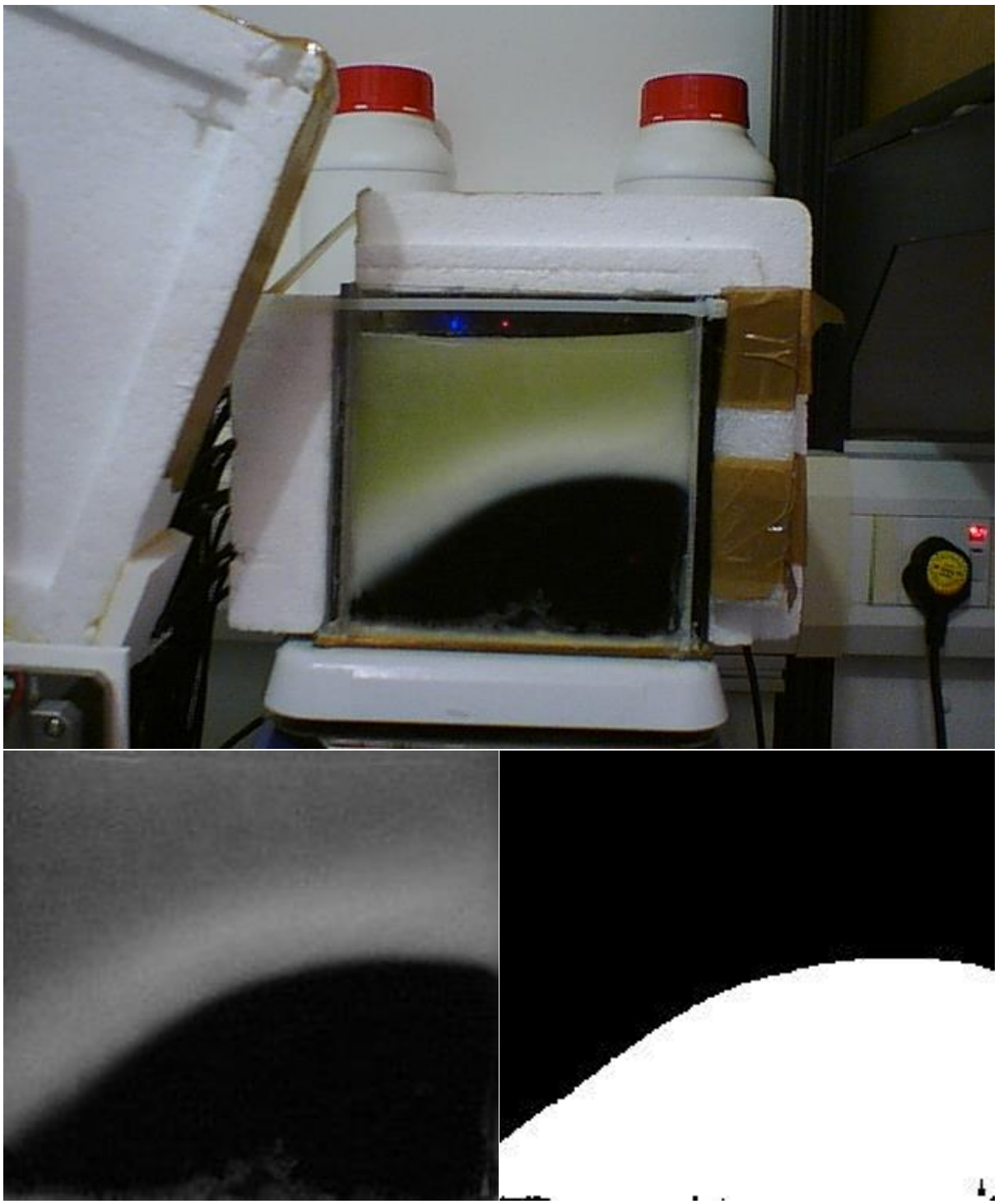

Figure 128- Visual Image processing methodology showing cropping of original image (top) and conversion to 8 bit monochrome (bottom left) into final binary white and black processed image (bottom right.)

7.2 Thermal Data Analysis Methodology

A similar process as for the visual imagery analysis is implemented to determine a melting track from the thermal data.

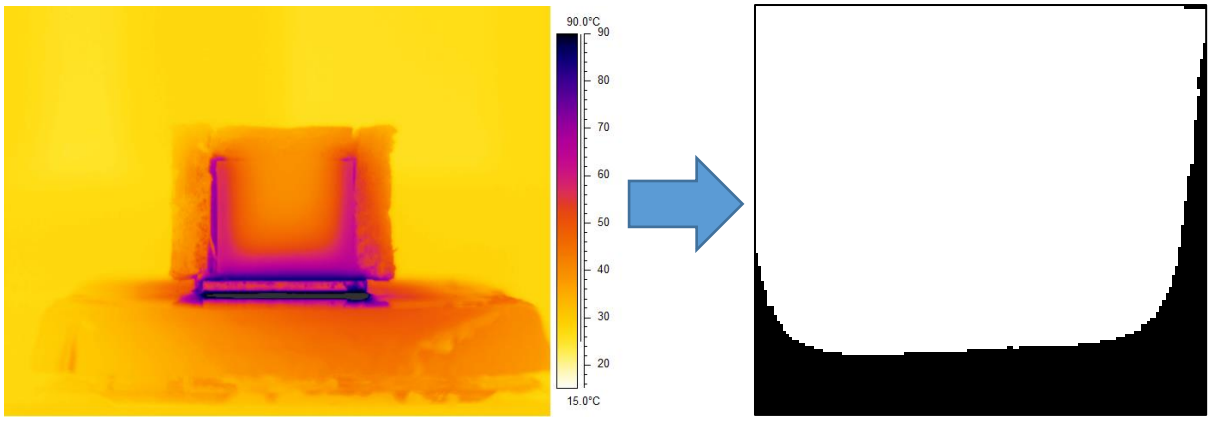

Figure 129 – Thermal image processing methodology showing cropping of original image (left) and conversion to 8 bit monochrome into final binary white and black processed image (right.)

The processing of the thermal imagery is complicated slightly by having first to use the ThermaCAM Researcher 2.10 PRO software, configure the correct thermal range (further detail on this in the results) and change the palette to one which will indicate with a bright hue where material is in the selected temperature range and thus melted material.

The process is then the same as the visual images with any rotation, cropping, conversion to 8-bit monochrome and finally being binarized and the areas of the portions of light and dark being measured. This process is repeated for each image and the data saved to CSV file format.

The processed image files are also saved in order to make comparisons in the results' sections below.

7.3 Actuated Removable insulation design

Heat losses from the exposed faces under imaging were identified as an issue in chapter 3 and as a result an additional system was developed in order to ensure the faces of experimental vessels under imaging were insulated while imaging was not taking place.

Both experiments in this chapter utilize the same system for the moving insulation. The details for this system are described below.

In order to make the required system the following materials were required.

A piece of 5cm thick and 15cm x 15cm polystyrene, extruded aluminium channels, various T-slot connectors, a stepper motor (NEMA17), stepper motor driver (DRV8825), 12 volt power supply, Raspberry Pi and two custom made 3D printed parts to connect the NEMA motor to the extruded channels and the polystyrene.

Using the aluminium channel and T-slot connectors, a framework was constructed to hold the

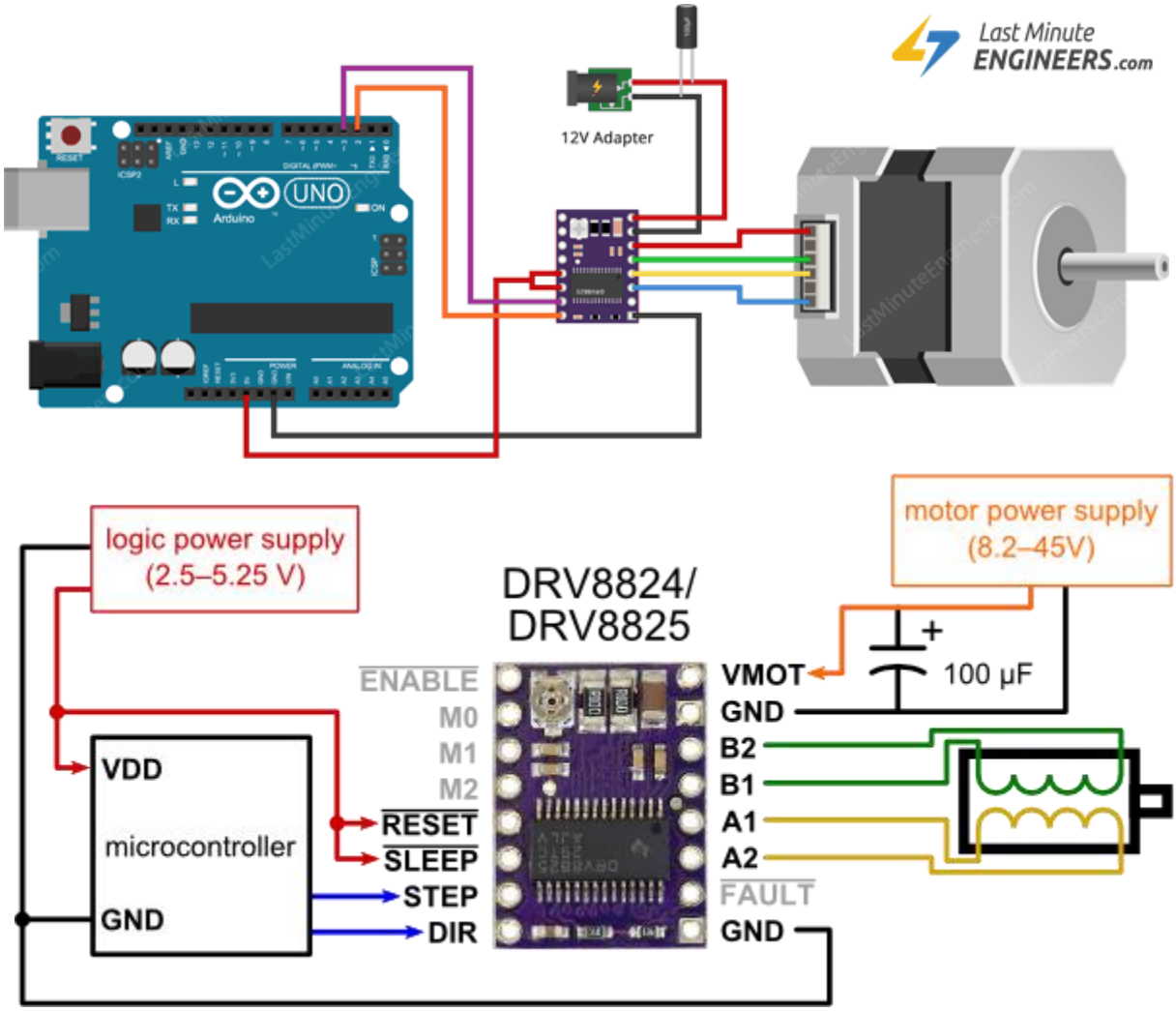

Figure 130 – Actuated removable insulation electronic circuit schematic.

stepper motor and insulation assembly. The lab top heater sat on top of the rectangular framework with a vertical column at the front of the framework with which to hold the stepper motor and insulation at the bottom left of the experimental vessel to reduce the torque required from the motor. This was necessary as rarely, even in this configuration, would the stepper motor be unable to fully lift the insulation. As a precaution, later proven necessary, the framework was placed on top of a large overflow basin in case of leakage.

Sequentially and synchronously to remove, image and replace a large piece of insulation over the imaged face, a small amount of Python and Bash programming code was developed for the Raspberry Pi. The Raspberry Pi utilized the Debian Operating system.

This code was also extended to support polling the DS18B20 temperature sensors for the larger 15cm vessel.

This insulation actuation was typically operated every 5 minutes or 1 minute.

Figure 131 - Larger experimental test vessel imagery showing actuated face removed for imaging (left) and moved to cover imaging face to prevent thermal losses (right.)

7.4 Introduction – 5cm Box Experimental

This section details the investigation of beeswax and paraffin wax in the 5cm experimental vessel detailed in Chapter 3. These experiments were intended to validate subsequently generated equivalent CFD models.

7.4.1 Vessel Design

The vessel design for this experiment is identical to the details found in chapter 3 with the addition of the previously described automated removable insulation for the imaged face and with the other pieces of insulation now permanently glued to the vessel.

7.4.2 Operation Methodology

The operation methodology was very similar to that of chapter 3 and was as follows:

The correct material was added to the vessel prior to experimentation and the cameras and automated insulation moving system tested. The test vessel was then placed on the non-heated lab top heater (IKA C-MAG HS 7), the cameras aligned and the apparatus straightened for optimum imaging.

Both beeswax and paraffin wax were supplied from Sigma Aldrich CAS numbers 8012-89-3 (bleached wax) and 8002-74-2 (paraffin wax 58-62 °C ASTM D 87.)

In order to match the subsequent models as closely as possible the lab top heater was set to provide heat isothermally at 80 °C and when ready the heating was activated.

The FLIR SC-Series thermal camera (SC640) (now operated via the ThermaCAM Researcher 2.10 PRO software which allows for improved analysis) and PLAYSTATION Eye ™ webcam were operated synchronously to take images at a pre-set interval of 5 or 1 minute with the latter operated via the Raspberry Pi.

Data recording was operated until melt completion and then data gathered for the solidification process. The assembly was allowed to cool for 24 hours and then more cycles operated.

This design proved functional; however there was small leakage of PCM during operation, albeit not enough perceptibly to change the fluid level.

7.4.3 Results

In this section the results of the 5cm box PCM melt experiments are presented, discussed and compared.

7.4.3.1 Beeswax 5cm box melt experiment

Table 9 - Beeswax 5cm box experimental melt completion times.

Type of Melt Track	Run 3 Time [s]	Run 4 Time [s]	Run 5 Time [s]	Time difference from Run 3 to 5 [s]
Non-normalised Thermal @98%	5160	4440	3900	360
Normalised Thermal @100%	4620	4080	3900	780
Normalised Thermal @98%	4320	3900	3600	780
Visual @98%	4200	3900	3900	300

As can be seen in Table 9, several different types of times are shown in different runs. The numbering of the run scheme is in order of experimentation and omitted runs are due to equipment failure or interference (e.g. equipment being knocked out of alignment, turned off

or equipment damaged during defacement by other lab users). The first is a non-normalised thermal time where the temperature range selected for masking to calculate the melted area was the melting temperature of beeswax (62.95 °C) or above. When observed by eye and compared to the standard camera data it was seen that the masking did not match the visual data. This like likely due to thermal attenuation through the imaged face resulting in a lower temperature on the surface compared to the fluid behind it. As such, an attempt to account for this was made using the normalised thermal time. This normalised thermal time adjusts the threshold temperature lower in an attempt to match the masking of the thermal imagery with the equivalent visual imagery. In this case, it was found that a temperature threshold of 58 °C and above appeared to match most closely. The final type of time provided is that of the visual imagery analysis and as such is the most accurate.

As this data is imperfect and data sets do not perfectly meet 100% melted in all cases, the highest % observed in all cases (98%) is provided for all types of time.

Observing the thermal melt times, it becomes apparent that the thermal imagery provides a less optimal melted fraction track with values requiring additional processing (tuning the thermal threshold) and still getting values of melt completion time between 0 – 5 minutes in error over processes 65 – 70 minutes long.

When comparing the melt times of beeswax in these cases with those found in Chapter 3, it is seen that the melt time has been dramatically reduced from 157 minutes (9420s) to 3900 – 4200 seconds demonstrating the effect of the increased insulation and the automatic actuated insulation.

Plots of each type of time can be found for beeswax in Figure 133, Figure 135 and Figure 136. When cross referenced, it is seen that normalised thermal imagery and visual imagery have very similar trends, with each subsequent run appearing to have a reduced melting time which is an intriguing result. It is thought that this reduction in melting time might be attributed to the beeswax material taking up copper / aluminium into solution as a result of galvanic corrosion / oxidation ongoing in the vessel materials. The increased aluminium reactivity compared to the copper, direct contact between the two materials from the base and wall with beeswax fluid, has visually changed the beeswax colour from bleached white to a tint of green and the vessel itself shows fouled surfaces. This galvanic corrosion phenomenon has been widely demonstrated with mixed copper-aluminium heat block water cooling systems and leads to severe material degradation. Due to the reducing melt times it is not possible to draw any conclusions about the difference in results when varying the sample rate.

Figure 132 - Comparison of virgin beeswax pellets (left) and beeswax after experimentation (right).

The omitted values in run 5 are due to the insulation failing to move and care has been taken to try to remove these types of corrupted data points from all figures and analysis.

The earlier section of the visual melt track for run 5 appears to show an increased rate, the latter section finishing at around the same time as run 4 in Figure 133. In contrast Figure 136 shows run 5 completing earlier than run 4 which is not accurate and may be partially due to increased thermal transmission with little solid material left or may be due to the dropped temperature threshold being sub optimal.

Figure 134 shows unprocessed and processed visual imagery for the melt process of beeswax in run 3. It is seen that the solid beeswax material contrasts highly with the dark melted material, giving the processed imagery very little noise with an extremely well defined solid-liquid interface. It is clear that the processed imagery matches the melt contours accurately and that if desired, programmatic shape analysis would be rudimentary.

The ongoing melt process shows that heat is being preferentially delivered to the sides of the vessel, likely as a result of the vessel design (metal walls) and the convective cell formation. As the melt develops material melts further and further inward until leaving a progressively thinner column. There appears to be a slight bias with increased melting on the left wall which is expected as this is the copper wall which has better thermal properties than the aluminium (right wall.)

When compared to the thermal imagery equivalents in Figure 138 they are visually extremely similar; however the comparative imagery provided in Figure 137 show that while the images are very similar, there are slightly different profiles for the thermal and visual imagery, giving rise to the differences observed in other plots. This discrepancy makes clear the short comings of the thermal imagery due to the heat dispersing through the vessel wall. This leads to less sharp definition and a different liquid-solid interface location compared to the visual imagery.

It was hoped that with the addition of the automated removable insulation that further detail into the convective fluid flow may be realised; however Figure 138 clearly shows no such detail. This could be due to a number of factors including camera distance, camera resolution and the geometry (size) of the test vessel.

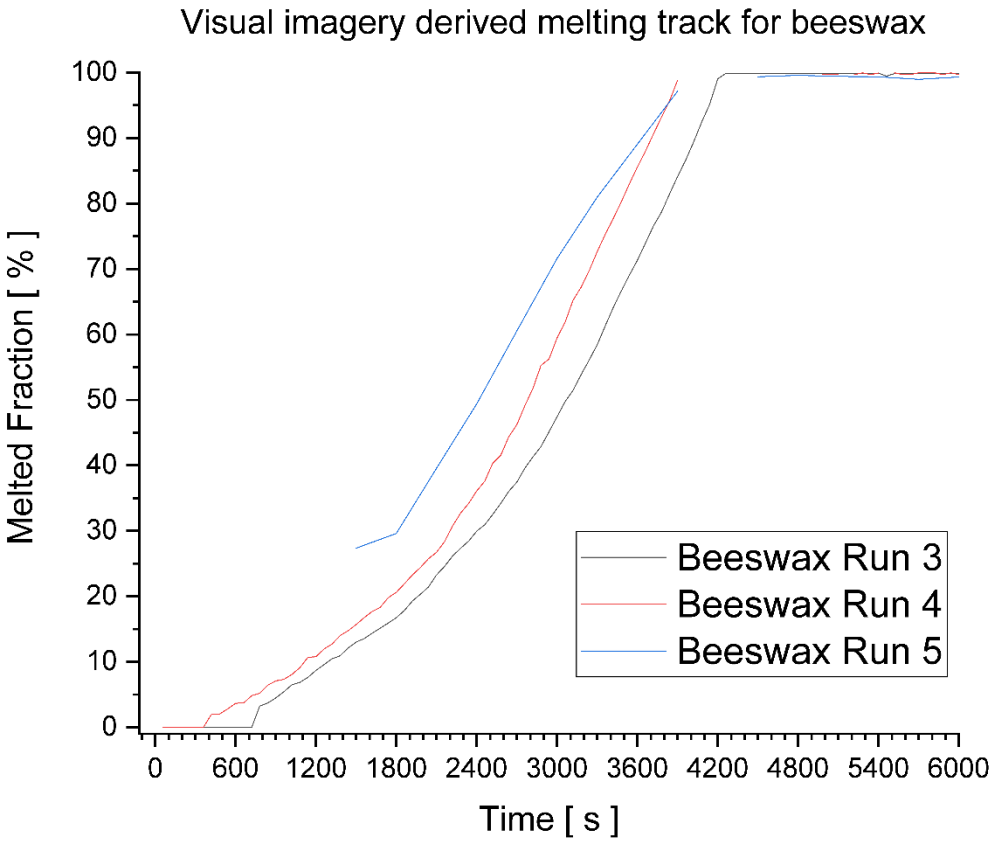

Figure 133 - Visual imagery derived melt track % for 5cm box beeswax experiments.

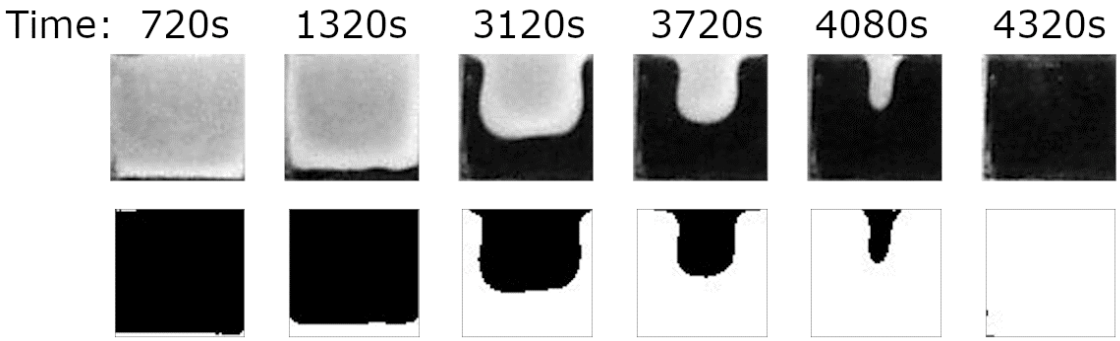

Figure 134 - Visual imagery unprocessed (top) and processed (bottom) at various times for 5cm vessel beeswax melt 3.

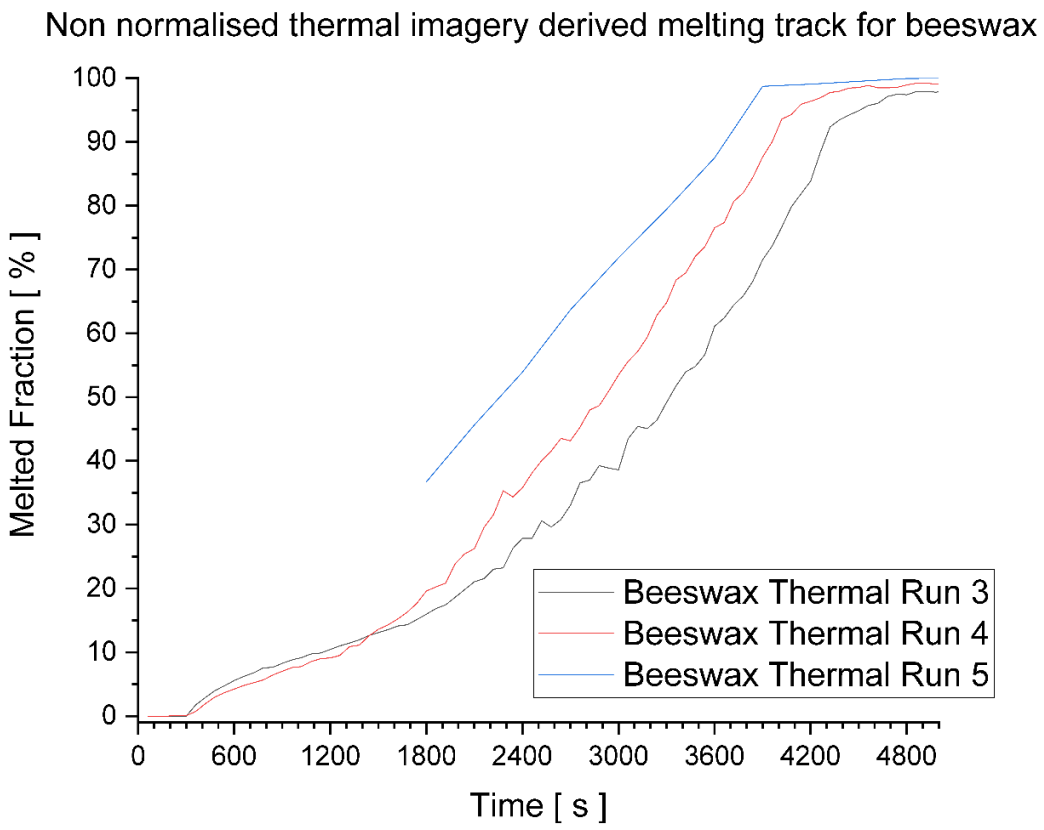

Figure 135 – Non-normalised thermal imagery derived melt track % for 5cm box beeswax experiments.

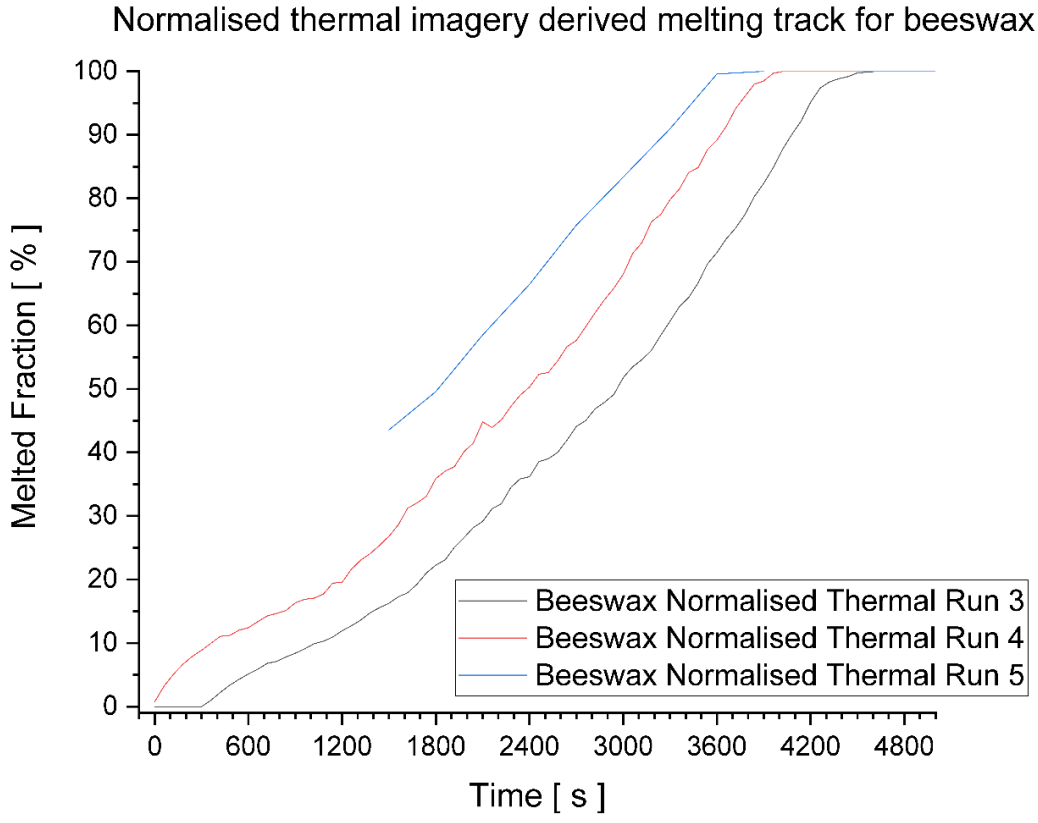

Figure 136 - Normalised thermal imagery derived melt track % for 5cm box beeswax experiments.

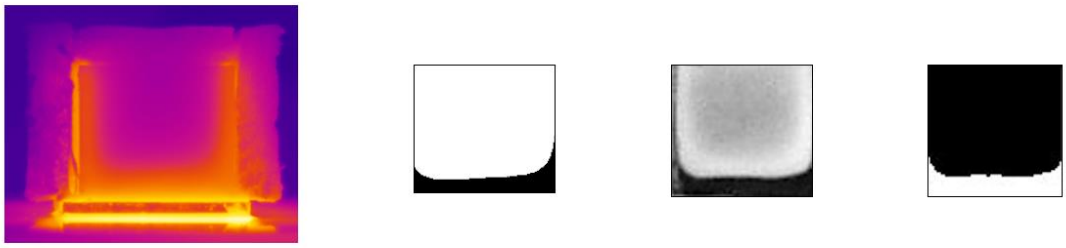

Figure 137 – Comparison of thermal unprocessed (far left), normalised thermal processed (middle left), visual unprocessed (middle right) and visual processed (far right) for 5cm vessel beeswax melt 3 at 1800s.

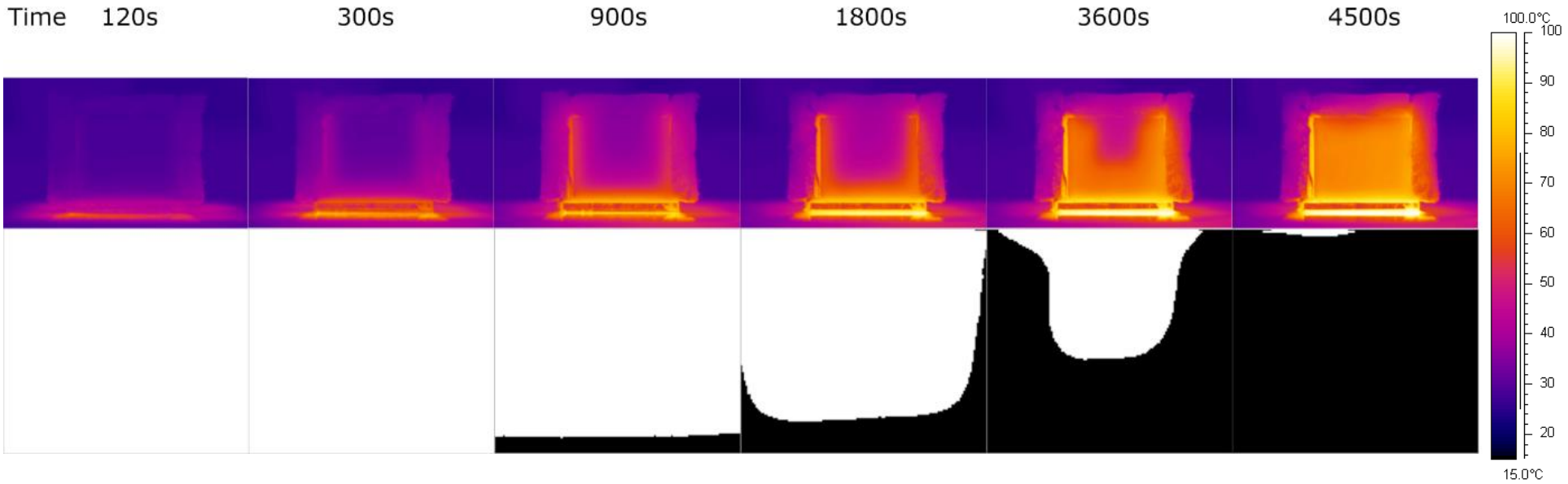

Figure 138 -Thermal imagery unprocessed (top) and normalised processed (bottom) at various times for 5cm vessel beeswax melt 3.

7.4.3.2 Paraffin wax 5cm box melt experiment

Table 10 - Paraffin wax 5cm box experimental melt completion times.

Type of Melt Track	Run 3 Time [s]	Run 5 Time [s]	Time difference from Run 3 to 5 [s]
Non-normalised Thermal @98%	5700	4500	1200
Normalised Thermal @100%	4800	4440	360
Normalised Thermal @98%	4500	3960	540
Visual @98%	4200	3840	360

Like the beeswax 5cm box melt time analysis, melt times for paraffin wax of the same time types can be found in Table 10. These classifications and the reasoning for such are the same as for beeswax, with the exception that the temperature threshold utilized for the normalized thermal analysis was 56°C and above. This difference in masking threshold is likely as a result of paraffin wax's different thermo-physical properties such as thermal conductivity and viscosity.

When comparing the melt times of paraffin wax in these cases with those found in Chapter 3, it is seen that the melt time, like the beeswax, has been dramatically reduced from 103 minutes (6180s) to 3840 – 4200 seconds, again demonstrating the effect of the increased insulation and the automatic actuated insulation. In addition, it is now seen that both paraffin wax and beeswax have a similar melt time.

Plots of each type of time can be found for beeswax in Figure 140 and Figure 142. Again, it is seen that normalised thermal imagery and visual imagery have very similar trends, with the subsequent run appearing to have a reduced melting time, likely a result of the aforementioned galvanic corrosion / oxidation as again the paraffin wax material started to develop a slight green hue.

Figure 139 - Comparison of virgin paraffin wax block (left) and paraffin wax after experimentation (right)

Unlike the beeswax 5cm box melt experiments, there are no discrepancies in trend between the runs in paraffin wax, although with only 2 successful runs it is difficult to conclude anything with certainty and it is likely that with further runs thermal imagery could be demonstrably less reliable.

Observing the thermal melt times for the paraffin wax it is reiterated that the thermal imagery provides a less optimal melted fraction track, with values requiring additional processing (tuning the thermal threshold) to attain more accurate melt time values and even when “tuned” these values are 0 – 5 minutes in error.

Figure 141 shows unprocessed and processed visual imagery for the melt process of paraffin wax in run 3. Much like the solid beeswax material the solid paraffin wax contrasts well with the darker melted material but less so than beeswax. The paraffin wax also shows a change in brightness in parts of the solid material that are hotter.

As the contrast between solid and liquid is decreased and with further graduation in brightness, there is additional noise in the processed imagery when compared to the beeswax images in Figure 134. Despite the increased noise the processed imagery matches the melt contours relatively well although further programmatic shape analysis would be complicated due to this increased noise.

The ongoing melt process again shows that heat is being preferentially delivered to the sides of the vessel as a result of the vessel design. In comparison with the beeswax melt process the shape of the ongoing paraffin melt differs significantly. The paraffin melts show the

development of a dual lobe column of material solid material being progressively melted away. This structure difference is likely as a result of paraffin wax's decreased viscosity although it should be again re-iterated that, despite the difference in structure, the melt completion times for both materials are virtually the same.

Figure 143 shows a comparison of the thermal and visual imagery of run 3 of the paraffin wax at 3000s and reiterates that while the imagery appears highly similar, the thermal image shows a slightly less sharply defined liquid-solid interface as a result of the heat dispersion through the vessel wall.

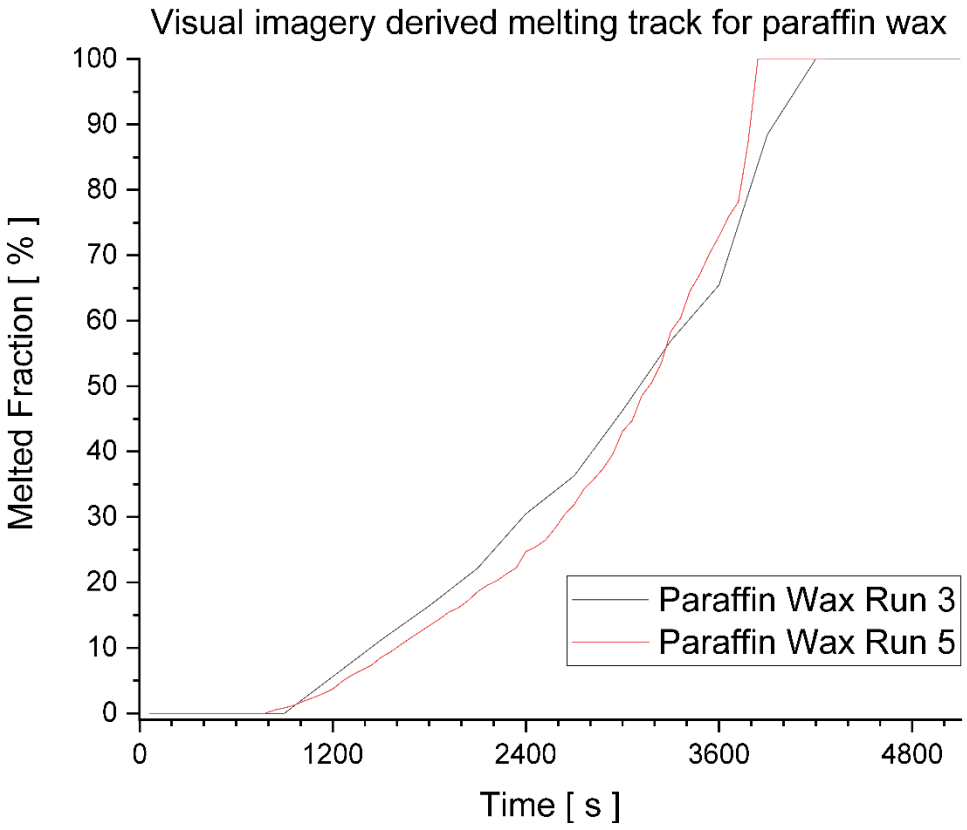

Figure 140 - Visual imagery derived melted fraction % for 5cm box paraffin wax experiments.

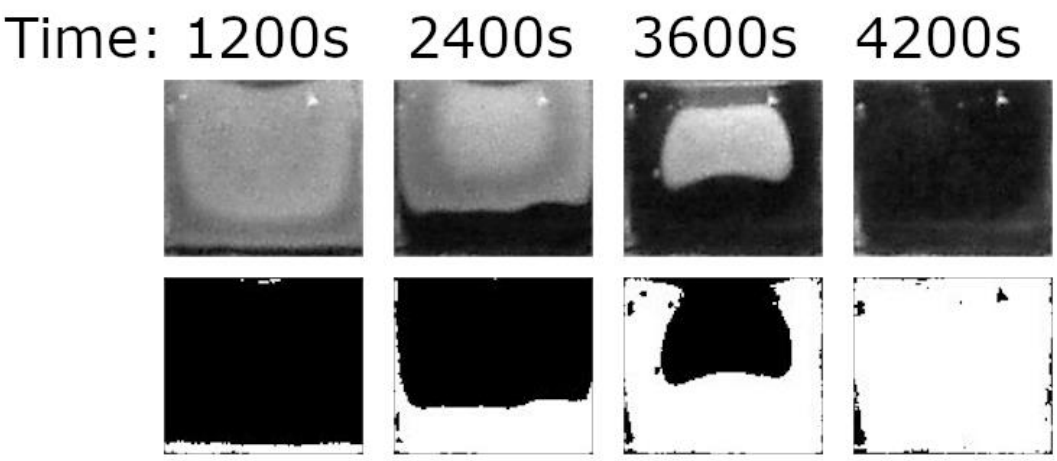

Figure 141 - Visual imagery unprocessed (top) and processed (bottom) at various times for 5cm vessel paraffin wax melt 3.

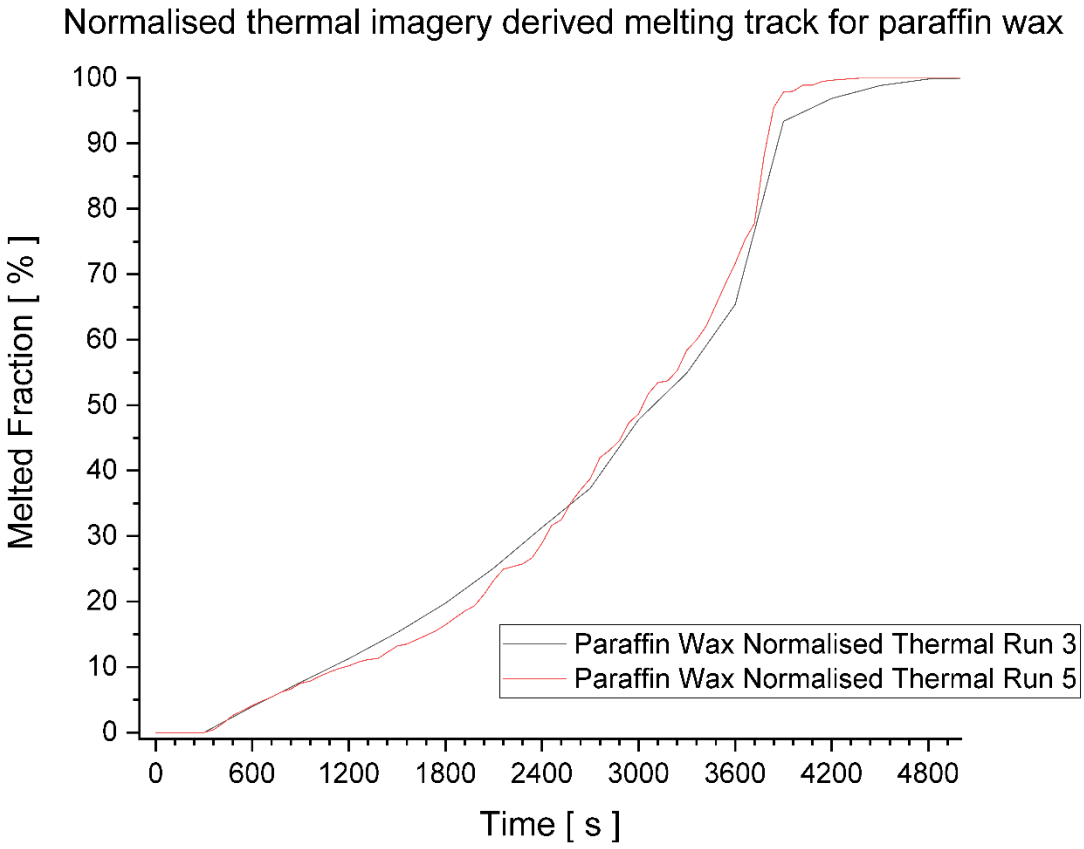

Figure 142 - Normalised thermal imagery derived melted fraction % for 5cm box paraffin wax experiments.

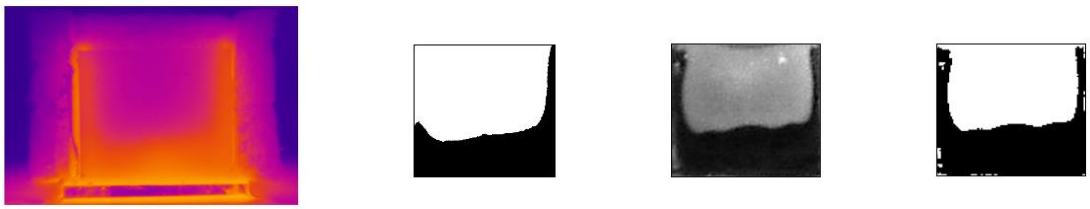

Figure 143 - Comparison of thermal unprocessed (far left), normalised thermal processed (middle left), visual unprocessed (middle right) and visual processed (far right) for 5cm vessel paraffin wax melt 3 at 3000s.

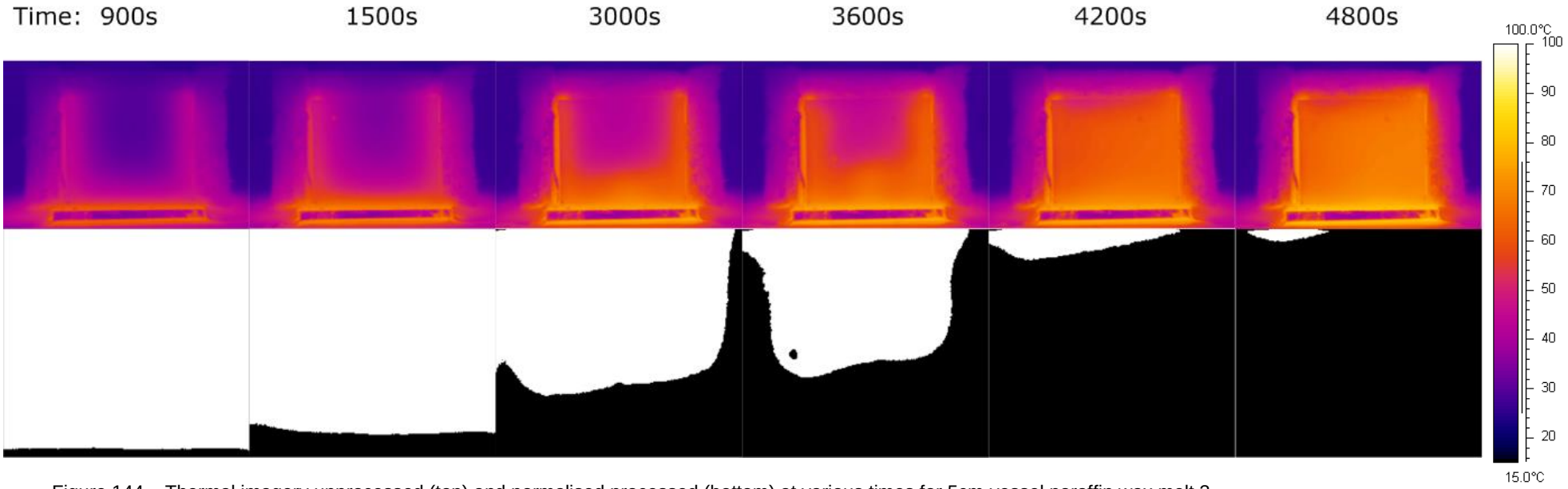

Figure 144 – Thermal imagery unprocessed (top) and normalised processed (bottom) at various times for 5cm vessel paraffin wax melt 3.

7.4.4 Conclusions

The previous section has detailed the investigation into the isothermally heated melting processes of paraffin wax and beeswax in an insulated 5cm dimensioned open top cube utilizing thermal and visual camera imagery.

Both materials were found to finish melting at approximately the same time of 4200s which is an interesting result when considering the larger latent heat and specific heat (40% and 100% respectively) of beeswax, indicating its superior characteristics in this case. In addition it was found that an oxidative or galvanic process lead to doping of the phase change materials resulting in quicker melt times in subsequent experiments for each material.

It was also found that the total melting time for both materials was significantly lower than in the exploratory experimentation in chapter 3 which can be attributed to increased amounts of insulation, particularly with respect to the imaged face now being insulated.

It was seen that visual imagery analysis gives clear imagery which can be processed to give reasonable melt fraction versus time plots. Visual imagery processing for this melt track was found to be slightly less optimal for the paraffin wax as the solid material was found to change in brightness before melting which lead to additional noise in subsequently processed images.

Thermal imagery was found to give a slightly less optimal track for both materials and required tuning of the thermal thresholds used for analysis to give accurate melted fraction versus time curves.

This thermal tuning was required due to thermal attenuation through the imaged wall indicating that the thermal camera was visualising significantly more thermal radiation via re-transmission from the wall rather than direct transmission from the phase change material inside the vessel. Despite thermal threshold tuning, results from these thermal images were still found to be negatively affected by thermal energy dispersing across the imaged face, leading to smooth gradients unlike the sharper visual images. As a result of this, smaller length scale phenomena which were hoped to be visualised were not seen.

While the thermal images confer a similar but lesser quality of data compared to the visual imaging, this investigation shows that the thermal imagery confers no additional useful information.

The utilization of a test vessel with metal walls proved to be undesirable due to significant reductions in isotropy which will complicate the subsequent validation.

7.5 Introduction – Validation of 5cm Geometry CFD Models

This section details the validation of the 5cm domain paraffin wax and beeswax melting CFD models against experiments conducted in the previous section of work.

7.5.1 Computational Domain and Initial and Boundary Conditions

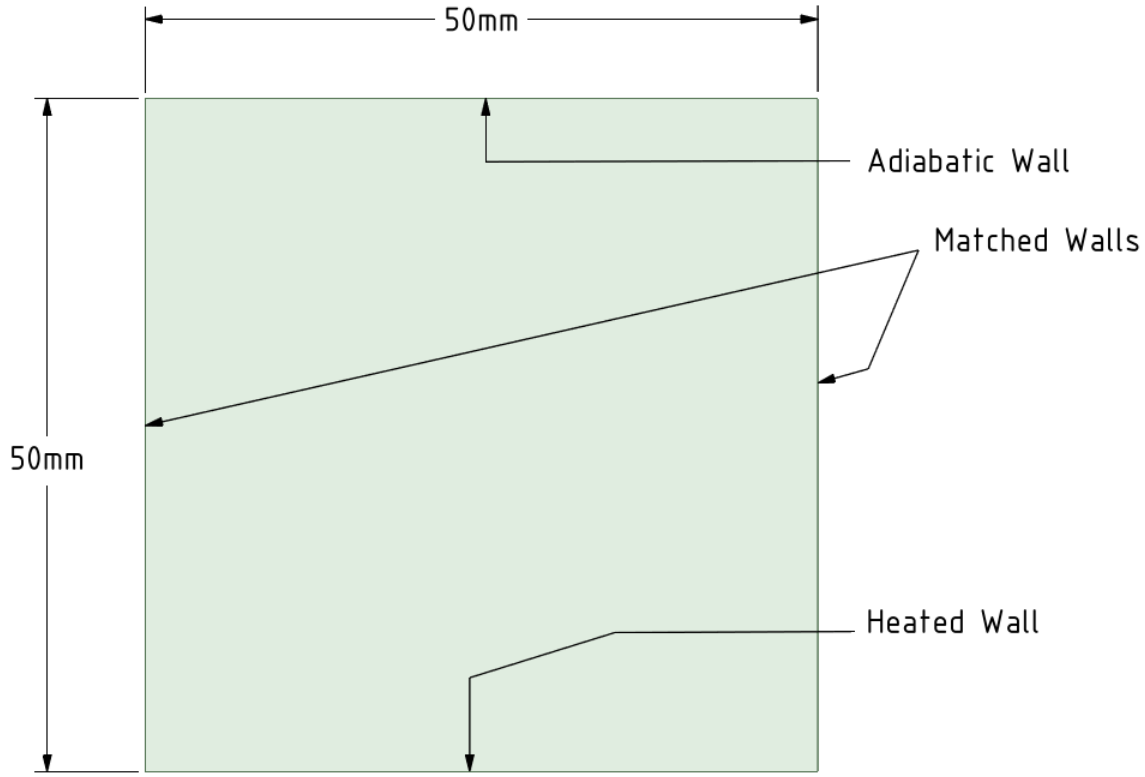

Figure 145 - 2D 50mm square computational domain used for investigation of beeswax and paraffin wax melt process.

These models were computed using Ansys 19.4 and the following assumptions are made in this study: (1) the top wall is adiabatic to represent ideal insulation; (2) flow is Newtonian and incompressible; (3) flow is laminar and under the effects of gravity; (4) joule friction heating is negligible; (5) physical properties are temperature dependant and accounted for using the linear multi-point data entry method for materials properties ; (6) heat transfer occurs by conduction and convection only; (7) volume change is ignored; (8) three dimensional convection is ignored.

The following initial and boundary conditions are applied:

- Bulk temperature - 25 °C.
- Bottom wall - 80°C.
- Top Wall – adiabatic.

- Side walls are matched and allow flow to pass in between.
- X velocity – 0 ms^{-1}.
- Y velocity – 0 ms^{-1}.
- Gauge pressure – 0 Pa.
- Gravity – on, set at -9.81 ms^{-2}

At time $t \geq 0$ the mushy constant value is set as:

$$C = 100{,}000$$

7.5.1.1 Solution Method and Controls:

For the numerical solution of the model the previously given methods and controls were utilized and super compute cluster 2 was exclusively utilized for computation (details of machine hardware and solution methods/ controls given in chapter 2.)

The transient formulation in use for these models was the first order and second order implicit scheme as indicated and the latter was investigated to aid in modelling convergence with respect to temporal step and mesh optimisation.

7.5.1.2 Thermo-physical properties:

Utilized thermo-physical properties are listed in chapter 3 with values in Table 7 and Table 8 and previously experimentally determined densities listed in Table 6. Linear interpolation of temperature dependant values for material characteristics has taken place.

7.5.2 Results – Beeswax First Order Model

This section details the results of the modelling of beeswax in the 5cm dimensioned domain utilizing the first order implicit transient formulation. Unfortunately, it is seen that these completed models do not offer a reasonable comparison to their equivalent experimentation and thus may be invalid. This is potentially due to model settings of boundary changes differing from real life conditions.

The following results are derived from the highest mesh resolution which still converged (higher resolution resulted in inability to find any settings resulting in convergence) with 78,000 cells and the smallest attempted time step of 0.1s. The results presented do not represent the real physical behaviour of the beeswax melt process with no optimal time step or mesh resolution found.

7.5.2.1 Evolution of Melt (time)

The time for total melt time computed for this model was found to be **24240s** and taken in conjunction with the comparison to the experimental time of **4200s** for beeswax run 3 proves conclusively that this model is incorrect. In addition, when comparing the normalised time curves for melt fraction in Figure 146, it is found that while the model shows a similar curve profile as previous beeswax models, it deviates significantly from the experimentally determined equivalent. This further indicates the invalidity of this model. Furthermore, when observing the melt contour comparison in Figure 147, significant differences are seen between the experiment and the model. The model does however follow the previously seen pattern of numerous convection cells forming early in the melt process eventually collapsing into one large cell at completion which is seen in Figure 150 and Figure 153.

While the experiment was non-ideal due to heat losses and metal walls decreasing isotropy, it would be expected that an ideal model of this nature would demonstrate if anything, a smaller melting time than the experimentally determined one and a relatively close curve fit with the model curve having an increased melt fraction for a given time.

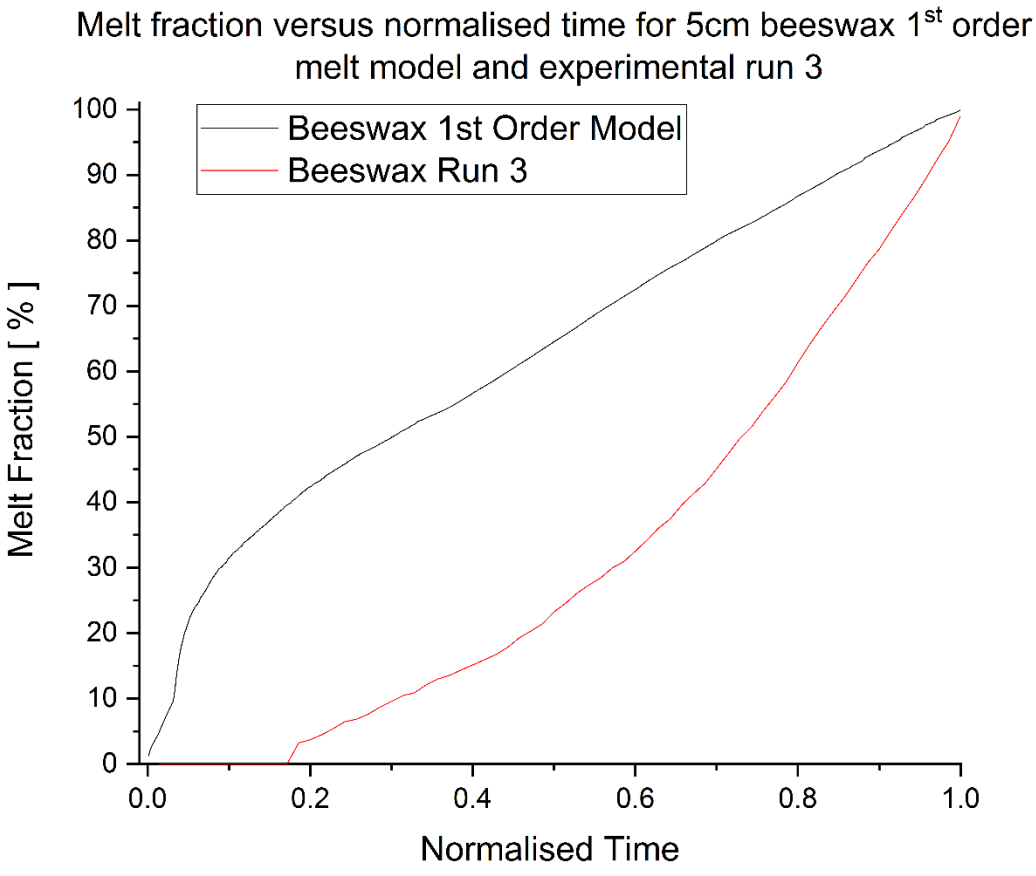

Figure 146 - Melt fraction over normalised time curves for 5cm beeswax 1st order model and beeswax experimental run 3.

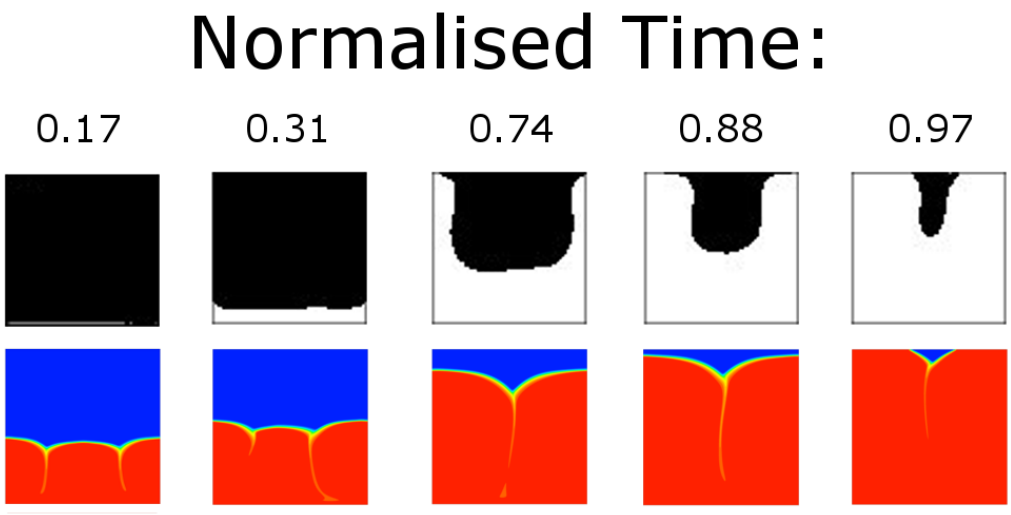

Figure 147 - Melt fraction contours of various normalised times for beeswax experimental run 3 (top) and 5cm beeswax 1st order model (bottom.)

7.5.2.2 Heat transfer power and convective heat transfer coefficient

As can be seen in Figure 148, an initial spike is seen to around 12000 Wm^{-1} attributable to conduction. This lower spike value than previous models is expected due to the decreased save rate for these models to every 30s to reduce total files saved to more manageable levels from 100GB+. The first step saves at 30 seconds resulting in the data before this point not being displayed. The onset of convection is then seen ~900s with the subsequent rise to 13000 Wm^{-1} which then steadily decreases to near 5000 Wm^{-1} at a new feature not seen in previous models around 9000s.

Like previous models, the power value after convection onset steadily decreases; however this model shows another increase in power before a subsequent decreasing trend.

Observing Figure 147 indicates why this is thought to happen; a smaller central convection cell is absorbed by and into the larger convection cell subsequently. It is thought that this process disturbs the convective process, decreasing the heat transfer as it takes place. This process can also be seen in Figure 150 and Figure 153.

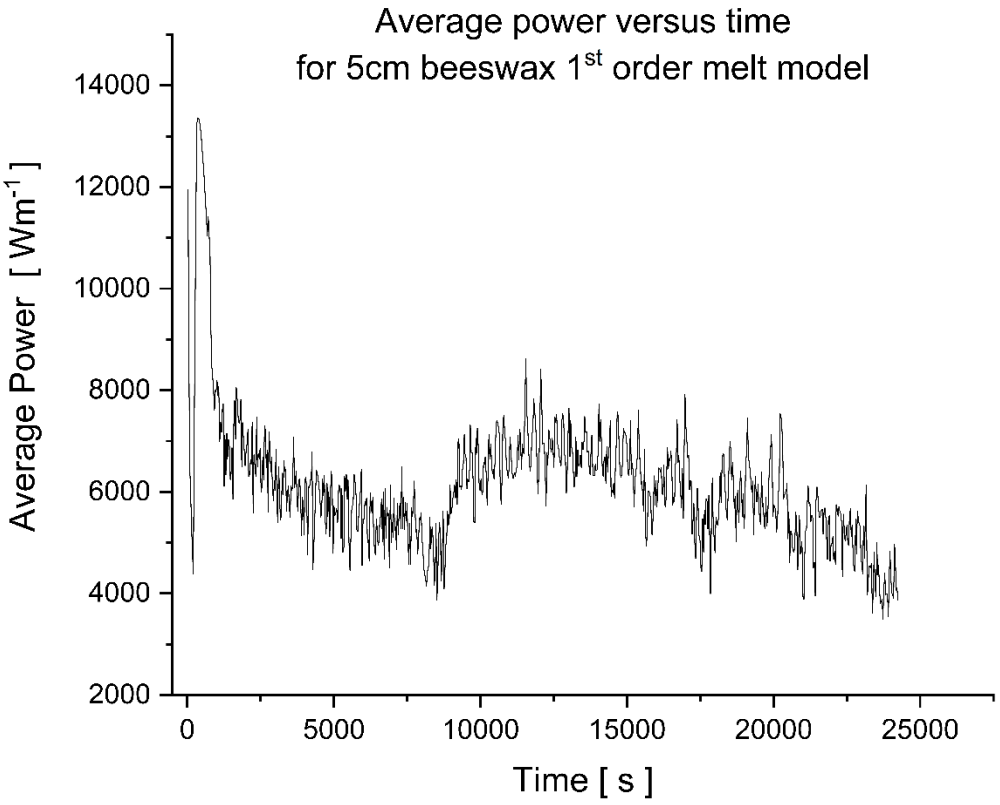

Figure 148 – Average power over time curves for 5cm beeswax 1st order model.

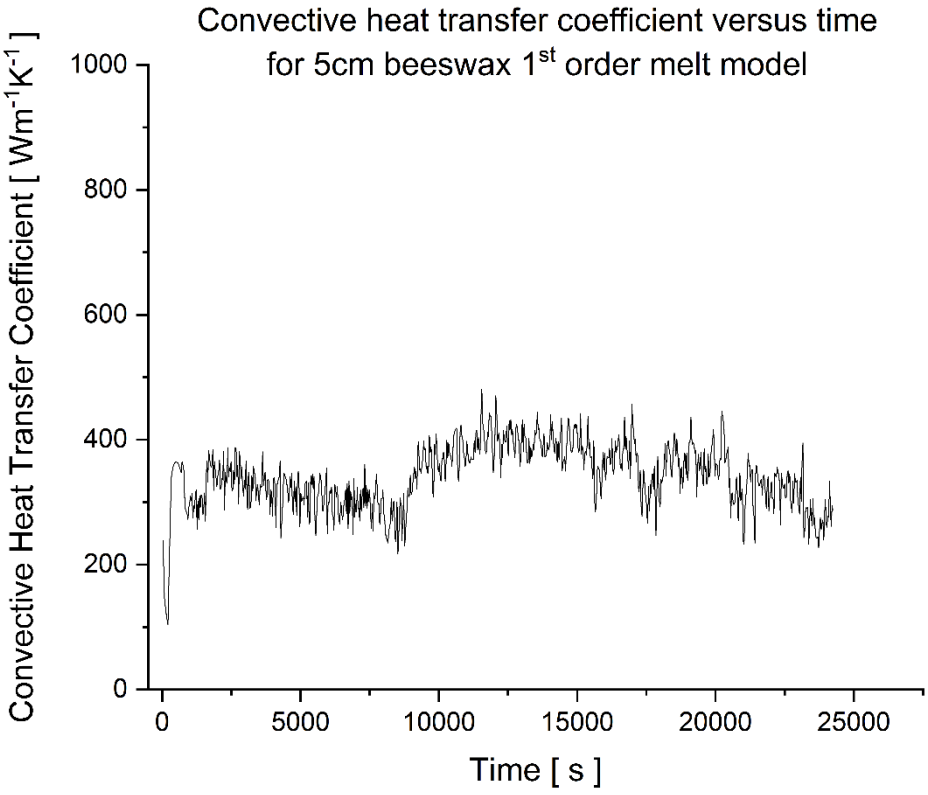

Figure 149 – Convective heat transfer coefficient over time curves for 5cm beeswax 1st order model.

This same power curve profile (albeit over a longer timescale) is also seen subsequently in the second order model and all other second order model plots also show very similar profiles to one another, which indicates that while these models are invalid, they are consistently so.

The convective heat transfer curve in Figure 149 follows the same profile as the power curve, with an initial conduction regime dominant value of ~240 $Wm^{-1}K^{-1}$ exponentially decreasing to ~110 $Wm^{-1}K^{-1}$ where convection begins and causes the increase to ~360 $Wm^{-1}K^{-1}$. The same second rise in value shown on the power curve also occurs on this figure but is reflected with a more modest increase to ~400 $Wm^{-1}K^{-1}$. The values are similar to those previously observed for the 2.5cm model.

Both figures demonstrate a noisy signal when convection is ongoing and decrease in value as they progress closer to melt completion.

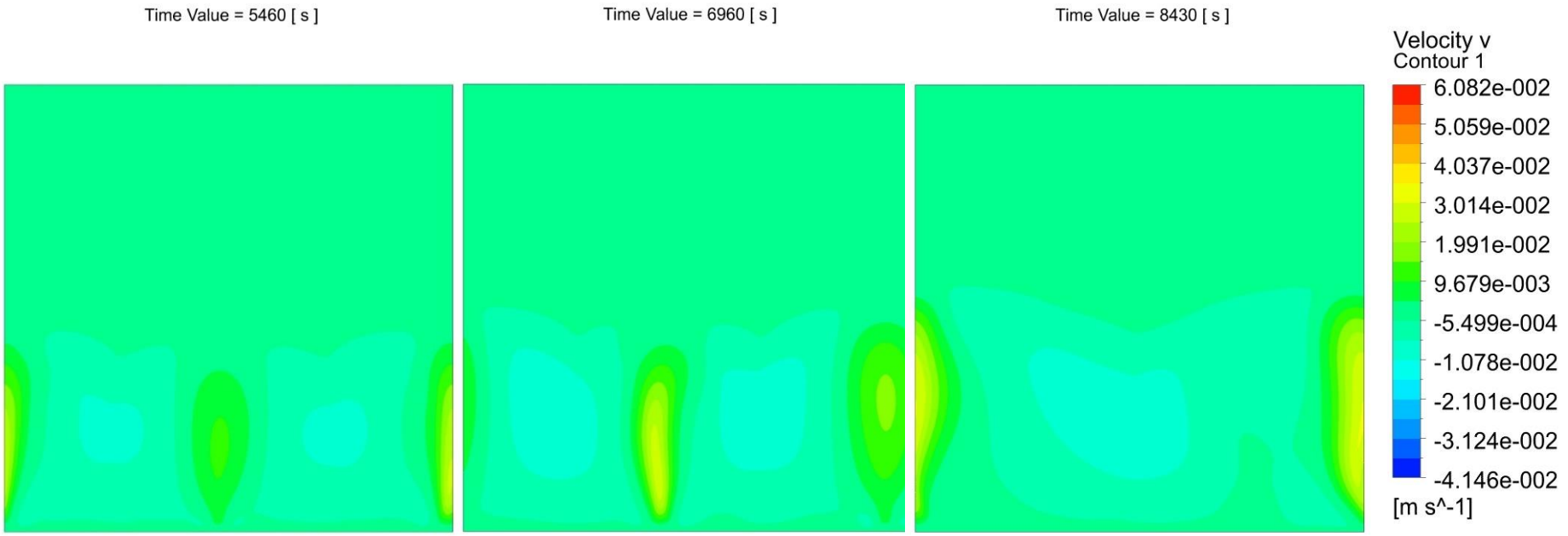

Figure 150 –Contours of Y velocity for 5cm beeswax 1st order model at (a) 5460s, (b) 6960s and (c) 8430s.

7.5.2.3 Rayleigh Numbers

Rayleigh number analysis is undertaken to assess to what extent convection is occurring in each material during the melt process. For this analysis the Rayleigh number and Grashof numbers are defined as follows [3]:

$$Ra = GrPr \tag{34}$$

$$Gr = \frac{g\beta(\tau_S - \tau_\infty){L_h}^3}{\nu^2} \tag{35}$$

Where $\beta_{Beeswax}$ =0.004170747 and L_H =0.05 (m) but would usually be the ratio of horizontal plate area to plate perimeter in 3 dimensions. In this case it has been assumed to be the 2D hot surface length [4].

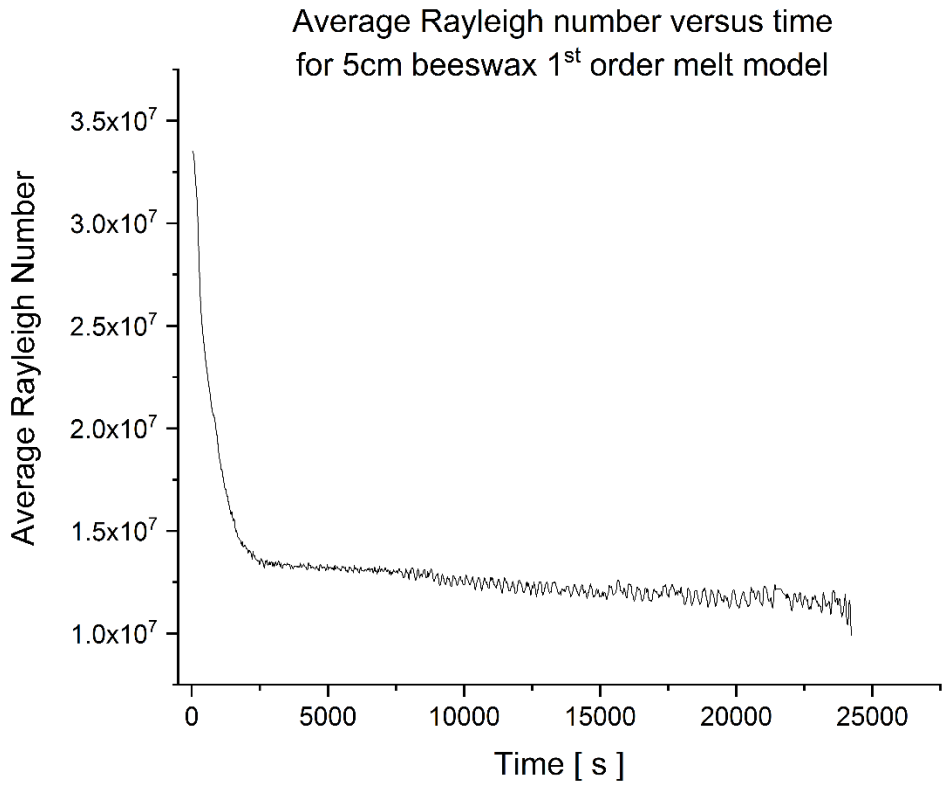

Figure 151 – Average Rayleigh number over time curves for 5cm beeswax 1st order model.

The values computed for average Rayleigh number shown in Figure 151 are determined from the heated surface and are showing a larger value of Rayleigh number with respect to previous models below 10^7. This model follows the same curve profile as previous models with a larger initial value ~ $3.3x10^7$, subsequently decreasing with time. In contrast with previous models

however, the value maintains a value consistently above 1x10^7 an order of magnitude larger than seen in the previous models.. This larger value may be due to the increased domain size giving a much larger heated surface leading to increased convection.

The magnitude of Rayleigh number by average and by contour (un-shown) indicates that the convection is taking place within a transitory regime between non-turbulent and the turbulent regime (transition begins near 10^7 [124] to 10^8 [125]). This may be the reason for the severe difficulty with no time step and mesh resolution insensitive model convergence and may require the utilization of an alternative turbulence viscosity model.

7.5.2.4 Peclet Numbers

Peclet number is calculated as follows using the cell Reynolds number and Prandtl number from the CFD-Post software:

$$Pe = RePr \tag{36}$$

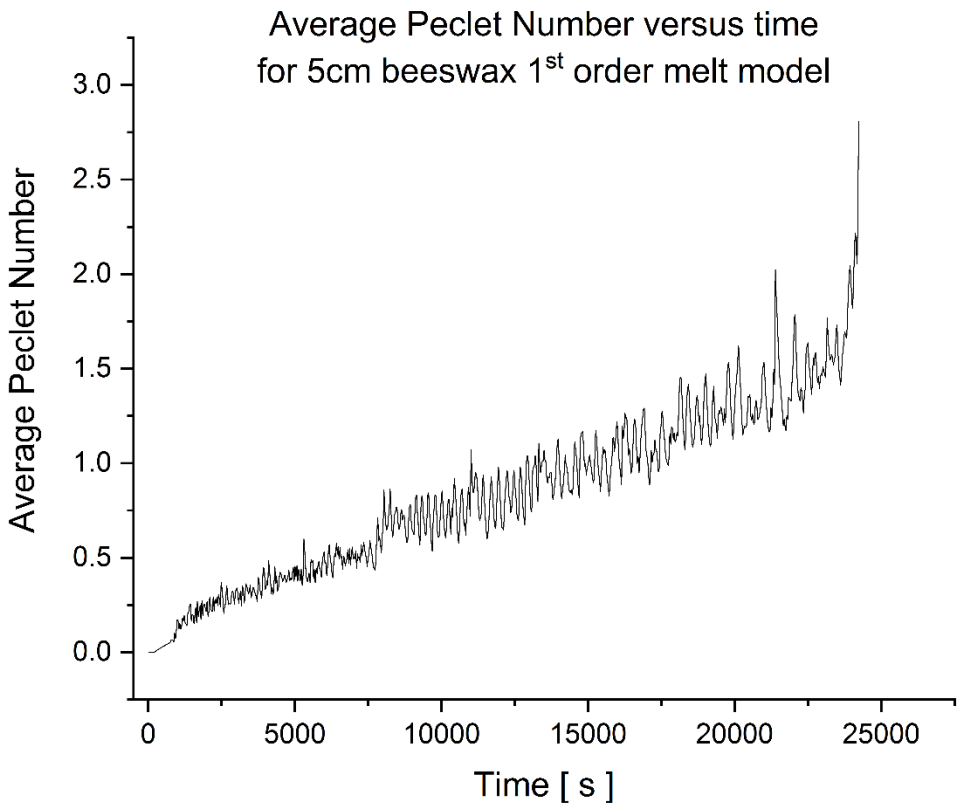

Figure 152 – Average Peclet number over time curves for 5cm beeswax 1st order model.

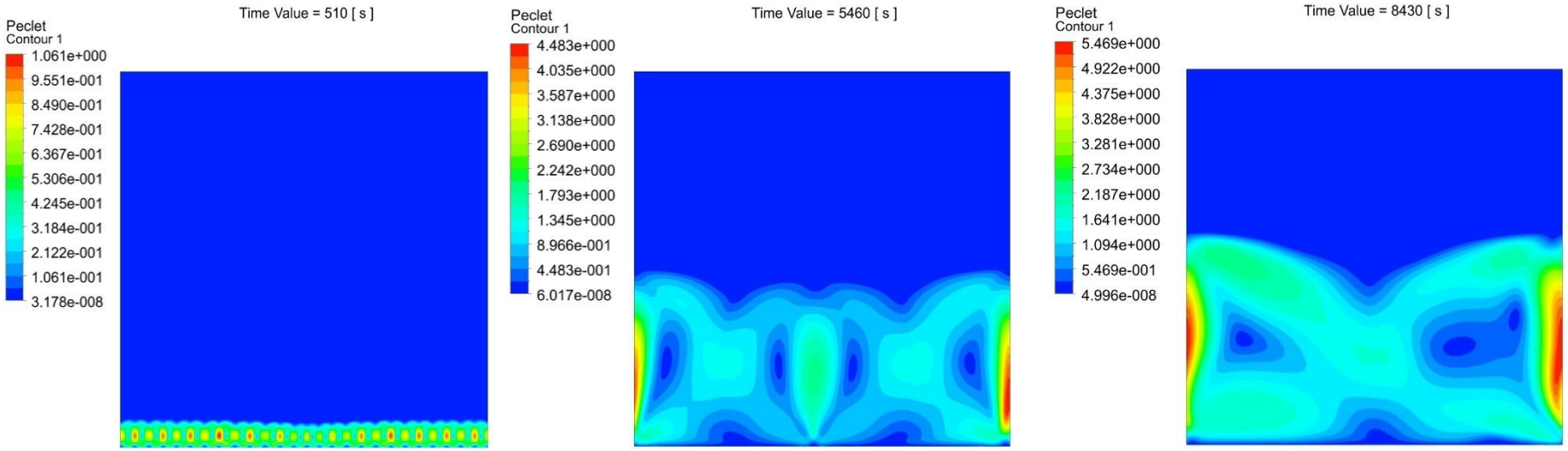

(a) (b) (c)

Figure 153 - Contours of Peclet number for 5cm beeswax 1st order model at (a) 510s, (b) 5460s and (c) 8430s.

The values computed for average Peclet number shown in Figure 152 have been computed over the whole domain and follow the previous model trends of an increasing value over time and a noisy signal with the onset of convection ~900s (decrease after melt completion is not shown).

As with the values for Rayleigh number being elevated, the plot of Peclet number also shows an increased final value of ~2.8 showing a larger ratio of convection-based heat transfer to conductive heat transfer than previously seen. This value being achieved is likely related to both the increased Rayleigh number and increased Nusselt number.

Figure 153 shows contours of Peclet number during the melt process early in the melt (a) showing the numerous small convection cells and later, (b) and (c), as the previously described disturbance occurs due to the collapse of the smaller central cell. The maximum Peclet values attained are found to be ~6.3, much larger than the maximum values seen in chapter 4.

7.5.2.5 Nusselt Numbers

As the specified configuration is one of bottom heated horizontal plates, coupled with the values of Rayleigh number, the Nusselt number correlation utilized is the following [107]:

$$Nu = 0.54\, Ra^{1/4} \tag{37}$$

Where:

$$(\tau_s + \tau_\infty)/2$$

$$1.0 < Ra < 1 \times 10^{10}$$

Nusselt number analysis was undertaken in order to quantify the ratio of heat transfer conducted and convected from the hot surface.

The average Nusselt number value has been computed from the entire heated surface and shows a dramatically increased value steeply decreasing from ~34.5 to ~27.4 before slowly decreasing over the remaining melt process to ~ 26.4. This is near double the values attained in previous models which were between ~10.5 to 8. With the similar convective heat transfer coefficient values, this is expected with the length of the heated surface also doubling.

This shows a significant increase in heat transfer at the surface, by convection compared to conduction, and is expected with the previous dimensionless number plots, such as the Rayleigh number with which a larger value (values $>10^7$) is associated with turbulent convection and better heat transfer.

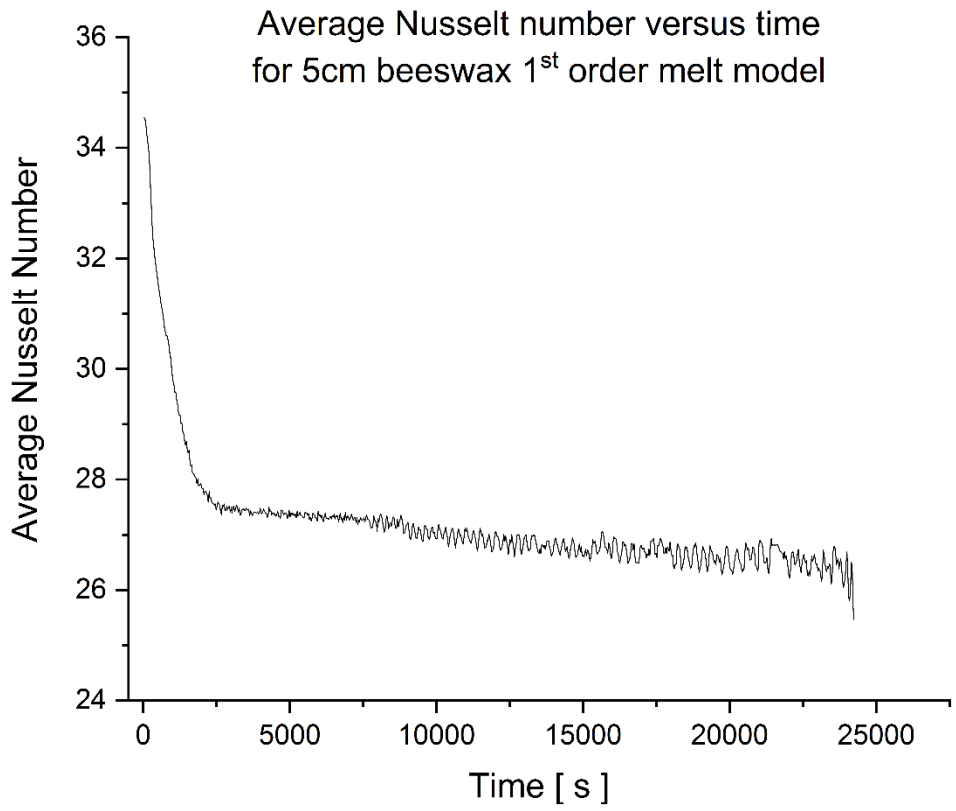

Figure 154 – Nusselt number over time curves for 5cm beeswax 1st order model.

Nusselt number values derived from the heat transfer coefficient show a relatively close agreement in range following but with a different curve profile (the same curve profile as Figure 149 with values between 50 -29). As mentioned in previous chapters, this may indicate that the use of Equation 37 is not appropriate in this case.

7.5.3 Results – Beeswax Second Order Model

This section details the results of the modelling of beeswax in the 5cm dimensioned domain, utilizing the second order implicit transient formulation option and was undertaken to see if better convergence may be attained than the first order transient formulation.

This model took significantly longer to converge and offers similar results to the first order transient formulation. Attempts to attain mesh and temporal resolution were further attempted with the second order settings but no optimal settings were found.

The model below represents the model with 78,000 mesh cells and a time step of 0.1s; other models with smaller mesh resolutions resulted in similar completed melt times only when using the same time step. The second order model demonstrated much larger time step sensitivity and progressively larger time steps resulted in decreased but still unrealistically large completed melt times. All models resulted in time of melt values above 18,000 seconds with an error between mesh resolution choices of ~10% (and additional model equivalent for the time step of 0.25 that was investigated resulted in a melt completion time of 20040s seconds).

The results and analysis below are brief and are provided for means of comparison with the first order model only and represent non valid and unphysical results.

Figure 155 shows the melted fraction versus time curve for beeswax in the 2nd order 5cm domain case and shows a total melt time of 34820s. This value is dramatically larger than the experimentally determined and first order model time and clearly demonstrates that this model is also invalid. This is likely as a result of using the laminar viscosity model with the second order transient formulation scheme. In addition, utilization of the second order transient formulation previously (not detailed in this thesis) proved exceptionally difficult to converge results for and in this case did not do so with mesh or time step independence.

Due to the lack of the independence in these factors there is little confidence to conclude anything about this model except it is invalid.

The curve does however show similar features to models in previous chapters with an initial section (~0-1100s) showing a fixed melting rate before the onset of convection with a rapid decreasing exponential curve followed by a relatively steady linear melting rate.

Observation of Figure 156, a time normalised melt fraction plot, also shows a dramatically different melt profile to that experimentally determined in the third run of the 5cm beeswax melting experimentation, further proving that this model is unphysical.

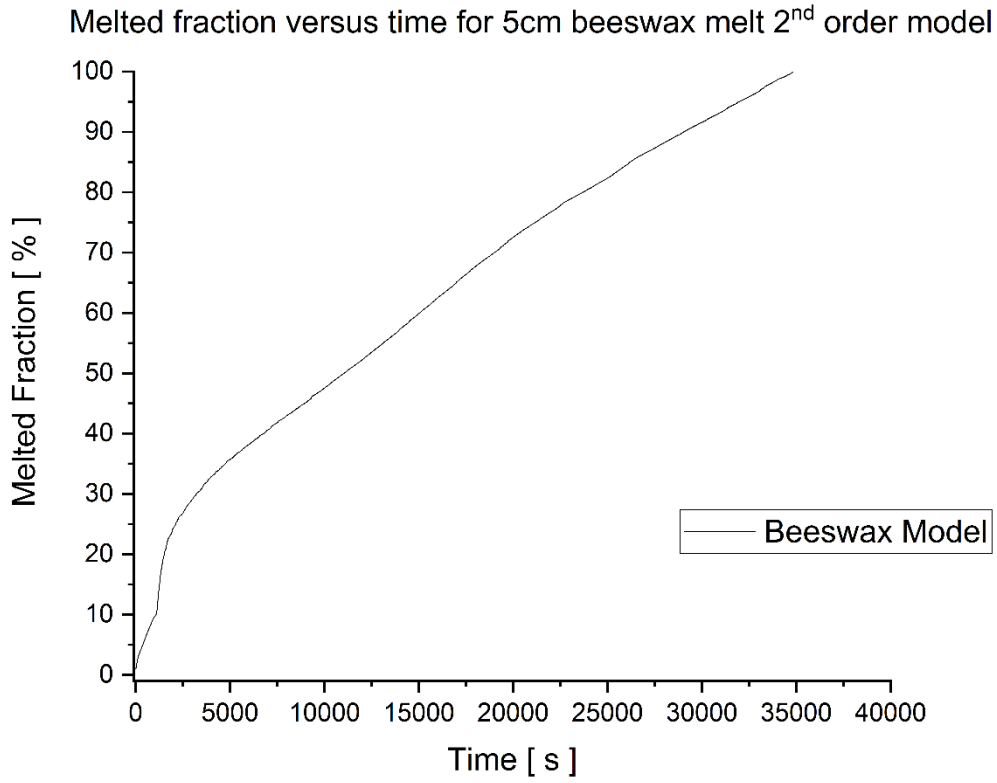

Figure 155 - Melt fraction over time curves for 5cm beeswax 2nd order model.

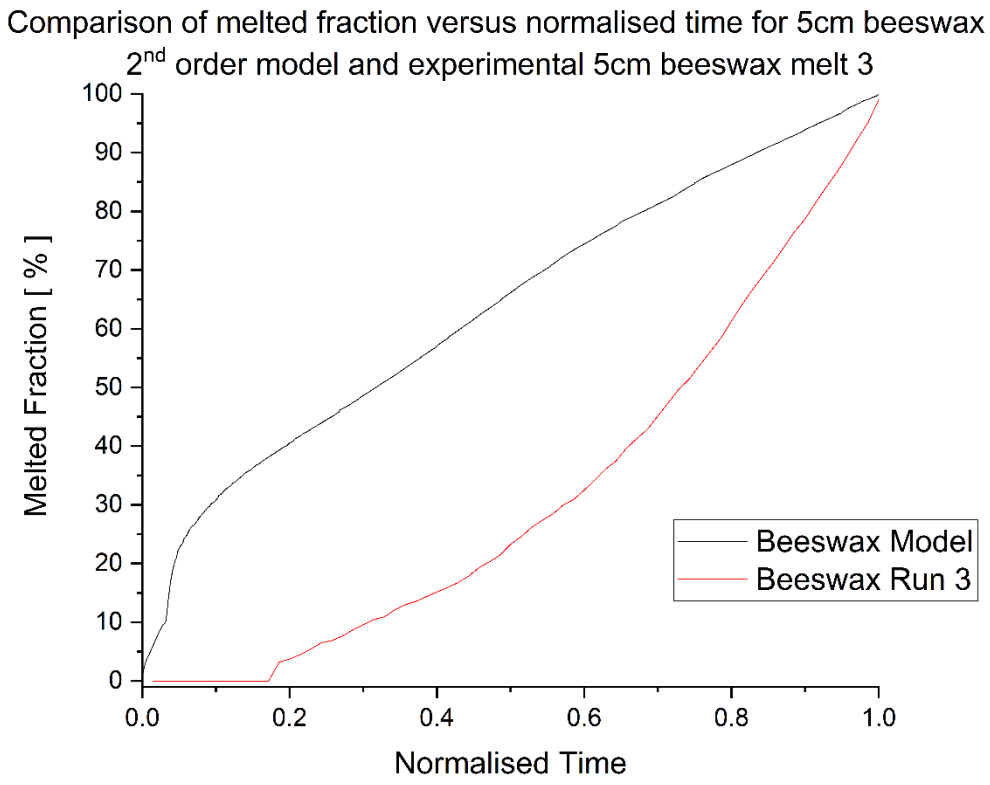

Figure 156 – Comparison of melt fraction over time curves for 5cm beeswax 2nd order model and 5cm beeswax experimental run3.

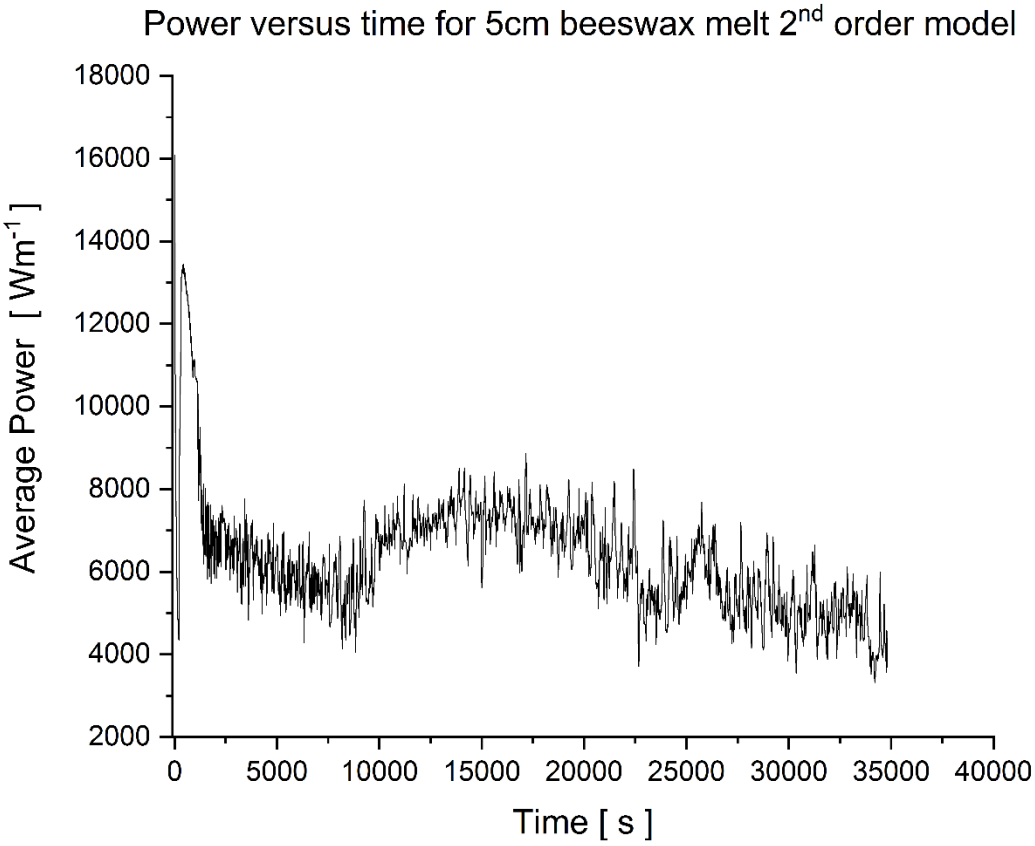

Figure 157 – Power over time curves for 5cm beeswax 2nd order model.

Figure 157 shows the power versus time curve for the second order 5cm beeswax model and shows an extremely similar power profile as found for the first order model albeit stretched over a longer timescale. Both plots show similar power values, despite a difference of around 10,000s in completed melt time, further demonstrating the unphysical and invalid nature of the model/s.

7.5.4 Results – Paraffin Wax

This section details the results of the modelling of paraffin wax in the 5cm dimensioned domain utilizing the first order implicit transient formulation.

The following results are derived from the highest mesh resolution attempted (78,000 cells) with the smallest attempted time step of 0.1s. The transient formulation utilized was of the first order.

7.5.4.1 Evolution of Melt (time)

The time for total melt time computed for this model was found to be 3720s and, taken in conjunction with the comparison to the experimental time of 4200s for paraffin wax run 3, indicates that this model is likely valid, although the constructed experimental vessel does deviate from the model design significantly. In contrast to the previous paraffin wax model in chapter 4, this model shows a different curve profile with significantly less time to melt completion, in addition to an apparent 3rd melt regime and when considered with the results of experimentation casts significant doubts about the validity of the previous model.

Like the previous paraffin wax model, the first regime is one characterised by conduction dominance and lasts from 0s to ~1250s where convection begins and becomes the dominant heat transfer method. This is also seen in the average power plot Figure 164, conductive heat transfer plot Figure 165, in addition to the Peclet contours and plot, Figure 167 and Figure 168 and in the Y velocity contours in Figure 162.

This convective regime is now followed by a reduced melting rate convective regime between 2700s to 3500s. The cause of this second convective regime appears to be due to movement along the x axis of the developed convective cell which can be seen in Figure 161 and as a disturbance in the other plotted figures.

Figure 159 shows a comparison of the model and experimental run 3 for the paraffin wax and it is seen that the agreement is imperfect albeit promising. This is the case as the experimental test vessel was non-ideal due to heat losses and metal walls decreasing isotropy. It would be expected that an ideal model of this nature would demonstrate if anything, a smaller melting time than the experimentally determined one and a relatively close curve fit with the model curve having an increased melt fraction for a given time. In addition, it is likely that the experimentally derived melt curves do not truly reflect the actual ratio of melted and solid material at a given time as a result of ongoing heat losses via the imaged face.

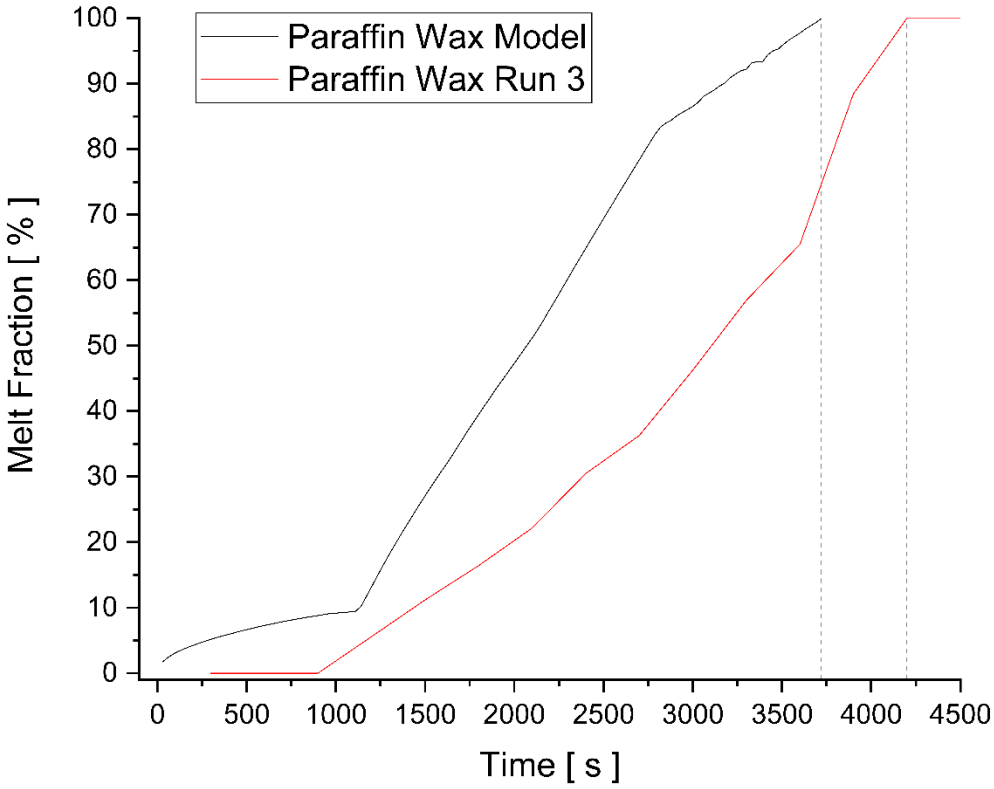

Figure 158 - Melt fraction over time curves for 5cm paraffin wax 1st order model.

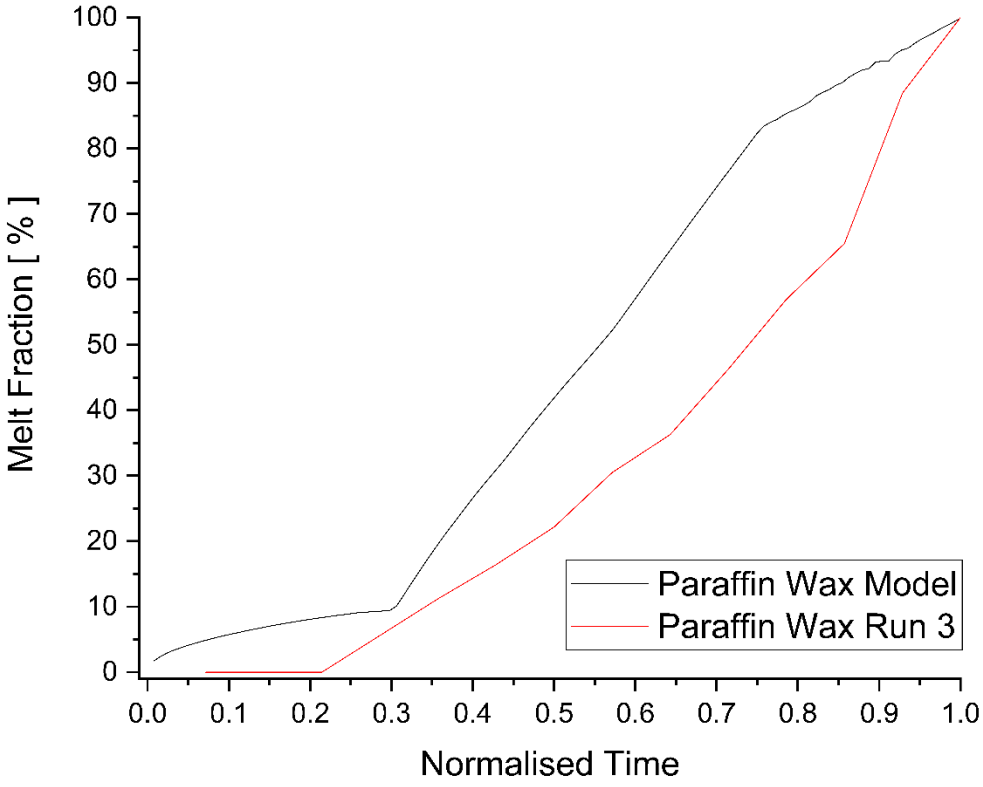

Figure 159 – Melt fraction over normalised time for 5cm paraffin wax 1st order model and experimental paraffin wax run 3.

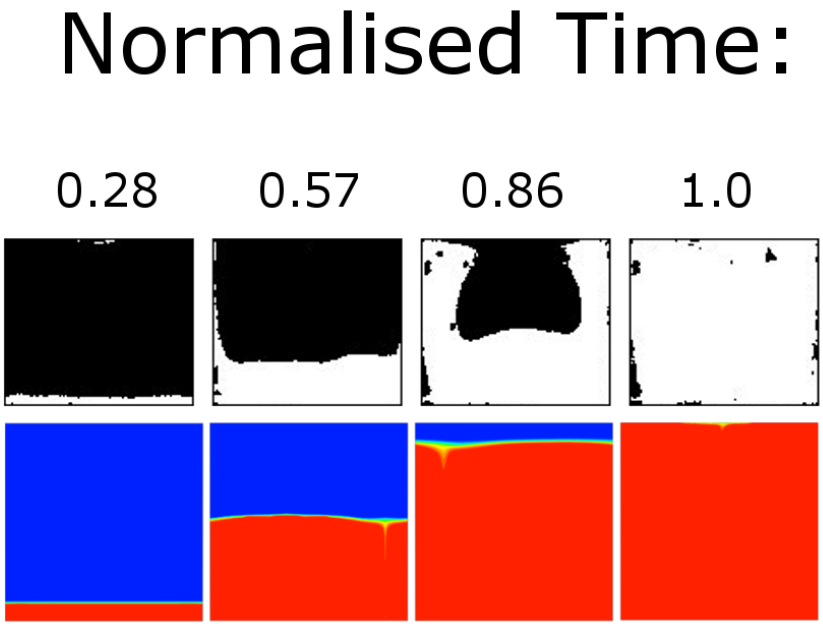

Figure 160 - Melt fraction contours of various normalised times for paraffin wax experimental run 3 (top) and 5cm paraffin wax 1st order model (bottom.)

It is seen in Figure 160, (a comparison of the melt contours for the experiment and model), that there is not good agreement. The model is seen to over predict the melted fraction with respect to normalised time. This may indicate invalidity but is likely related to the lack of isotropy of the test vessel and the lack of heat losses in the model. This lack of isotropy in the vessel is clearly visible due to the increased melting of material to the left and right of the domain during the melt process. The lack of close agreement in these images is not surprising as a result.

.

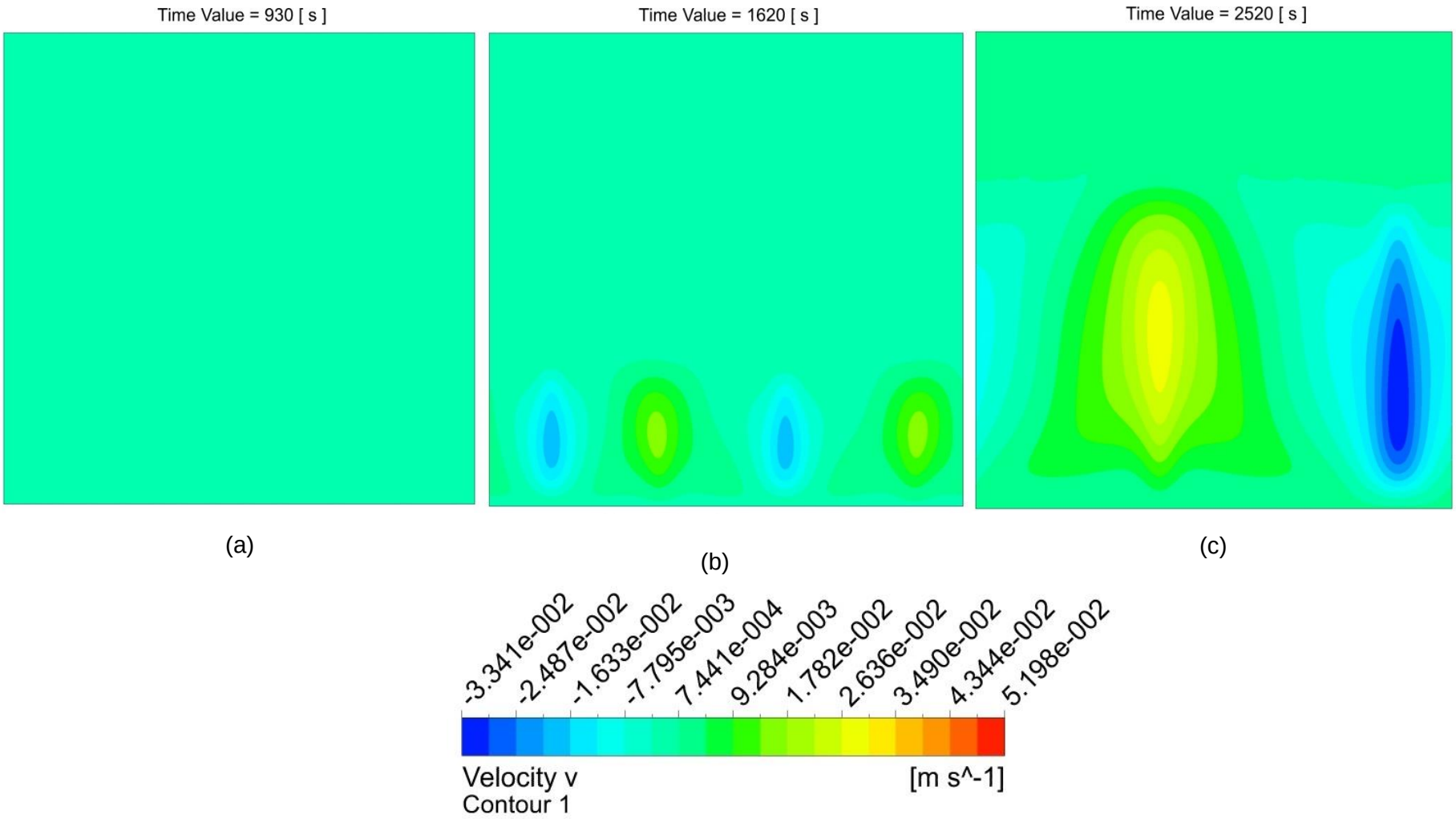

Figure 162 - Y velocity contours for 5cm paraffin wax 1st order model at (a) 930s, (b) 1620s and (c) 2520s.

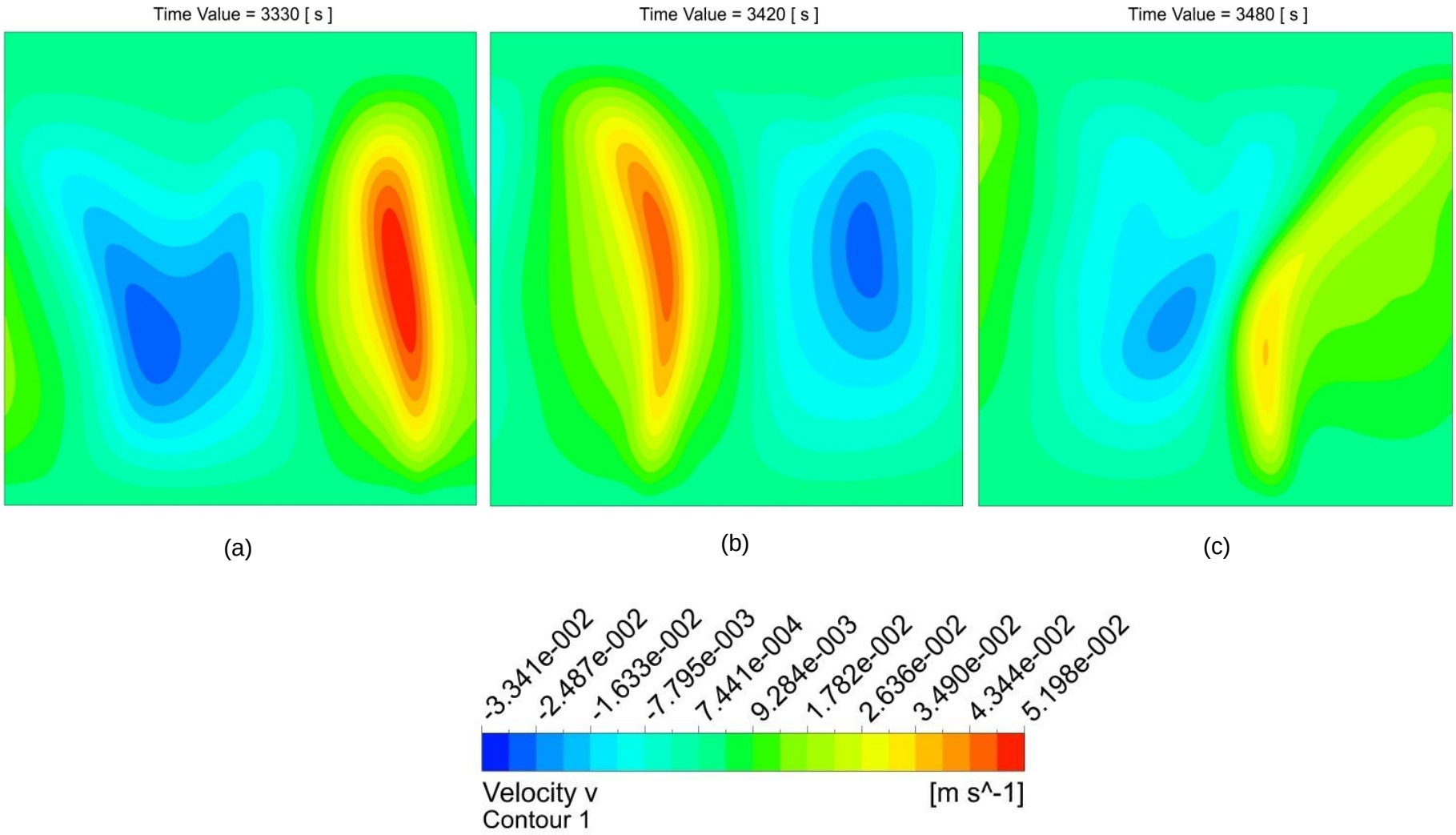

Figure 163 - Y velocity contours for 5cm paraffin wax 1st order model at (a) 3330s, (b) 3420s and (c) 3480s.

7.5.4.2 Heat transfer power and convective heat transfer coefficient

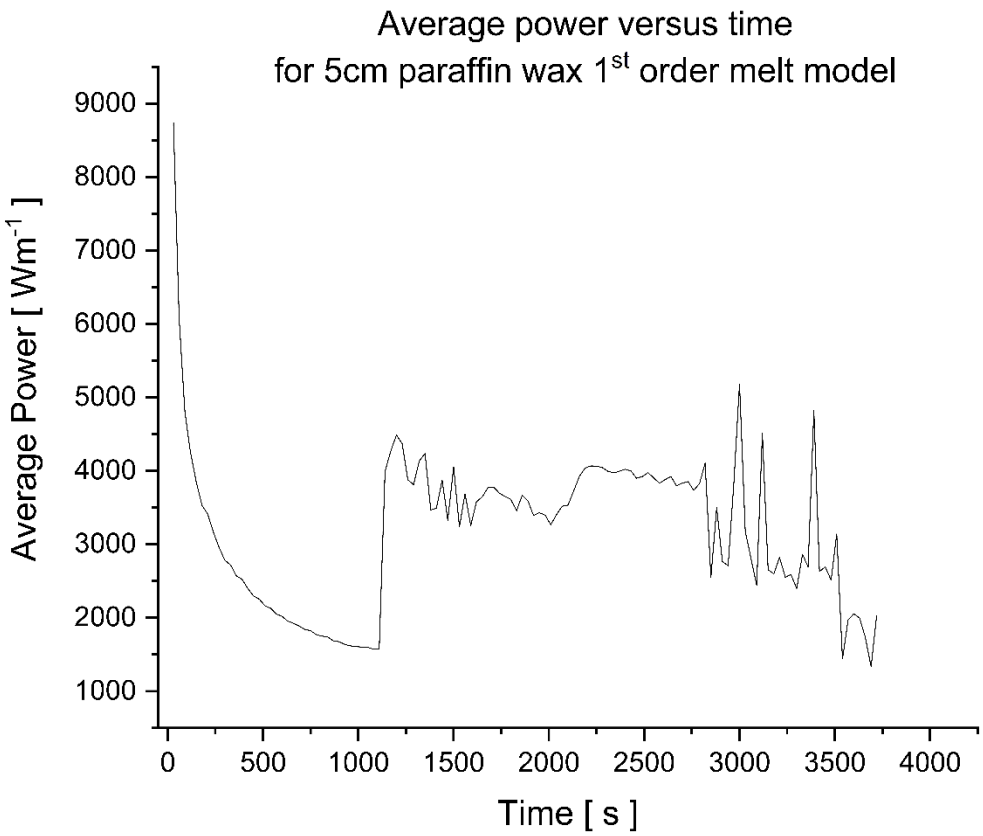

Figure 164 - Average power over time curves for 5cm paraffin wax 1st order model.

The value of average heat transfer power is calculated as an average of the entire heated surface and the plot of this variable versus time can be found in Figure 164Figure 132. It is seen the trends in this figure match closely with those of the convective heat transfer coefficient in Figure 165.

The first regime dominated by conductive heat transfer shows large initial values ~ 8700Wm^{-1} and 180 $Wm^{-1}K^{-1}$ before exponentially decreasing to values of around 1500 Wm^{-1} and to 74 $Wm^{-1}K^{-1}$ where convection starts and is seen as a peak back to ~ 4000 Wm^{-1} and 215 $Wm^{-1}K^{-1}$ respectively. The signal oscillates somewhat in both figures as seen in the previous model in chapter 4. After the first convective regime there is another characterised by a reduced rate of melting. On both figures this is seen with the sudden increasingly noisy signal and decreased values seen between 2700s – 3500s. As previously mentioned, this seems to be a result of the formed convection cell being disturbed and moving along the x dimension in the domain as seen in Figure 161.

The sustained power of ~ 4000 Wm^{-1} seen in Figure 164 raises questions the validity of the previous model in chapter 4 which had an equivalent sustained rate of 5000 Wm^{-1}.

Despite significantly more convection ongoing, the sustained convective heat transfer coefficient is similar to the previous paraffin wax model which reached ~350 - 200 $Wm^{-1}K^{-1}$ raising further concerns about the previous model's validity.

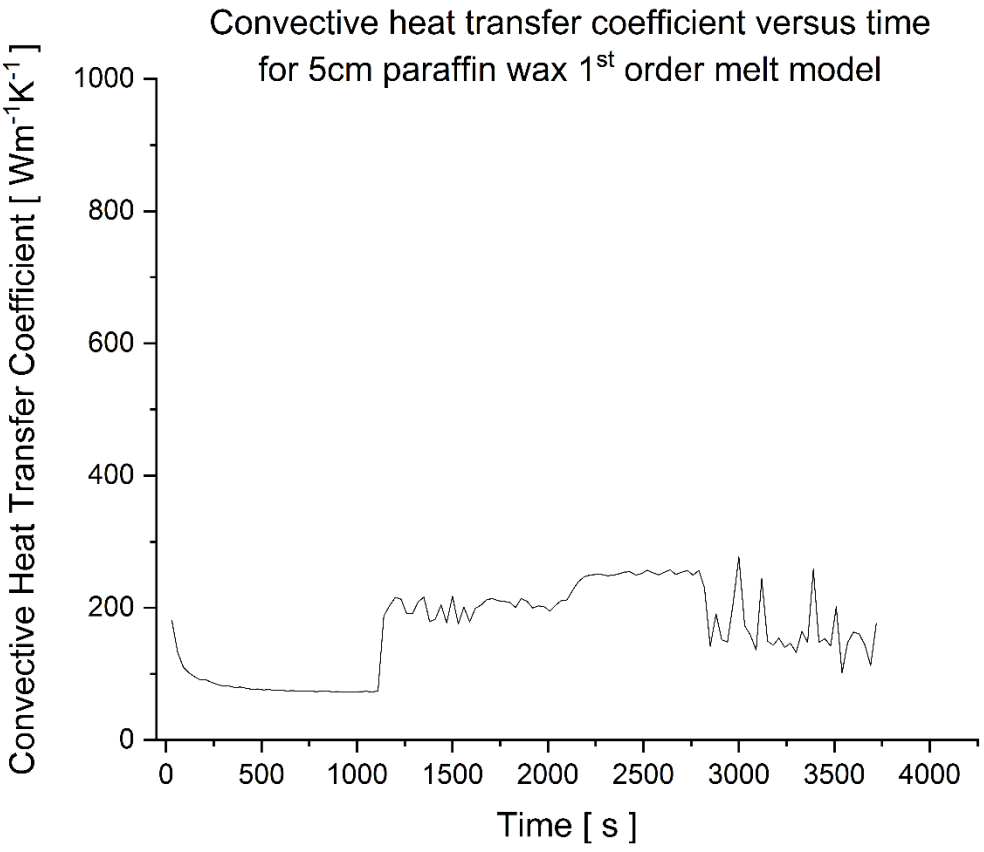

Figure 165 – Convective heat transfer coefficient over time curves for 5cm paraffin wax 1st order model.

7.5.4.3 Rayleigh Numbers

Rayleigh number analysis is undertaken to assess to what extent convection is occurring in each material during the melt process. For this analysis the Rayleigh number and Grashof numbers are defined as follows [3]:

$$Ra = GrPr \tag{38}$$

$$Gr = \frac{g\beta(\tau_S - \tau_\infty){L_h}^3}{\nu^2} \quad (39)$$

Where $\beta_{Paraffin\ wax}$ = 0.001247723 and L_H =0.05 (m) but would usually be the ratio of horizontal plate area to plate perimeter in 3 dimensions. In this case it has been assumed to be the 2D hot surface length [4].

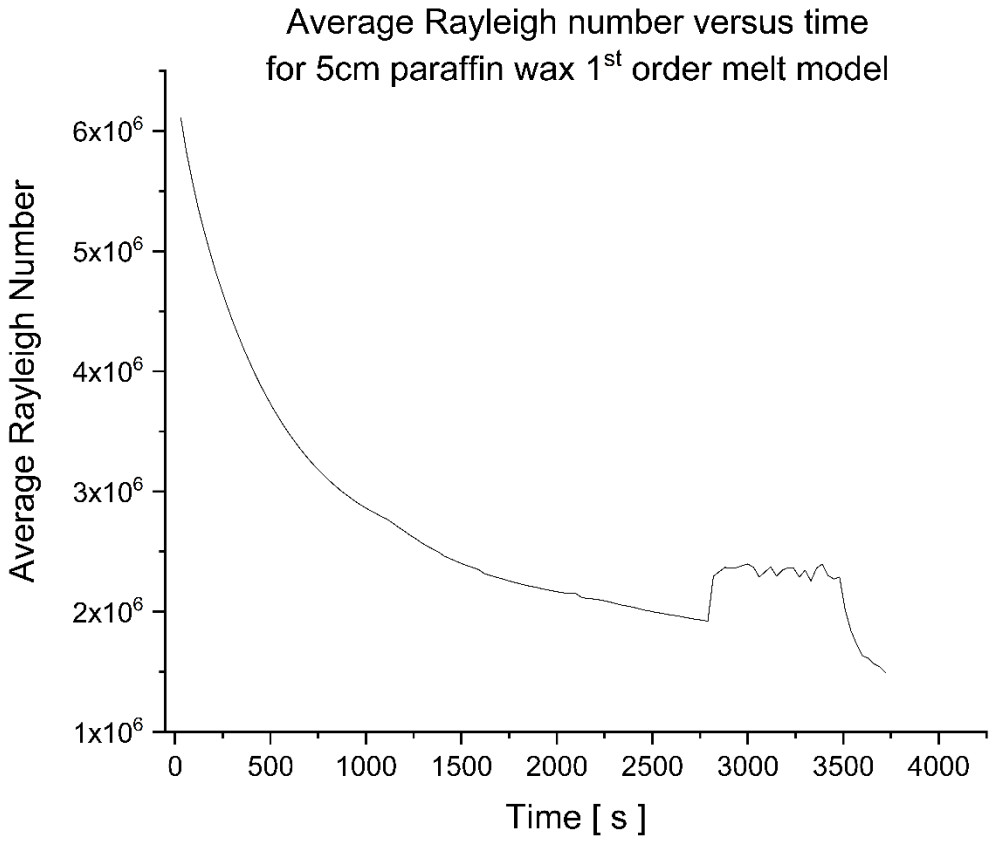

Figure 166 – Average Rayleigh number over time curves for 5cm paraffin wax 1st order model.

Figure 166 shows the average value of Rayleigh number computed from the hot surface over time. Like previous models trends (not magnitude), it shows a large initial value near $6.1x10^6$ before reducing as expected as the convective process continues. The increased values seen in this figure coincide with values determined for Peclet and Nusselt number analysis.

In line with the decreased melting time and increased amount of convection, this initial value and the reduction to $1.9x10^6$ is larger than those (~ 0.75×10^6 to ~ 0.625×10^6) seen in the paraffin wax model of chapter 4, again casting further doubt over the accuracy of this first model.

As previously mentioned, the flow disturbance is also seen on this plot with an increase in Rayleigh number around 2700s – 3500s believed to be as a result of the convection cell being disturbed and re-establishing itself in a more optimal condition.

7.5.4.4 Peclet Numbers

Peclet number analysis was undertaken in order to quantify the ratio of heat transfer conducted and convected in the fluid/bulk and is computed as an average across the whole domain.

$$Pe = RePr \tag{40}$$

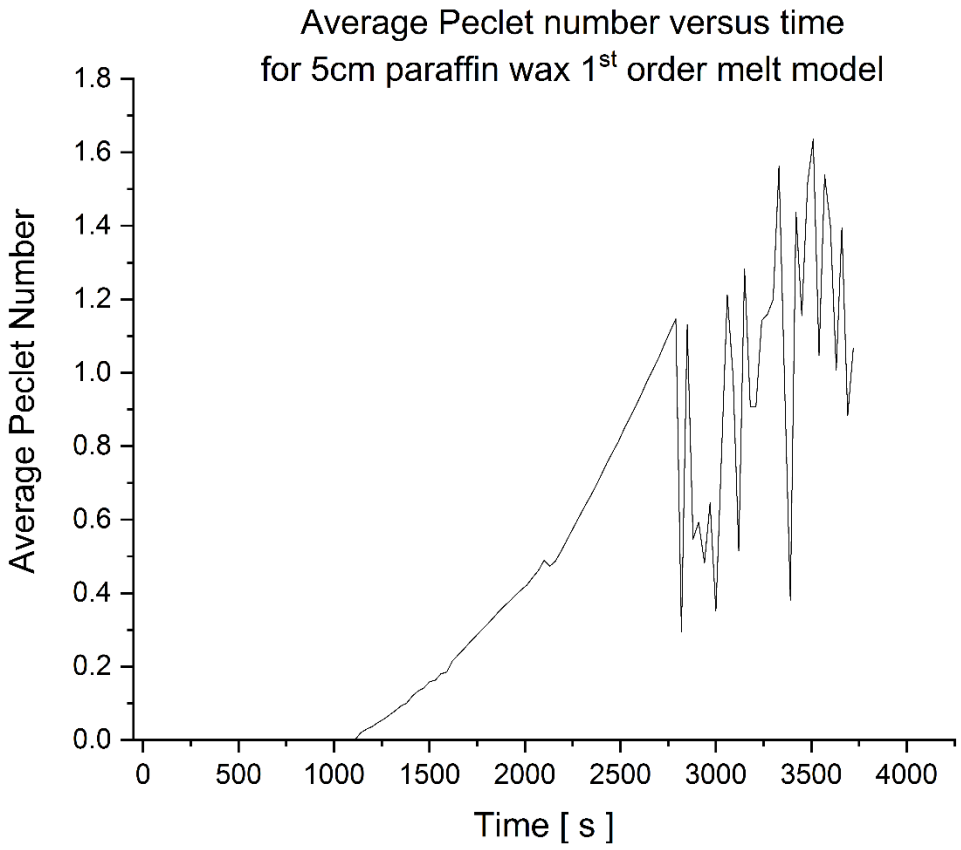

Figure 167 – Average Peclet number over time curves for 5cm paraffin wax 1st order model.

Figure 167 shows the average Peclet number curve versus time and shows the onset of convection very clearly ~ 1100s before steadily increasing to near 1.2 as convection gets stronger. Peclet contours in Figure 168 show this onset of convection early in the melt at 1020s and then 1320s and again confirms the previously seen behaviour where numerous smaller

convective cells form and eventually collapse into one cell by the time of melt completion. The Peclet number also gets significantly larger than the previous model ~ 0.28 and becomes convection dominant (greater than 1) showing the dramatically increased amount of convection resulting in the decreased total melt time.

Around 2700s this plot reflects the effect of the disturbance previously mentioned, with the convection cell moving across the x dimension, causing the oscillatory response before melt completion and a rapid decrease in value.

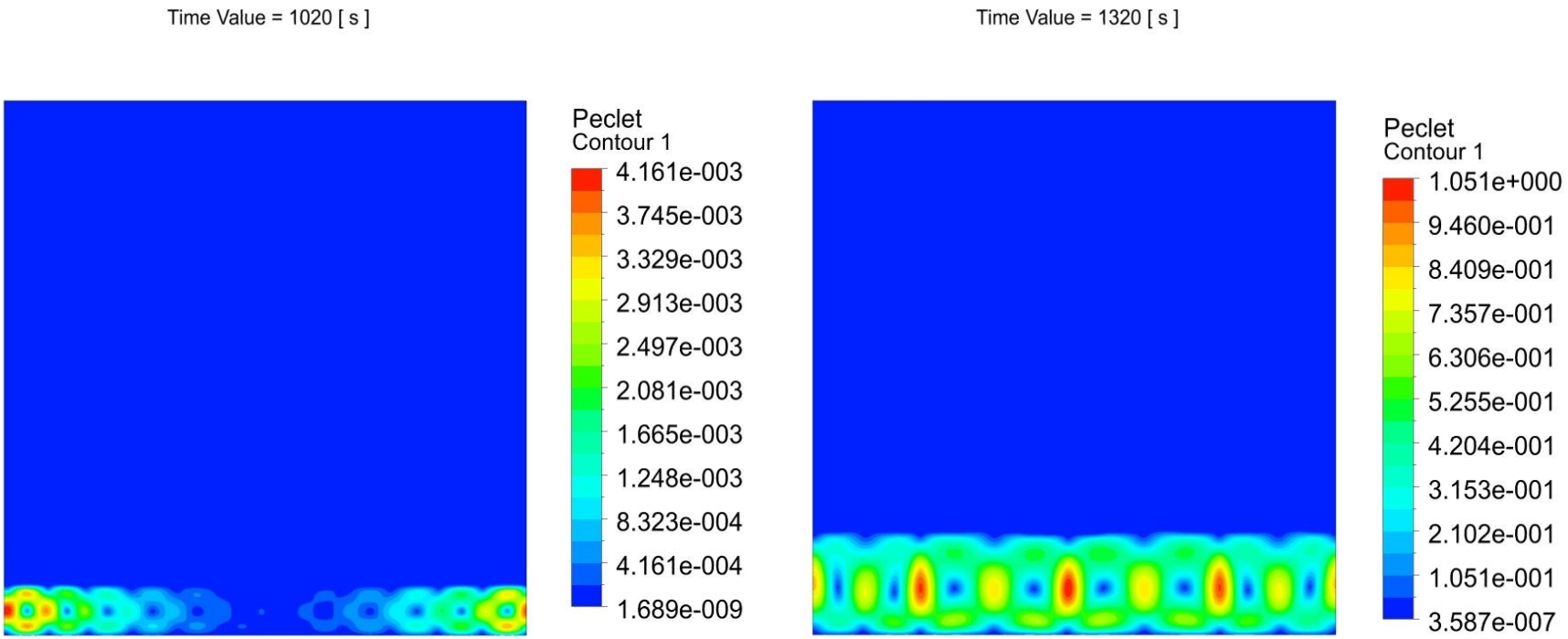

Figure 168 –Contours of Peclet number for 5cm paraffin wax 1st order model at (a) 1020s and (b) 1320s.

7.5.4.5 Nusselt Numbers

As the specified configuration is one of bottom heated horizontal plates, coupled with the values of Rayleigh number, the Nusselt number correlation utilized is the following [107]:

$$Nu = 0.54\, Ra^{1/4} \tag{41}$$

Where:

$$(\tau_s + \tau_\infty)/2$$

$$1.0 < Ra < 1 \times 10^{10}$$

Nusselt number analysis was undertaken in order to quantify the ratio of heat transfer conducted and convected from the hot surface and is calculated as an average across the heated surface.

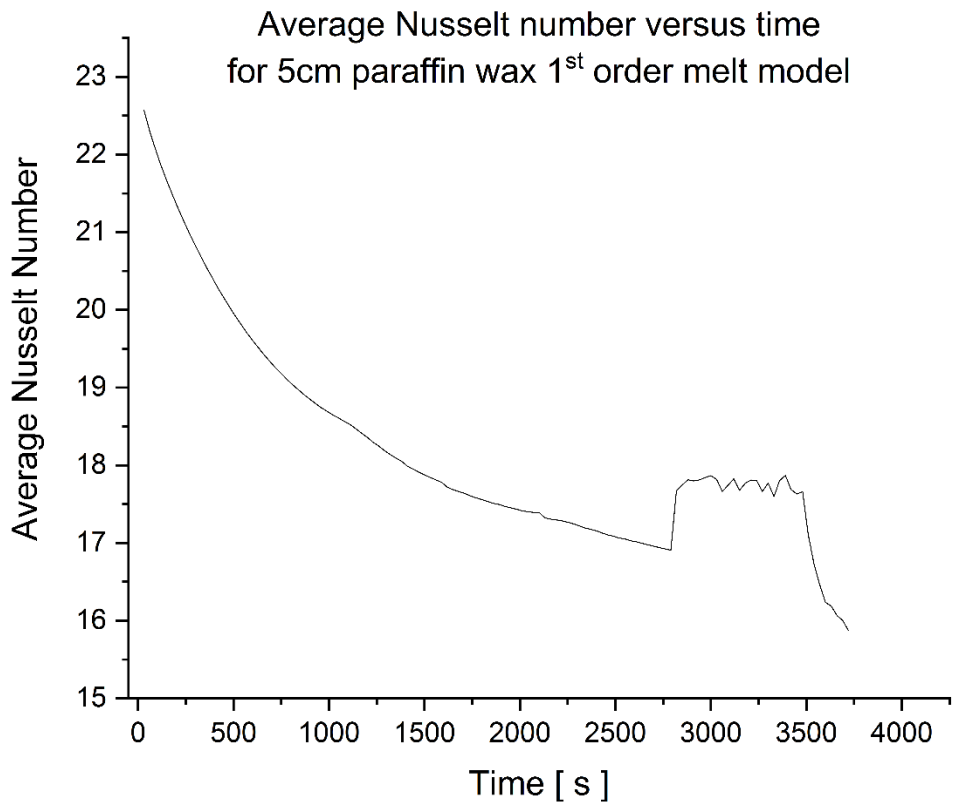

Figure 169 – Average Nusselt number over time curves for 5cm paraffin wax 1st order model.

The Nusselt curve seen in Figure 169 closely follows the expected behaviour with relation to the Rayleigh and Peclet curves, including the disturbance to the convective flow seen in the latter stages of the melt process around 2700s.

This figure starts with a large initial value of 22.5 decreasing exponentially to 17 where this disturbance occurs. This value is approximately double the fixed value ~10.5 seen in chapter 4, which is not surprising given the dramatically reduced time of melt and other dimensionless value results. It is interesting that with the similar convective heat transfer coefficient values and doubled length of heated surface in the current model, the increase is as you would expect despite the previous model taking a much longer time to melt and likely erroneous and invalid results.

The disturbance seen at 2700s increases the value from 17 to ~17.8 and is coincidental with an increase of ~0.4×10^6 in the Rayleigh number and oscillatory signals in the Peclet and power curves. This oscillation and increasing values of Nusselt and Rayleigh number indicate an increasing importance of convective heat transfer, thought to be as a result of the disturbance moving colder material in proximity to the heated surface. This may however indicate issues with model validity/convergence given the lack of temporal or mesh sensitivity. **This model was re-ran and the same disturbance resulted.**

After 3480s the convection cell appears to re-establish stability, leading to the decrease in values seen in the figure and returns to the previous decreasing trend. It is notable that the melting rate decreases during this disturbed period, indicating that thermal energy is not being delivered optimally to the liquid-solid interface which can be seen in Figure 170 at 3000s.

Values of Nusselt number derived from the heat transfer coefficient follow the same curve profile as Figure 165 with values between 9 – 35 again showing a similar range of values but a different curve profile to Figure 169, which may indicate that the use of equation 41 is not appropriate in this case.

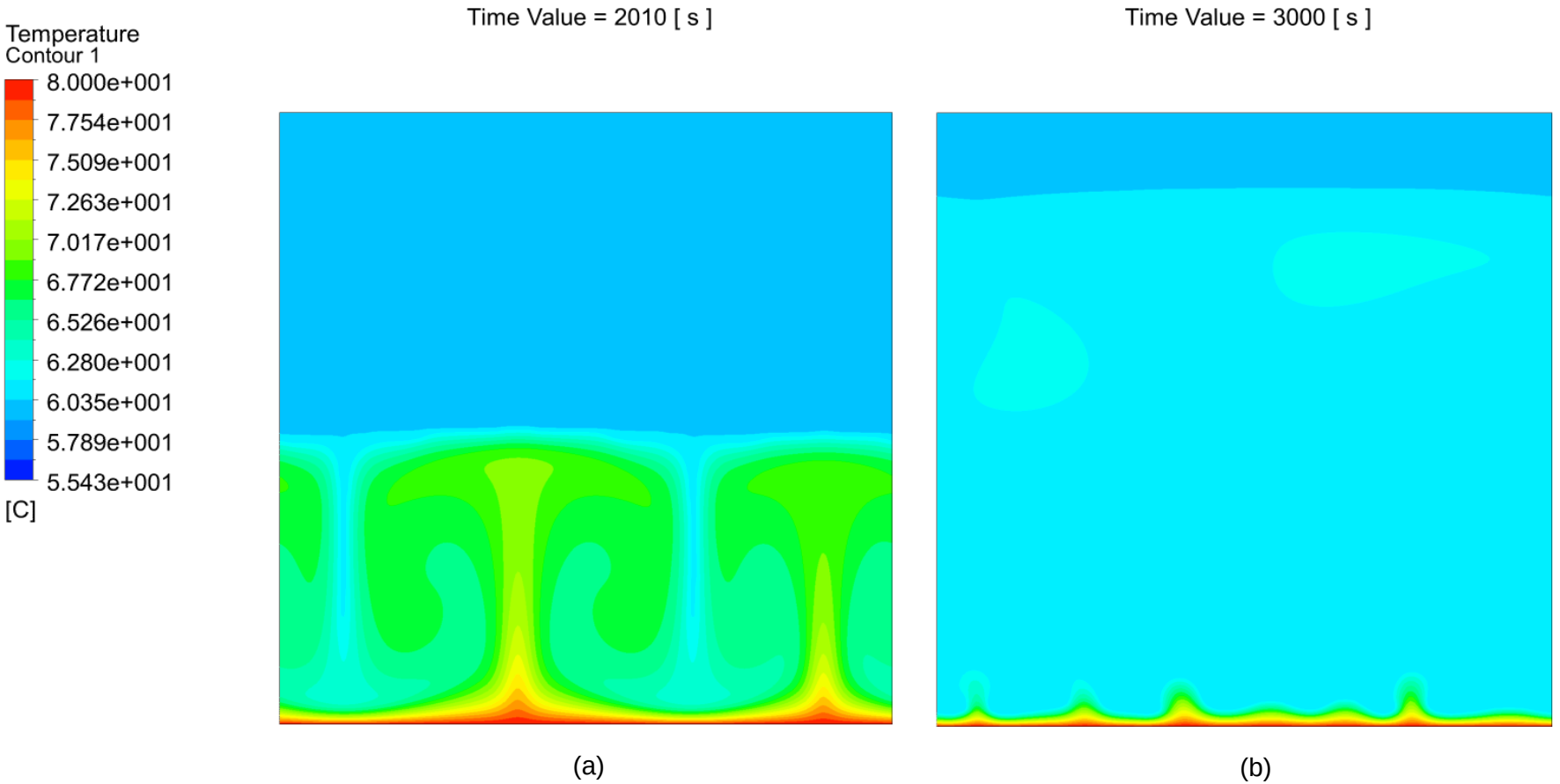

Figure 170 - Contours of temperature for 5cm paraffin wax 1st order model at (a) 2010s and (b) 3000s.

7.5.5 Mesh and Temporal Dependency

As was previously mentioned, the beeswax 5cm models did not find a configuration with mesh and temporal insensitivity for either first or second order transient formulation likely as a result of turbulent convection. Modelling for this material explored various mesh resolutions, from 35,000 cells to 98,000 cells. For the first order transient formulation, it was found that the 98,000 cell mesh would not converge with any settings and decreasing the resolution was associated with easier convergence and reduced completed melt time. Adjusting the time step was seen to result in large changes in melt time, with a melt time 10x smaller for the 0.25s time step compared with the 0.1s time step. For the second order transient formulation similar trends were found with melt times increased by around 50%.

In contrast, it was found that paraffin wax had a mesh and time insensitive solution with models of 62,000 cells and 0.1s time step giving 3780s and 78,000 cells, 3720s with time steps of 0.1 and 0.25s.

7.5.6 Conclusions

This section of work has attempted to validate the melt process of beeswax and paraffin wax in a 5cm experimental vessel heated isothermally at 80°C against CFD modelling.

It was found that the generated models for beeswax did not agree well with experimental data, likely as a result of the inability to find a mesh and time step independent solution. The first order transient formulation determined a melt time of 24240s and the second order transient formulation with the same mesh and time step found a melt time of 34820s, compared to experimentally determined melt times of ~4200s.

This may be as a result of the values of Rayleigh number attained being of the order of 10^7 and flow potentially being in a transitory regime between non-turbulent and turbulent convection. This increased Rayleigh number observed is likely a result of the increased dimensions of the computational domain. Further increasing mesh resolution resulted in none convergence, in addition to resulting in dramatic increases in computational workload.

In contrast, the generated model for paraffin wax agreed far more closely with the experimental melt times, with the model reaching melt completion at 3720s compared to experimentation ~4200s. Despite the close melting completion time, the paraffin wax melt profile does not perfectly match that of the experiment although this is likely as a result of the vessel design's imperfect isotropy and heat losses from the face being imaged.

When making a comparison between the current chapter's paraffin wax model and chapter 4's equivalent, it is obvious that the newer model and close results raise questions about the

previous model's results; with a greater amount of paraffin wax melting quicker in the current model. The cause of the previous model's deviation is unknown but may be as a result of a mistake in model development given the mesh and temporal independence; may be a result of utilizing a more up to date version of Fluent or potentially some form of systematic error as a result of the hardware (PC 1- 3) used; this is unlike the current model being exclusively calculated on super compute cluster 2. It is highly recommended that the previous model be re-constructed and re-run on super compute cluster 2 as a result.

Given the greater success with the paraffin wax model and the reduced Rayleigh numbers observed in comparison to the beeswax model in the current scheme of work, it indicates the cause of the beeswax model's failure to attain mesh and temporal insensitivity is related to the material's thermo-physical properties, potentially the much larger viscosity. It is clear that the beeswax models could be investigated using an alternative turbulence viscosity model in which it is likely more optimal models can be generated.

7.6 Introduction – 15cm Box Experimental

This section details the investigation of beeswax in a new 15cm dimensioned experimental vessel detailed below. This configuration was intended to validate the subsequently generated equivalent CFD model.

7.6.1 Vessel Design

After the investigation into materials for thermal analysis and preliminary data from the smaller experimental cube, a larger test vessel was designed and constructed to investigate better the melting phenomena. The detail of the design of this vessel can be seen in Figure 171 and is of larger 15cm dimensions and features a temperature sensor matrix intended to investigate whether this inspection method is of value to melting analysis.

The larger size was intended to assist in resolving further detail e.g. convection currents and their macroscopic effects as these effects should be more apparent with a larger length scale.

The vessel was composed of a 1 cm thick copper base, 3 polycarbonate faces and 1 IR transparent PMMA (Bay Plastics LTD) face 0.5cm thickness to form an open topped cube. One of the polycarbonate faces has a matrix of DS18B20 sensors spaced 25mm apart in the configuration shown in Figure 171.

The temperature sensor array data was acquired synchronously via the Raspberry Pi running the Debian Operating system. The software to achieve data acquisition was a combination of C for BitBanging (https://github.com/danjperron/BitBangingDS18B20) and Python for data processing into CSV files.

BitBanging (emulating the DS18B20 One wire protocol) was implemented on several GPIO pins to minimise acquisition time. Subsequent data was then passed to be parsed into CSV files via a small Python script.

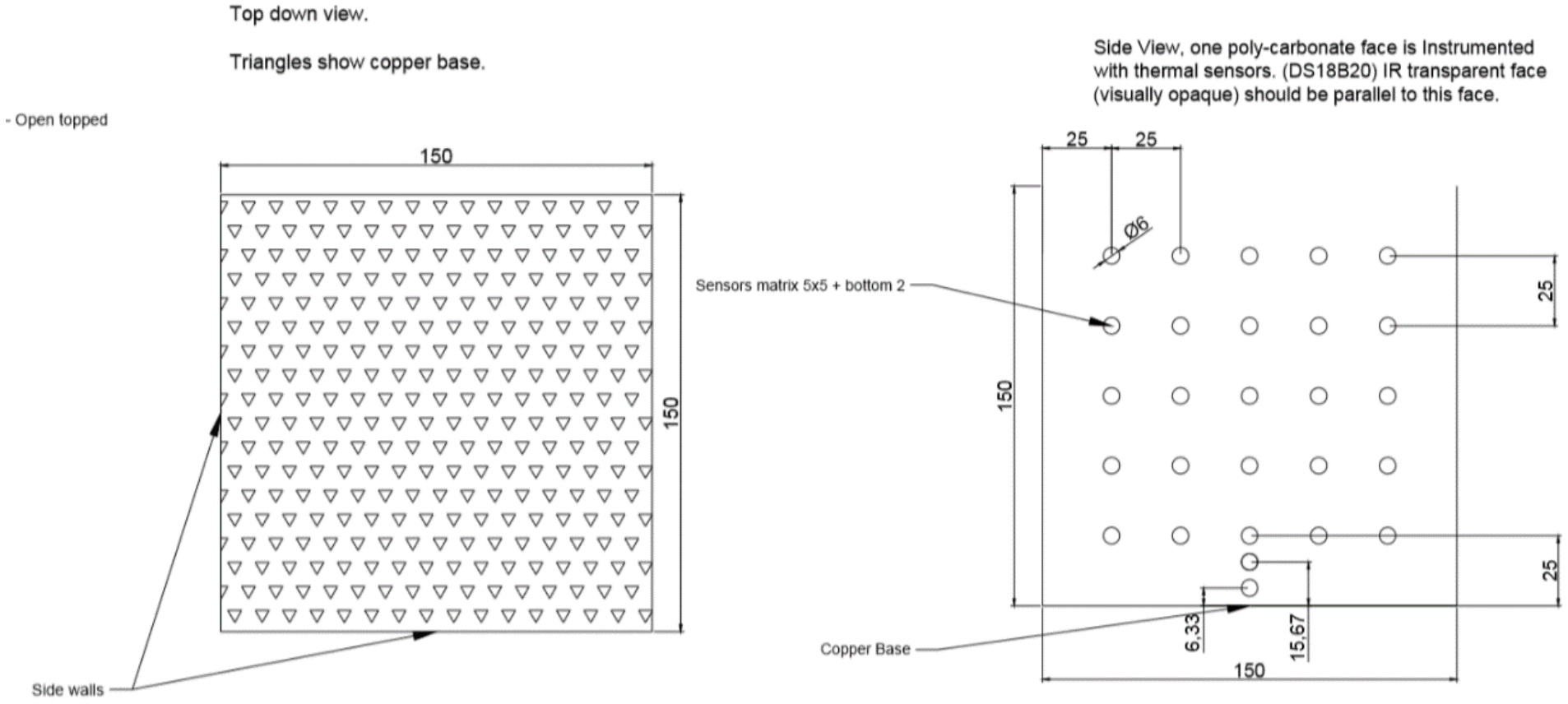

Figure 171 - Schematic Diagram of larger 15cm x 15cm x 15cm PCM melting experimental vessel.

7.6.2 Operation Methodology

The operation methodology for this larger vessel is almost identical as for the previous 5cm experimentation with some small modification:

The beeswax was added to the vessel once prior to experimentation and the cameras, automated insulation moving system and matrix of temperature sensors tested. The test vessel was then placed on the non-heated lab top heater (IKA C-MAG HS 7), the cameras aligned, and apparatus straightened for optimum imaging in addition to ensuring wires were tidy.

Beeswax was supplied from Sigma Aldrich CAS number 8012-89-3 (bleached wax.)

In order to match the subsequent models as closely as possible the lab top heater was set to provide heat isothermally at 80 °C and when ready the heating was activated.

The FLIR SC-Series thermal camera (SC640) (now operated via the ThermaCAM Researcher 2.10 PRO software which allows for improved analysis) and PLAYSTATION Eye ™ webcam were operated synchronously to take images at a pre-set interval of 5 or 1 minute with the latter operated via the Raspberry Pi. The Raspberry Pi also initiates a read of all temperature sensors synchronously, sorting and saving this data alongside each image.

Both cameras image a polycarbonate face.

Data recording was operated until melt completion and then data gathered for the solidification process. The assembly was allowed to cool for 24 hours and then more cycles operated.

7.6.3 Matrix Data Analysis Methodology

In order to utilize the data generated from the experimental temperature matrix, a series of small python and javascript programs were developed.

Live display of temperature data was then shown via heatmap which was produced and displayed via the Plotly (https://plot.ly/) Javascript library and NodeRed web application (https://nodered.org/)

Further processing was undertaken on completed experimental data using a combination of Python programming and the Python Plotly library to generate virtual heatmap images from the empirical data acquired from the temperature sensors. These generated heatmaps come in two variants: one utilizes the same thermal scaling and palette as the thermal camera imagery for easy comparison.

The second variant uses a dual-tone palette and omits the offset bottom two temperature sensors. The palette has the melt temperature set as the change in colour to easily show the liquid-solid interface location. The latter heatmaps are also processed to determine a track of % melted material versus time using the ImageJ program. This program is used to process the dual tone into an 8 bit monochrome image which is binarized and then the mean brightness value measured. This process is repeated for all images to generate mean brightness values between 0 and 255 for each image which is saved to a CSV data.

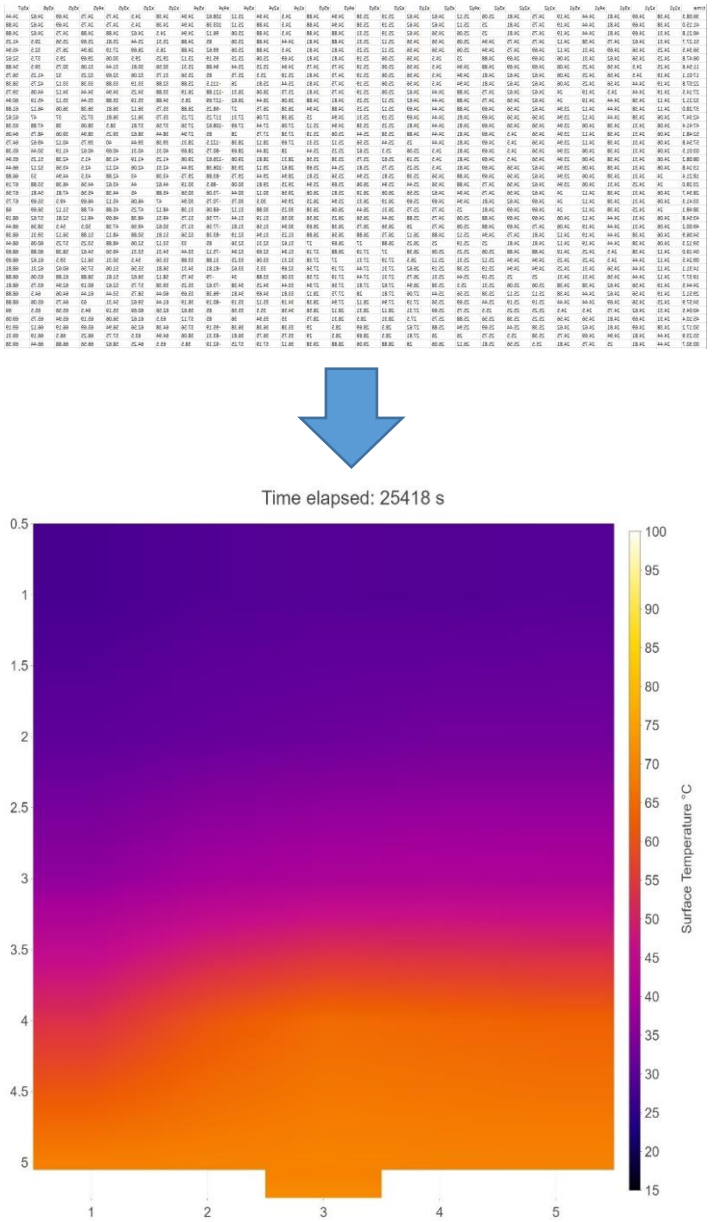

Figure 172 - Example showing a python program was used to convert CSV data into virtual heatmaps.

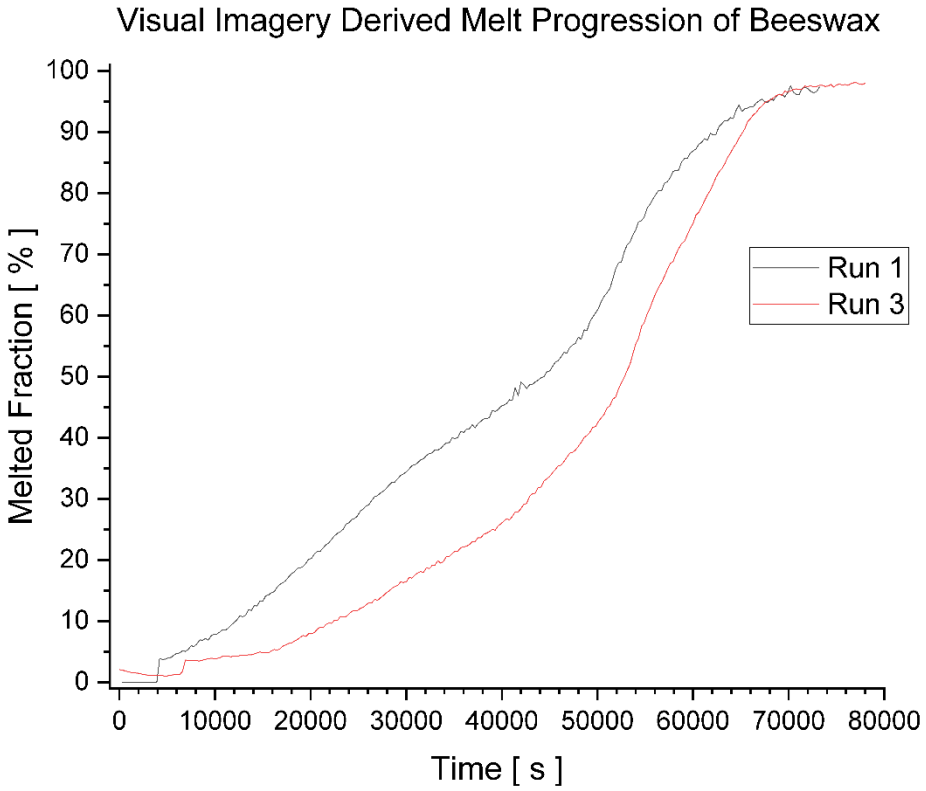

Figure 173 - Visual imagery derived melted fraction % for 15cm box beeswax experiments.

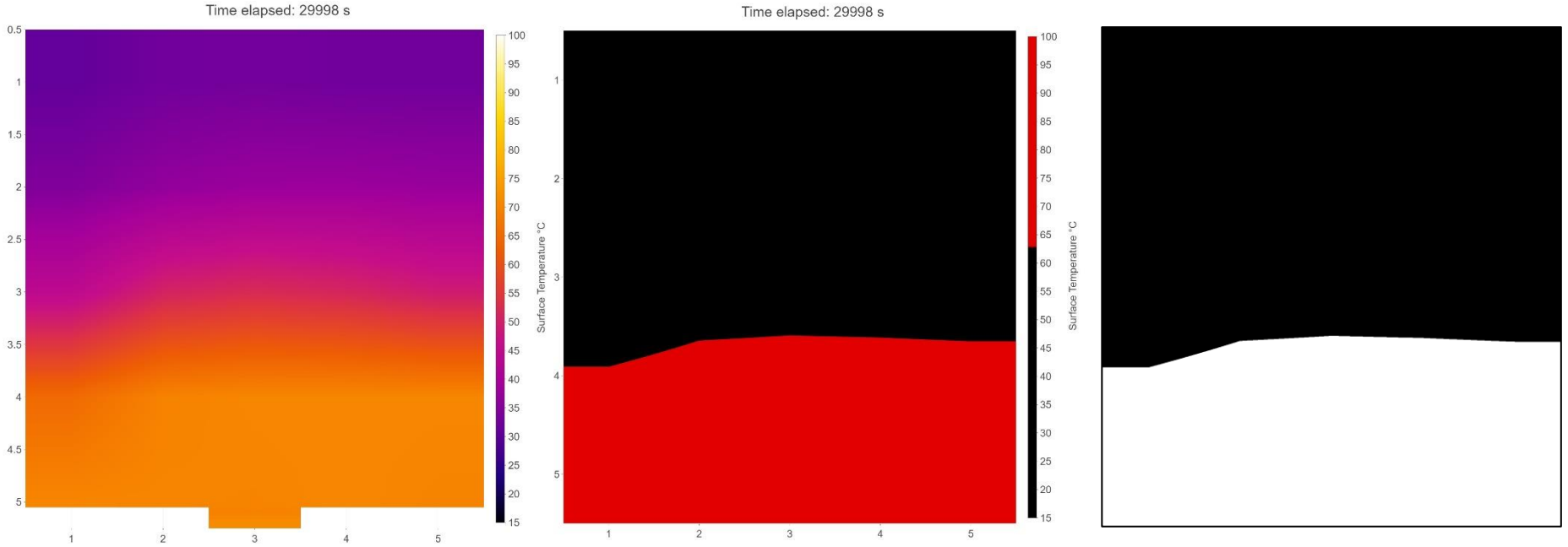

Figure 174 – Conversion process of matrix data showing the ironbow palette (left), dual-tone palette with change set at melting temperature (middle) and processed binary image from dual-tone palette (right.)

7.6.4 Results

As with previous experimentation, gathering useful data has proved difficult due to lab conditions and sub-optimal experimental vessel construction. As has been demonstrated in chapter 2, both PCM materials have demonstrated large density changes over the studied temperature range and like many organic PCMs this results in significant volume expansion during a melt process. While the vessel was designed with an open top to facilliate movement in the melting material, it was seen that solid material above the melting material acted as a plug, causing this volume expansion to exert high pressure on the walls of the vessel and in particular at the joints to the base.

As a direct result, this vessel had multiple serious leaks which fortunately caused no danger or damage due to the placement of the assembly over an overflow basin and the liquid cast off design of the lab top heater. The vessel was taken back to the workshop for resealing on two occasions to progress with experimentation. Incidentally, before commencement of experimentation, one of the temperature sensors (located in position x-4, y-4 which can be located in Figure 174) developed a fault, resulting in data at this location being interpolated from the sensors adjacent to it. From observation of data successfully gathered from this sensor despite its failure, it was seen than this linear interpolation was not without basis.

Upon returning the vessel for a second time it was found that instead of the requested design, with walls sunken into slots in the copper base to assist with resistance to volume expansion related pressure, the walls were simply placed, resin glued and sealed with silicone. This likely is a direct cause of leakage issues. In addition, the timescale of design to manufactured larger vessel was over 6 months and for the smaller 5 cm vessel ~ six months. As of September 2019, the larger vessel is still awaiting repair due to a major leak at the end of June 2019.

This series of events was extremely disappointing and lead to severe issues with work progression and a great deal of uneeded distress.

As can be seen in Table 11, several different types of melt time are provided analogous to those calculated for the smaller 5cm box melting experiments with the addition of the value determined via the analysis of matrix generated heatmap data. In this analysis the normalised thermal threshold temperature was set as 50° C and above, several degrees lower than the previous analysis and is potentially as a result of the larger surface area of the imaged wall. In addition, as thermal and visual data sets did not reach 100% melted, likely in part due to signal noise and imperfect imaging, these melt completion times have been set at complete at 97% melted material. Both runs were operated with images taken every 5 minutes to minimise heat losses from the imaged face.

Table 11 - Beeswax 15cm box experimental melt completion times.

Type of Melt Track	Run 1 Time [s]	Run 3 Time [s]	Time difference from Run 1 to 3 [s]
Matrix @100%	59625	65735	6110
Normalised Thermal @97%	67200	72600	5400
Visual @97%	73200	72000	1200

Comparing all melt completion time types between Run 1 and 3, it is seen that there is disagreement between the visual analysis and other types which have a similar time difference, albeit a different time. Figure 177 shows the unprocessed visual imagery of both melt processes and not only confirms the melt times but also demonstrates the trends of melted fraction versus time for the visual analysis (Figure 173) are confirmed: the earlier section of the melt process in Run 3 does have a significantly reduced rate despite both runs completing in very similar times (within 20 minutes out of a total of 1220). It is believed that the reason for the difference in melt curve and on the figures is due to the moving insulation coming out of close contact with the imaged face, leading to the decreased amount of melted material in the bottom left of the images for a given elapsed time. The same pattern found in Figure 173 is found in the comparative thermal imagery but is unshown. One unforseen consequence of using the larger vessel, appears to be that the melt fraction curves derived from thermal and visual imagery have increased noise compared to the smaller 5cm experimental equivalents. This is most likely only an apparent increase due to the significantly larger melt times required.

The normalised thermal melt fraction track (Figure 179) and melt completion times show relatively good agreement with the visual imagery equivalents however, as mentioned in the previous section, the agreement is not optimal and requires tuning via the adjustment of the temperature threshold.

In addition, when comparing like for like imagery (Figure 178 and Figure 180), images at a given elapsed time look extremely similar but are slightly different due to thermal attenuation through the imaged wall leading to smoothing of gradients unlike the visual equivalents. These figures also make clear that the matrix of temperature sensors is having a severely degrading effect on the isotropy of the vessel. The liquid-solid interface is initially parallel but becomes

more and more angled as the melt progresses and completes in the top left. This is likely as a result of significant amounts of thermal energy being lost through the metal in the sensors and their wires. While this effect was expected, this magnitude of the effect was not. This is not ideal and has deleterious effects when utilized to validate an ideal CFD model. Both visual and thermal imagery again like the previous section show good contrast between melted and solid material and it is clear in some images that the thermal sensors are sufficiently shiny to be seen.

With the increased face size under thermal imaging it was hoped that the development of smaller features than those seen with the visual camera would be realised. This has again, however, been demonstrated not to have occurred; Figure 180 confers no such additional detail.

Comparing the matrix tracked melt times found in Table 11, it is seen that they show a significantly reduced value for melt completion time when compared to the other melt time types. This is due to two factors and they are limitations with respect to the design of the vessel. Due to the placement of the matrix of sensors centrally, and with linear interpolation for the heatmap, the melt progression above the top most values of the heatmap correspond to the sensors – not the top of the vessel or the melting material.

As can be seen in Figure 174, the generated heatmaps from this data show a more clear visualisation with the dual-tone images despite having the ironbow matching palette available.

Figure 176 shows the ongoing melt process in melt run 1 and has some interesting features which can be attributed to the heat loss through the imaged face (on the left of the Figure). Despite the actuated removable insulation it is clear that heat is still being lost via this imaged face leading to the symmetry in the leftmost image. This distinct lack of isotropy is not going to be reflected in the subsequent model. The middle and rightmost images of this figure demonstrate a central core of melted material reaching the top of the sensors before either the left or right most sensors which is expected as the core flow should be the most insulated and thus hottest.

Figure 175 shows the melt fraction versus time progression derived from the heat map data and also shows run 3 having a reduced rate of melting in comparison to run 1. Like the equivalent visually derived track however, it does not show the melt times at completion being similar. These values are below those of the visual equivalent as expected but the reasoning for the disparity in completed melt time is not known. Figure 175 also shows a wavy profile to both curves which is likely as a result of the interpolation between the rows of sensors as the melt progresses upward.

The current matrix configuration gives some insight into the ongoing melt process and demonstrates some efficacy but clearly gives erronous total melt times. In future works it would be prudent to utilize a design with an increased matrix sensor density and where edges of the vessel itself are also instrumented to avoid both this error in melt time and also reduce the "wavy" melt progress curves.

It should be noted that there is no attempt to compare the chosen matrix heatmap imagery directly with the equivalent thermal or visual imagery as not only is the imaged face having non isotropic heat losses but, as can be seen in Figure 178 and Figure 180, the sensors themselves are causing significant amounts of heat loss through their housing and wiring, leading to the dramatically increasing angle to the liquid-solid interface as the melt progresses.

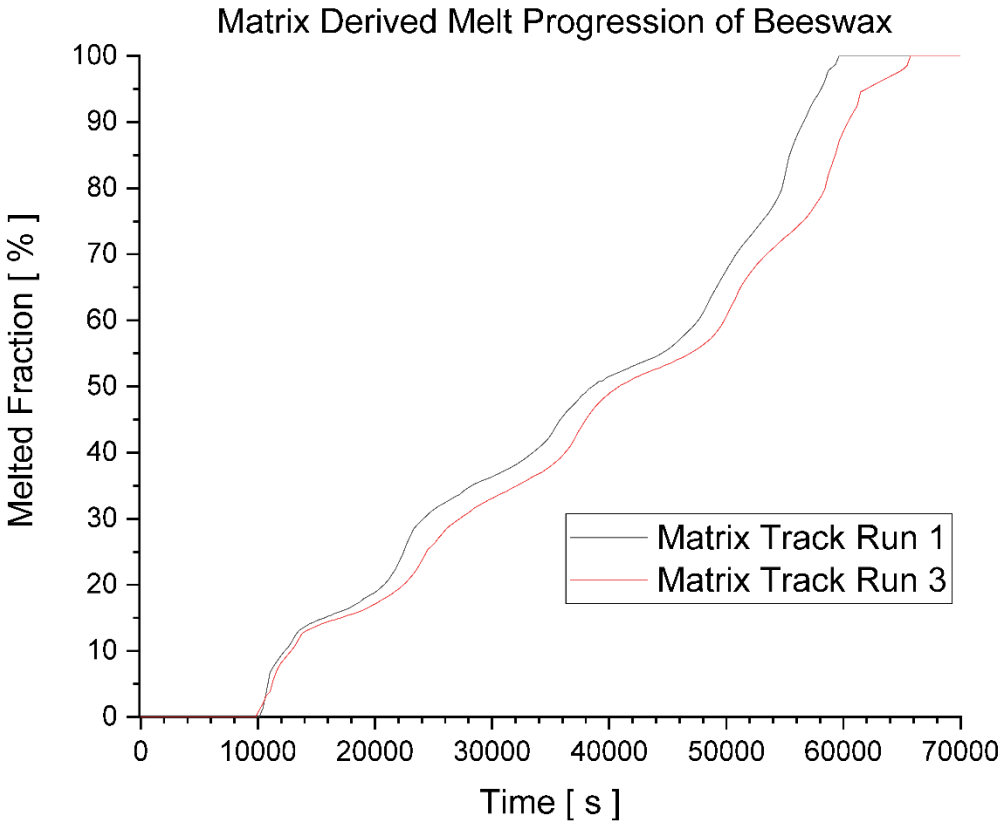

Figure 175 - Matrix imagery derived melted fraction track % for 15cm box beeswax experiments.

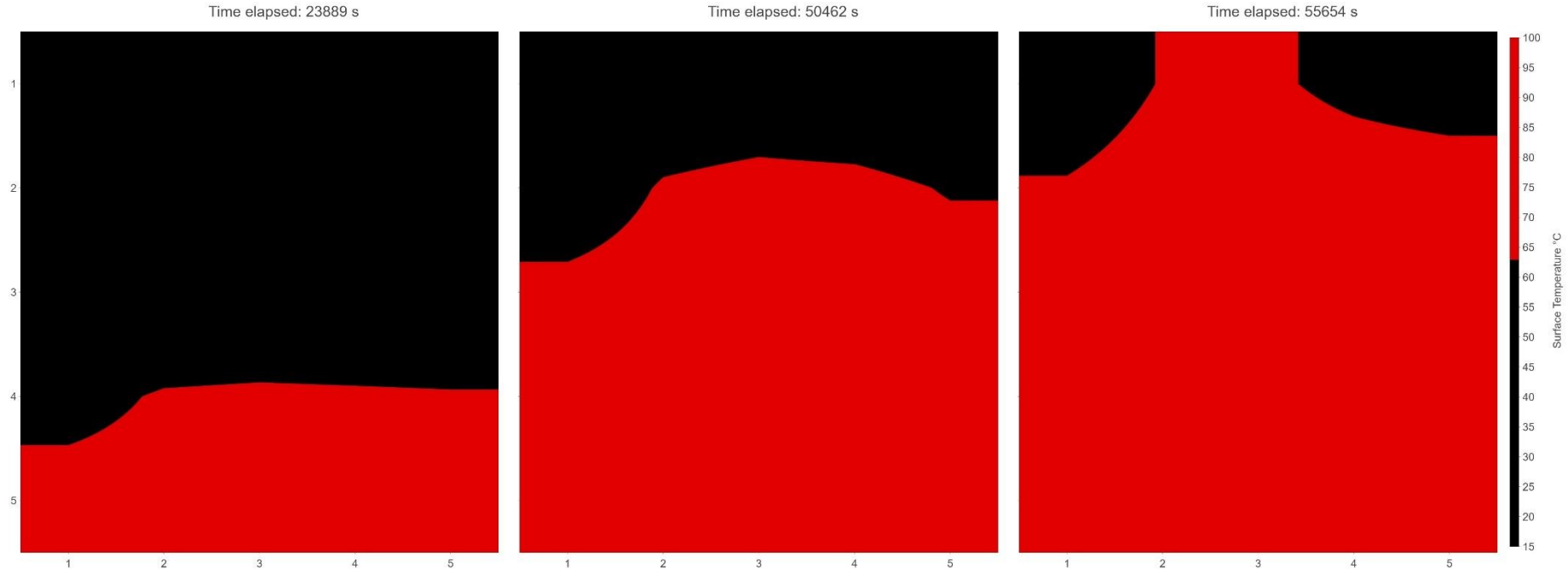

Figure 176 -Matrix derived dual-tone images of solid-liquid interface location at various times for 15cm vessel beeswax melt 1 (red shows liquid.) at 23889s (left), 50462s (middle) and 55654s (right.)

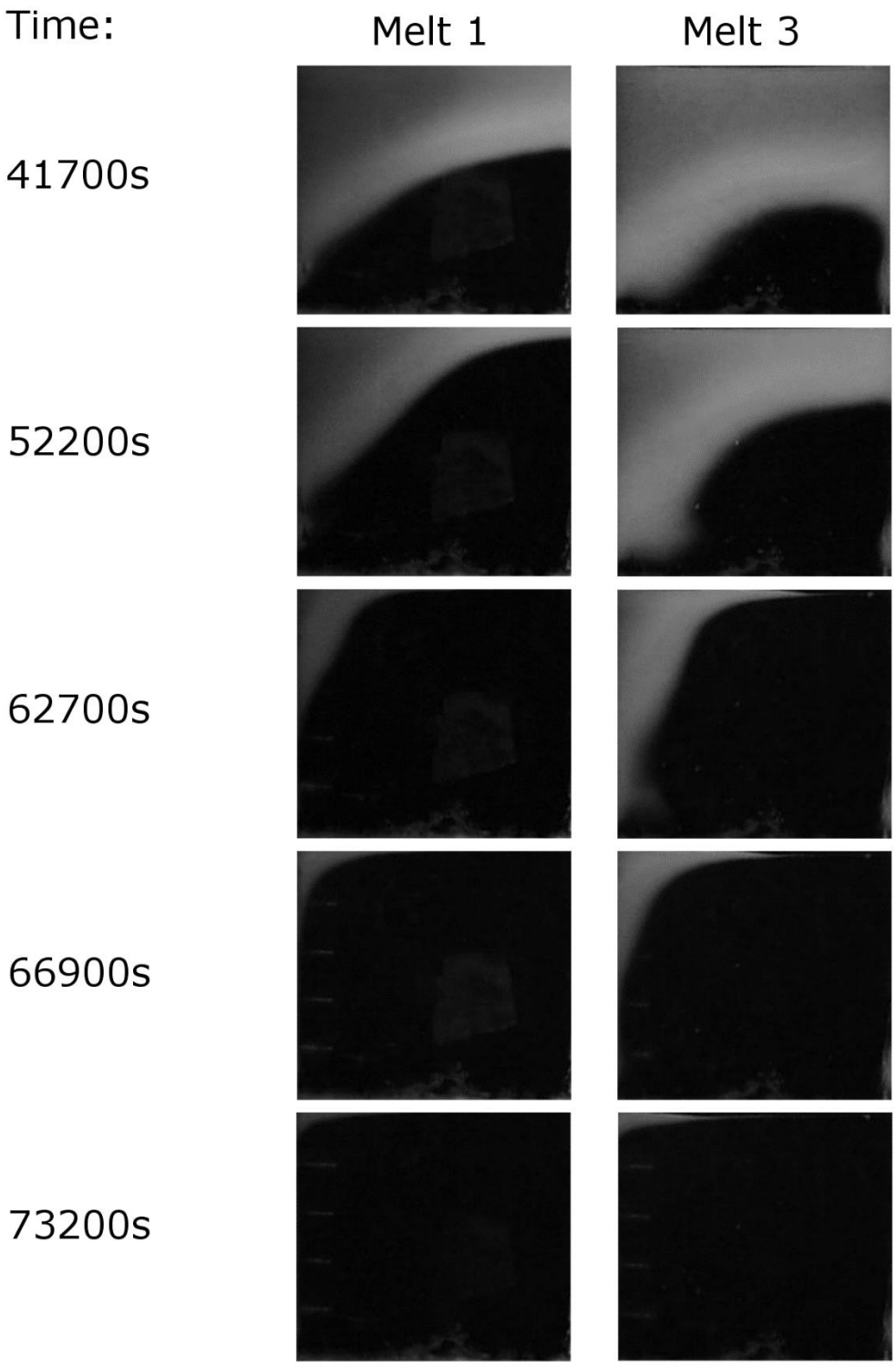

Figure 177 - Visual imagery unprocessed at various times for 15cm vessel beeswax melt 1 and melt 3.

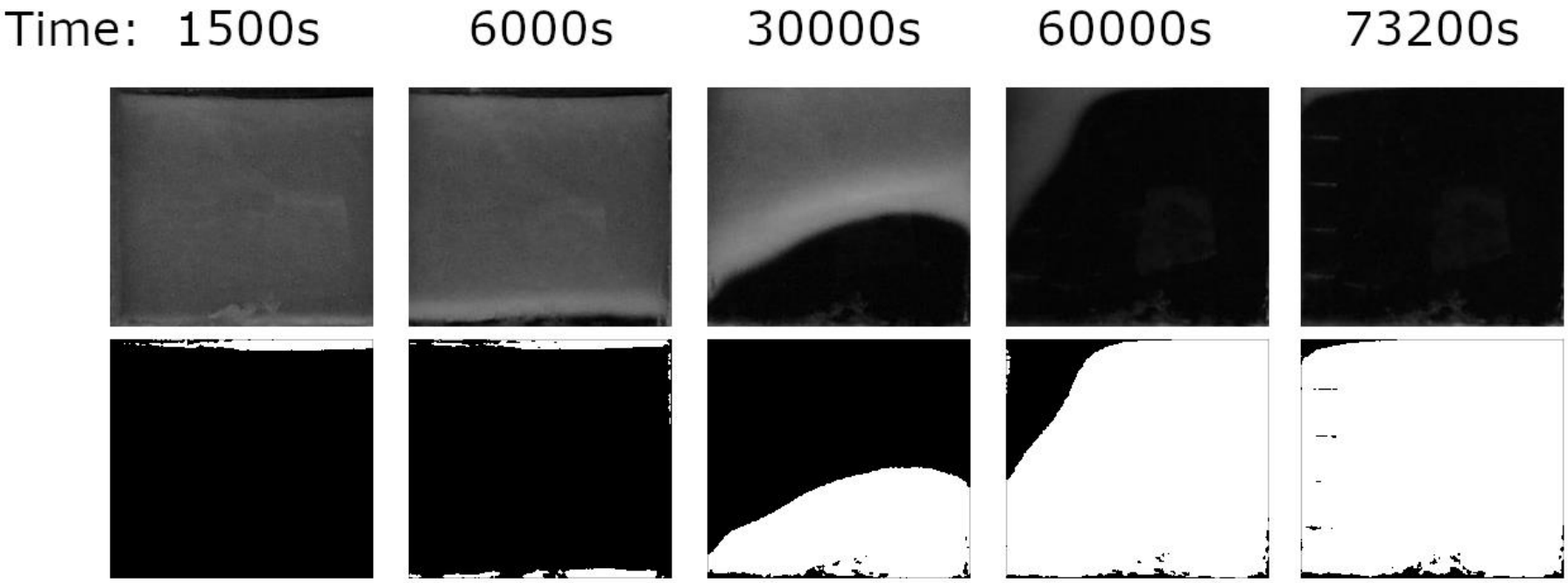

Figure 178 - Visual imagery unprocessed (top) and processed (bottom) at various times for 15cm vessel beeswax melt 1.

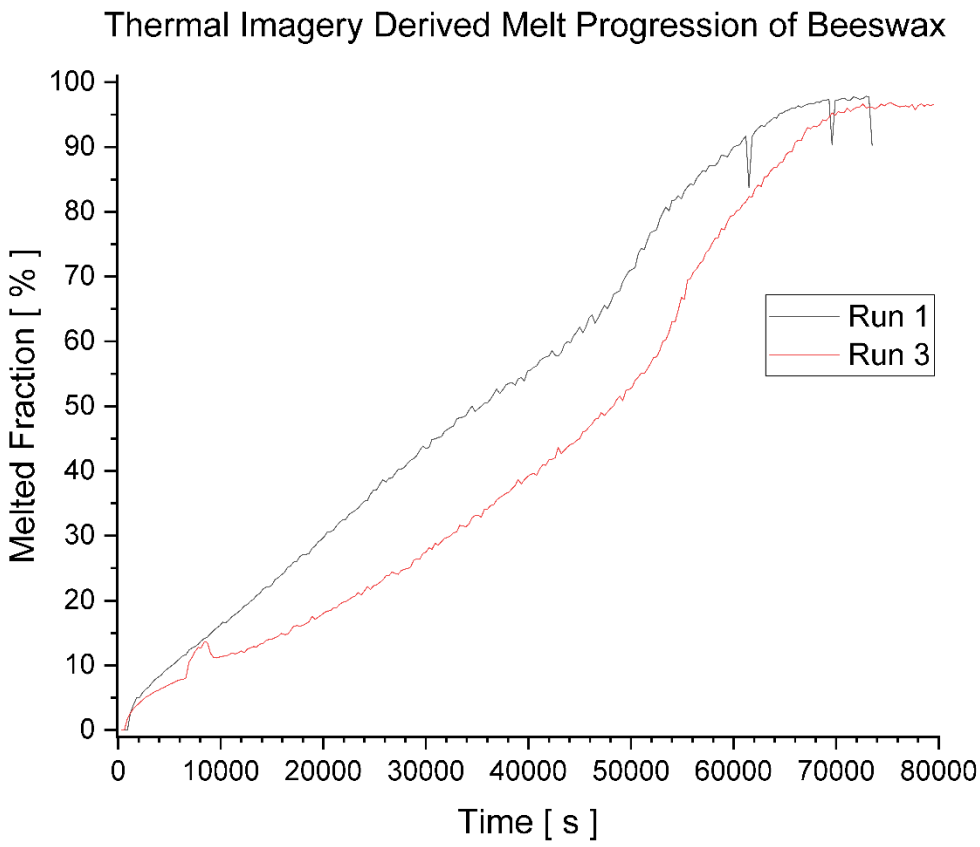

Figure 179 – Normalised thermal imagery derived melted fraction % for 15cm box beeswax experiments.

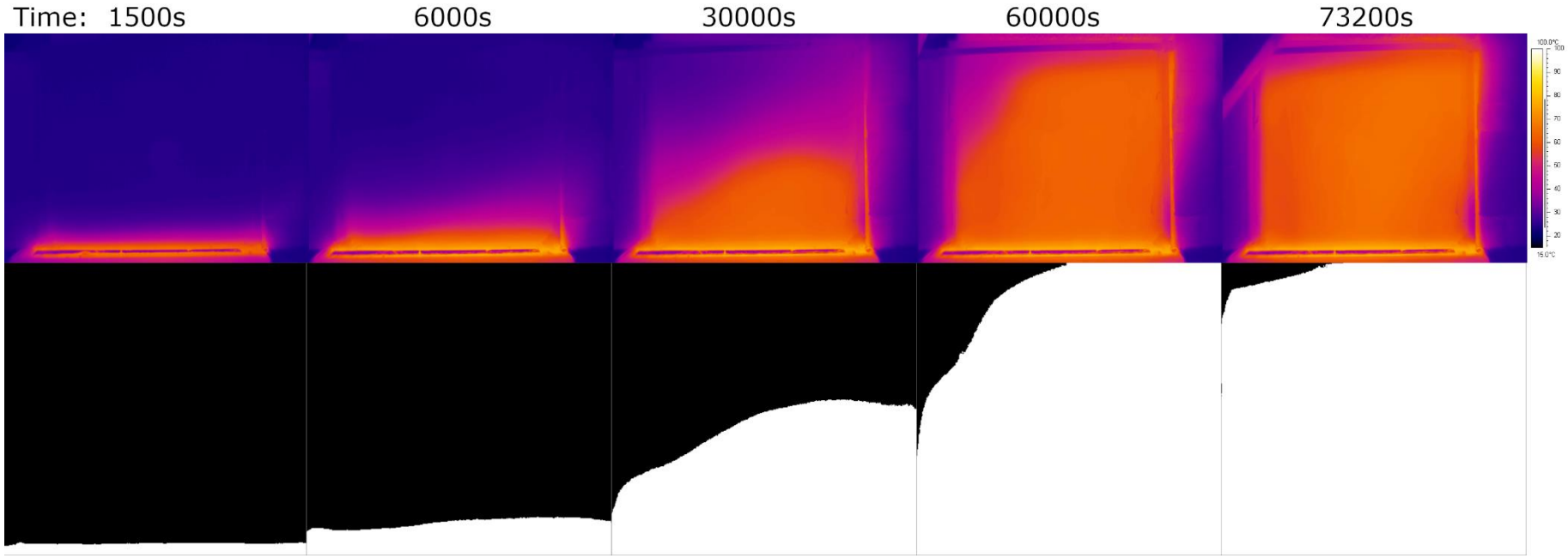

Figure 180 - Thermal imagery unprocessed (top) and processed (bottom) at various times for 15cm vessel beeswax melt 1.

7.6.5 Conclusions

The section of work has detailed the investigation into the isothermally heated melting processes of beeswax in an insulated 15cm dimensioned open top cube, utilizing a matrix of temperature sensors with thermal and visual camera imagery.

Beeswax was found to finish melting at approximately 72000s with similar doping of the phase change material by the copper surfaces as previously found with the 5cm experiments.

It was found again that visual imagery analysis gives clear imagery which can be processed to produce reasonable melt fraction versus time plots. Thermal imagery was again found to give a slightly less optimal track and again required tuning of the thermal thresholds used for analysis to give more accurate melted fraction versus time curves. The requirement of the thermal tuning again indicates the thermal camera was visualising significantly more thermal radiation via re-transmission from the wall rather than direct transmission from the phase change material inside the vessel. Smoothing due to thermal energy spreading through the imaged wall was visualised again and the smaller length scale phenomena which were hoped to be visualised were again not seen.

This fairly conclusively proves that thermal imaging is highly unlikely to confer additional or higher quality data when visualisation of the melt process of a given material is possible with a visual imagery camera. In this case the thermal imagery conferred no additional useful information.

In future work, it would be prudent to investigate whether further external insulation or changing the wall under thermal imaging to one with excellent insulation (such as airogel) will assist in showing phenomena that cannot be imaged with a visual camera; however it is likely that the thermal energy will be of insufficient gradient across the small lengthscale phenomena for this to be possible. It may also be possible to construct an imaging face from a grid of highly insulating material with gaps filled with highly conductive material which will give superior performance, such a configuration will function like an LCD matrix within a television and is likely to confer useful results via each separated cell.

The matrix of temperature sensors was found to given adequate data with a number of shortcomings.The lack of sensors at the edges of the vessel lead to over prediction of the melt fraction for a given time. In addition, the presence of the sensors themselves contributed negatively to the isotropy of the vessel as a result of heat losses via their electrical connections. To address these shortcomings it would be recommended to use more sensors toward the edges of the vessel, in addition to a higher density of sensors, if it is possible to reduce heat losses from these sensors. Reduction of heat losses from the sensors may be

achievable by using sensors made from a less conductive material than steel and reducing the length of the wiring connecting these sensors.

It was found that the lack of stability in the actuated insulation assembly lead to a lack of close contact with the imaged face for one run resulting in differences in the melt fraction curve profile. In subsequent work, upgrading this system to use a series of rails with a gearing system would significantly reduce the gap between the insulation and the imaged face, in addition to dramatically increasing the reproducability of this close fit and superior results.

Due to a multitude of leaks, further work into investigating the melt process of paraffin wax was not able to be completed, emphasing the need for good vessel design / manufacture and safety precautions.

7.7 Introduction – Validation of 15cm Geometry CFD Model

This section details the attempted modelling and validation of the 15cm beeswax domain against the experiments conducted in the previous section.

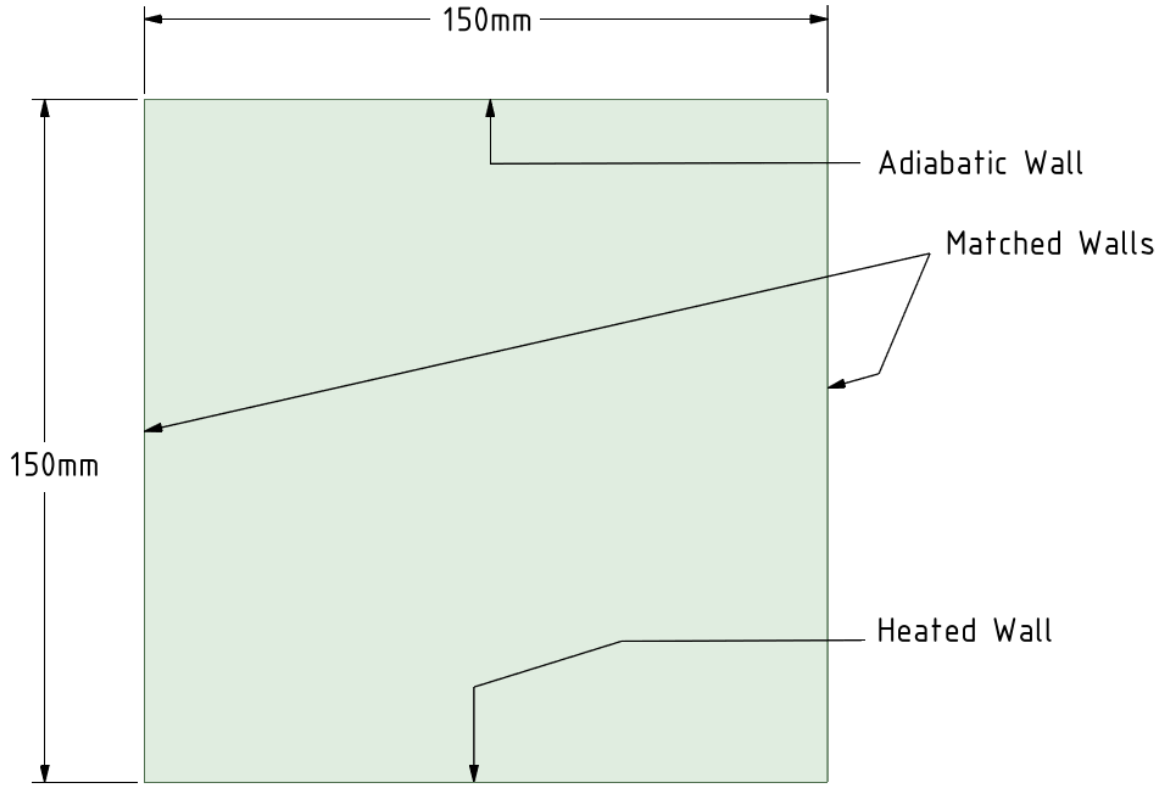

Figure 181 -2D 150mm square computational domain used for investigation of beeswax melt process.

7.7.1 Computational Domain and Initial and Boundary Conditions

These models were computed using Ansys 19.4 and the following assumptions are made in this study: (1) the top wall is adiabatic to represent ideal insulation; (2) flow is Newtonian and incompressible; (3) flow is laminar and under the effects of gravity; (4) joule friction heating is negligible; (5) physical properties are temperature dependant and accounted for using the linear multi-point data entry method for materials properties ; (6) heat transfer occurs by conduction and convection only; (7) volume change is ignored; (8) three dimensional convection is ignored.

The following initial and boundary conditions are applied:

- Bulk temperature - 25 °C.

- Bottom wall - 80°C.
- Top Wall – adiabatic.
- Side walls are matched and allow flow to pass in between.
- X velocity – 0 ms^{-1}.
- Y velocity – 0 ms^{-1}.
- Gauge pressure – 0 Pa.
- Gravity – on, set at -9.81 ms^{-2}

At time $t \geq 0$ the mushy constant value is set as:

$$C = 100{,}000$$

7.7.1.1 Solution Method and Controls:

For the numerical solution of the model the previously given methods and controls were utilized and super compute cluster 2 was exclusively utilized for computation (details of machine hardware and solution methods / controls given in chapter 2).

The transient formulation in use for these models was the first order implicit scheme.

7.7.1.2 Thermo-physical properties:

Utilized thermo-physical properties are listed in chapter 3 with values in Table 7 and Table 8 and previously experimentally determined densities listed in Table 6. Linear interpolation of temperature dependant values for material characteristics has taken place.

7.7.2 Results

This section details the results of the modelling of beeswax in the 15cm dimensioned domain utilizing the first order implicit transient formulation. Unfortunately, it is seen that the modelling undertaken has been unsuccessful with no conditions giving reasonable mesh or temporally insensitive results. The believed reasons for this are the same as for the previously detailed 5cm beeswax model, with values of Rayleigh number and contour analysis indicating turbulent convection.

The results below detail the result from various attempted models and do not represent the real physical behaviour of a beeswax melt process due to inability to reliably converge or the determination variables for temporally and mesh insensitive results.

7.7.2.1 Evolution of Melt (time)

Figure 182 shows the melt fraction versus time curves for various mesh resolution models of the first order explored, to try to find mesh independence compared to the 3rd experimental

run in the 15cm vessel. The 62,000 and 78,000 cell models have a completed melt time of 9820s and 18390s respectively. This figure has several trends of importance:

1. The trend of melt fraction versus time for models is seen to be an ongoing decreasing rate trend after the onset of convection, unlike the experimentation which shows the opposite for the majority of the melt process.
2. Higher mesh resolutions are associated with longer melting times but are unlikely to approach a similar melting time as experimentation.
3. Observing the curves for the explored models, it is seen that lack of convergence is seen in the later stages of each model as noise, where the melted fraction actually decreases and increases with an increasing trend which is unphysical behaviour. However, this unphysical behaviour started to occur while the model was still converging.
4. The onset of this inability to converge takes place at earlier stages of the melt process for models with increased mesh resolution.

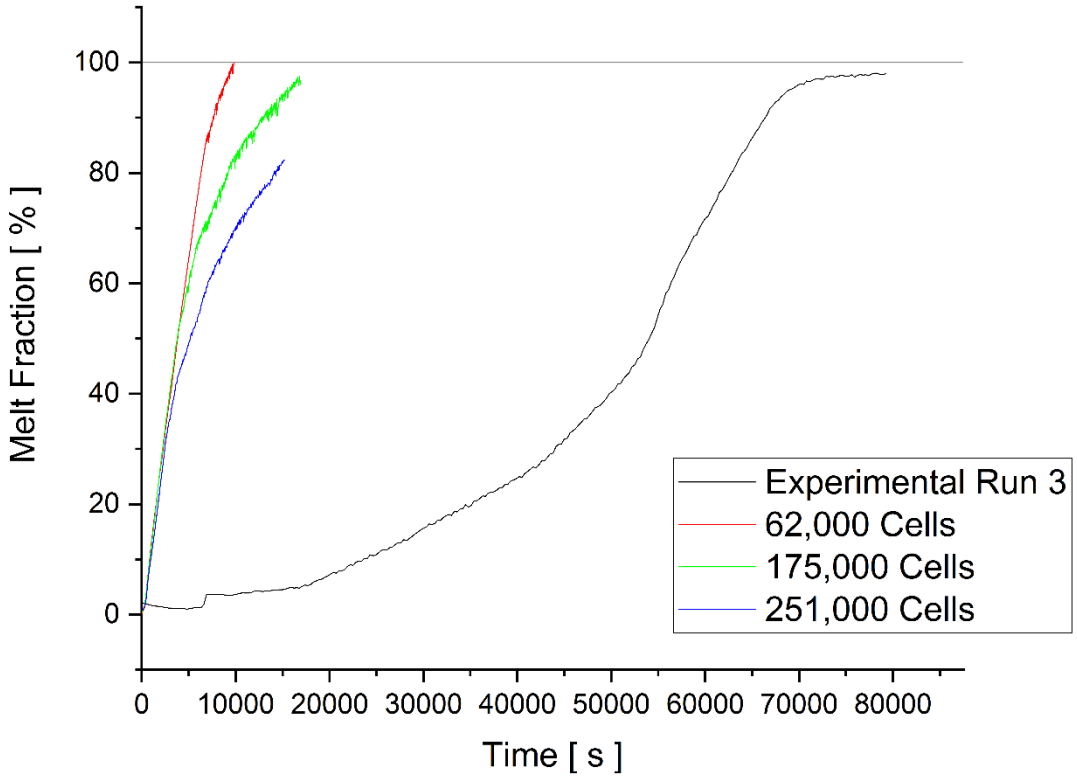

Figure 182 - Melt fraction versus time for various mesh resolutions of 15cm beeswax model and experimental melt 3 for beeswax.

The different trends between the models and experimentation indicate that even with modelling insensitivity to time step or mesh resolution these models are invalid. In addition, the same trend seen in these models is reflected in all previous beeswax models including

those with insensitivity to time step size and mesh resolution, indicating even if such conditions were found the resulting model would still be invalid. Looking at the same melt fraction curves for the mushy zone exploration also has this same trend, which indicates no selection of mushy constant is likely to give valid results, which indicates the models are unable to capture the behaviour of the melt process for beeswax accurately with the current configuration.

With higher mesh resolutions reaching the point where convergence is no longer attained in earlier stages of the melt and with longer times to melt completion, it is likely that further exploration will result in models taking multiple months to converge in computational time alone. If a similar trend occurs as found with the 5cm beeswax model, above a certain mesh resolution – no explored settings will result in convergence. With a linear increased number of cells, based on the previous 5cm model area and its highest mesh resolution, the highest resolution with success likely lies within the range of 312,000 and 392,000 cells for this 15cm model. No higher mesh resolutions than shown were attempted due to perceived futility in such effort and time constraints.

It was found that reducing the liquid fraction update solution control was able to retain model convergence in the later stages of a given model melt process at the expense of dramatically increasing the number of iterations and time required to do so. It was also found that the unphysical behaviour still occurred **despite** convergence being attained with these settings.

Like the previous 5cm models, exploration of time step sensitivity was undertaken which found reducing the time step was coincidental with reducing the unphysical oscillation in melt fraction, but also a reduced total melt time. Further exploration below 0.1s time step was not attempted due to the exorbitant computation and time of such models to complete, with successful results highly unlikely.

Given the behaviour observed for the second order transient formulation and the increased Rayleigh numbers found in the 15cm model, (Figure 184), investigation of this setting was not undertaken. It is believed that the cause of the difficulty with these models is related to the magnitude of the Rayleigh number, (10^8), and turbulent convection. Evidence of this can be seen in Figure 183 which shows the Y-velocity contours of flow development between 5670s and 6300s with multiple smaller plumes and significant flow disruption. Visualisation of this is also seen in other dimensionless number plots and contour plots.

7.7.2.2 Rayleigh Numbers

Rayleigh number analysis is undertaken to assess to what extent convection is occurring in each material during the melt process. For this analysis the Rayleigh number and Grashof numbers are defined as follows [3]:

$$Ra = GrPr \tag{42}$$

$$Gr = \frac{g\beta(\tau_S - \tau_\infty){L_h}^3}{\nu^2} \tag{43}$$

Where $\beta_{Beeswax}$ =0.004170747 and L_H =0.15 (m) but would usually be the ratio of horizontal plate area to plate perimeter in 3 dimensions. In this case it has been assumed to be the 2D hot surface length [4].

As can be seen in the average Rayleigh number plot (computed from the heated surface) Figure 184 and Figure 185, the values are elevated to the range of 10^8, now in the turbulent convective regime [125]. This model follows the same curve profile as previous models with a larger initial value ~ $9x10^8$, subsequently decreasing with time. Like the 5cm beeswax model this value maintains a value consistently above $1x10^8$. This larger value is partially due to the increased domain size giving a much larger heated surface leading to increased convection.

Perturbation and plumes can be seen in the contours confirming this. Further confirmation of these plumes and the perturbation can also be found in the subsequent contour plots for Peclet number, Figure 187.

Like the 5cm beeswax model, the elevated Rayleigh number and turbulent convection are likely the reason for the severe difficulty with none time step and mesh resolution sensitive model convergence / failure to converge and may require the utilization of an alternative turbulence viscosity model.

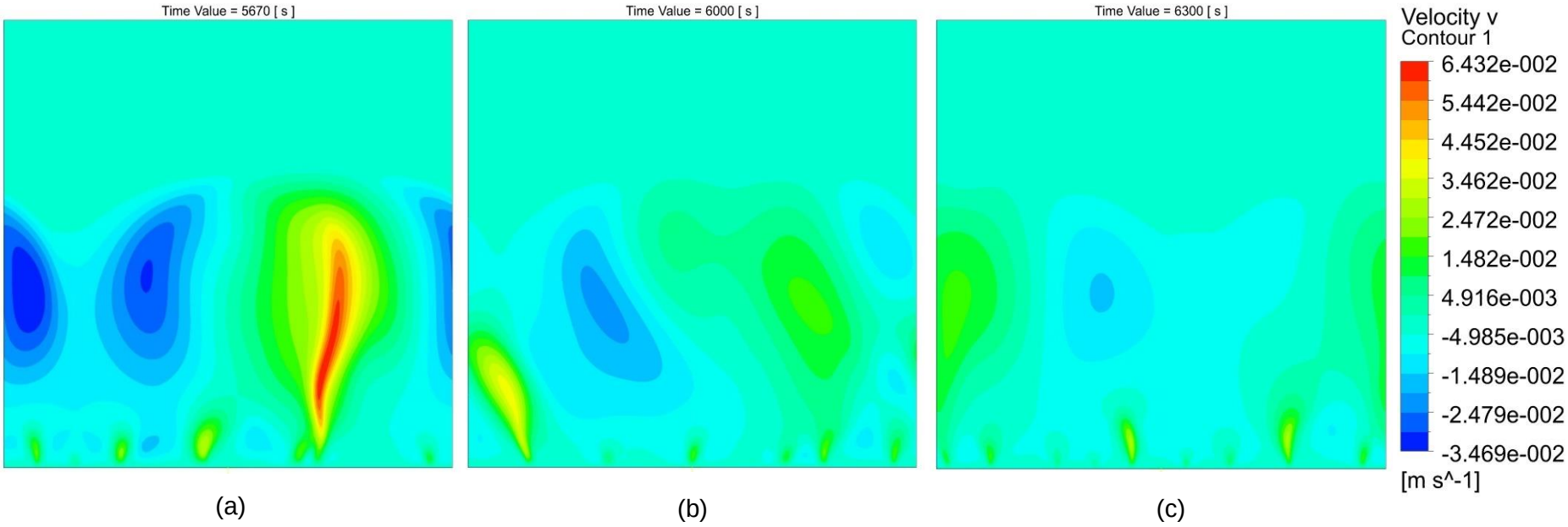

Figure 183 - Contours of Y Velocity for 15cm beeswax model of mesh resolution 175,000 cells at (a) 5670s, (b) 6000s and (c) 6300s.

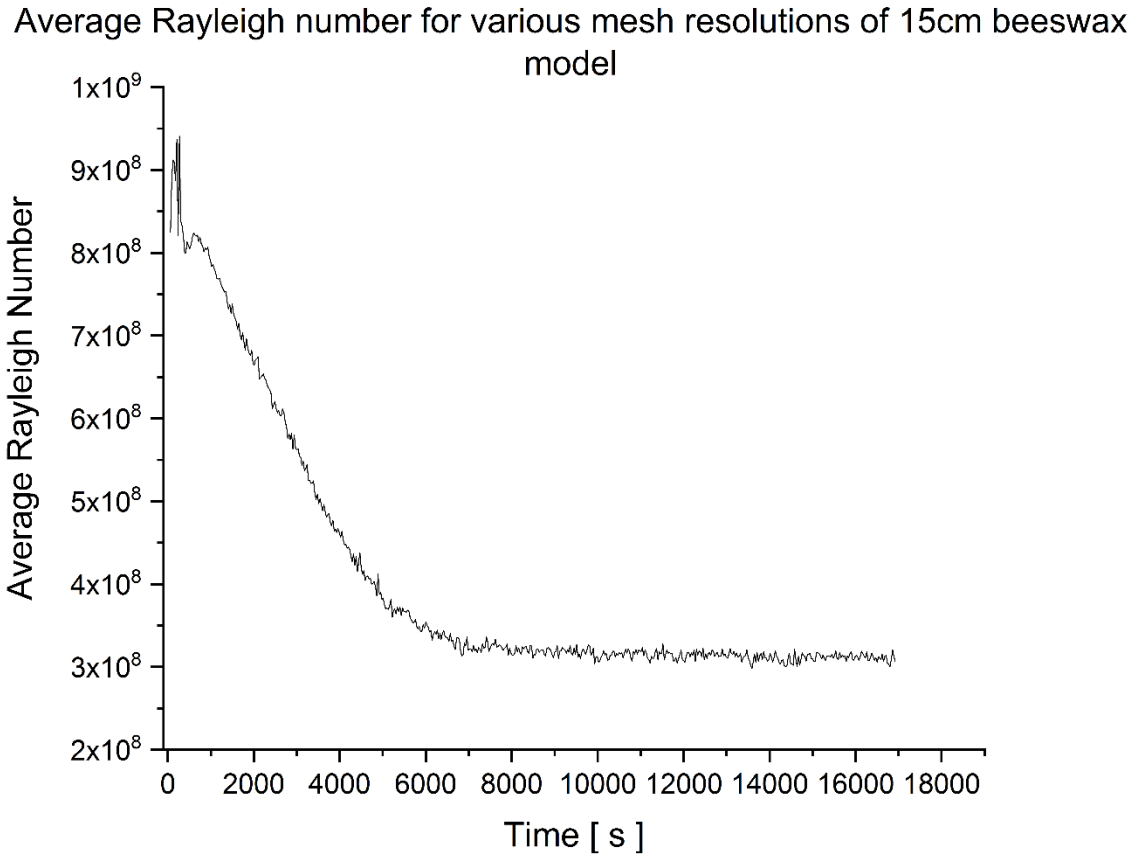

Figure 184 - Average Rayleigh number versus time for 15cm beeswax model of mesh resolution 175,000.

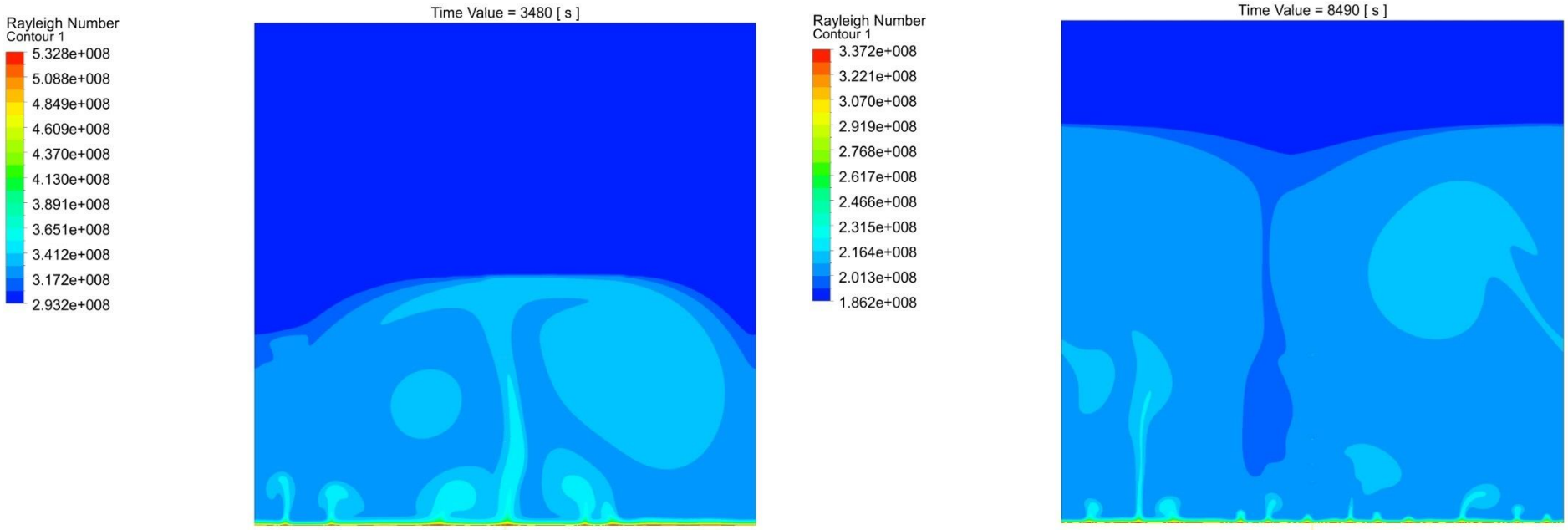

(a) (b)

Figure 185 - Contours of Rayleigh number for 15cm beeswax model of mesh resolution 175,000 cells at (a) 3480s and (b) 8490s.

7.7.2.3 Peclet Numbers

Peclet number is calculated as follows using the cell Reynolds number and Prandtl number from the CFD-Post software and is an average value across the domain:

$$Pe = RePr \tag{44}$$

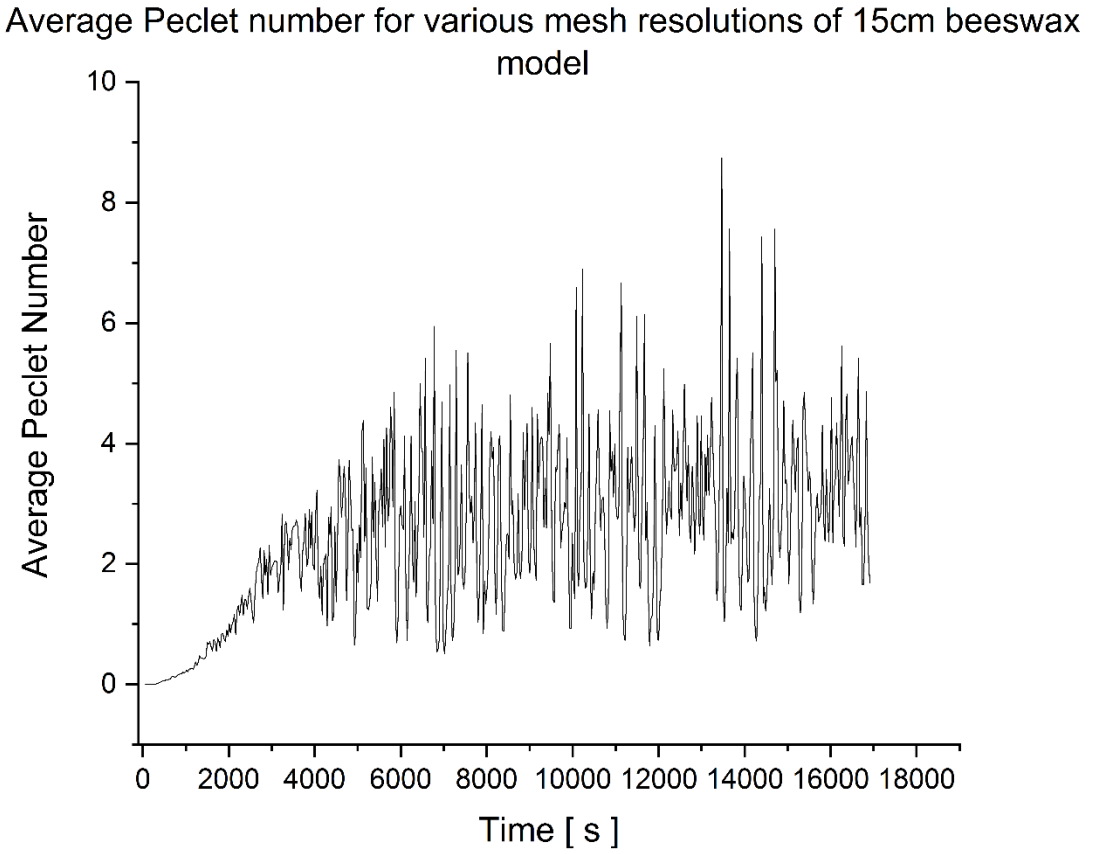

Figure 186 - Average Peclet number versus time for 15cm beeswax model of mesh resolution 175,000.

Figure 186, the average Peclet number versus time follows the 5cm model trend of an increasing value over time and a noisy signal with the onset of convection ~900s. It is seen however, that the larger domain has resulted in a much noisier profile, with a larger range between 0 – 9 compared to the 5cm domain's 0 -3.

The values being achieved are related to both the increased Rayleigh number and increased Nusselt number.

Figure 187 shows contours of Peclet number during the melt process early in the melt at 9750s and 10050s which show the cell instability and multiple plumes associated with turbulent convection.

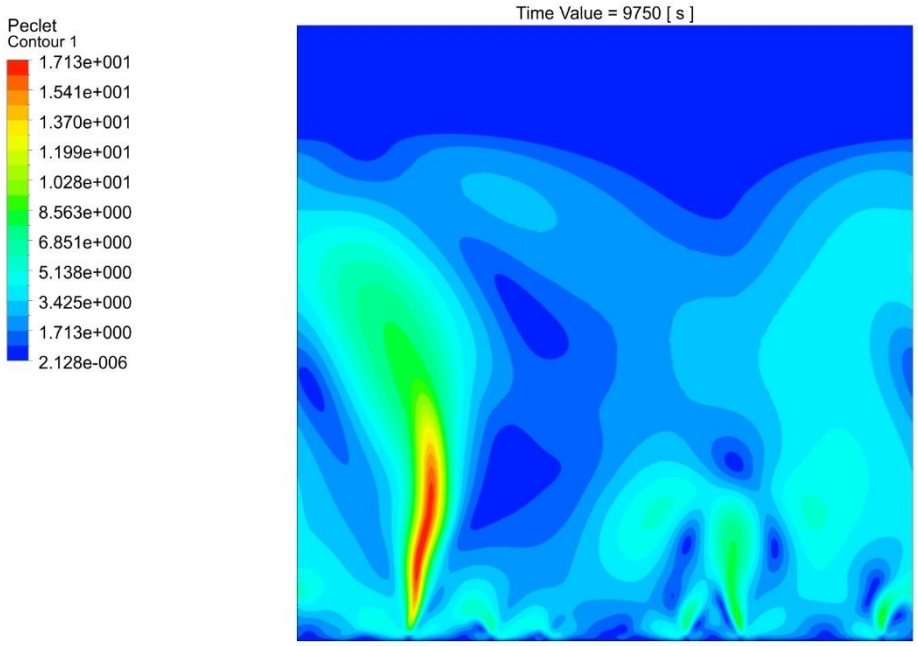

(a)

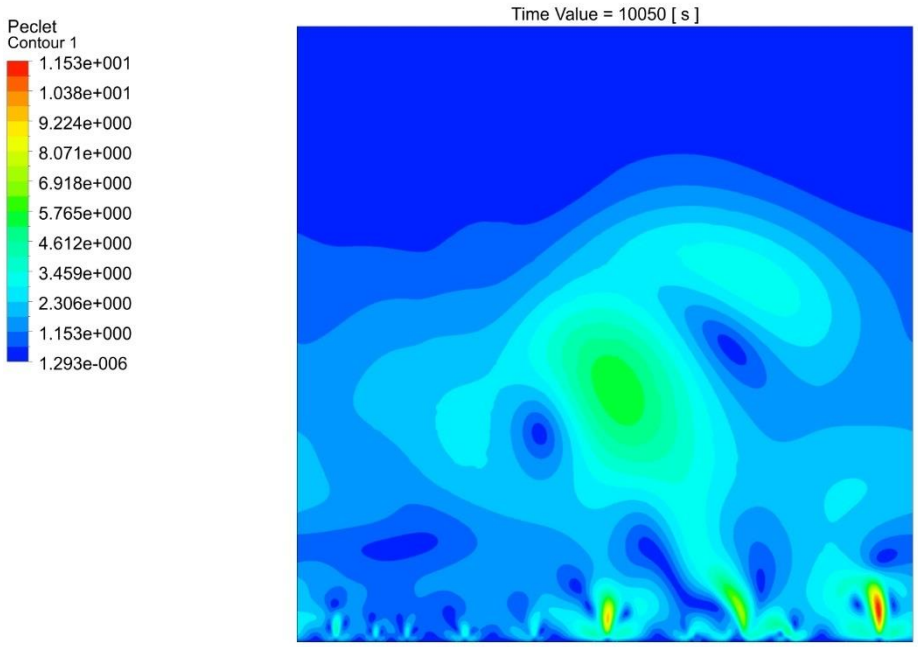

(b)

Figure 187 - Contours of Peclet number for 15cm beeswax model of mesh resolution 175,000 cells at (a) 9750s and (b) 10050s.

7.7.2.4 Nusselt Numbers

As the specified configuration is one of bottom heated horizontal plates, coupled with the values of Rayleigh number, the Nusselt number correlation utilized is the following [107]:

$$Nu = 0.54\, Ra^{1/4} \tag{45}$$

Where:

$$(\tau_s + \tau_\infty)/2$$

$$1.0 < Ra < 1 \times 10^{10}$$

Nusselt number analysis was undertaken in order to quantify the ratio of heat transfer conducted and convected from the hot surface.

The values and curve profile found in Figure 188 for average Nusselt number are extremely similar to those found for the 5cm beeswax model in Figure 154, starting from initial values of ~34 before decreasing to a plateau ~27. This is unexpected as the heated surface (the characteristic length) is 3 times larger, thus the Nusselt number is expected to be larger. This may be related to the relationship, (Equation 45), being inappropriate or more likely as a result of the 15cm model being time step / mesh resolution sensitive with difficulty in convergence. The significantly noisier signal is also likely related to this but could also be a result of the increased turbulent convection indicated by the Rayleigh number analysis.

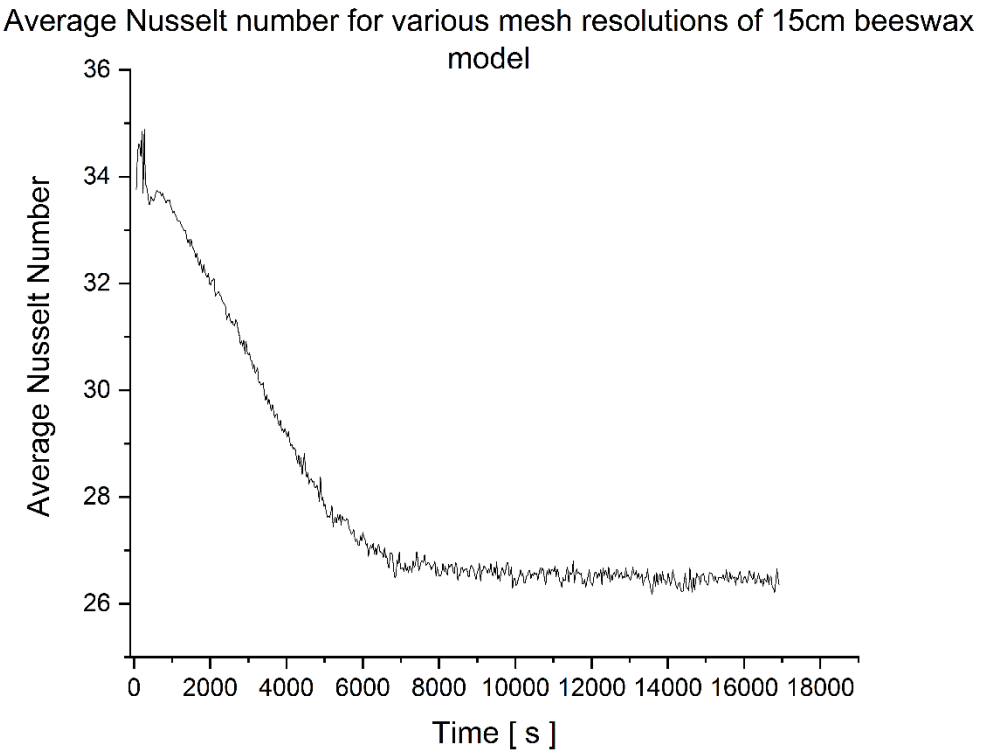

Figure 188 - Average Nusselt number versus time for 15cm beeswax model of mesh resolution 175,000.

7.7.3 Mesh and Temporal Dependency

As was previously mentioned, the beeswax 15cm model did not find a configuration with mesh and temporal insensitivity likely as a result of turbulent convection. Modelling explored various mesh resolutions, from 62,000 cells to 251,000 cells. Mesh resolution / time step insensitivity could not be found due to time constraints and likely the modelling configuration and turbulent convection.

7.7.4 Conclusions

This section of work has attempted to validate the melt process of beeswax in a 15cm experimental vessel heated isothermally at 80°C against a comparative CFD model.

It was found that the generated model for beeswax was invalid and did not agree well with experimental data, likely as a result of the inability to find a mesh and time step independent solution, which itself is likely related to the presence of turbulent convection and the selection of the laminar viscosity model. It is speculated however, that adjusting the turbulence viscosity model in use will enhance model accuracy.

The first order transient formulation determined a melt time of 18390s for the 175,000 cell model and as results for the previous 5cm model for the second order transient formulation

deviated from experimental behaviour, no attempt was made with this setting in the larger vessel. The experimentally determined melt times were found to be around ~72000s.

As was speculated for the previous 5cm beeswax model, with the large value of Rayleigh numbers observed in this model (10^8), the convective flow is now in a turbulent regime [125]. The Rayleigh number values observed are larger than those found for the 5cm beeswax model, likely a result of the further increased dimensions of the computational domain. Further confirmation of a turbulent convective regime was seen in contour plots of various dimensionless variables.

Observing the melt fraction versus time plots for models demonstrated a curve profile similar to the previous beeswax models which was however different to that of the experiment. Even though optimal time step and mesh resolution insensitive results were not found, this repeated trend indicates that even if such conditions were found, the resulting model would still deviate from experimental behaviour.

With progressively higher mesh resolutions, reaching a point where convergence was no longer attained occurred in progressively earlier stages of the melt process, which itself would elongate.

Increasing mesh resolution from those shown would likely result in non-convergence in addition to resulting in dramatic increases in computational workload. If the same trend occurred as was found in the 5cm model, there would also be a point at which further mesh resolution enhancement would result in no convergence at any settings. No higher mesh resolutions than shown were attempted due to the likely wasted effort and time constraints.

Considering the previous 5cm models and greater success with the paraffin wax model, it is likely the cause of the beeswax model's failure to attain mesh and temporal insensitivity is related to the material's thermo-physical properties, potentially the much larger viscosity. It is recommended that the beeswax models be investigated using an alternative turbulence viscosity model to determine if more optimal / valid models can be generated as it is clear that success with the current modelling conditions is unlikely.

If further investigation of the modelling with the current settings is undertaken it is recommended that researchers assess whether their time and computational resources are sufficient to do so as such an investigation may take many months of computational time.

As a result, it has been seen modelling with the current settings is sub-optimal for design exploratory work given the timescales for these simulations to give results (if valid) and the effort required to attain time step and mesh resolution insensitivity.

8 Conclusions

8.1 Overall Conclusions

Thermal energy storage as a subclass of energy storage is expected to play a primary role in the UK's target to reduce greenhouse gas emissions in line with the UK Climate Change Act by 2050, via the temporal displacement of demand from supply.

Phase change storage has a plethora of demonstrable advantages over conventional / sensible thermal storage but has a complex heat transfer process which is difficult to investigate or model, due to complex phenomena in addition to time dependency. Additional complexity in heat transfer arises due to geometry design, heat source orientation, etc.. From comparative modelling research work, there appear to be several areas for improvement related to use of experimentally determined, temperature dependent properties. In addition, there is a lack of critical investigation of mushy zone constant variation and decreasing discussion or verification of time step and mesh independence. There are also relatively few models explicitly intended to represent an underfloor heat storage system.

This thesis presents the work undertaken to investigate modelling the melt process of the phase change materials, beeswax and paraffin wax with temperature dependant properties. Various 2D configurations were generated, intended to represent ideal underfloor phase change material-based heat storage and modelled with the Ansys Fluent program. The importance of a key modelling parameter, the mushy constant, has been explored. Validation of models has been attempted and the methods of investigating the experimental melt process explored for efficacy.

Experimental work was undertaken to determine the thermo-physical properties of both PCMs which successfully determined the temperature dependant density data and latent heat capacities. Further exploration to determine appropriate materials' selection for later experimental vessels undergoing photography was explored, which found polycarbonate to be an optimal wall choice for visual and thermal photographic analysis.

Initial modelling work explored the generation of 2D 2.5cm square domains isothermally bottom heated to determine the modelling conditions likely needed for successful convergence without temporal or mesh resolution sensitivity. These models showed much higher mesh resolutions were required than in other research, likely as a result of using more empirical temperature dependant properties rather than phase dependant or formulaic based approximation of properties. In this configuration it was found that beeswax fully melted in 800s and paraffin wax in 10062.5s. Dimensionless variable analysis indicated significantly larger amounts of convection in the beeswax model, resulting in the dramatically lower melt

time compared to paraffin wax. With subsequent models of paraffin wax obtaining significantly reduced melt times, the validity of this initial paraffin wax model is questionable, despite its time step and mesh resolution insensitivity. This section of work also modelled a top heated beeswax configuration with the same settings which determined a melt completion time almost 10x larger than the bottom heated equivalent showing the dramatic effect of convective heat transfer.

Further configurations with isothermally heated pipes with varied pipe location and domain width were investigated to quantify a different heating method. These found that increasing domain widths were coincidental with the melt time increasing, albeit non-linearly, as material directly adjacent to the heated pipe melted via conduction only. Increased width domains resulted in a larger convective heat transfer coefficient which was attributed to a larger volume of material available to convect by virtue of there being a larger distance between adjacent pipes.

The melting time is also significantly affected by the placement of the pipe, with placement in the middle of the domain causing a longer period of conduction - dominated melting, thus a completed melt time was almost 9 times longer than for a pipe at the bottom of the domain. As such it would be highly recommended always to mount heating surfaces in such a way that the proportion of phase change materials above the heated surface is maximised.

The importance of the mushy constant was subsequently explored for the bottom mounted pipe and bottom flat plate, isothermally heated configurations which found that, as in previous studies, a larger mushy constant has led to an increased time for melt completion. The magnitude of this effect appears to vary depending on the geometry being investigated, with proportional increases of melt time differing for the pipe and flat plate geometries. Contour analysis also shows that larger mushy constant values appear to result in decreasing curvature of the liquid-solid interface. It is also seen that the elongation of melt time is related to delayed onset of convection.

Investigation of model validation and validation methods was undertaken with both a 5cm and a 15cm experimental vessel and their equivalent models for beeswax and paraffin wax for the former and beeswax only for the latter.

For the smaller vessel both materials were found to finish melting at approximately the same time of 4200s. This was an interesting result when considering the larger latent heat and specific heat (40% and 100% respectively) of beeswax, indicating its superior thermal characteristics. The larger vessel had a melt time of ~72000s for beeswax. In all experimentation it was found that an oxidative or galvanic process led to doping of the phase change materials resulting in quicker melt times in subsequent experiments for each material.

Visual imagery analysis was found to give clear imagery, able to be processed to give reasonable melt fraction versus time plots, although thermal imagery was found to give a slightly less optimal track for both materials and required tuning of the thermal thresholds used for analysis to give similar results. Despite thermal threshold tuning, results from these thermal images were still found to be negatively affected by thermal energy dispersing across the imaged face, leading to smooth gradients unlike the sharper visual images. The requirement of the thermal tuning indicates the thermal camera was visualising significantly more thermal radiation via re-transmission from the wall, rather than direct transmission from the phase change material inside the vessel. As a result of these factors, smaller length scale phenomena which were hoped to be visualised, were not seen in either vessel. Visual imaging has been conclusively shown to be a useful method for determination of the liquid-solid interface position for suitable materials and thermal imaging should present a valid method on materials where visual imagery is not suitable.

It was found that the generated validation models for these experiments using beeswax did not agree well with experimental data, likely as a result of the inability to find a mesh / time step independent solution caused by turbulent convection. This was ascertained via observation of the Rayleigh number 10^7 / 10^8 [125] and flow contours.

The generated model for paraffin wax agreed far more closely with the experimental melt times, with the model reaching melt completion at 3720s compared to experimentation ~4200s. Despite the close melting completion time, the paraffin wax melt profile does not perfectly match that of the experiment although this is likely as a result of the vessel design's imperfect isotropy and heat losses from the face being imaged.

Given the greater success with the paraffin wax model and the reduced Rayleigh numbers observed in comparison to the beeswax, it appears the cause of the beeswax model's failure to attain mesh and temporal insensitivity is related to the geometry in concert with the material's thermo-physical properties, potentially the much larger viscosity. It is clear that the beeswax models could be investigated using an alternative turbulence viscosity model to determine whether more optimal models can be generated, assuming researchers have significant time and computational resources available.

A matrix of temperature DS18B20 sensors on the larger 15cm vessel was found to give adequate data for liquid-solid interface tracking with a number of shortcomings. The lack of sensors at the edges of the vessel led to overprediction of the melt fraction for a given time. In addition, the presence of the sensors themselves contributed negatively to the isotropy of the vessel as a result of heat losses via their electrical connections.

Given the long timescale for model generation and validation (months to years), it has been shown that for exploratory design work, this configuration of CFD modelling is inappropriate due the enormous amount of time and resources (computational) required to attain results even if they are found to be valid. It would be quicker and potentially easier simply to conduct experimentation.

Improvement or extensions of the current work for the future can be seen in the section below.

8.2 Recommendations for future work

1. **2D to 3D modelling**

The present studies have investigated the heat transfer into phase change materials and the presence of convection during a phase change transition to liquid from solid. The experimental vessels have shown significant deviation from the ideal isotropy required to accurately compare to a 2D infinite width computational domain.

With this shortcoming considered, it is essential that future studies account for these discrepancies by utilizing 3D geometries.

2. **Investigate mushy zone parameter optimisation based on temperature difference**

It has been reported that a useful method for optimising the mushy zone constant value, to achieve good agreement between numerical modelling using the enthalpy-porosity method and experimental data for melting, is to use the driving temperature difference [104].
Investigation and verification of this could provide a much needed improvement in the rapid development of accurate models for phase change melting.

3. **Investigate mushy zone constant modelling validity with respect to dependency on mesh and temporal resolution**

In this body of work the effect of mushy constant value has been investigated without ascertaining mesh and temporal independence for each value of mushy constant. It is likely that this will have an effect on the stability of the solution and the changing of a parameter key to the model, how changing the mushy constant value affects the needed mesh and temporal resolution is of great importance despite the laboriousness of this process.

4. **Investigate utilization of second order upwind spatial discretization and other solution methods or stabilization settings**

The work in this thesis presents results of first order transient formulation and first order upwind spatial discretization. While no success has been found with the second order transient formulation, only brief exploration of the second order upwind spatial discretization was undertaken (not detailed) with no success.

In addition, exploration of the PISO and Coupled pressure velocity couplings was also investigated early during the PhD which found great difficulty in convergence and demonstrated inordinate calculation times with respect to computational resources available.

A new stabilisation method available in the recent versions of Ansys Fluent called generalized minimum residual method (GMRES) may provide additional convergence efficiency which is critical in reducing the large amount of time spent converging these models.

These other model configurations/settings may provide additional insight into phase change melt processes if researchers can attain reasonable convergence or have additional computational resources available.

5. Volume expansion causing undesirable pressure build-up

Due to both beeswax and paraffin wax having significant volume expansion when undergoing a phase change from solid to liquid, a bottom heated configuration results in significant pressure build up within even open top vessels due to remaining solid material above acting as a plug.

This resulted in small amounts of PCM leakage during successful testing and 2 critical failures in the larger test vessel resulting in large leaks, a damaged test vessel and significant losses of time. This occurred due to the construction of the vessel not using a slot into the base material in order to hold the walls. When manufactured the walls were located using a routed edge and subsequently glued with resin and sealed with silicone.

In future works this problem may be avoided by ensuring design is followed correctly and bottom walls are located in slots to ensure no differential movement from the base can take place to damage the seals.

6. Solidification cycles

The present study does not engage with any modelling or experimental investigation of solidification cycles due to volume of work and difficulty of analysis/implementation. In reality, these PCM storage systems will operate with a full melting and solidification cycle and thus should be investigated.

This may be particularly challenging work to model due to likely conduction dominance, long re-solidification times and thus much larger amounts of computational work.

7. Asymmetric experimental melt profiles

The larger test vessel has demonstrated significant asymmetry in the melting profiles and it is likely due to heat being commuted down the metal casing of the sensors and their wiring.

In future works the effect of these matrix of sensors could be minimised by utilizing smaller casings of a different material than steel and / or by reducing the sensor wire length to minimise heat losses.

8. Investigate varied wall construction for imaged face

Thermal imaging was unable to resolve small length scale phenomena and sharp definition is lost due to thermal energy spreading in the x and y dimensions of the imaged wall. Future work could investigate the development and utilization of a wall composed of a matrix grid of highly insulating material, filling the gaps with highly conductive material or short wave infra-red transparent material, to prevent the thermal energy spreading across the face from adjacent parts of the wall or the heated base.

9. Investigate other flow visualization techniques for convection cell imaging and modelling validation

While utilizing thermal imaging to visualise convection cell formation has proved non-viable for small length scales, it is likely possible to utilize Schlieren visualisation techniques in order to show density gradients. The visualisation of density gradients should show the convective flow by virtue of the associated density change; however these visualised gradients may be difficult to utilize for validation of modelling and may require significant visual processing.

This technique has been widely utilized for flow visualisation for both air and water [126]. This technique may have some efficacy investigating transparent PCMs such as paraffin wax, although the materials utilized for the containment vessel may increase the difficulty of using this technique.

Other techniques such as particle image velocimetry may also be of interest but have their own limitations to implementation, such as finding a suitable reflective doping material that does not affect thermo-physical properties.

9 References

[1] Parliament of the United Kingdom, “Climate Change Act 2008,” *HM Gov.*, 2008.

[2] P. Eames, D. Loveday, V. Haines, and P. Romanos, “The Future Role of Thermal Energy Storage in the UK Energy System : An Assessment of the Technical Feasibility and Factors Influencing Adoption Research Report The Future Role of Thermal Energy Storage in the UK Energy System : An assessment of the Techni,” *Ukerc*, 2014.

[3] G. Nellis and S. Klein, *Heat Transfer*. Cambridge University Press, 2009.

[4] DECC, “Digest of UK Energy Statistics: Chapter 5 Electricity,” pp. 113–155, 2015.

[5] BM Reports, “U.K. National Grid status,” 2016. [Online]. Available: http://www.gridwatch.templar.co.uk/. [Accessed: 08-Feb-2016].

[6] I. A. G. Wilson, A. J. R. Rennie, Y. Ding, P. C. Eames, P. J. Hall, and N. J. Kelly, “Historical daily gas and electrical energy flows through Great Britain’s transmission networks and the decarbonisation of domestic heat,” *Energy Policy*, vol. 61, pp. 301–305, 2013.

[7] J. Hong, N. J. Kelly, I. Richardson, and M. Thomson, “Assessing heat pumps as flexible load,” *Proc. Inst. Mech. Eng. Part A J. Power Energy*, vol. 227, no. 1, pp. 30–42, 2012.

[8] J. Palmer, I. Cooper, and (Department of Energy and Climate Change), “United Kingdom Housing Energy Fact File,” pp. 1–172, 2013.

[9] Energy Saving Trust, “Measurement of Domestic Hot Water Consumption in Dwellings,” *Energy Savings Trust*, 2008.

[10] A. Hepbasli and Y. Kalinci, “A review of heat pump water heating systems,” *Renew. Sustain. Energy Rev.*, vol. 13, no. 6–7, pp. 1211–1229, 2009.

[11] G. Florides and S. Kalogirou, “Ground heat exchangers—A review of systems, models and applications,” *Renew. Energy*, vol. 32, no. 15, pp. 2461–2478, 2007.

[12] J. Ji, T. T. Chow, G. Pei, J. Dong, and W. He, “Domestic air-conditioner and integrated water heater for subtropical climate,” *Appl. Therm. Eng.*, vol. 23, no. 5, pp. 581–592, 2003.

[13] The Association for Decentralised Energy, “District Heating Installation Map of the UK,” 2016. [Online]. Available: http://www.theade.co.uk/district-heating-installation-map_790.html. [Accessed: 01-Aug-2016].

[14] DECC, “Deep Geothermal Review Study Final Report,” 2013.

[15] Y. Ding and S. B. Riffat, “Thermochemical energy storage technologies for building applications: a state-of-the-art review,” *Int. J. Low-Carbon Technol.*, vol. 8, no. 2, pp. 106–116, 2012.

[16] ETSAP/IRENA, “Thermal Energy Storage. Technology Brief,” no. January, p. 24, 2013.

[17] A. A. El-Sebaii, M. R. I. Ramadan, S. Aboul-Enein, and A. M. Khallaf, “History of the solar ponds: A review study,” *Renew. Sustain. Energy Rev.*, vol. 15, no. 6, pp. 3319–3325, 2011.

[18] A. Z. A. Saifullah, A. M. Shahed Iqubal, and A. Saha, “Solar pond and its application to desalination,” *Asian Trans. Sci. Technol.*, vol. 02, no. 03, pp. 2221–4283, 2012.

[19] M. Bakr, N. van Oostrom, and W. Sommer, “Efficiency of and interference among multiple Aquifer Thermal Energy Storage systems; A Dutch case study,” *Renew. Energy*, vol. 60, pp. 53–62, 2013.

[20] S. Haehnlein, P. Bayer, and P. Blum, “International legal status of the use of shallow geothermal energy,” *Renew. Sustain. Energy Rev.*, vol. 14, no. 9, pp. 2611–2625, 2010.

[21] B. Sanner, F. Kabus, P. Seibt, and J. Bartels, “Underground Thermal Energy Storage for the German Parliament in Berlin, System concept and operational experiences,” *Proc. World Geotherm. Congr. Antalya*, no. April, p. paper 1438, 1-8, 2005.

[22] E. Hahne, “ITW solar heating system: An oldtimer fully in action,” *Sol. energy*, vol. 69, no. 6, pp. 469–493, 2000.

[23] L. Mesquita, D. McClenahan, J. Thornton, J. Carriere, and B. Wong, “Drake Landing Solar Community: 10 Years of Operation,” in *ISES Solar World Congress 2017*, 2018, pp. 1–12.

[24] G. Alva, Y. Lin, and G. Fang, “An overview of thermal energy storage systems,” *Energy*, vol. 144, pp. 341–378, 2018.

[25] Z. Zhao, M. T. Arif, and A. M. T. Oo, “Solar Thermal Energy with Molten-salt Storage for Residential Heating Application,” *Energy Procedia*, vol. 110, no. December 2016, pp. 243–249, 2017.

[26] R. I. Dunn, P. J. Hearps, and M. N. Wright, “Molten-salt power towers: Newly commercial concentrating solar storage,” *Proc. IEEE*, vol. 100, no. 2, pp. 504–515, 2012.

[27] T. Schmidt and D. Mangold, “The multi-functional heat storage in Hamburg-Bramfeld – innovative extension of the oldest German solar energy housing estate,” in *conference proceedings of the "5th International Renewable Energy Storage Conference“ (IRES*

2010), 2010, pp. 0–5.

[28] N. Yu, R. Z. Wang, and L. W. Wang, “Sorption thermal storage for solar energy,” *Prog. Energy Combust. Sci.*, vol. 39, no. 5, pp. 489–514, 2013.

[29] L. Scapino, H. A. Zondag, J. Van Bael, J. Diriken, and C. C. M. Rindt, “Sorption heat storage for long-term low-temperature applications: A review on the advancements at material and prototype scale,” *Appl. Energy*, vol. 190, pp. 920–948, 2017.

[30] A. Hauer, “Thermal energy storage with zeolite for heating and cooling applications.,” in *ISHPC 2002-International Sorption Heat Pump Conference*, 2002.

[31] R. B. Boer de, W. G. Haije, J. B. J. Veldhuis, and S. F. Smeding, “Solid-Sorption Cooling With Integrated Thermal Storage: The SWEAT Prototype,” *Int. Conf. Heat Powered Cycles, Larnaca, Cyprus*, no. August, 2004.

[32] S. K. Henninger, H. A. Habib, and C. Janiak, “MOFs as Adsorbents for Low Temperature Heating and Cooling Applications,” *J. Am. Chem. Soc. (ACS Publ.*, pp. 2776–2777, 2009.

[33] J. L. C. Rowsell and O. M. Yaghi, “Metal-organic frameworks: A new class of porous materials,” *Microporous Mesoporous Mater.*, vol. 73, no. 1–2, pp. 3–14, 2004.

[34] S. K. Henninger, F. Jeremias, H. Kummer, and C. Janiak, “MOFs for use in adsorption heat pump processes,” *Eur. J. Inorg. Chem.*, no. 16, pp. 2625–2634, 2012.

[35] S. P. Casey, J. Elvins, S. Riffat, and A. Robinson, “Salt impregnated desiccant matrices for ‘open’ thermochemical energy storage - Selection, synthesis and characterisation of candidate materials,” *Energy Build.*, vol. 84, pp. 412–425, 2014.

[36] K. Korhammer *et al.*, “Sorption and thermal characterization of composite materials based on chlorides for thermal energy storage,” *Appl. Energy*, vol. 162, pp. 1462–1472, 2016.

[37] Science Applications International Corporation, “Compact Thermal Energy Storage Technology Assessment Report,” no. 104748553, 2013.

[38] R. Barker, “The reactivity of calcium oxide towards carbon dioxide and its use for energy storage,” *J. Appl. Chem. Biotechnol.*, vol. 24, no. 4–5, pp. 221–227, 1974.

[39] R. Barker, “The reversibility of the reaction CaCO3 ⇄ CaO+CO2,” *J. Appl. Chem. Biotechnol.*, vol. 23, no. 10, pp. 733–742, 1973.

[40] P. Pardo *et al.*, “A review on high temperature thermochemical heat energy storage To cite this version : HAL Id : hal-01345714,” *Renew. Sustain. Energy Rev. Elsevier*, vol.

32, pp. 591–610, 2014.

[41] Y. Kato, M. Yamada, T. Kanie, and Y. Yoshizawa, “Calcium oxide/carbon dioxide reactivity in a packed bed reactor of a chemical heat pump for high-temperature gas reactors,” *Nucl. Eng. Des.*, 2001.

[42] Y. Kato, N. Harada, and Y. Yoshizawa, “Kinetic feasibility of a chemical heat pump for heat utilization of high-temperature processes,” *Appl. Therm. Eng.*, vol. 19, no. 3, pp. 239–254, 1999.

[43] M. Paskevicius, D. A. Sheppard, and C. E. Buckley, “Thermodynamic changes in mechanochemically synthesized magnesium hydride nanoparticles,” *J. Am. Chem. Soc.*, vol. 132, no. 14, pp. 5077–5083, 2010.

[44] M. Felderhoff and B. Bogdanović, “High temperature metal hydrides as heat storage materials for solar and related applications,” *Int. J. Mol. Sci.*, vol. 10, no. 1, pp. 335–344, 2009.

[45] F. S. Yang, G. X. Wang, Z. X. Zhang, and V. Rudolph, “Investigation on the influences of heat transfer enhancement measures in a thermally driven metal hydride heat pump,” *Int. J. Hydrogen Energy*, vol. 35, no. 18, pp. 9725–9735, 2010.

[46] D. N. Harries, M. Paskevicius, D. A. Sheppard, T. E. C. Price, and C. E. Buckley, “Concentrating solar thermal heat storage using metal hydrides,” *Proc. IEEE*, vol. 100, no. 2, pp. 539–549, 2012.

[47] A. Sharma, V. V. Tyagi, C. R. Chen, and D. Buddhi, “Review on thermal energy storage with phase change materials and applications,” *Renew. Sustain. Energy Rev.*, vol. 13, no. 2, pp. 318–345, 2009.

[48] B. Zalba, J. M. Marin, L. F. Cabeza, and H. Mehling, “Review on thermal energy storage with phase change: materials, heat transfer analysis and applications,” *Appl. Therm. Eng.*, vol. 23, no. 3, pp. 251–283, 2003.

[49] F. Agyenim, N. Hewitt, P. Eames, and M. Smyth, “A review of materials, heat transfer and phase change problem formulation for latent heat thermal energy storage systems (LHTESS),” *Renew. Sustain. Energy Rev.*, vol. 14, no. 2, pp. 615–628, 2010.

[50] M. M. Farid, A. M. Khudhair, S. A. K. Razack, and S. Al-Hallaj, “A review on phase change energy storage: Materials and applications,” *Energy Convers. Manag.*, vol. 45, no. 9–10, pp. 1597–1615, 2004.

[51] S. D. Sharma and K. Sagara, “International Journal of Green Energy Latent Heat Storage Materials and Systems: A Review LATENT HEAT STORAGE MATERIALS

AND SYSTEMS: A REVIEW," *Int. J. Green Energy*, vol. 2, no. 2, pp. 1–56, 2005.

[52] H. Mehling and L. F. Cabeza, *Heat and cold storage with PCM: an up to date introduction into basics and applications*. 2008.

[53] K. Swaminathan Gopalan and V. Eswaran, "Numerical investigation of thermal performance of PCM based heat sink using structured porous media as thermal conductivity enhancers," *Int. J. Therm. Sci.*, vol. 104, pp. 266–280, 2016.

[54] N. R. Jankowski and F. P. McCluskey, "A review of phase change materials for vehicle component thermal buffering," *Appl. Energy*, vol. 113, pp. 1525–1561, 2014.

[55] A. Sharma, V. V. Tyagi, C. R. Chen, and D. Buddhi, "Review on thermal energy storage with phase change materials and applications," *Renew. Sustain. Energy Rev.*, vol. 13, no. 2, pp. 318–345, 2009.

[56] J. R. Turnpenny, D. W. Etheridge, and D. A. Reay, "Novel ventilation cooling system for reducing air conditioning in buildings.," *Appl. Therm. Eng.*, vol. 20, no. 11, pp. 1019–1037, Aug. 2000.

[57] K. Lin, Y. Zhang, X. Xu, H. Di, R. Yang, and P. Qin, "Experimental study of under-floor electric heating system with shape-stabilized PCM plates," *Build. Environ.*, vol. 39, no. 12, pp. 1427–1434, Dec. 2004.

[58] M. J. Stalin, S. M. Krishnan, and P. Barath, "Cooling of Room with Ceiling Fan Using Phase Change Materials," *Proc. World Congr. Eng.*, vol. III, pp. 2024–2027, 2013.

[59] J. Jeon, J. H. Lee, J. Seo, S. G. Jeong, and S. Kim, "Application of PCM thermal energy storage system to reduce building energy consumption," *J. Therm. Anal. Calorim.*, vol. 111, no. 1, pp. 279–288, 2013.

[60] M. Liu, W. Saman, and F. Bruno, "Review on storage materials and thermal performance enhancement techniques for high temperature phase change thermal storage systems," *Renewable and Sustainable Energy Reviews*. 2012.

[61] A. Hoshi, D. R. Mills, A. Bittar, and T. S. Saitoh, "Screening of high melting point phase change materials (PCM) in solar thermal concentrating technology based on CLFR," *Sol. Energy*, 2005.

[62] B. C. Shin, S. D. Kim, and W. H. Park, "Ternary carbonate eutectic (lithium, sodium and potassium carbonates) for latent heat storage medium," *Sol. Energy Mater.*, 1990.

[63] R. Aringhoff, M. Geyer, U. Herrmann, R. Kistner, P. Nava, and R. Osuna, "AndaSol-50 MW Solar Plants with 9 hour storage for Southern Spain," *Proc. 11th SolarPACES Int. Symp. Conc. Sol. Power Chem. Energy Technol.*, no. March 2016, pp. 37-42 TS-

BibTeX, 2002.

[64] C. Richter *et al.*, “Solar Power and Chemical Energy Systems Annual Report,” *Int. Energy Agency*, 2008.

[65] D. Laing, T. Bauer, W. D. Steinmann, and D. Lehmann, “Advanced High Temperature Latent Heat Storage System - Design and Test Results,” in *International Conference on Thermal Energy Storage - Effstock*, 2009, no. June, pp. 1–8.

[66] A. Trigui, M. Karkri, and I. Krupa, “Thermal conductivity and latent heat thermal energy storage properties of LDPE/wax as a shape-stabilized composite phase change material,” *Energy Convers. Manag.*, vol. 77, pp. 586–596, 2014.

[67] Y. Du and Y. Ding, “Towards improving charge/discharge rate of latent heat thermal energy storage (LHTES) by embedding metal foams in phase change materials (PCMs),” *Chem. Eng. Process. Process Intensif.*, vol. 108, pp. 181–188, 2016.

[68] Z. Jiang *et al.*, “Form-stable LiNO3–NaNO3–KNO3–Ca(NO3)2/calcium silicate composite phase change material (PCM) for mid-low temperature thermal energy storage,” *Energy Convers. Manag.*, vol. 106, no. 3, pp. 165–172, 2015.

[69] R. Baby and C. Balaji, “Experimental investigations on thermal performance enhancement and effect of orientation on porous matrix filled PCM based heat sink,” *Int. Commun. Heat Mass Transf.*, vol. 46, pp. 27–30, 2013.

[70] H. Cui, W. Tang, Q. Qin, F. Xing, W. Liao, and H. Wen, “Development of structural-functional integrated energy storage concrete with innovative macro-encapsulated PCM by hollow steel ball,” *Appl. Energy*, vol. 185, pp. 107–118, 2017.

[71] K. O. Lee, M. A. Medina, X. Sun, and X. Jin, “Thermal performance of phase change materials (PCM)-enhanced cellulose insulation in passive solar residential building walls,” *Sol. Energy*, vol. 163, no. January, pp. 113–121, 2018.

[72] L. Liu, D. Su, Y. Tang, and G. Fang, “Thermal conductivity enhancement of phase change materials for thermal energy storage: A review,” *Renew. Sustain. Energy Rev.*, vol. 62, pp. 305–317, 2016.

[73] S. A. Mohamed *et al.*, “A review on current status and challenges of inorganic phase change materials for thermal energy storage systems,” *Renew. Sustain. Energy Rev.*, vol. 70, pp. 1072–1089, Apr. 2017.

[74] L. Colla, L. Fedele, S. Mancin, L. Danza, and O. Manca, “‘Nano-pcms for enhanced energy storage and passive cooling applications,’” *Appl. Therm. Eng.*, vol. 110, pp. 584–589, 2016.

[75] L. Cao, D. Su, Y. Tang, G. Fang, and F. Tang, “Properties evaluation and applications of thermal energystorage materials in buildings,” *Renew. Sustain. Energy Rev.*, vol. 48, pp. 500–522, Aug. 2015.

[76] K. E. Kasza and M. M. Chen, “Improvement of the Performance of Solar Energy or Waste Heat Utilization Systems by Using Phase-Change Slurry as an Enhanced Heat-Transfer Storage Fluid,” *J. Sol. Energy Eng.*, vol. 107, no. 3, p. 229, 1985.

[77] P. Charunyakorn, S. Sengupta, and S. K. Roy, “Forced convection heat transfer in microencapsulated phase change material slurries: flow in circular ducts,” *Int. J. Heat Mass Transf.*, vol. 34, no. 3, pp. 819–833, Mar. 1991.

[78] L. Vorbeck, S. Gschwander, P. Thiel, B. Lüdemann, and P. Schossig, “Pilot application of phase change slurry in a 5m3 storage,” *Appl. Energy*, 2013.

[79] R. Yang, H. Xu, and Y. Zhang, “Preparation, physical property and thermal physical property of phase change microcapsule slurry and phase change emulsion,” *Sol. Energy Mater. Sol. Cells*, 2003.

[80] Y. Jin, W. Lee, Z. Musina, and Y. Ding, “A one-step method for producing microencapsulated phase change materials,” *Particuology*, 2010.

[81] T. Kawanami *et al.*, “Thermophysical properties and thermal characteristics of phase change emulsion for thermal energy storage media,” *Energy*, 2016.

[82] M. Goel, S. K. Roy, and S. Sengupta, “Laminar forced convection heat transfer in microcapsulated phase change material suspensions,” *Int. J. Heat Mass Transf.*, 1994.

[83] L. Huang, M. Petermann, and C. Doetsch, “Evaluation of paraffin/water emulsion as a phase change slurry for cooling applications,” *Energy*, vol. 34, no. 9, pp. 1145–1155, Sep. 2009.

[84] The Engineering Toolbox, “Water - Boiling Points at High Pressure.” [Online]. Available: https://www.engineeringtoolbox.com/boiling-point-water-d_926.html. [Accessed: 23-Apr-2019].

[85] T. R. Whiffen and S. B. Riffat, “A review of PCM technology for thermal energy storage in the built environment: Part I,” *Int. J. Low-Carbon Technol.*, vol. 8, no. 3, pp. 147–158, Sep. 2013.

[86] T. R. Whiffen and S. B. Riffat, “A review of PCM technology for thermal energy storage in the built environment: Part II,” *Int. J. Low-Carbon Technol.*, vol. 8, no. 3, pp. 159–164, Sep. 2013.

[87] H. Akeiber *et al.*, “A review on phase change material (PCM) for sustainable passive

cooling in building envelopes," *Renew. Sustain. Energy Rev.*, vol. 60, pp. 1470–1497, 2016.

[88] M. K. A. Sharif *et al.*, "Review of the application of phase change material for heating and domestic hot water systems," *Renew. Sustain. Energy Rev.*, vol. 42, pp. 557–568, Feb. 2015.

[89] A. M. Khudhair and M. M. Farid, "A review on energy conservation in building applications with thermal storage by latent heat using phase change materials," *Energy Convers. Manag.*, vol. 45, no. 2, pp. 263–275, 2004.

[90] K. Biswas, J. Lu, P. Soroushian, and S. Shrestha, "Combined experimental and numerical evaluation of a prototype nano-PCM enhanced wallboard," *Appl. Energy*, vol. 131, no. 1, pp. 517–529, Oct. 2014.

[91] A. Fateh, D. Borelli, F. Devia, and H. Weinläder, "Summer thermal performances of PCM-integrated insulation layers for light-weight building walls: Effect of orientation and melting point temperature," *Therm. Sci. Eng. Prog.*, vol. 6, no. December 2017, pp. 361–369, 2018.

[92] K. O. Lee, M. A. Medina, E. Raith, and X. Sun, "Assessing the integration of a thin phase change material (PCM) layer in a residential building wall for heat transfer reduction and management," *Appl. Energy*, vol. 137, pp. 699–706, 2015.

[93] R. Ansuini, R. Larghetti, A. Giretti, and M. Lemma, "Radiant floors integrated with PCM for indoor temperature control," *Energy Build.*, vol. 43, no. 11, pp. 3019–3026, 2011.

[94] H. Inaba, Y. Zhang, A. Horibe, and N. Haruki, "Numerical simulation of natural convection of latent heat phase-change-material microcapsulate slurry packed in a horizontal rectangular enclosure heated from below and cooled from above," *Heat Mass Transf. und Stoffuebertragung*, vol. 43, no. 5, pp. 459–470, 2007.

[95] J. F. Belmonte, P. Eguía, A. E. Molina, and J. A. Almendros-Ibáñez, "Thermal simulation and system optimization of a chilled ceiling coupled with a floor containing a phase change material (PCM)," *Sustain. Cities Soc.*, vol. 14, no. 1, pp. 154–170, 2015.

[96] Y. Xia and X. S. Zhang, "Experimental research on a double-layer radiant floor system with phase change material under heating mode," *Appl. Therm. Eng.*, vol. 96, pp. 600–606, 2016.

[97] X. Jin and X. Zhang, "Thermal analysis of a double layer phase change material floor," *Appl. Therm. Eng.*, vol. 31, no. 10, pp. 1576–1581, 2011.

[98] Y. Dutil, D. R. Rousse, N. Ben Salah, S. Lassue, and L. Zalewski, "A review on phase-

change materials: Mathematical modeling and simulations," *Renew. Sustain. Energy Rev.*, vol. 15, no. 1, pp. 112–130, 2011.

[99] V. Verma Prashant and S. K. Singal, "Review of mathematical modeling on latent heat thermal energy storage systems using phase-change material," *Renew. Sustain. Energy Rev.*, vol. 12, no. 4, pp. 999–1031, 2008.

[100] A. de Gracia and L. F. Cabeza, "Numerical simulation of a PCM packed bed system: A review," *Renew. Sustain. Energy Rev.*, vol. 69, no. October 2014, pp. 1055–1063, Mar. 2017.

[101] A. A. Al-Abidi, S. Bin Mat, K. Sopian, M. Y. Sulaiman, and A. T. Mohammed, "CFD applications for latent heat thermal energy storage: A review," *Renew. Sustain. Energy Rev.*, vol. 20, pp. 353–363, 2013.

[102] A. C. Kheirabadi and D. Groulx, "the Effect of the Mushy-Zone Constant on Simulated Phase Change Heat Transfer," *Proceedings of CHT-15 ICHMT International Symposium on Advances in Computational Heat Transfer*, no. MAY 2015. pp. 1–22, 2015.

[103] M. Kumar and D. J. Krishna, "Influence of Mushy Zone Constant on Thermohydraulics of a PCM," *Energy Procedia*, vol. 109, no. November 2016, pp. 314–321, 2017.

[104] C. Pan *et al.*, "Experimental, numerical and analytic study of unconstrained melting in a vertical cylinder with a focus on mushy region effects," *Int. J. Heat Mass Transf.*, 2018.

[105] T. Jonsson, "On the one dimensional Stefan problem with some numerical analysis," *Thesis, Dept Math. Math. Stat. UMEA*, 2013.

[106] I. Ansys, "ANSYS FLUENT 12 . 0 UDF Manual," *Knowl. Creat. Diffus. Util.*, vol. 15317, no. April, pp. 724–746, 2009.

[107] ASHRAE, *Handbook of Fundamentals, SI Edition*. 2017.

[108] ANSYS, "ANSYS Fluent Software: CFD Simulation." [Online]. Available: http://www.ansys.com/en-gb/products/fluids/ansys-fluent. [Accessed: 30-Oct-2017].

[109] V. R. Voller and C. Prakash, "A fixed grid numerical modelling methodology for convection-diffusion mushy region phase-change problems," *Int. J. Heat Mass Transf.*, vol. 30, no. 8, pp. 1709–1719, 1987.

[110] Fluent Inc, "FLUENT 6.3 User's Guide - 24.2 Theory for the Solidification/Melting Model," 2006. [Online]. Available: https://www.sharcnet.ca/Software/Fluent6/html/ug/node973.htm. [Accessed: 15-Aug-2017].

[111] H. Shmueli, G. Ziskind, and R. Letan, “Melting in a vertical cylindrical tube: Numerical investigation and comparison with experiments,” *Int. J. Heat Mass Transf.*, 2010.

[112] A. A. Al-Abidi, S. Bin Mat, K. Sopian, M. Y. Sulaiman, and A. T. Mohammed, “CFD applications for latent heat thermal energy storage: A review,” *Renewable and Sustainable Energy Reviews*. 2013.

[113] S. W. Hughes, “Measuring liquid density using Archimedes’ principle,” *Phys. Educ.*, vol. 41, no. 5, pp. 445–447, 2006.

[114] A. V. Arasu and A. S. Mujumdar, “Numerical study on melting of paraffin wax with Al 2O 3 in a square enclosure,” *Int. Commun. Heat Mass Transf.*, vol. 39, no. 1, pp. 8–16, 2012.

[115] N. Ukrainczyk, S. Kurajica, and J. Šipušiæ, “Thermophysical Comparison of Five Commercial Paraffin Waxes as Latent Heat Storage Materials,” *Chem. Biochem. Eng. Q.*, vol. 24, no. 2, pp. 129–137, 2010.

[116] H. Ettouney, I. Alatiqi, M. Al-Sahali, and K. Al-Hajirie, “Heat transfer enhancement in energy storage in spherical capsules filled with paraffin wax and metal beads,” *Energy Convers. Manag.*, vol. 47, no. 2, pp. 211–228, 2006.

[117] S. Sinaringati, N. Putra, M. Amin, and F. Afriyanti, “THE UTILIZATION OF PARAFFIN AND BEESWAX AS HEAT ENERGY STORAGE IN INFANT INCUBATOR,” vol. 11, no. 2, 2016.

[118] M. F. At, “DSC Investigation of Polymers.”

[119] M. S. K, R. Aikkara, and A. Kadengal, “Analysis and Optimisation of Melting Rate of Solids PCM for Various Shapes and Configurations,” vol. 2, no. 7, pp. 173–183, 2014.

[120] R. Kandasamy, X. Q. Wang, and A. S. Mujumdar, “Transient cooling of electronics using phase change material (PCM)-based heat sinks,” *Appl. Therm. Eng.*, vol. 28, no. 8–9, pp. 1047–1057, 2008.

[121] M. Avci and M. Y. Yazici, “Experimental study of thermal energy storage characteristics of a paraffin in a horizontal tube-in-shell storage unit,” *Energy Convers. Manag.*, vol. 73, pp. 271–277, 2013.

[122] M. Masae, P. Pitsuwan, L. Sikong, K. Kooptarnond, P. Kongsong, and P. Phoempoon, “Thermo-physical characterization of paraffin and beeswax on cotton fabric.”

[123] M. N. Ozisik, *Boundary Value Problems of Heat Conduction*. Dover Publications, 2013.

[124] R. D. Clear, L. Gartland, and F. C. Winkelmann, “An empirical correlation for the outside convective air-film coefficient for horizontal roofs,” *Energy Build.*, vol. 35, no. 8, pp. 797–

811, 2003.

[125] Ansys, “ANSYS FLUENT 12.0 Theory Guide - 5.2.2 Natural Convection and Buoyancy-Driven Flows Theory,” 2009. [Online]. Available: http://www.afs.enea.it/project/neptunius/docs/fluent/html/th/node108.htm. [Accessed: 14-Jan-2018].

[126] M. Fossa, M. Misale, and G. Tanda, “Schlieren visualization of water natural convection in a vertical ribbed channel,” *J. Phys. Conf. Ser.*, vol. 655, no. 1, 2015.

[127] S. Wilson, “Dwelling size survey,” *Analysis*, no. April, p. 16, 2010.

[128] M. Economidou, J. Laustsen, P. Ruyssevelt, D. Staniaszek, D. Strong, and S. Zinetti, *Europe’ s buildings under the microscope*. 2011.

[129] Department for Communities and Local Government, *English Housing Survey HOUSEHOLDS 2013-14*. 2015.

10 Appendices

10.1 Description of 'Energy Storage '

Energy is defined as the capacity to do work and exists in numerous forms such as electricity, light and heat. Energy storage is the procedure of storing energy to perform work at a time later than the energy's generation and typically utilizes the conversion of one form of energy to another.

At the present, energy storage is used sparingly at National Grid scale and only where necessary. Within the consumer environment energy storage is abundant and found in many devices from mobile phones to solar thermal heat storage tanks. The former and latter cases are set to change dramatically in the near future, driven by the increasing use of energy, electrification of transport and heat, in addition to the growing penetration of unstable electrical generation sources such as wind and solar.

A characteristic and familiar example of energy storage would be a hot water tank in a person's home. The tank is pre-charged with cold water and heated to provide a reservoir of hot water for use in showers, baths etc… This includes a conversion step of electrical or chemical energy into heat energy and unlike other forms of energy storage, heat storage usually only has one conversion of energy. Other forms such as pumped hydro-electrical storage have two conversions, one of electrical energy into gravitational potential energy stored in the water at a great height and the other a conversion in reverse back into electricity for use in the National Grid.

The unstable generation sources in the UK National Grid coupled with increasing demand lead to sharper peaks and troughs in electrical supply and demand. This is straining already ageing generation and transmission infrastructure even further. A solution must be found to avoid blackouts, over capacity equipment and backward flow of electricity.

In addition, the electrification of heat and de-carbonisation of heat presents a particularly large hurdle in the UK for the future, as due to this energy requirement being almost exclusively fossil fuelled, heating buildings presents a third of the total UK energy use. A significant amount of this is likely to be electrified leading to further increased demand due to the UKs' policy goals of becoming carbon free. Furthermore, UK transport is also set to be electrified either directly or indirectly contributing even further to energy demand. Combined these factors can potentially triple the current energy supplied via electrical means in the future decades.

Energy storage alongside complimentary methods (such as demand side management, smart grid and grid re-enforcement as envisaged as the economic solution for this problem in the

approaching decades), will flatten the supply and demand curves in a safe and economic manner.

10.2 Description of 'Heat Storage '

Thermal energy storage or heat storage is any technology which stores and releases heat or "cold" on demand. These technologies are widely varied, both commercial and emerging. They are typically utilized for conditioning the air and water servicing within a building.

Heat storage technologies of the sensible type (utilizing the specific heat of a material and a temperature change to store energy) are well understood and widely used commercially and residentially.

Other technologies such as phase change (storing energy in the change of phase of a material) and thermochemical (using a chemical reaction to store energy) however are not very well understood or widely used and still require significant amounts of research.

10.3 Economy 7 Calculated table comparison of tariffs

Table 12 - Comparison of Economy 7 tariffs with respect to costs for different day night ratios of energy usage.

		Economy 7							
		Cost with ratio (Day:Night)							
Supplier	**Tariff**	**80 20**	**70 30**	**60 40**	**50 50**	**40 60**	**30 70**		**Standard Tariff**
British Gas	Standard	£ 2,903.42	£ 2,697.28	£ 2,491.13	£ 2,284.98	£ 2,078.84	£ 1,872.69		£ 2,383.77
British Gas	Fixed Price March 2018	£ 3,059.99	£ 2,853.84	£ 2,647.70	£ 2,441.55	£ 2,235.40	£ 2,029.26		£ 2,540.34
British Gas	Fix & Reward January 2017	£ 2,903.42	£ 2,697.28	£ 2,491.13	£ 2,284.98	£ 2,078.84	£ 1,872.69		£ 2,383.77
First Utility	iSave Fixed December 2016 v5 electricity only	£ 1,933.79	£ 1,839.45	£ 1,745.12	£ 1,650.79	£ 1,556.46	£ 1,462.13		£ 2,134.64
Extra Energy	Fresh Fixed Price Dec 2016 v6	£ 2,032.56	£ 1,932.69	£ 1,832.82	£ 1,732.95	£ 1,633.09	£ 1,533.22		£ 2,162.59
Extra Energy	Clear Fixed Price Dec 2016 v3	£ 2,036.61	£ 1,936.74	£ 1,836.87	£ 1,737.00	£ 1,637.14	£ 1,537.27		£ 2,084.22
Ovo Energy	Better Energy Fixed (all online)	£ 2,152.13	£ 2,054.28	£ 1,956.42	£ 1,858.57	£ 1,760.71	£ 1,662.86		£ 2,173.75
Scottish Power	Online Fixed Price Energy November 2016	£ 2,266.77	£ 2,129.86	£ 1,992.96	£ 1,856.06	£ 1,719.15	£ 1,582.25		£ 2,173.57
EDF Energy	Blue+Price Promise November 2016	£ 2,515.91	£ 2,344.25	£ 2,172.58	£ 2,000.92	£ 1,829.25	£ 1,657.59		£ 2,123.34
E.ON	E.ON Energy Fixed 1 year v16 (Paperless Billing)	£ 2,806.61	£ 2,619.12	£ 2,431.63	£ 2,244.14	£ 2,056.65	£ 1,869.16		£ 2,580.67
E.ON	Age UK Fixed 2 year v5 (Paperless Billing)	£ 2,808.48	£ 2,620.99	£ 2,433.50	£ 2,246.01	£ 2,058.52	£ 1,871.03		£ 2,584.59
EDF	Standard	£ 2,786.55	£ 2,587.11	£ 2,387.68	£ 2,188.24	£ 1,988.80	£ 1,789.36		£ 2,577.79
npower	Price Fix March 2017	£ 2,630.93	£ 2,485.12	£ 2,339.31	£ 2,193.49	£ 2,047.68	£ 1,901.87		£ 2,687.41

Note:

Scaling from red to white backgrounds on Economy 7 tariffs indicates the most expensive to least expensive. Scaling from green, white to red on standard tariffs shows the least expensive to the most expensive standard tariff and font colouring from green or black on Economy 7 tariffs indicates whether the Economy 7 tariff is cheaper or more expensive that the same provider's standard tariff.[129]

10.4 System Constraints

Constraints are extremely important for the potential of any of the available technologies, both in terms of whether they will physically fit, and whether the occupants would be comfortable with the health, safety and any other trade-offs of a particular system.

It is important to document what sizes of residences is available, with what available utilities services, floor, utility and garden space.

10.4.1 Size and form Constraints

In order to determine how large a system can be or what form it can take, it is important to review where it can be situated, this will include what the types of houses are, how large they are, who owns them and where the properties are located.

The types and sizes of houses could indicate for example whether the internal utility space of the house is important in terms of sizing or whether a system could be installed externally into a garden etc…

10.4.2 Domicile accessible indoor and outdoor space trends

Figure 189 - Average Usable floor area of residences by occupier type [152].

Usable floor area information was also gathered and indicated owner occupiers have the largest usable floor area followed by private renters and then social renters, 109 m^2, 78m^2 and 66 m^2 respectively. (Translated to usable space per person, owner occupiers 55 m^2, private renters 39 m^2 and social renters 38 m^2.)

A dwelling size study undertaken by the Commission for Architecture and the Built Environment which also gave similar results relating the DECC comparison of who typically owns which kind and size of property.

Table 13 - Results of gross internal area (m^2) of the Commission for Architecture and the Built Environment's dwelling sizes study of 200 dwellings by type [127].

Typology	Mean	Median
Studio	32.1	31.9
1 Bedroom flat	46.6	46.3
2 Bedroom flat	60.7	59.1
3 Bedroom flat	86.5	89.6
1 Bedroom house	64.3	69.1
2 Bedroom house	71.2	69.2
3 Bedroom house	95.6	92.1
4 bedroom house	120.6	117.0
5 bedroom house	163.5	158.7

The same study also generated individual median values for specific areas within the properties which are shown below. The availability of utility space is particularly important as this is where a heat storage system would be situated.

Table 14 - Results of gross internal area (m^2) of specific types of area the Commission for Architecture and the Built Environment's dwelling sizes study of 200 dwellings by type [127].

Typology	Storage	Utility	Kitchen	Notional corridor*
All Tenures				
Studio	0.43	0.46	3.81	1.84
1BF	0.69	0.49	6.06	1.49
2BF	0.70	0.53	6.45	1.69
3BF	0.92	0.36	8.27	1.70
1BH	1.21	0.50	5.27	2.31

Typology	Storage	Utility	Kitchen	Notional corridor*
2BH	1.15	0.60	6.85	3.20
3BH	1.70	0.83	7.84	2.54
4BH	1.59	0.95	8.69	1.79
5BH	4.12	3.54	10.25	1.88